Visual Methods of Monitoring the Effect of Wettability on Fines Migration in Sandstones

SELLICK, CATRIONA,HELEN

Visual Methods of Monitoring the Effect of Wettability on Fines Migration in Sandstones

Catriona Sellick

Abstract

Global energy demands are changing, with focus on replacement of hydrocarbons with renewables. However, the reliance on hydrocarbons cannot be removed in the short term, so any methods to improve the efficiency and environmental profile of hydrocarbon extraction are needed. Hydrocarbon extraction rate may be reduced if the formation becomes damaged during the extraction process. This damage may be particularly problematic during low salinity enhanced oil recovery (EOR) and although there are many mechanisms by which this may happen, the mechanism which is of particular interest in this work is that of fines migration, especially in combination with variation of wettability.

This work considers a variety of different methods to investigate the ways in which fine mineral particles move when encountering surfaces with variable wettability, and new test methods to rapidly assess the fines migration potential of a sandstone. Throughout this work, 3D printing is used to assist in these investigations, and hence firstly a comprehensive study of the wettability of commonly used 3D printing materials was undertaken which showed good agreement with the literature. Contributions to the wettability of aspects of the printing process resulting in variation of roughness was also evaluated but did not correlate at the length scales studied. Secondly, a study of the likelihood of removal of fines from sandstones by ultrasonic treatment in various salinity brines was performed, finding increased removal in low salinity brines and giving general agreement to those previously reported in the literature. Finally, several conceptual experiments looking at methods to monitor the movement of fine particles over surfaces of variable wettability, including drop spread and flow through 3D printed flow cells with individual particle tracking, were carried out. The results were compared to flow simulations and showed good agreement between particle tracking and simulated flow.

Visual Methods of Monitoring the Effect of Wettability on Fines Migration in Sandstones

Catriona Sellick

A Thesis presented for the degree of Doctor of Philosophy

Department of Earth Sciences

Durham University

March, 2022

Declaration

The work in this thesis is based on research carried out in the Greenwell Group, Department of Earth Sciences, Durham University. No part of this thesis has been submitted elsewhere for any other degree or qualification and it is all my own work unless otherwise stated in the text.

Copyright

Acknowledgements

Firstly, I would like to thank my supervisor, Prof. Chris Greenwell, for making this PhD possible. His expertise and willingness to allow students to find their own direction in research, combined with his guidance and encouragement when things weren't quite going to plan, were invaluable. I would also like to thank my second supervisor Dr Kate Dobson for her advice, encouragement, expertise and creativity as without those a large part of this work would not have been possible. Thank you also to others who have helped and guided me along the way – Dr Pablo Cubillas and Leon Bowen in Durham, and the team at BP Sunbury, especially Dr Ian Collins and Dr Kuhan Chellappah – for comments, training and discussions. And also John Bucknall and Chris Mescall (and supervisor Prof. Peter Holliman) for letting me into their labs to measure the surface roughness of hundreds of little pieces of plastic. Without all of these people my PhD would not have come together so completely.

Secondly, I must thank the NERC Oil and Gas CDT for funding my PhD and providing world-class training in aspects of geoscience that I had never even considered, let alone participated in. The good times I had with the CDT cohort in the rain in Manchester, snow in Fort William and glorious sunshine in Tenby were memorable, and the knowledge I gained has helped me considerably. John Underhill, Lorna Morrow and Anna Clark truly put together a fantastic CDT programme.

Back in Durham, I have to thank all the members of the Greenwell group for putting up with me and my 3D printers – Rikan, Tom, Valentina, Vicky, Nikos, Christos, Daud, Tara, Hector, Catherine, Katie and many more. Working in the office and lab has been great fun with all of you (apart from the times when the lab was a mess).

Finally, I'd like to thank my family. To my parents, Carolyn and Neil, and my sisters, Kirsten and Alex - I'm fairly sure listening to me talk about 3D printing and lab work and writing and deadlines must have been rather tedious at times, but thanks for putting up with it. To my husband, William – without your love, support and encouragement I would never have managed to start this PhD, let alone finish. Thank-you.

Contents

List of Tables

List of Figures

Chapter 1 Introduction

During oil production water is often injected via a well into the subterranean rock formation where oil is held, to maintain a pressure gradient to the well where the oil is extracted from. The migration of fines (small mineral particles) in sandstone rocks in the near-wellbore of this water injection well (typically the area of concern spans a radius of under 30 m, and even more importantly in the closest 30 cm) is of consequence as fines may become mobilised and move in the small pore spaces and potentially cause blockage or reservoir damage. The blockage of the pore spaces may lead to loss of flow rates, and hence increase in pressure, reduction in production rate and, ultimately, a loss in revenue. This problem is especially of concern during enhanced oil recovery operations where desalinated water is injected, which is known to be reactive towards quartz-surface bound clay minerals.

This PhD will look at methods of visualising aspects of fines migration (small mineral particle movement) in sandstones near the injection well during enhanced oil recovery operations. The research will focus on examining the effect of wettability (the preference for a mineral surface to be coated by a certain fluid, e.g. oil versus water) on the adhesion, release and movement of fine particles at high and low salinity and during changes in salinity, and, in particular the development of new methods of monitoring the movement. The insight gained will inform whether careful engineering controls or chemical treatment during an enhanced oil recovery operation may mitigate the detrimental effects of the migration of fines.

To evidence fines migration and to quantify the effect of injection water chemical and physical parameters a number of different techniques will be used. These include scanning electron microscopy (SEM), x-ray diffraction (XRD), micro-computed tomography x-ray scanning (micro-CT), and light microscopy.

To place this work in context, this chapter will describe the oil drilling process, and give the thesis objectives and outline.

1.1 Oil Exploration and Production

In 2019, fossil fuels provided 80% of the global energy demand (BP, 2022). Increase in efficiencies suggests that the global energy demand will decline by 2050, but it is estimated that fossil fuels will still provide 20% to 60% of that energy, with natural gas being the primary fossil

fuel utilised and oil moving from fuel use to feedstock use (BP, 2022). However, combustion of hydrocarbons as fuel and their impact on global temperatures is currently cause for concern. Continued use of hydrocarbon fuels without mitigation and the associated production of greenhouse gases (GHGs) are predicted to cause an increase in global temperature of 2 – 3 °C by 2100 (Hansen et al., 2006). The Paris Agreement (United Nations, 2015) aimed to reduce greenhouse gas emissions to a level that will prevent global average temperature rise increasing above 2 °C compared with pre-industrial levels, and additionally the more recent COP26 summit highlights the need to reduce the temperature rise to 1.5 °C (COP26, 2021). Strategies have been put into place by the EU, Canada, Mexico and the United States to reduce greenhouse gas emissions by 80% in order to ensure this happens (United Nations, 2017). Hence, although the need for oil and gas exploration and production is still present, global demand is changing, and extraction targets and methods may need to change in order to help meet emissions targets to safeguard the future.

The process of oil exploration and production is an extremely complex, time consuming, labour intensive and expensive process, with potential costs in the millions of dollars (Augustine et al., 2006). However, even with the continued reduced price of crude oil and profit margins seen since 2008 (Petroff and Yellin, 2015, Baumeister and Kilian, 2016), the annual profits of large oil and gas companies, such as BP and Chevron are generally in the billions of dollars, making the difficulties worthwhile. A number of books have been written on the subject, including good overviews by Gluyas (2004), Baker and Service (1996) and Bommer (2008), and numerous texts on specific aspects of the process. What follows will give a very brief overview to place the current work in context and the interested reader is referred to the texts mentioned.

There are a number of phases during oil exploration and production. These may be categorised as exploration, appraisal, development and production (Gluyas, 2004).

The first step that must be undertaken is to find a location to drill. Initially, this may involve the use of satellite images and gravimetric and magnetic data to assess potential locations for further exploration. Following the selection of the geographic location, further exploration often makes use of seismic surveys. These allow characterisation of the structures in the shallow earth, and recommendations as to the most likely favourable drilling locations to be made.

Given the recommendation based on the data above, one or more exploration wells are drilled. These wells will usually aim to drill into the region most likely to contain hydrocarbons, in order to assess the quality of the reservoir and hydrocarbon therein.

The hydrocarbons found in the reservoir may be oil or gas, and the composition of the oil may vary from heavy oils and tars to light, volatile oils. Oils with a lower viscosity tend to have a higher proportion of lower molecular weight hydrocarbons, which may make recovery and processing easier and the oil more desirable. However, the level of sulphur of the oil must also be taken into account, as hydrocarbons with a low sulphur content are also desirable due to the increased ease of processing. In contrast higher viscosity oils tend to come with higher recovery and processing costs, making recovery more expensive and hence lowering the economic viability of the oil during times of low oil price. Consideration must be given to the economic viability of the crude oil produced from the well before decisions can be made as to whether, or how, to go ahead with production.

Initial production is termed “primary recovery”, and may recover up to 75% (Ahmed, 2010) of the original oil in place (OOIP) for water driven reservoirs (illustrated in Figure 1-1 c, d, e and f), although across all reservoirs the recovery is generally quoted as around 30% (Kokal and Al-Kaabi, 2010). Primary recovery is driven by natural mechanisms, such as natural aquifer water drive, gravity drainage, and gas drive, either from gas expansion or gas coming out of solution from the oil as the pressure decreases. It is found that the efficiency of primary recovery mechanisms is highly variable, depending on the reservoir characteristics.

As production slows, secondary recovery mechanisms may be employed to recover up to approximately 35% of the OOIP. The decision as to whether this will take place will be based on the whether the additional recovery will be economic, but this will now often have been planned into the initial field development strategy and so will, nearly always, take place. These involve the drilling of an additional injection well, often at the same time as the initial production well to reduce the costs associated with hiring a drilling rig and injecting either gas or water to displace the oil towards the production well. The positioning of injection wells in relation to the reservoir and the production wells is illustrated in Figure 1-1.

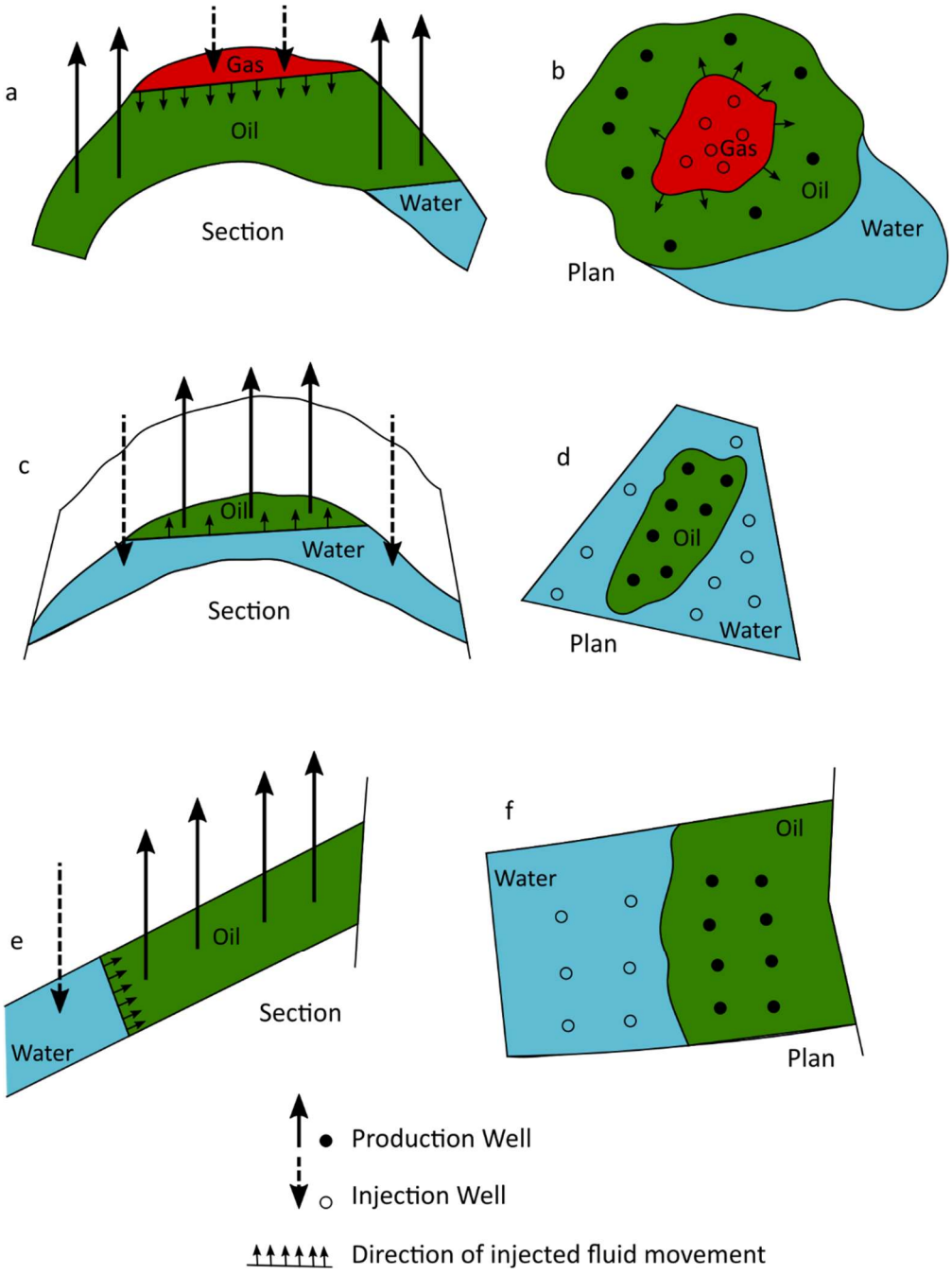

Figure 1-1: Illustration of positioning of injection and production wells for different hydrocarbon reservoirs. a, b: Location of injection wells for gas injection. c, d, e, f: location of injection wells for water injection. Adapted from Latil (1980).

An injection well is a well drilled to be used to place fluids underground. Injection wells are used in a wide range of industries for many different reasons. Often, there is concern over potential aquifer contamination, especially when related to oil and gas operations or waste storage. In order to regulate and monitor injection wells in the United States, the United States Environmental Protection Agency defines 6 different types of injection well and defines carefully

where these wells may be drilled and what controls must be put in place to prevent aquifer contamination. The 6 classes of injection wells are listed below.

“Class I wells are used to inject hazardous and non-hazardous wastes into deep, isolated rock formations.

Class II wells are used exclusively to inject fluids associated with oil and natural gas production.

Class III wells are used to inject fluids to dissolve and extract minerals.

Class IV wells are shallow wells used to inject hazardous or radioactive wastes into or above a geologic formation that contains a USDW.

Class V wells are used to inject non-hazardous fluids underground. Most Class V wells are used to dispose of wastes into or above underground sources of drinking water.

Class VI wells are wells used for injection of carbon dioxide (CO_2) into underground subsurface rock formations for long-term storage, or geologic sequestration.”(United States Environmental Protection Agency, 2016b)

For fluid injection for enhanced oil recovery, the wells are classified as Class II. Currently there are approximately 160,000 Class II wells in the United States; of these, in 2019, 122,011 were recovery wells, with 37,649 being used for disposal of fluids associated with oil and gas production (United States Environmental Protection Agency, 2022).This represents an increase from 144,000 Class II injection wells in total in 2005 (Gómez, 2014), although this number has decreased from the 2015 number of approximately 180,000 total, with 145,000 being recovery wells (United States Environmental Protection Agency, 2016a).

Injection wells for enhanced oil recovery by low salinity water injection are typically located anywhere up to a couple of kilometres from the production well, towards the edge of the producing formation. The injection wells may be planned during the initial field planning phase of the oil recovery operation, or may be drilled at a later stage as more information is obtained about the precise location of the oil and its flow patterns following information obtained about the drainage of the reservoir during initial production. The formation is usually of the same rock type, but in a position where the formation may not be saturated with oil. This means that although the mineralogy of the rock may be the same as that of the formation, the properties of the rock may be different to the rock that is producing oil due to changes in wettability and

pore fluid composition. See Figure 1-1 for an illustration of relative positioning of injection and production wells.

In order to recover further oil than secondary methods allow, tertiary, or enhanced, oil recovery (EOR) mechanisms are utilised in order to recover the maximum economical volume of oil from the well. These methods look to alter the properties of either the oil or the reservoir to make more of the oil economically recoverable. There are a number of techniques that may be used, including injection of low salinity fluids, polymer flooding, surfactant injection or introduction of heat or gas to reduce the viscosity of the oil (Taber et al., 1997). Using EOR methods to increase the percentage of OOIP recovered may however have the undesired consequence of reducing the permeability of the formation (Civan, 2007); this phenomenon is often termed formation damage. Of particular interest to this study is the injection of low salinity fluids into the injection well region, as this has been shown to promote fines migration in sandstones (Mungan, 1965, Bernard, 1967, Rosenbrand et al., 2015), which is one of the accepted formation damage mechanisms. Indeed, all the commonly used EOR methods may potentially cause damage to the formation if not used carefully, as discussed below.

1.1.1 Formation Damage

Formation damage is defined by Clegg (2007) as “Any unintended impedance to the flow of fluids into or out of a wellbore”. This is important as any reduction in the flow of fluids in the wellbore may affect the amount of oil recoverable from the reservoir, thereby affecting the economic viability of the drilling operation.

There are numerous mechanisms by which formation damage may occur. The general damage mechanisms may be divided into 4 general categories: mechanical, chemical, thermal and biological (Bennion, 1999, Faergestad, 2016).

1.1.1.1 Mechanical damage

Mechanical damage may be defined as the damage to the formation due to non-chemical means by direct or non-direct interaction of fluids or equipment with the formation. Causes may include:

Fines migration – movement of small solid particles in the pore spaces of a clastic rock, potentially causing loss of permeability due to pore blockage (discussed further in Section 2.2). This may be seen particularly where low salinity fluids are used, especially at high flow rates.

Migration of external fluid solids into the formation – whereby the solid particles in the drilling fluid providing increased density, viscosity, fluid loss reduction, lost circulation prevention or other properties move into the pore spaces in the formation and may block those pore spaces. This, in general, only affects the very near (1 – 2 cm) wellbore. In some instances this may be desirable (such as when large volumes of drilling fluid is being lost to the formation), but in general, and especially in the reservoir, this should be avoided.

Glazing or mashing of the wellbore surface by the drill bit – glazing is the change in surface of the wellbore due to poor heat removal during drilling, whereas mashing is the forcing of cuttings and other wellbore fines into the wellbore surface by the movement of the drill string contacting the formation wall. Mashing may be more problematic during horizontal drilling, as in general, hole cleaning is less effective in high-angled wells.

Disintegration of the rock matrix into smaller particles by perforation explosions – during perforation operations, explosive charges are used to fracture the rock in the vicinity of the wellbore in order to improve permeability. This may be related to fines migration, as additional fines are created in this damage mechanism, which may cause damage in a similar manner to fines migration.

Proppant crushing – during hydraulic fracturing, the increased stress on the rock causes pressure on the proppant particles high enough to cause the proppant particles to break apart, and either embed themselves into the fracture surface, or produce fines which, again, may migrate and block pores.

Phase Trapping – where the introduction of an immiscible fluid causes a reduction in the relative permeability of the formation. See Figure 1-2.

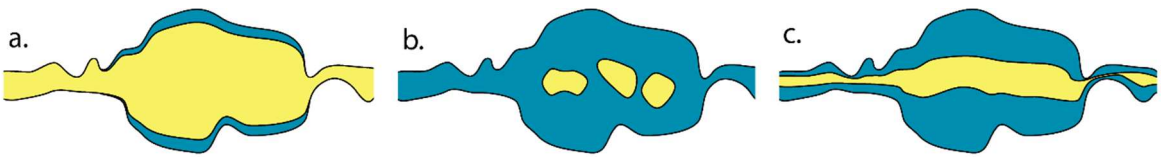

Figure 1-2: Illustration of formation damage by phase trapping resulting in reduced permeability around injection wells. Blue = water, cream = gas. a. Pore surface is coated with water, with gas in the majority of the pore space. b. Flushing with water leaves small pockets of gas in the pores, with the majority of the pore now water-filled. c. Relative permeability of the pore is now reduced due to the larger volume of water in the pore space. Adapted from Bennion et al. (1996)

1.1.1.2 Chemical Damage

Chemical damage may be defined as the damage due to adverse reactions between the introduced fluid and the formation, or the formation fluids and the introduced fluids. Mechanisms may include:

Clay swelling or dispersion (deflocculation) – the interaction of water with certain clay types may cause the clays to increase in volume (swell) or disperse and migrate, thereby reducing the permeability of the formation. This may occur alongside fines migration and cause additional damage.

Polymer adsorption – polymers (and other large molecules) present in the fluid encountering the formation may adsorb onto the pore surface, thereby reducing the pore diameter and hence the porosity. The presence of the polymer coating the pore surface may also modify the wettability of the pore surface.

Formation dissolution – depending on the chemistry of the fluid encountering the formation, some components in the formation may be susceptible to dissolution. One example of this is the dissolution of salts by water-based fluids or carbonates by acidic fluids, and another quartz at high temperature and pH conditions (Reed, 1982), for example as may be encountered during a steam injection operation during heavy oil recovery. In some cases this may be desirable (potentially in the case of carbonate reservoirs and carbonate dissolution by acid) as this may increase the permeability of the formation. However, the dissolution of salts is usually undesirable, as this will cause poor hole gauge and potential formation collapse, as well as changes in the chemistry of the fluid encountering the formation.

Formation of solids – these may be either precipitates due to incompatible fluids encountering each other or components of the fluids flowing in the well (either reservoir fluids or fluids that have been placed into the reservoir) precipitating out due to changes in temperature.

Formation of emulsions – many of the fluids introduced into the wellbore and formation may contain surfactant molecules or enable surfactants to form at the crude oil-fluid interface. When an immiscible fluid is then encountered, an emulsion may then be created. Emulsions often cause an increase in the viscosity of the fluid flowing, thereby potentially causing blockages as high enough pressures cannot be applied to cause the fluid to flow through the small pore spaces.

Wettability alteration – again, a potential problem encountered with the use of surfactant molecules. These molecules, especially the surfactants designed as “wetting agents”, may adsorb onto the wellbore and pore walls and alter the wettability of the surface. See Section 2.2.1.5 for further details.

1.1.1.3 Biological Damage

Biological damage generally refers to the introduction of bacteria into the formation in water-based fluids (either drilling fluids or injection water), or the rapid stimulation of populations of existing bacteria. There are two main damage mechanisms associated with the introduction of bacteria.

Firstly, bacteria may behave like solid particles, and cause physical blocking of the pores by mechanical mechanisms (similar to fines migration). This property is enhanced by the extracellular polysaccharide substances (EPS) often excreted by bacteria, which adheres the bacteria to surfaces and may contribute to pore blocking. Most bacteria do not actively propagate at typical down-hole temperatures (> 90 °C), but as fluids from the surface are repeatedly pumped to the bottom of the well, the down-hole temperature may begin to reduce to a temperature at which the bacteria are able to grow. The growth of further bacteria may also contribute to pore blockage.

Secondly, sulphate-reducing bacteria may degrade the oil in the reservoir, producing H_2S and thereby souring the well. The presence of H_2S may cause the previously economically viable recoverable oil to become unviable, as the cost to mitigate the potentially dangerous consequences of encountering H_2S may be too high compared to the revenue gained from the oil.

1.1.1.4 Thermal Damage

Thermal formation damage is classified as the damage associated with the increase in temperature of the formation above the normal down-hole temperature, due to use of enhanced recovery methods such as steam injection or *in-situ* combustion. There are a number of proposed mechanisms:

Mineral transformation – at elevated temperatures, kaolinite, which is generally considered not to swell or disperse in fresh water, may be transformed to smectite in the presence of elevated temperature and solubilised quartz.

$$Al_2Si_{12}O_4 + SiO_2 + M^{2+} \rightarrow MAl_7S_{11}O_{30}OH_6 + H_2O$$

Kaolinite + Quartz (aq) + Divalent Cation (Ca, Mg or Fe) → Smectite + Water

Mineral dissolution – In addition to the previously mention problems of poor hole gauge and the potential of wellbore collapse, minerals which have dissolved in high temperature fluids may re-precipitate as the fluid cools, potentially blocking pores as it does so. This is a particular problem in sandstone reservoirs where steam injection is employed as an enhanced recovery mechanism, as quartz may be seen to dissolve (Reed, 1982). In addition, minerals are often precipitated around insoluble materials, which, as the material holding them in place dissolves, may become mobilised and again may move to cause pore blockage, and hence reduction in permeability.

Wettability alteration – wettability is descried in more detail in Section 2.2.1.5. In order for a formation to be oil-wet, the naturally water-wet minerals have an adsorbed coating of polar organic molecules. This coating may be disrupted at higher temperatures, thereby making the formation more water-wet. An abrupt change in wettability may occur when a hot water flood is replaced by a steam flood, as the oil surrounded by water in the water-wet pores is suddenly put into contact with, and adsorbs to, the pore wall when the water is vaporised by the injected steam.

Emulsion formation – fresh water tends to emulsify in high density, high viscosity crude oils. The hot water or steam being used to promote the release of these crudes therefore is highly susceptible to emulsification. This will cause similar problems to the emulsion formation mentioned above.

1.1.1.5 Combination of effects

It is clear that when considering the individual formation damage mechanisms that some may interrelate and change the severity of others. For example, it is known that fines migration will only occur if the phase that wets the fines is moving (Muecke, 1979). If then formation damage by phase trapping occurs, the reduction in permeability may become amplified as the space available for particle movement has become reduced. Similarly for wettability alteration – if the wettability of fines is changed due to polymer or surfactant adhesion, these fines may become mobile where they would not have been before and again the resulting formation damage may be amplified.

It is also expected that at different times during the lifetime of a well, different formation damage mechanisms may be of more importance. For example, during perforation of a well, fines migration due to fines created from the perforation explosions may dominate, but later

during the operation fines migration of the fines in the pore spaces may dominate. Similarly, the fluids encountered by the formation will change during the lifetime of the well. Initially, the drilling fluid used to drill the well may contain polymers or surfactants which may invade into the formation (although normally only by a couple of centimetres). These may change the wettability of the near-wellbore region. However, later in the lifetime of the well, the injection fluids used may be water or a simple brine, without polymers or surfactants. These fluids may promote fines migration due to their low salinity.

The complex nature of the various formation damage mechanisms means that a detailed history of the conditions encountered by the formation is required in order to predict how the formation may react to further treatments. A greater understanding therefore of how fines migration and wettability interplay may be desirable to help prevent formation damage and improve the efficiency of fluid injection operations.

1.2 Thesis objectives

This thesis aims to examine novel methods to monitor fines migration in sandstones when salinity changes from high salinity to low salinity (mimicking the conditions in particular during a low salinity EOR operation, but this may be expanded to any other injection operation where the high salinity formation brine may be replaced by a lower salinity injection fluid), and to assess the effect of variable wettability on the movement of fines across surfaces under the same salinity conditions. 3D printing will be considered for its applicability in producing models which may give a good representation of sandstone properties, and will then be used to produce new model systems which will be assessed for their potential to give information about how fine particles may move. This work will be divided into three main themes:

1. Assessment of 3D printing materials and how the wettability varies with material chemistry and surface roughness with a view to use this data to 3D print synthetic sandstones with wettability variation similar to that seen in a natural sandstone.
2. A study of the effect of ultrasound on sandstone and whether sandstone cleaning by ultrasound is affected by the salinity of the brine in which the sandstone is cleaned, similarly to how brine salinity affects fines migration in sandstones.
3. The use of 3D printed models in studies to look at the movement of fine particles across different surfaces (with variable wettability) and in various model pore geometries to explore new ways in which fines migration can be visualised.

1.3 Thesis outline

This thesis is divided into 7 chapters. At this time, no part of the thesis has been published, but plans for publication are detailed in Appendix D

Chapter 2 - Literature review: This chapter reviews the current state of understanding of fines migration, and provides a background context for where this work sits.

Chapter 3 - Experimental Methods: This chapter describes in detail the main experimental techniques used throughout this thesis.

Chapter 4 - Roughness and Wettability of 3D printed surfaces: This chapter examines a large number of 3D printing materials and assesses whether the wettability measured by sessile drop contact angle is reproducible and representative of the wettability of the materials previously reported. The limitations of wettability measurement are also assessed, and the suitability of the sessile drop technique for such materials is analysed. Additionally, the roughness of the 3D printing materials is varied and correlated with wettability. Roughness parameters are extracted from the surface profiles obtained from roughness measurements and correlation is sought between the roughness parameters and the measured contact angle.

Chapter 5 - Controlled Ultrasonic Fines Disruption: Here, a new method of assessing the fines migration potential of a sandstone is developed. Small pieces of sandstone are subjected to ultrasound in brines of different salinities, and the concentration of fines released into solution following the treatment are measured using colorimetry. Singular salinities and a repeated treatment in a series of brines of reducing salinity, replicating the conditions which may be experienced by a sandstone reservoir during a low salinity water flood, are compared.

Chapter 6 - Monitoring Particle Flow on Surfaces and in 3D prints: In this chapter, a number of methods of visualising particle flow are examined. Flow of bulk clay suspensions highlighted using fluorescent dye monitored as singular drops and continuous flow over surfaces of variable wettability in salinity conditions resembling low salinity EOR is imaged and analysed. Methods of visualising individual particles in micro-CT in flow conditions are developed, and particle tracking in flow is compared to simulation in flow cells.

Chapter 7 - Conclusions, current work and future potential: The findings of the previous experimental chapters are summarised, and the work is placed into context with the aims of the thesis and the current work being carried out in the area. Future work which may be based on the results obtained in this thesis is also discussed.

Chapter 2 Literature Review

Global hydrocarbon demand is changing and although the demand may reduce, the impact of immediately ceasing hydrocarbon extraction on the global economy would be extreme. It is therefore necessary to continue with oil and gas exploration and production in the future, but looking to do so in a way which considers and mitigates as far as possible the environmental impact of doing so. One method of achieving this is to look to understand how to maximise the efficiency of production by reducing the effects of formation damage, discussed in the previous chapter. In this chapter, two aspects of formation damage are examined together – fines migration and how wettability may contribute. Fines migration around the injection well of a sandstone reservoir may occur if fluid injection is not carefully planned and controlled. But what are fines, and what are they composed of? And what conditions, aside from wettability, need to be controlled for to prevent the migration of fines and the subsequent formation damage? In order to understand this problem, much experimental work has been undertaken. The experimental work on fines migration often uses models and analogues rather than reservoir rock; these are also examined and the advantages and limitations are discussed.

2.1 Fines in Sandstones

Geologically, granular materials, sediment and particles in clastic rock may be classified by their grain size. The Wentworth scale is most commonly used.

Table 2-1: Geological classification by grain size, from Wentworth (1922).

Size range (metric)	**Aggregate name (Wentworth class)**
>256 mm	Boulder
64–256 mm	Cobble
4–64 mm	Pebble
2–4 mm	Granule gravel
1–2 mm	Very coarse sand
0.5–1 mm	Coarse sand
0.25–0.5 mm	Medium sand
125–250 µm	Fine sand

62.5–125 µm	Very fine sand
3.9–62.5 µm	Silt
<3.9 µm	Clay

Sandstones are comprised of a framework of cemented, sand-sized (62.5 µm – 2 mm) grains, with smaller (silt- or clay-sized) grains surrounding the framework as matrix material. The sand-sized grains are formed from weathering or erosion processes acting upon pre-existing rocks, whereas the matrix material is generally comprised of quartz, calcite or feldspar deposition, or clay minerals. Of these, the clay minerals are generally considered to be the most reactive and mobile, and therefore more damaging. Following deposition, which may occur in a wide variety of different environments, from deep marine to floodplains, continued burial will cause increased temperature and pressure on the grains, which will then cause compaction and dissolution of some minerals followed by subsequent precipitation and cementation and the formation of sandstone. It should be noted that the matrix is distinct from the cement that holds the sandstone together, as the matrix is deposited at the same time as the sand-sized grains, whereas the cement is precipitated during diagenesis (Nichols, 2009).

The precise composition of the sandstone will vary depending on the depositional environment and diagenetic history, and hence the composition of the fines associated with the sandstone will also vary. The main minerals considered as fines are discussed below.

A number of definitions for “fines” in sandstones have been proposed. Muecke (1979) considers fines to be “particles that passed through the 400-mesh screen”. Synthetic cores prepared by Gabriel and Inamdar (1983) also contain fines of this size, but measured fines released during a core flood experiment were determined to have a mean diameter of 2 – 2.5 µm, with 98 % < 10 µm. Monaghan et al. (1959) assume that all particles smaller than 1 µm obtained from crushed Sub-Clarksville formation cores are composed of clay. Sharma et al. (1985) define the < 2 µm fraction of crushed Berea sandstone as the “clay” fraction, which is analysed and found to contain mainly kaolinite and quartz.

As described in Table 2-1, classification of grain size may give a definition of “fines”. It may be considered that particles below 3.9 µm (i.e. clay-sized particles or smaller) are “fines”. However, this definition confuses size and mineralogy – clay-sized particles may not be necessarily composed of clay minerals. This is also noted in the “Glossary of Geology” (Bates et al., 1980), where three definitions are given for clay, the first being size-based (< 4 µm) and the second

being based on bulk material properties when wet (namely plasticity and the ability to be moulded when wet and retaining the shape) and some limitation on composition (>50% clay-sized particles and >25% clay minerals) Wentworth considers this in the naming of his aggregate terms, and accepts that, although the clay fraction may not necessarily contain only clay minerals, often a large proportion of the materials that form this size grade are formed of clay minerals and therefore the description will fit the majority of cases. It is clear though, from the wide ranging definitions, that the word “fines” when associated with sandstones does not have a clear definition. Perhaps Muecke defines “fines” in sandstones most effectively, saying “these particles are not held physically in place by the natural cementitious material that binds larger sand grains together”, and therefore any solid free to move in a sandstone, regardless of mineralogy or size, may be considered a “fine”. For the purposes of this work, this definition will be used unless otherwise specified.

Many of the fines in sandstone may be characterised using scanning electron microscopy, on either thin sections or coated rock chips. In the thin section (a preparation technique whereby a sliver of rock is cut from a sample and mounted on a glass slide, then ground down until optically flat and approximately 30 μm thick), the minerals present may be characterised by chemical mapping (using energy dispersive x-ray (EDX) analysis, discussed in Section 3.6) and cathodeluminescence which uses photons emitted from the sample after absorbing electrons to show changes in the lattice structure (such as strain or damage) of the material. Kareem (2016) illustrates the use of these techniques in the characterisation of Berea sandstone. In the rock chip, minerals are most often identified by characteristic morphology and correlation with both thin section and x-ray diffraction data. Additionally, atomic force microscopy (AFM) may be use to characterise the smallest (10 nm – 400 nm) fines on sandstone pore surfaces (Kareem, 2016).

2.1.1 Quartz

Quartz is a crystalline material composed of a continuous matrix of SiO_4 tetrahedra with the oxygens on the corners being shared between two tetrahedra, giving an overall formula of SiO_2. In its ideal form, crystals of quartz will form 6-sided prisms with 6-sided pyramids at either end, giving it a characteristic shape which is easily identified under SEM. Most quartz is formed by crystallisation from magma, and is extremely hard and resistant to chemical degradation and weathering. These properties mean that quartz is one of the most common minerals found in sandstones.

Sand beds are formed of sand-sized grains. The sand-sized grains occur as a result of the break-up of larger rocks, for example during transport, chemical deposition of suspended salts, or biological production. Sand-sized quartz grains have often been transported a great distance from where they were originally formed, breaking and becoming more rounded along the way. The small particles that break off may be incorporated into the sandstone as detrital quartz. Alternatively, during cementation, quartz may be deposited as microcrystalline quartz cement overlying amorphous quartz, which is again characteristic under SEM.

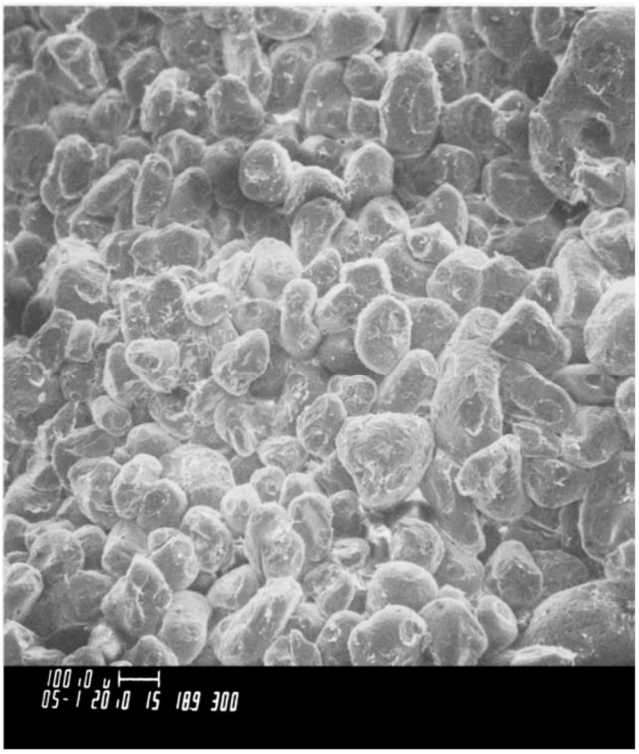

Figure 2-1: Rounded detrital quartz grains. SEM at 50x magnification. From Welton (2003).

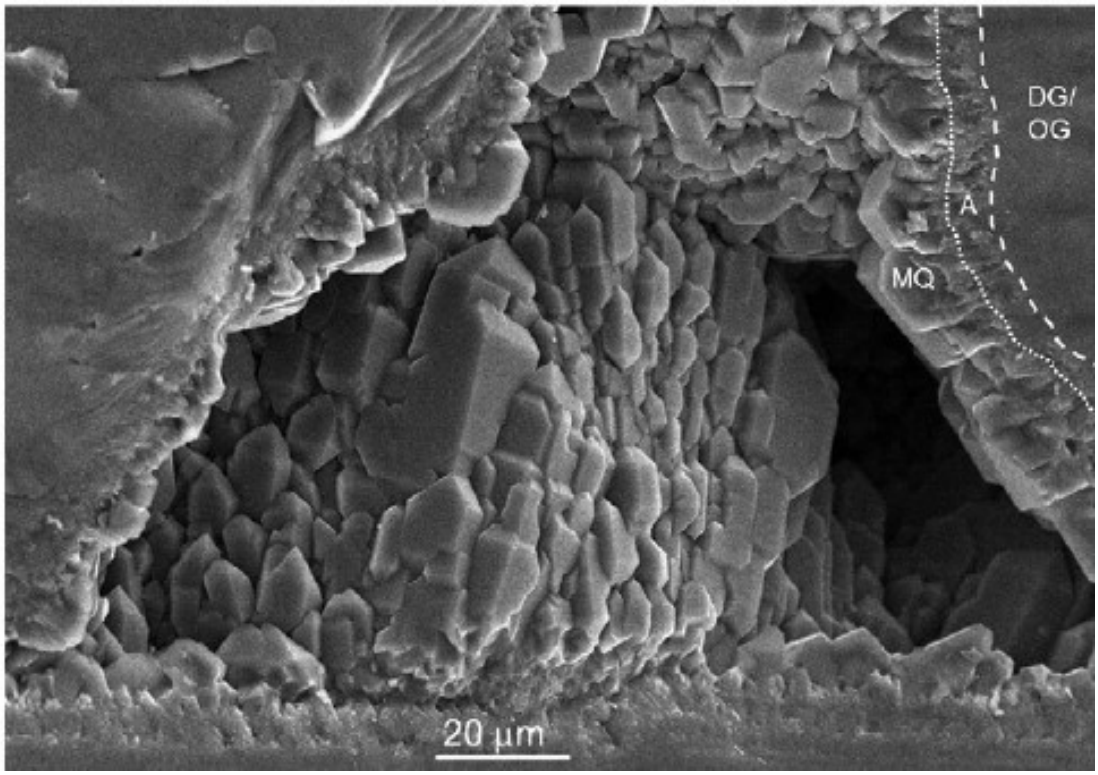

Figure 2-2: Microcrystalline quartz (MQ) overlying amorphous silica (A) layer, which has formed on top of a detrital grain/quartz overgrowth surface (DG/OG). From French and Worden (2013).

2.1.2 Clay minerals

Clay minerals are phyllosilicates, composed of silicon, oxygen, aluminium, and depending on the clay, iron, magnesium, potassium, sodium or other cations. They are composed of octahedral AlO_4 and tetrahedral SiO_4 or AlO_4 sheets, and the arrangement of these sheets, and the substitution pattern of the Al^{3+} or Si^{4+} for other cations in order to change the charge on the sheet, will determine the properties of the clay mineral.

Clay minerals are divided into two groups based on the arrangement of tetrahedra and octahedra in the sheets. A clay mineral described as a 1:1 clay mineral will contain one octahedral (O) and one tetrahedral (T) sheet bonded together to form an OT clay layer. A 2:1 clay will be formed of a “sandwich” of one octahedral sheet between two tetrahedral sheets (TOT). The layers then stack to give clay mineral crystals, their layers being held together by either hydrogen bonds between the layers, or bonding with the interlayer cations, present due to change deficiencies in the sheets due to isomorphic substitution of Si^{4+} or Al^{3+} for less highly charged cations in the tetrahedral or octahedral sheets.

Clay minerals in sandstones may be either detrital or authigenic. Detrital clays are incorporated into the matrix as relatively large clasts during sediment deposition, and later become cemented

into the sandstone matrix. Consequently, much of the surface area of these clays is not available to the pore fluid, and therefore these clays are less likely to be mobile in the pores (Aksu et al., 2015). Authigenic clay minerals are thought to be more mobile and damaging (Sharma et al., 1985) as they form inside the pore space as grain coating or pore lining deposits, and hence have a much larger surface area exposed to the pore fluids. The larger surface area, combined with the direct exposure of the clay minerals to the pore fluids, makes them more vulnerable to swelling and migration (Aksu et al., 2015).

2.1.2.1 Kaolinite

The unit formula of kaolinite is $Si_4O_{11}Al_4$ $(OH)_8$. Kaolinite is a 1:1 clay with no isomorphic substitution. The layers are bonded together with hydrogen bonds between the OH groups on adjacent layers. Due to this, kaolinite is considered a dispersive clay, in that, rather than swelling and becoming cohesive, kaolinite grains will break up and migrate along pore spaces rather than swelling and blocking pores.

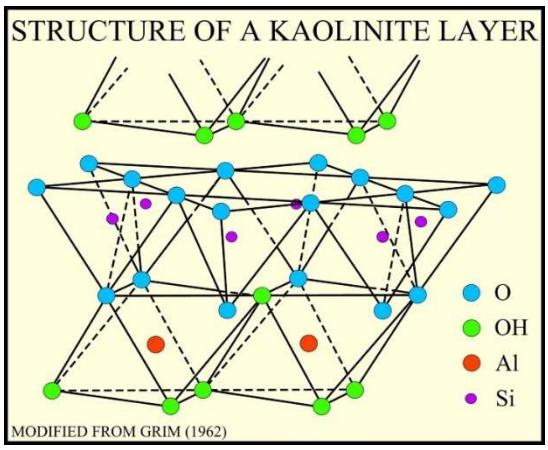

Figure 2-3: Layer structure of Kaolinite

Kaolinite is easily identified in SEM images, as it can be seen as stacks or “booklets” of regularly shaped hexagons in discrete particles (Neasham, 1977).

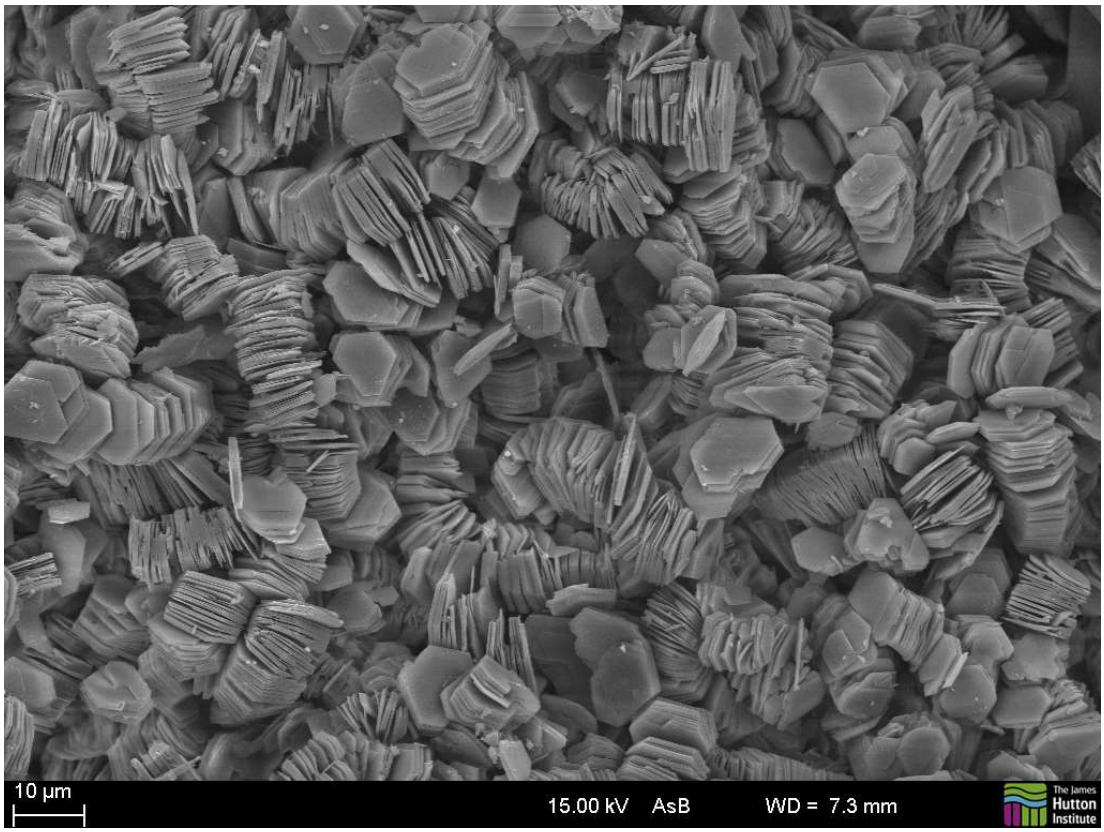

Figure 2-4: Kaolinite SEM. Image reproduced from the 'Images of Clay Archive' of the Mineralogical Society of Great Britain & Ireland and The Clay Minerals Society (www.minersoc.org/gallery.php?id=2)

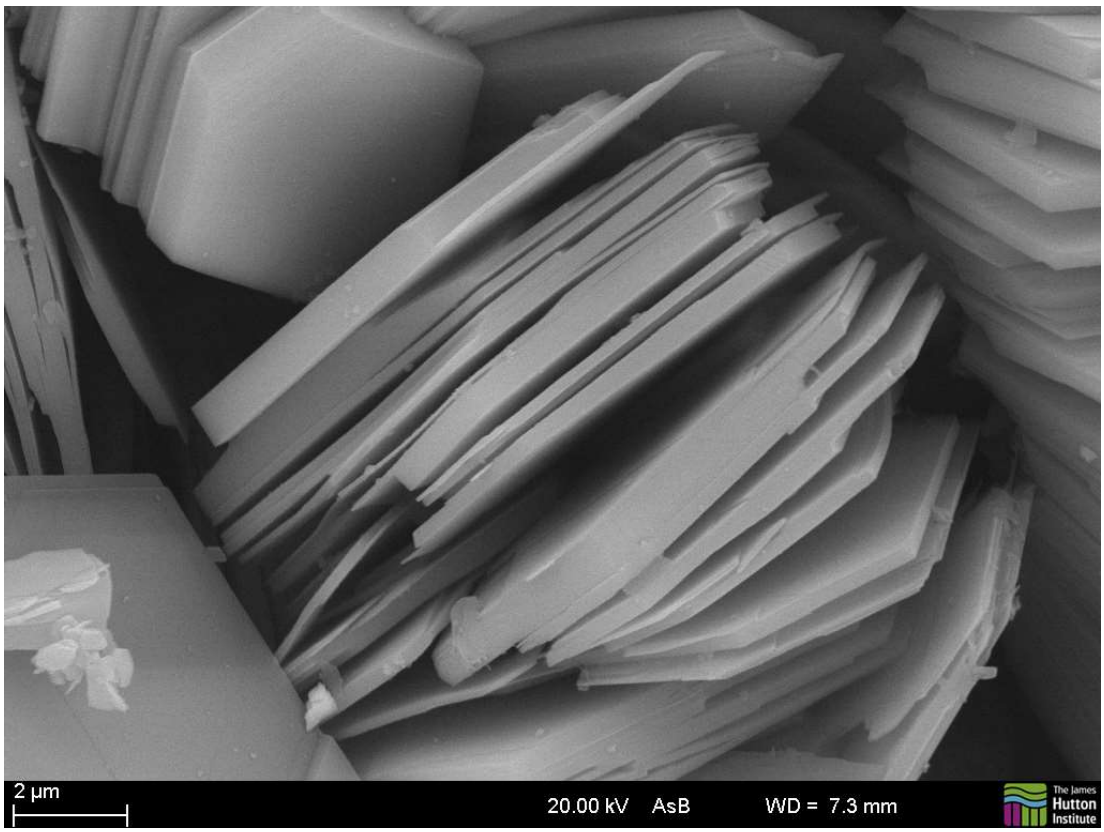

Figure 2-5: Kaolinite SEM, higher magnification. Image reproduced from the 'Images of Clay Archive' of the Mineralogical Society of Great Britain & Ireland and The Clay Minerals Society (www.minersoc.org/gallery.php?id=2)

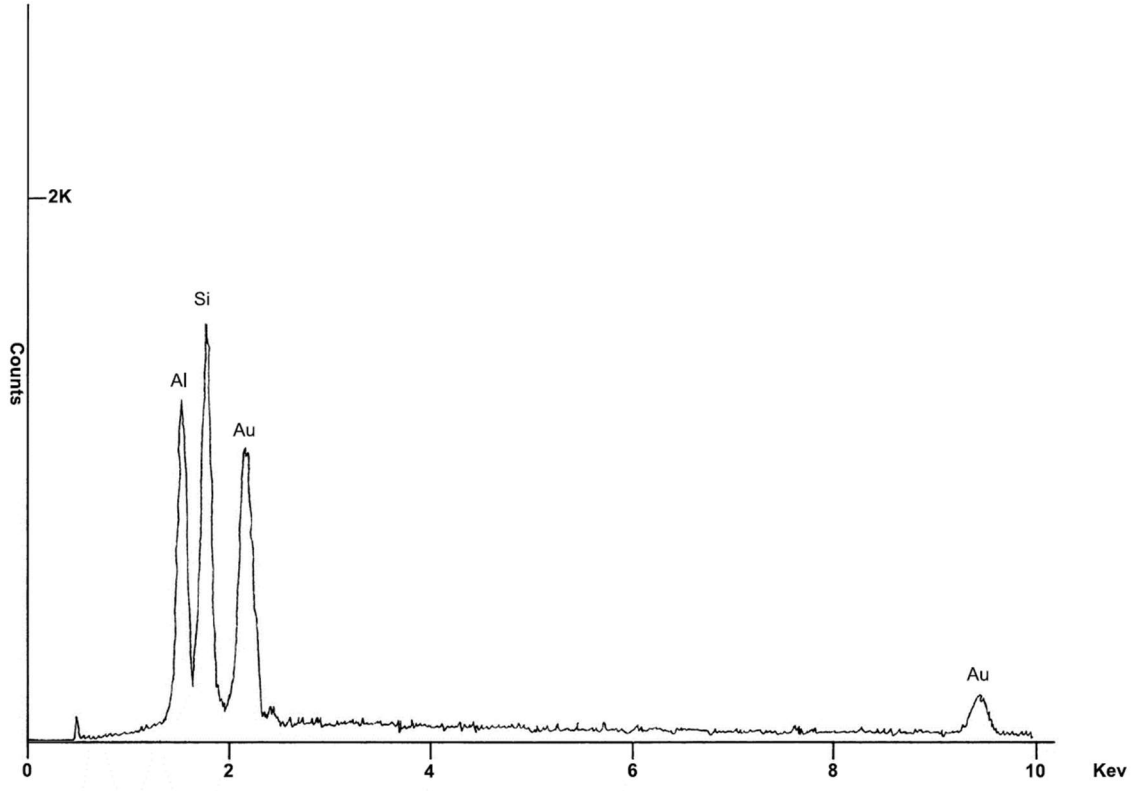

Figure 2-6: EXD spectrum of gold-coated kaolinite. From Welton (2003).

2.1.2.2 Chlorite

The clay mineral chlorite has a unit formula of $(Mg,Al,Fe)_{12}$ $[(Si,Al)_8O_{20}]$ $(OH)_{16}$. Its structure differs from others, in that the interlayer is comprised of a brucite-like layer of $(Mg^{2+}, Fe^{3+})(OH)_6$ rather than cations. It is clear therefore that, as there are no substitutable cations or water molecules in the interlayer, that chlorite is not likely to swell or disperse in the presence of water or other cations. This leads to chlorite being known commonly as a "non-reactive" clay mineral (Wilson et al., 2014).

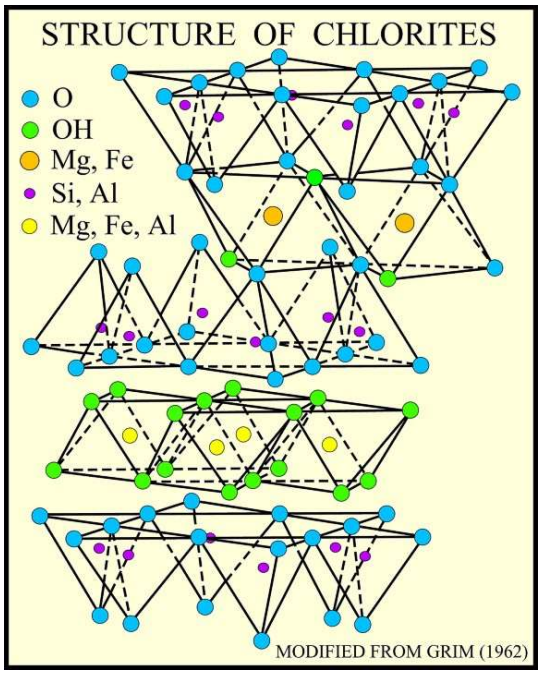

Figure 2-7: Layer structure of chlorite

Chlorite can be seen in SEM images with its faces perpendicular to the grains upon which it is deposited, with very little ordered stacking seen. It rarely is found as discrete particles, but may often be found as pore lining material, or bridging across pores (Neasham, 1977).

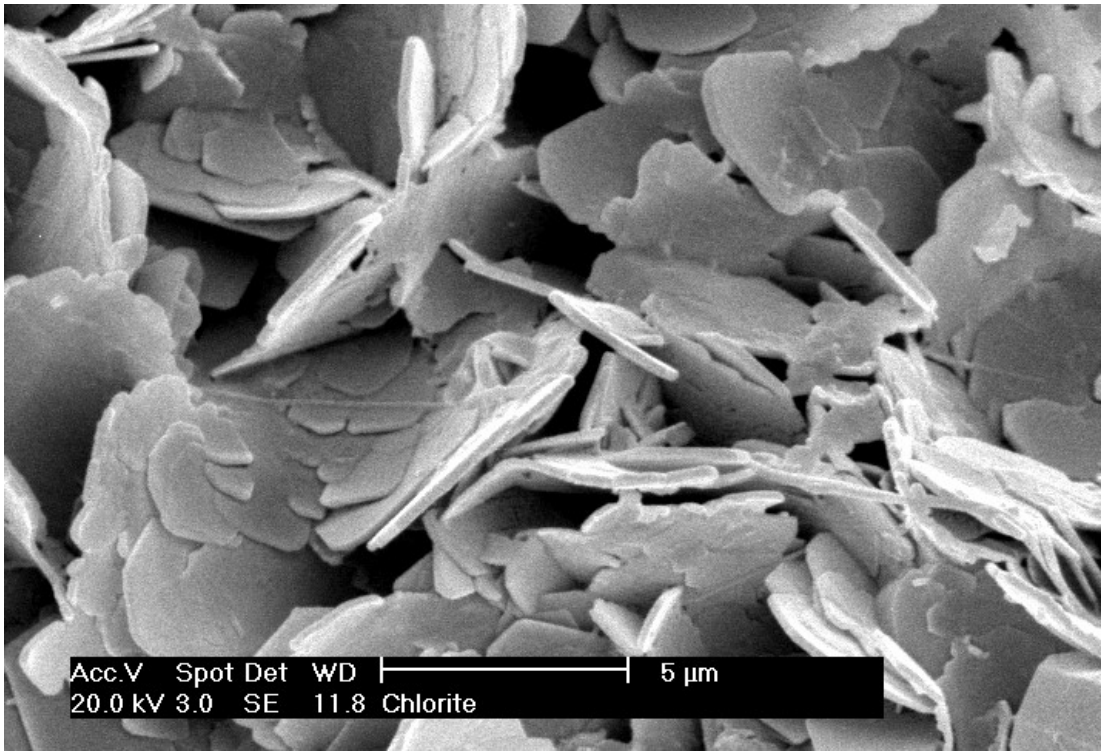

Figure 2-8: Chlorite. Image reproduced from the 'Images of Clay Archive' of the Mineralogical Society of Great Britain & Ireland and The Clay Minerals Society (www.minersoc.org/gallery.php?id=2.)

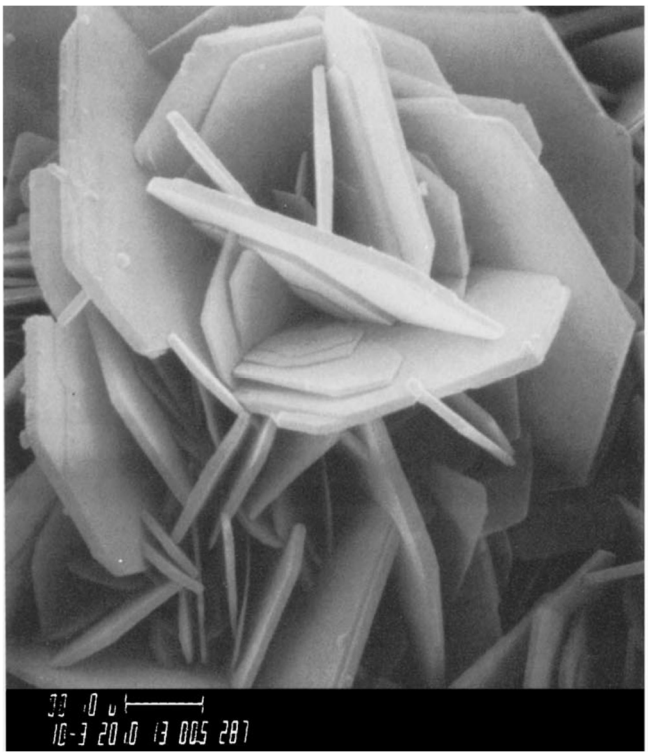

Figure 2-9: Chlorite rosette SEM at 10,000x magnification. From Welton (2003).

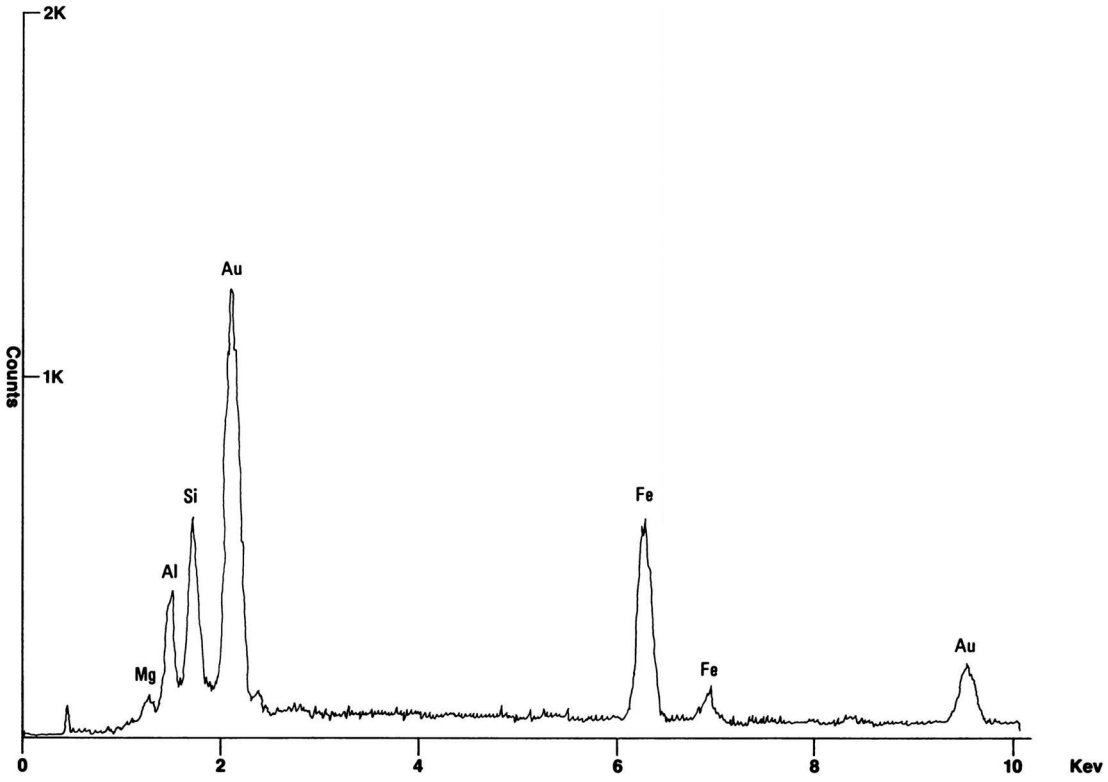

Figure 2-10: EXD spectrum of gold-coated chlorite. From Welton (2003).

2.1.2.3 Smectite

Smectite clays have the unit formula $(½Ca, Na)_{0.7}$ $(Al, Mg, Fe)_4$ $[(Si, Al)_8O_{20}]$. nH_2O. These are 2:1 clay minerals, with the layers held together by attraction of water and interlayer cations. The presence of water in the interlayer gives smectitic clays a swelling, rather than a dispersive, reaction when in contact with water or other solvents (Anderson et al., 2010). This was first described in detail by Norrish (1954), and occurs in two distinct regimes: crystalline swelling and osmotic swelling. Crystalline swelling occurs as additional water molecules are included, in a step-wise fashion, into the interlayer region. Depending on the amount of water present, there may be either one, two, three or four layers of water molecules in the interlayer region, giving an interlayer spacing of up to 20 Å, and seen both micro- and macroscopically as clay swelling, in addition to the individual hydration levels being visible using X-ray diffraction. Further swelling may occur as osmotic swelling. Additional water or solvent entering the clay particle causes the formation of diffuse double layers, and changes the forces between the clay layers from electrostatic attractive to repulsive. This is associated with a sudden jump in interlayer spacing to around 40 Å. This phenomenon has been observed by Mohan and Fogler (1997), who describe it as a "microquake", and claim that the microquakes may cause smectite fines to be released, allowing them to migrate and also block pores.

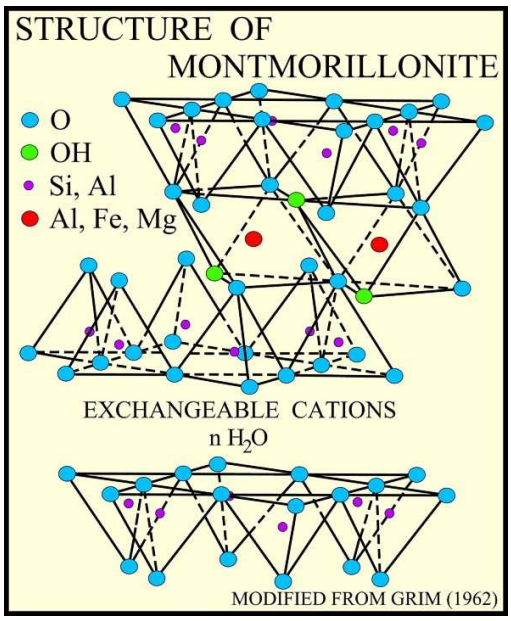

Figure 2-11: Layer structure of smectite (specifically montmorillonite)

Smectite is seen as a highly crenulated grain coating under SEM (Neasham, 1977). Flaky sheets of smectite may also be seen in some cases.

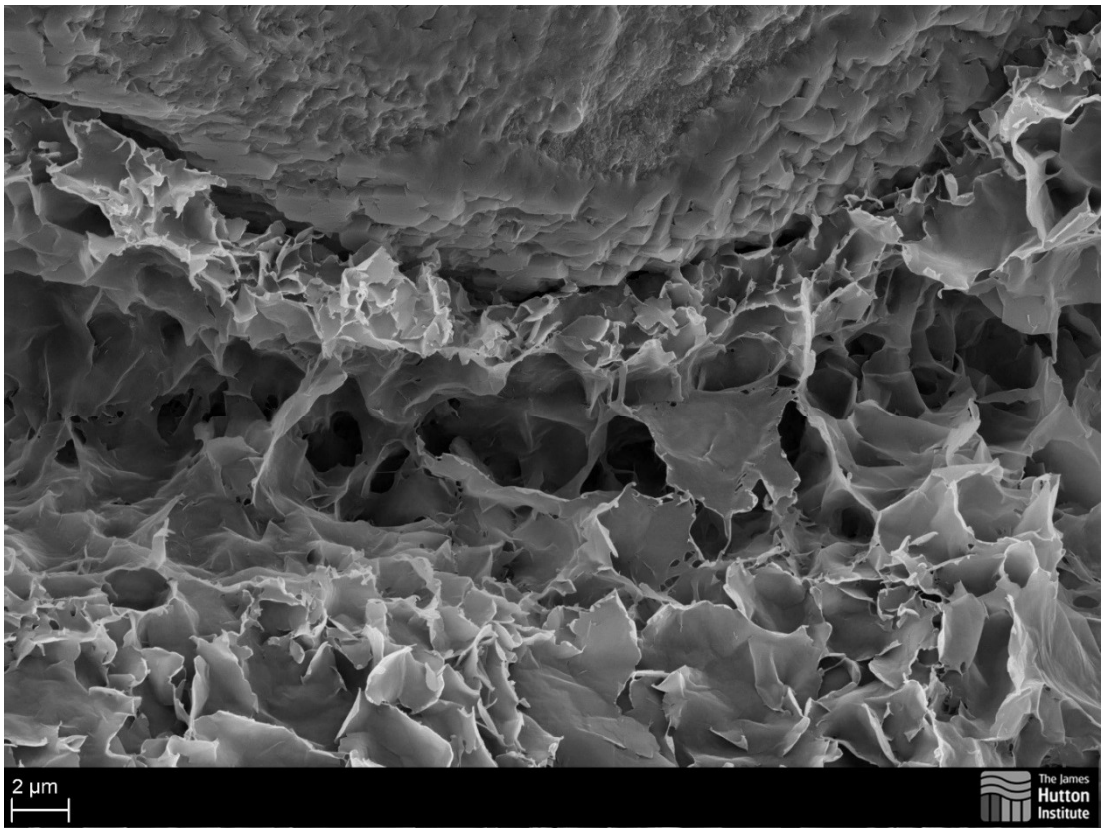

Figure 2-12: Pore-lining smectite. Image reproduced from the 'Images of Clay Archive' of the Mineralogical Society of Great Britain & Ireland and The Clay Minerals Society (www.minersoc.org/gallery.php?id=2.)

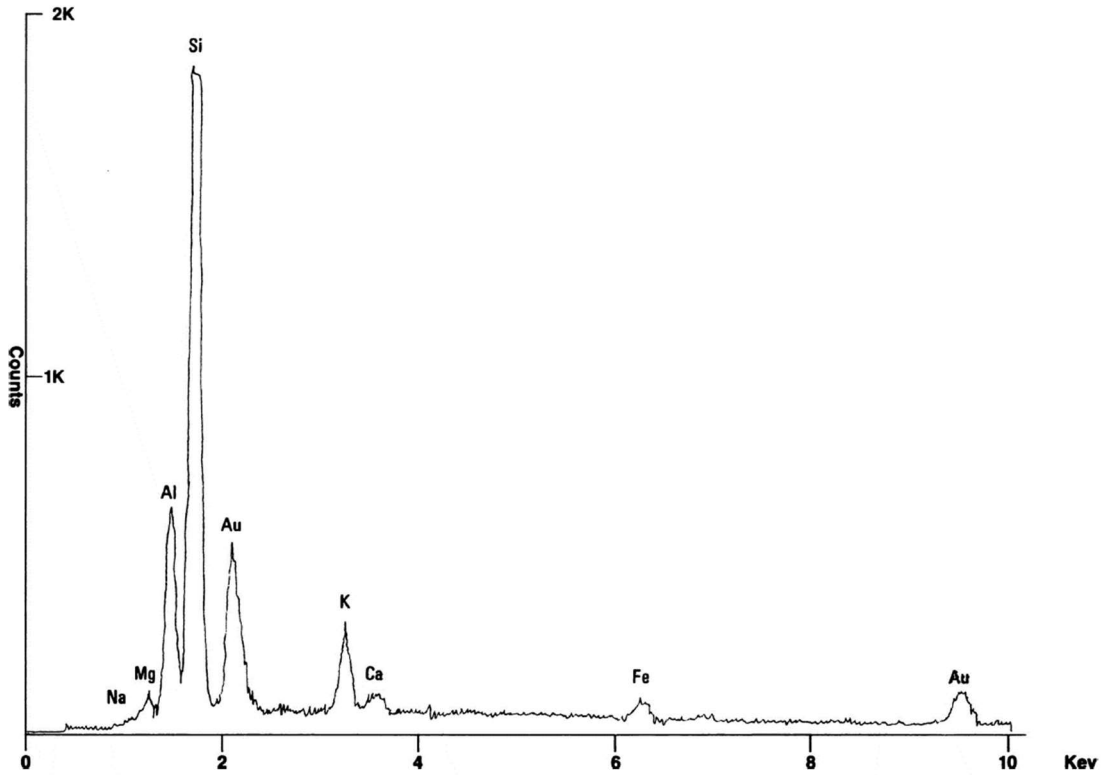

Figure 2-13: EXD spectrum of gold-coated smectite. From Welton (2003).

2.1.2.4 Illite

Illite has a unit formula of $K_{1\text{-}1.5}Al_4$ $[Si_{7\text{-}6.5}Al_{1\text{-}1.5}O_{20}]$ $(OH)_4$, and is a 2:1 clay, with the layers held together by potassium ions and a very small amount of water. As there is such a low amount of water in the interlayer, the illite will not swell like smectite, but the particles may instead disperse and migrate along pore throats.

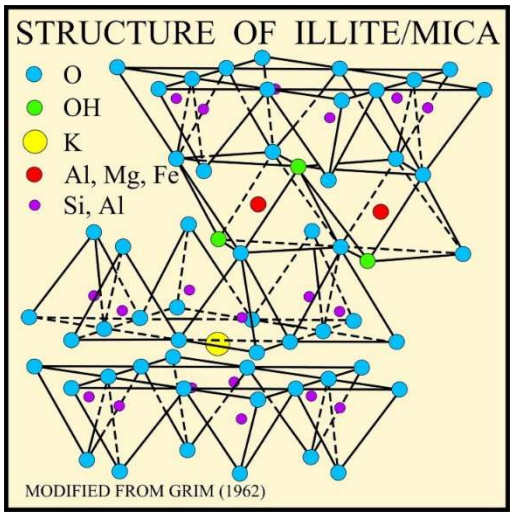

Figure 2-14: Layer structure of illite.

Under SEM, illite will often appear as filaments (sometimes called hairy illite) or needles. Some arrangements of filaments may be sufficiently large as to extend fully across the pore spaces (Neasham, 1977). Illite will often also appear as a thin “dust line” separating detrital and authigenic quartz.

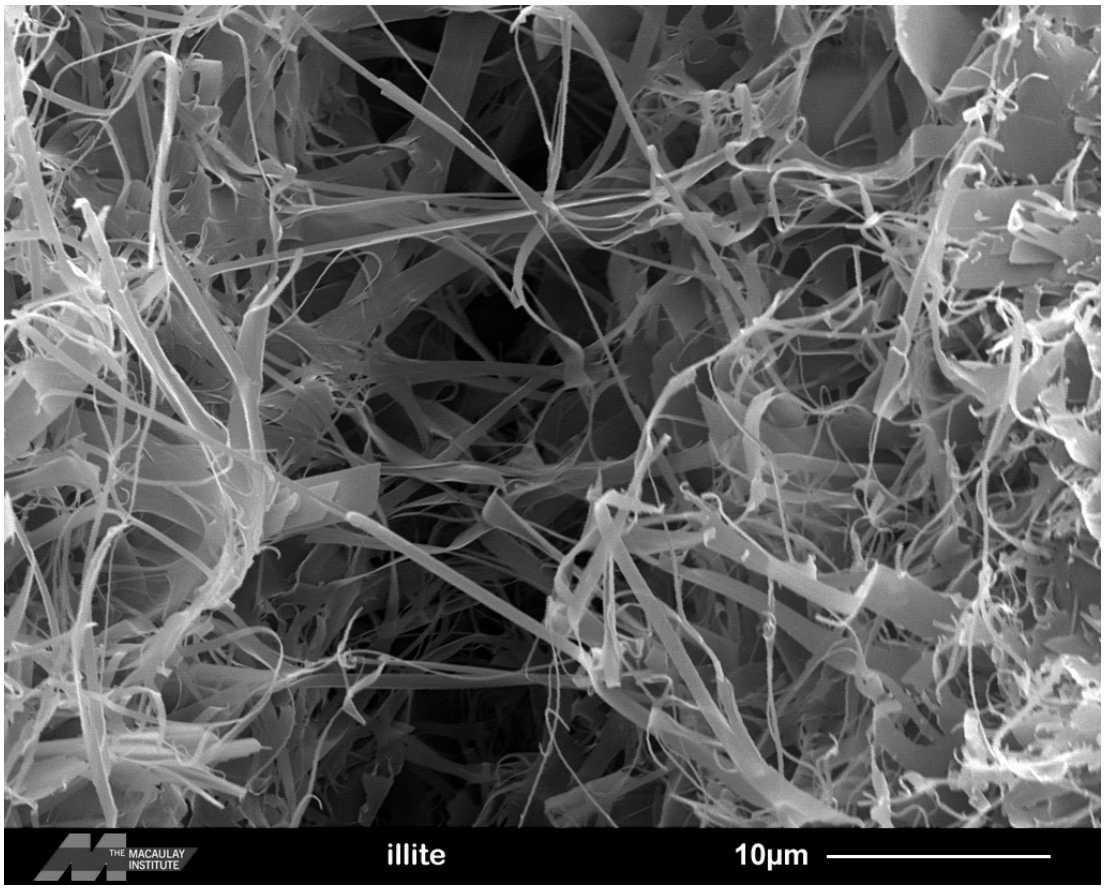

Figure 2-15: Illite grain coating bridging the pore space.. Image reproduced from the 'Images of Clay Archive' of the Mineralogical Society of Great Britain & Ireland and The Clay Minerals Society (www.minersoc.org/gallery.php?id=2.)

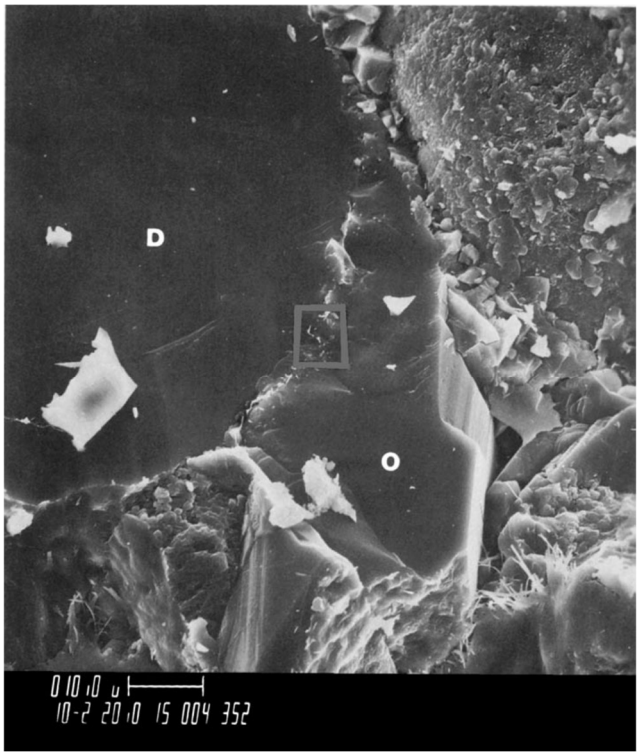

Figure 2-16: Illite "dust line" separating detrital (D) from authigenic (o) quartz. SEM at 1,000x magnification. From Welton (2003).

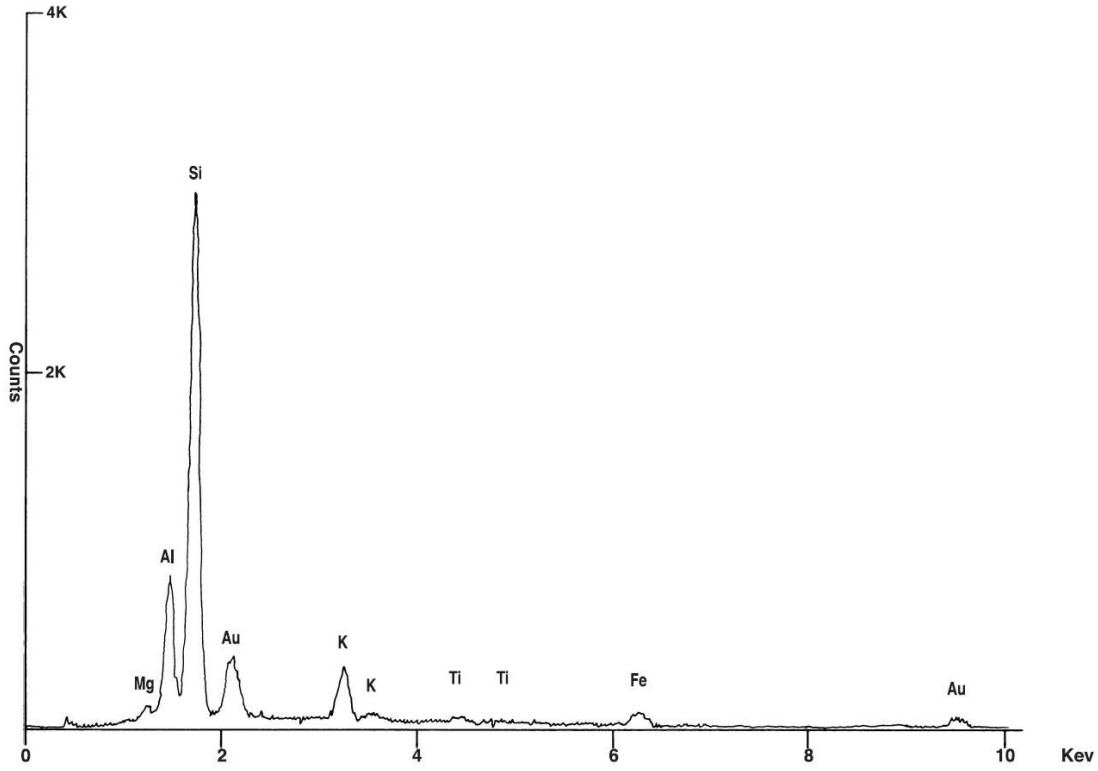

Figure 2-17: EXD spectrum of gold-coated illite. From Welton (2003).

2.2 Fines Migration in Sandstones

Fines migration in sandstones can be defined as the movement of non-framework grains in the pores of a sandstone in response to the flow of fluid through those pores.

Conceptually, it may be assumed that a fine particle has balanced forces acting on it that cause it to be held in the rock of which it is part – the attachment forces acting on the particle are greater than the detachment forces. When the attachment force is overcome, either by lowering of the attachment forces or increasing of the detachment forces, the particle will detach and migrate along the pore, until the force balance changes again.

$$V_T = V_A + V_R = V_{LVA} + V_{BR} + V_{DLR} + V_{HR} \qquad (1)$$

Where:

V_T = resulting interaction energy

V_A = attractive energy (structural force of interfacial hydrate layers)

V_R = repulsive energy (hydrodynamic force, which will depend on the viscosity and velocity of the fluid flowing in the pore)

V_{LVA} = London Van-der-Waals energy of interaction (attractive)

V_{BR} = Born interaction energy (repulsive, significant at distances < 5 Å)

V_{DLR} = double-layer energy of interaction (repulsive when double layers overlap)

V_{HR} = hydrodynamic forces (lift force generated by flowing fluid)

These forces are all functions of the distance between the particle and the pore wall (Khilar and Fogler, 1998, Sokolov and Tchistiakov, 1999, Tchistiakov, 2000, Blume et al., 2002).

It can be seen from this equation that a number of external factors may influence the force balance between the particle and the pore wall. Firstly, the repulsive force will be affected by velocity and viscosity of the flowing fluid. Secondly, changes in fluid chemistry (salinity, pH, nature of ions in solution) will affect the size of the double layer around a fine particle (particularly, in the case of pH, a clay particle), and hence the force associated with the double layer. The double layer is illustrated in Figure 2-18, and the size of the double layer surrounding a charged particle varies with salt concentration. At high salt concentration the high concentration of ions in solution can balance the surface charge close to the particle, and hence the double layer is small. Therefore if two particles were to interact in a high salt environment, they would need to be very close together to experience the repulsive force due to their double layers overlapping. The opposite situation is true in a low salt environment – the double layers extend a larger distance from the particle and hence repulsive interactions may occur over larger distances.

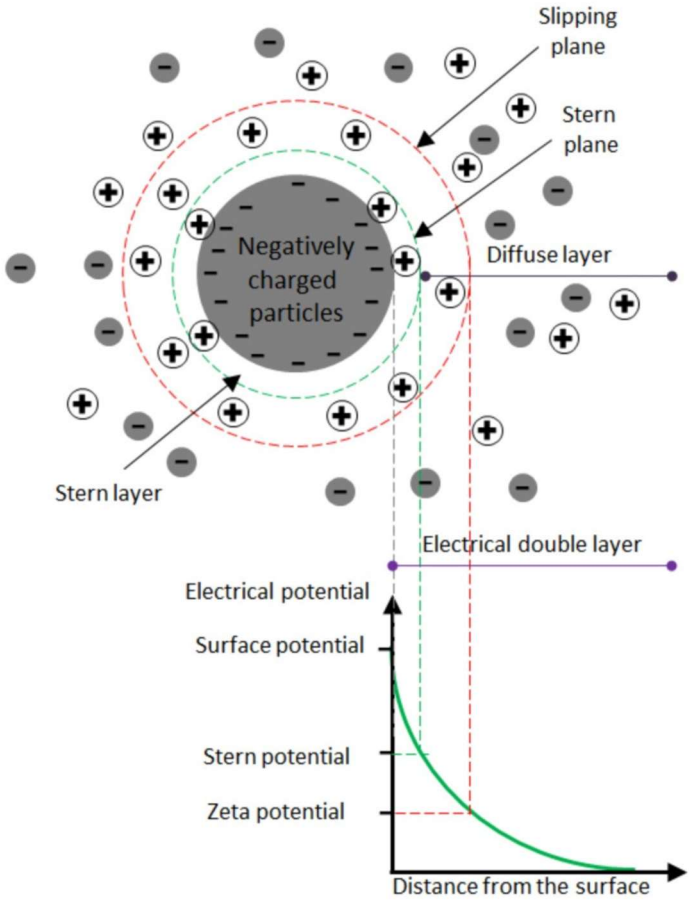

Figure 2-18: Schematic of the electrical double layer. From Nasralla and Nasr-El-Din (2014)

Further complication may occur if the particle is formed of a mineral which may swell or disperse in the presence of fresh or saline water, such as the clay minerals kaolinite and smectite. In these cases, the particle may change as the conditions of the fluid surrounding it change, either by swelling or breaking up, thereby increasing the reactive surface area. The increase of reactive surface area will cause a further change in the balance of forces dictating attachment or detachment, and may further change the potential for migration.

Often, the literature considers the fines to be composed of clay minerals alone, (discussed above) and does not consider the effects that any other materials might have. However, Sharma et al. (1985) acknowledge that fines of different mineralogies (mica, fine-grained quartz and feldspar in particular) may be present, but then go on to indicate that clay minerals are the predominant source of formation damage by fines migration. Additionally, they note that specific clay minerals, in particular a mixture of kaolinite and illite, may be more susceptible to mobilisation.

Fines migration is of great importance to a range of industries such as geothermal energy (Rosenbrand and Fabricius, 2012), carbon capture and storage (Lu et al., 2011) and oil and gas exploration and production (Valdya and Fogler, 1992, Bennion, 1999, Tang and Morrow, 1999). Blume et al. (2002) state that transport of contaminants that are attracted to the solid phase may be transported during fines migration, potentially causing aquifer contamination. During oil and gas production, fines migration may have a number of adverse effects, including reservoir damage, pore plugging, loss of flow rate, loss of fluids and ultimately loss of revenue (Monaghan et al., 1959, Hewitt, 1963). It is clear therefore that a good understanding of the factors that may contribute to and mitigate fines migration is of vital importance.

When considering the injection of fluids underground, fines migration is considered a problem that is concentrated mainly in the near wellbore region, and is generally most significant within the nearest 30 cm (Gruesbeck and Collins, 1982). This is because flow velocities and detaching forces in this region are in the region of 2 – 3 orders of magnitude higher than in the reservoir (Bedrikovetsky and Caruso, 2014), and there exist threshold values below which fines will not migrate.

2.2.1 Factors affecting fines migration

2.2.1.1 Velocity

It has been shown many times that for fines migration to occur, there must be a fluid flowing with a flow rate greater than the critical flow velocity (CFV) for that system (Gruesbeck and Collins, 1982, Gabriel and Inamdar, 1983, Sharma et al., 1985, Khilar and Fogler, 1987a, Howard et al., 2012).

Gruesbeck and Collins (1982) first showed that a critical velocity existed that below which, fines would not migrate. This was shown to be very dependent on the properties (viscosity and oil:brine ratio) of the fluid flowing in the porous medium. Gabriel and Inamdar (1983) showed that the CFV when 2% KCl brine was flowed through Berea sandstone cores was 0.007 cm/s. The CFV has been shown to be very high by Howard et al. (2012) if the flowing fluid contains a high salt concentration for a given sandstone, and much lower for fluids of a low salinity (10 – 15 ml/minute for a 0.25% (w/w) NaCl solution flowing through a Berea sandstone core at room temperature, vs > 50 ml/minute for a 3% NaCl solution flowing under the same conditions). However, Khilar and Fogler (1984) found that varying the velocity from 3.2 to 570 cm/hr (0.0009 to 0.15 cm/s) did not have an effect on the critical salt concentration measured for NaCl solution flowing through Berea sandstone. Typical fluid velocities for waterflooding in heavy oil wells may

be as low as 0.001 ft/day (3.5×10^{-7} cm/s) , or as high as 116.1 ft/day (0.04 cm/s), hence fines migration has the potential to be experienced under typical flow rates (Arab et al., 2020).

Priisholm et al. (1987) looked at how the variation of velocity for brines of varying salinity affected the fines migration in geothermal reservoir sandstones. It was found that changes in velocity, including pauses then restoration of flow, promoted fines migration whereas steady flow produced more stable conditions. These results replicated field data obtained by the authors.

2.2.1.2 Salinity

Swelling clays were originally thought to be the cause of loss of permeability and formation damage during fresh water floods. However, Johnston and Beeson (1945) were among the first to attribute the loss of permeability in sand when flooded with fresh water to clay particles being "disturbed and redistributed, possibly causing drastic changes in observed permeability.". This has historically been termed "water sensitivity", and has been previously studied by Gray and Rex (1966), Jones (1964) and Mungan (1965). These early studies concentrate on the effect of a flow of fresh water on fines migration in a core following pre-treatment with a brine.

Khilar and Fogler (1984) expanded on this, and go on to define a critical salt concentration (CSC) below which fines migration will take place. In their experiments using Berea sandstone and NaCl brine flowing at 19 cm/h, they found the CSC to be 4,125 ± 125 ppm (0.070 ± 0.02 M). This was likened to the critical flocculation concentration for NaCl with kaolinite and quartz, as the numbers were found to be of a similar magnitude. Additionally, it was found that the cation concentration alone affected the CSC; the concentration of anion (studied by looking at mono- and divalent anions) had no effect on the CSC. Additional work has taken place looking at low salinity fluids and their effects on fines migration and is in agreement with previous studies (Schembre and Kovscek, 2004). The CSC found is similar to the upper salinity limit for the low salinity fluids used in low-salinity EOR, which is quoted as 5,000 ppm (Morrow and Buckley, 2011)

Valdya and Fogler (1992) monitored pH and pressure drop during a gradual decrease in salinity to below the CSC of a 0.51 M NaCl saturated Berea core. It was noted that the pH did not increase to the same value at low salinity as the pH reached during a freshwater shock, and the often associated significant reduction in permeability was not seen. A model was developed that assumes cation exchange takes place during a gradual salinity change between the injected Na^+

and the H^+ assumed to be present in the clays, resulting in greater stability. This model is able to predict the observed behaviour with great accuracy.

Ochi and Vernoux (1998) studied a combination of CSC and CFV. Using models and experimental data, they show that as the salinity of the flowing fluid increases, so does the CFV. In addition, they state that the velocity contribution to particle mobilisation is less severe than the salinity, or chemical, contribution. This, they explain, is due to the small number of particles being released due to velocity; these may easily be re-deposited upon entering a region of lower fluid velocity.

2.2.1.3 Temperature

Schembre and Kovscek (2004) looked at the effect of increasing temperature (23°C – 180°C) on fines production from Berea sandstone when fluids with different pH (7 – 10) and NaCl concentrations (10^{-6} M – 1 M) were flowed through at 1 m/day. In all cases, a reduction in permeability was shown as temperature increased. Rosenbrand and Fabricius (2012) presented a review of the effects of temperature on sandstone permeability. They show that at > 0.7 M for NaCl, heating will have little effect on mobility of fines. They conclude that, based on the review of the existing literature, heating may cause porosity reduction, but it is likely to be negligible under laboratory conditions. Permeability reduction resulting from heating was seen as kaolinite was mobilised in both brines and fresh water. They also noted that in some cases, contamination arose from corrosion of equipment leading to potentially misleading results.

In their study of critical salt concentration, Khilar and Fogler (1984) found that increasing the temperature increased the critical salt concentration from 0.056 ± 0.002 mol/l NaCl at 0 °C to 0.090 ± 0.004 mol/l NaCl at 60 °C. This is in general agreement with the review by Rosenbrand and Fabricius (2012); an increase in temperature makes fines release more likely. Temperatures of below 60 °C would appear to be typical temperatures of injected water of low salinity brine, given an average geothermal gradient of 30 °C/1000 m, an average well depth of around 2000 m (U.S. Energy Information Administration, 2020) and calculations provided by Moradi et al. (2020) which in Case 1 shows a temperature of approximately 40 °C at a depth of 1800 m.

In tests where the temperature exceeds 270 °F (132 °C) however, Howard et al. (2012) showed that fines migration, even in the presence of fresh water, did not occur to any significant level. This was in agreement with data presented by Scheuerman and Bergersen (1990b) on a variety of reservoir formations at different temperatures – little or no fines migration was seen in formations at temperatures over 210 °F (98.9 °C), even when they contained 22%

montmorillonite/illite (250 °F, 121 °C) or 13% illite (210 °F, 98.9 °C), whereas migration was seen in other formations with similar clay compositions at lower temperatures.

2.2.1.4 pH

Valdya and Fogler (1992) systematically assessed the pH and salinity of fluids flowing through Berea sandstone. At zero salinity, when according to Khilar and Fogler (1984) fines migration should take place, a pH of 2 was found to prevent fines migration at between 1 and 2 ml/min (0.33 – 0.66 m/s). This contrasted with a severe reduction in permeability for the zero salinity fluid at pH 11. In models developed based on this study, it was shown that when DLVO analysis is applied to the system the interaction between the surface and clay particle reduced to zero at pH 11, which is in agreement with the observation of the dramatic reduction in permeability at pH 11.

Schembre and Kovscek (2004) consider the effect of pH on reduction in permeability due to fines migration in Berea sandstone. They show that there is a reduced reduction in permeability at pH 7 vs pH 10 for a 0.01 M NaCl solution flowing through Berea sandstone at 1 m/day.

When considering pH, additional fines release mechanisms must be considered. Increased pH may dissolve the amorphous silica cement in a sandstone which holds the grains and fine particles together. This was observed by Mungan (1965) in Berea sandstone cores.

2.2.1.5 Wettability

Wettability associated with fines migration is generally of greater concern in the reservoir, where the pore surfaces and fines may be water-, oil- or mixed-wet. The wettability of a surface is defined by Craig (1971) as "…the tendency of one fluid to spread on or adhere to a solid surface in the presence of other immiscible fluids." In practical terms, this will dictate whether oil or water will preferentially contact a surface when more than one of these fluids is present. For example, in the situation where the pore network of a sandstone is water wet, and oil is present in those pores, the water will be in contact with the pore walls and the oil will be found in the centre of the pores surrounded by the water. The converse is true for an oil-wet formation; oil will be in contact with the pore walls, surrounding water in the middle of the pores. There additionally exists a state of neutral wetting, whereby the pore walls have preference for neither water nor oil, and both may be found in contact with the walls.

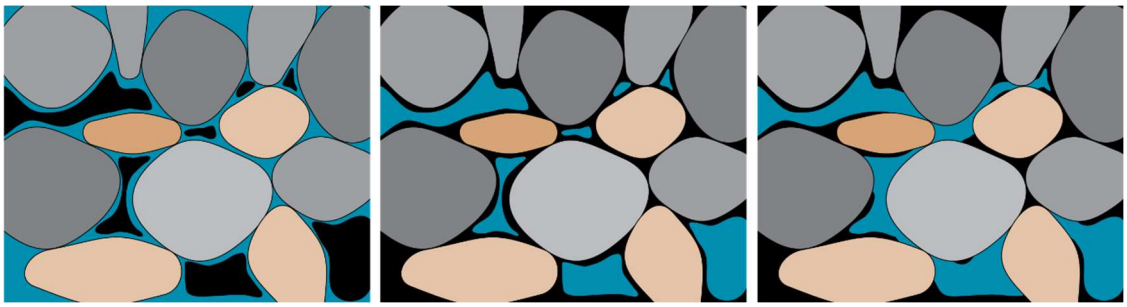

Figure 2-19: Wettability illustration. grey/brown: rock grains, blue: water, black: oil. Left to right: water-wet, oil-wet, mixed-or neutral-wet.

A convenient method to further classify wettability involves the measurement of the contact angle a droplet of water placed on that surface has with the surface (Yuan and Lee, 2013). If the contact angle is below 90°, the surface is said to be water-wet (the water droplet appears flat and spreads out over the surface). If the contact angle is above 90°, the surface is said to be oil-wet (the water droplet will stand proud above the surface, with an acute angle being made between the surface and the surface of the droplet). If the contact angle is found to be exactly 90°, the surface is said to be neutrally wet.

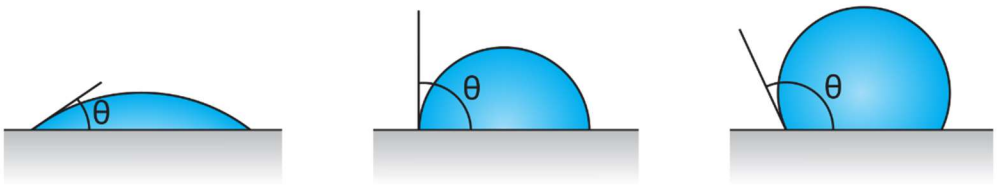

Figure 2-20: Illustration of contact angles vs surface wettability. Left to right: water-wet, neutral-wet, oil-wet.

The natural state of sandstones, and almost all minerals in their natural state (Bennion et al., 1992) (with the exception of sulphur, graphite, talc, coal, many sulphides, pyrophyllite and other silicates with a sheet structure (Anderson, 1986)), is water-wet. It was therefore believed historically that all oil-producing reservoirs were water-wet, until Nutting (1934) reported otherwise. If the crude oil in the reservoir contains asphaltenes or other polar compounds, these may interact with the formation and may change the formation to oil-wet. It has been found that up to half of all sandstone reservoirs have been altered from water-wet to neutral- or oil-wet due to this mechanism (Treiber and Owens, 1972). The transformation from water-wet to oil-wet is however a complex, and poorly understood, process (Buckley, 1998). The wettability therefore may then have an effect on the permeability of the rock as in a water-wet formation the oil is likely to be located in the middle of the pores, whereas in oil-wet, the oil is more likely to be located throughout the pore, hence having a larger cross-sectional area to flow through

(Gluyas, 2004). Most reservoirs however have been found to have “mixed wettability”; larger pores may be both water- and oil-wet, but smaller pores generally remain water-wet (Muggeridge et al., 2014).

In a water-wet formation, the fines associated with the sandstone are also water-wet. Water-wet fines may be more susceptible to migration than oil-wet, as the injected fluids are usually water-based during an enhanced oil recovery operation.

In an oil-wet formation, the fines associated with the sandstone may be oil-wet. When a water-based fluid contacts an oil-wet fine in an oil-wet formation, the fines are less mobile, as non-reactive fines have only been seen to move when the phase that wets them is mobile (Muecke, 1979).

Many of the smaller pores may be associated with the fines or clay-based minerals in the formation, and will therefore most likely be water-wet in a sandstone formation, even if the majority of the larger pores are oil-wet. This may lead to the fines being more easily mobilised than expected. However, the wettability of clays and shales is complex, with potentially illite and smectite behaving in a more water-wet manner despite the presence of oil, whereas kaolinite may behave in a more hydrophobic manner after exposure to oil (Borysenko et al., 2009).

2.2.1.5.1 What influences wettability?

Measuring the contact angle that a droplet makes on a surface (also called the sessile drop method) is a convenient method to quickly assess the wettability of that surface. The contact angle (sometimes termed the Young contact angle, θ_Y) is dictated by the relative surface energies (the excess energy at the surface of a material compared to the bulk), or interfacial energies, between the surface and vapour (γ_{sv}) , surface and liquid (γ_{sl}) and liquid and vapour (γ_{lv}) at mechanical equilibrium, as first described by Young (1805):

$$cos\theta_Y = \frac{\gamma_{sv} - \gamma_{sl}}{\gamma_{lv}} \qquad (2)$$

Note that the vapour can be substituted with another immiscible phase.

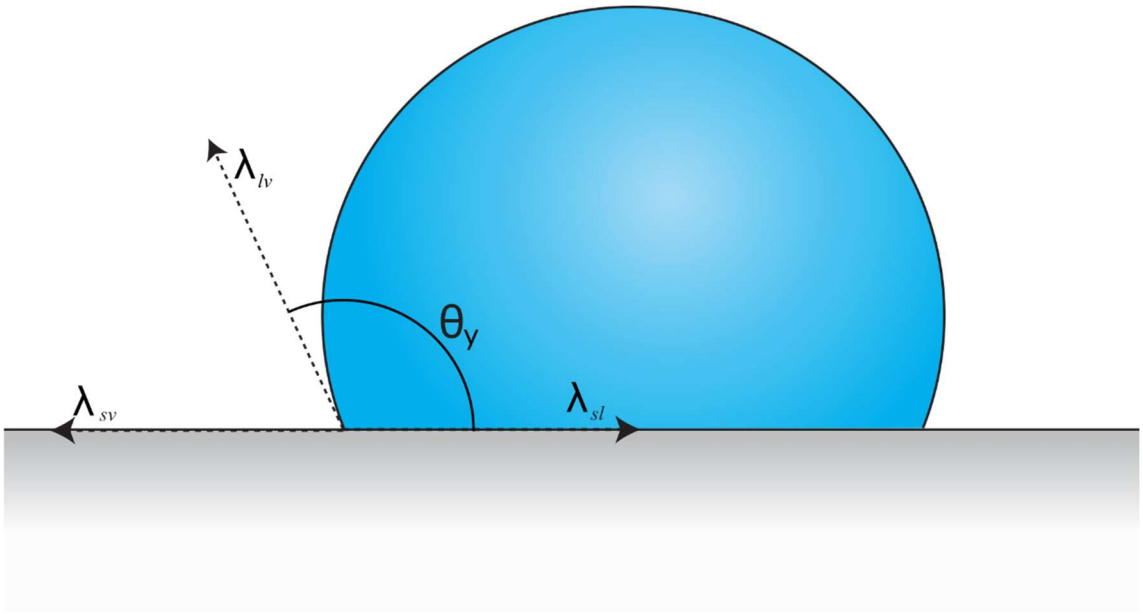

Figure 2-21: Illustration of contact angles with surface energies

This measurement represents the ideal contact angle of the material. It requires a smooth and chemically homogenous surface which is non-soluble and non-reactive. It also assumes that the surface tensions do not influence each other. In the case of relatively large droplets this appears to be the case, but in the case of measurements at nanometre length scales, this may not hold and the concept of line tension (the excess free energy of a three phase contact line) may become important (Marmur, 1997, Pompe et al., 1999).

2.2.1.5.2 Wettability and roughness

The measurement of the wettability of a surface using the sessile drop method requires that the surface be smooth. However, it is often the case that surfaces under study are not able to be made sufficiently smooth to obtain the Young contact angle. For any rough surface, the apparent contact angle measured may be different from the Young contact angle, illustrated in Figure 2-22.

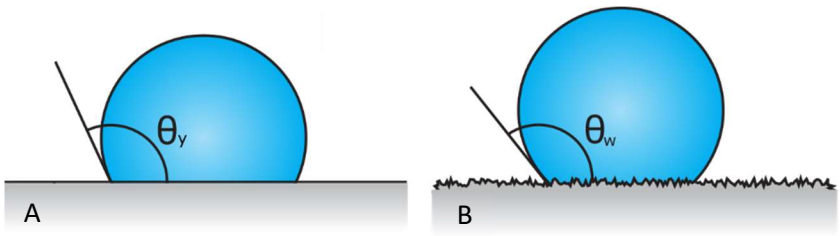

Figure 2-22: Illustration of smooth (A) vs rough (B) contact angle

This was first described by Wenzel (1936), who gave the following equation for the ratio of the Wenzel contact angle (i.e. that which a droplet makes with a rough surface; the stable equilibrium state of the system, θ_Y) to the Young contact angle shown in equation (3). The r term is described as the ratio of the actual surface area to the projected surface area.

$$\cos\theta_W = r\cos\theta_Y \tag{3}$$

In the case of a drop which is large compared to the scale of the roughness (Brandon et al., 2003), this has been found to give a good approximation of the Young contact angle. Equation (3) assumes that the liquid is in contact with the whole surface (Marmur, 2006), illustrated in Figure 2-23.

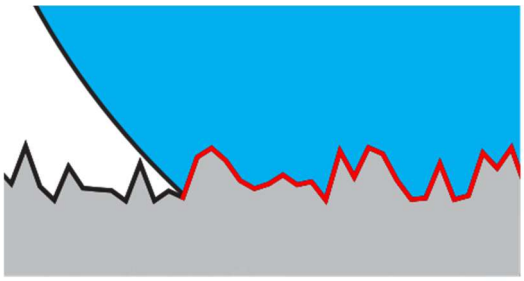

Figure 2-23: Illustration of Wenzel approximation of rough contact angle measurement, with wetted surface highlighted in red. White: air, blue: water, grey: surface of interest.

However, in some cases, air bubbles may become trapped under the drop (Figure 2-24). In this case, equation (3) does not apply as this assumes the surface is fully wetted. A further equation (4) was developed by Cassie and Baxter (1944) which accounts for this in the ϕ_{LS} term – the fraction of the projected area of the solid surface which is wetted.

$$\cos\theta_C = r\phi_{LS}(\cos\theta_Y + 1) - 1 \tag{4}$$

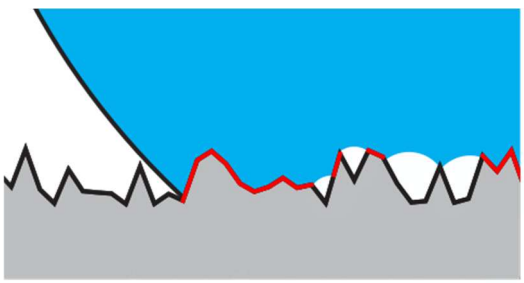

Figure 2-24: Cassie-Baxter model assumption illustration - incomplete wetting of surface. Red line highlights wetted surface. White: air, blue: water, grey: surface of interest.

2.2.1.5.3 Fines migration and wettability

Muecke (1979) observed the movement of fines through synthetic cores formed of unconsolidated sand which had been made oil-wet by flowing Isopar M (an isoparaffinic fluid supplied by Exxon) through until no water was produced. It was noted that the non-reactive fines, either oil, water or mixed-wet, would only move if the phase that wetted them was mobile. This was an important observation, which was expanded on by Tang and Morrow (1999) when they attempted to explain the phenomenon of enhanced oil recovery using low salinity fluids as relying on fines mobilisation.

2.2.1.6 Viscosity

Gruesbeck and Collins (1982) investigated the effect of increasing the viscosity of the flowing KCl brine solution using a polymer (polyvinylpyrolidone) to 10 mPa/s (an approximate 10-fold increase in viscosity). It was found that this caused a decrease in the critical velocity for fines migration in the unconsolidated sand and $CaCO_3$ particle model system that they studied. It was thought that the reason for this was that the forces holding the particle onto the surface must be overcome by a viscous drag force of the fluid in order for the fine particle to begin moving.

2.2.1.7 Nature of Cations

Khilar and Fogler (1984) showed that pretreatment of Berea sandstone cores with a divalent cation solution at 0.51 M, followed by a water "shock" (i.e. the flowing of fresh water through the core) prevented a reduction in permeability of the core during the shock. Additionally, the CSC for cations larger than Na^+ was shown to reduce as the ionic radius increased. The experiments of Kia et al. (1987) confirm these results. They additionally look at mixed Na^+/Ca^{2+}, and show that an increase in the proportion of Ca^{2+} infers a reduction in fines release following a water shock. Valdya and Fogler (1992) also show that fluids containing Ca^{2+}, even at high pH, do not promote fines migration.

2.2.1.8 Summary of effects

Table 2-2: Summary of the parameters shown to affect fines migration in sandstones

Parameter	Effect
Velocity	↑ velocity, ↑ migration (above CFV)
Salinity	↓ salinity, ↑migration (below CSC)
Temperature	↑ temperature, ↑ migration
pH	↑ pH, ↑ migration
Nature of cation	↑ ionic radius, ↑ migration

	↓ charge, ↑ migration

2.2.2 Zeta potential

The zeta potential (also known as electrokinetic potential) of a colloidal suspension may give an indication of the stability of the suspended particles. It is a measure of potential relative to the bulk fluid potential at the location of the slipping plane of the electric double layer around the particle (shown in Figure 2-18). At high magnitudes of zeta potential, a colloidal suspension will generally be stable and conversely at lower magnitudes of potential, a colloidal suspension will tend to flocculate.

Sharma et al. (1985) constructed stability diagrams based on zeta potential calculations for Berea sandstone, and use these to predict the stability of Berea sandstone for a given ionic strength of NaCl. The predicted value of instability < 0.05 M was found to be in good agreement with that measured by Khilar and Fogler (1984). Kia et al. (1987) use zeta potential measurement in their analysis of the effect of cation valence and size on the effect of water shock on fines in Berea sandstones.

2.2.3 "Shock" Effects

The term "shock" can be used to describe a sudden change in the properties (e.g. salinity, pH or temperature) of the fluid flowing in a formation or sample. The result of a sudden change of external environment can often be seen to promote fines migration where, if the properties are changed more gradually, fines migration may be reduced or even prevented.

The effect of a sudden change in salinity versus a more gradual change was first reported by Mungan (1965), in experiments using 30,000 ppm NaCl, fresh water and Berea sandstone cores. By changing the fluid flowing from brine to fresh water in a 30 cm core, a reduction in overall permeability was seen. When the core was sliced into 2.5 cm long segments, and the permeability of each piece measured, the piece furthest from the inlet of fluid flow was found to have a much smaller reduction of permeability than the piece closest to the inlet. This phenomena was explained by the mixing of fluids in the pore space of the sandstone preventing the sandstone furthest from the inlet from encountering the sudden switch to fresh water. Further experiments by the author using a carefully prepared setup to gradually reduce the salinity of the fluid flowing through the core from 30,000 ppm to 0 ppm over a period of time showed no reduction of permeability, thereby confirming the results of the previous experiment.

Ochi and Vernoux (1998) confirm previous studies by observing a permeability decrease when fresh water was flowed through a Berea sandstone core after 0.5 M NaCl brine. They additionally showed that this was independent of flow rate.

Khilar et al. (1983) assume that there is not only a shock effect, but that there exists a critical rate of salinity decrease (CRSD) below which fines migration takes place at a sufficiently low rate so as to prevent pore blockage and, therefore, drastic permeability reduction.

Scheuerman and Bergersen (1990b) suggest that the effect of a low total cation concentration fluid flowing through a core may be mitigated by a pretreatment with a salt solution, and a reduction in fines released when a $CaCl_2$ solution is applied prior to a lower salinity waterflood both in lab and field tests. In the case of the lab test, a pre-treatment volume of 0.6 M $CaCl_2$ brine sufficient to treat the whole of a synthetic sand/clay pack showed no change in pressure require to pump fluids through the pack before and after the treatment, where the fluids after the treatment were low salinity fluids. In the case of the field test, a comparison of production wells converted into injection wells showed that wells pre-treated with $CaCl_2$ following reconditioning with 7.5% HCl/1.5 % HF had between two and eight times better injectivity that the untreated wells.

Howard et al. (2012) also confirmed the previously observed shock phenomenon, but additionally showed that the effects of the water shock may be reduced by inclusion of additives such as organic clay stabilisers (tetramethyl ammonium chloride at 0.2% v/v – 14% permeability following initial brine flow vs 5% permeability following initial flow for deionised water) or potassium or magnesium salts (KCl or $MgCl_2$ at 0.25% w/w – 77% and 82% permeability respectively following initial brine flow vs 5% for deionised water) in a test which simulated production at a rate above the critical velocity determined for the Berea core used in the study.

2.3 Sandstone Reservoir Analogues for fines migration studies

Since the first report of the movement of fine particles affecting the permeability of a sandstone by Johnston and Beeson (1945), the analysis of fines migration in sandstones has been investigated, with data being gathered from field reports, experimental data and numerical simulation and analysis. When fines migration occurs, fine particles become detached, move and re-deposit on the pore surfaces. In order to more precisely study what might promote these behaviours, a study of the movement of individual particles would be advantageous. Often, the results of fines migration are only seen in the loss of permeability of a sandstone core in laboratory experiments, or an increase in pump pressures at an injection well in the field.

Visualisation of the movement of the fines in the matrix, either in real time or in snapshots before and after the experiment has taken place, can prove very advantageous in defining the parameters for movement. When sandstones are considered however, a number of problems can be identified which may affect experimental results.

Sandstones, by their very nature, are not a homogeneous material. Sandstones form from the burial and compaction of sand-sized grains of minerals such as quartz, feldspar, dolomite, clays etc. The precise composition of these grains, and the proportions in which they are found in the sandstone however varies with depth and location. It cannot therefore be said that fines migration in sandstones is promoted by a specific set of conditions; rather that for the sandstone studied, this set of conditions may promote fines migration. The non-homogeneous nature of sandstones may further be considered by looking at the composition of the minerals that make up the pore lining. When viewed under SEM, a variety of minerals may be seen on the surface of the pore. Some parts of the pore may be covered with a coating of clay, whereas other parts may have the bare grain exposed to the pore, or the cement which holds the grains together may be exposed. How then can the precise composition of the sandstone at the point at which the fine particle was released or subsequently trapped be known? It has been shown, by Sharma et al. (1985), that the electric potential of the fine particle and the grain surface may be important in the release and deposition of fine particles in porous media. It is possible to measure the contact angle of a liquid droplet in a pore, but this requires measurement in ESEM: a destructive process (Kareem, 2016). As this measurement would be required before the test was carried out (due to the nature of the core changing following core flooding) this is not a feasible option, due to the requirement to know the precise initial nature of all parts of all pores in the sandstone. The potential for reactivity of sandstones, when considering fines migration, requires each test to be carried out on a fresh core (unless the experiment is designed to look at repeated core floods on the same core): each core flood test may therefore be considered destructive as the test cannot be repeated under precisely the same initial conditions. How can the experiment be repeated to ensure experimental validity?

A number of different experimental techniques used as reservoir sandstone analogues to assess the movement of fines in the pore matrix have been reviewed. These techniques may be categorised into three main categories: loose material, laboratory fused loose material and naturally fused loose material. A summary of the techniques is shown in Table 2-3. Each of these categories is discussed below.

Table 2-3: Summary of sandstone analogues for fines migration study.

Category	Technique	Description	Use	References
Loose Material	Sand Pack	Sized sand packed into a column or core holder	Model core	Mungan (1965), Muecke (1979), Gruesbeck and Collins (1982), Gabriel and Inamdar (1983), Selby (1987), Himes et al. (1991), Pang and Liu (2013)
	Beads or grains coated with clay	Soda lime beads or quartz grains coated with montmorillonite or kaolinite	Model core	Aksu et al. (2015)
	Glass Bead Pack	Sized glass beads packed into a column	Model core	Selby (1987), Mohan and Fogler (1997), Griffin (2016), Blume et al. (2002)
	Silica pack	Sided silica packed into a column	Model core	Selby (1987)
	Sand between two microscope slides	0.15mm layer of sand held between two microscope slides	Microscope analysis	Cerda (1988)
Laboratory fused loose material	Sintered quartz between glass slides	Single layer of sized quartz chips	Microscope analysis	Muecke (1979)

	Synthetic sandstone	Sand, clay and Lucite powder exposed to elevated temperature and pressure	Model core	Bernard (1967)
Naturally fused loose material	Outcrop	Sandstone sourced from large, homogeneous outcrops	Model Core	Mungan (1965), Bernard (1967), Gabriel and Inamdar (1983), Lever and Dawe (1984), Kia et al. (1987), Sarkar and Sharma (1990), Himes et al. (1991), Valdya and Fogler (1992), Ochi and Vernoux (1998), Tang and Morrow (1999), Conway et al. (2000), (Schembre and Kovscek, 2004), Nasralla et al. (2011), Howard et al. (2012), Rosenbrand et al. (2015), Ezzat and Shedid (2016)

2.3.1 Loose Material

One reservoir sandstone analogue used frequently in the laboratory is a granular, loose material packed into a column for core flood cell. Sand is the most commonly used material, either as clean sized sand (Muecke, 1979, Gruesbeck and Collins, 1982), cleaned outcrop sand (Mungan, 1965), sand containing natural fines (Muecke, 1979) or sand containing added fines (Gruesbeck and Collins, 1982, Gabriel and Inamdar, 1983). Selby (1987) studied the effect of particle shape on fines migration through a sand pack by comparing packs composed of silica or sand (angular particle shape) with those composed of glass beads (spherical particle shape). In these three packs, all of the substrates are formed primarily of SiO_2, so should behave similarly in regards to surface charge interactions with clay. It was found that more fines were produced from spherical, small-grained packs than angular, large grained packs. This may have implications for the choice of sand for use in a sand pack – grain shape, as well as grain size, should be considered when assessing fines migration in order to be a good representation of the particular reservoir under study where appropriate.

Other loose material used to assess fines migration include clay-coated soda lime and quartz particles (Aksu et al., 2015), and glass beads. Glass beads are often used as a very clean, monodisperse, well characterised surface in order to provide a model substrate for fundamental experiments (Selby, 1987, Mohan and Fogler, 1997, Blume et al., 2002, Griffin, 2016). Aksu et al. (2015) used montmorillonite or kaolinite-coated quartz particles or soda lime beads to monitor primarily swelling of montmorillonite but also movement of fines by micro-CT scan. The fines in this case were chemically attached to the particles via polymer bridging with PVA. Despite the bridging, migration of fines was seen when kaolinite was used as the attached clay by a reduction in flow rate as water was flowed through the pack.

In addition to 3-dimensional loose material experiments Cerda (1988) produced a "2-dimensional" matrix whereby sand was sandwiched between two glass slides for viewing the movement of fines via optical microscopy to validate the developed theory of colloidal forces between quartz grains and mobile quartz fines under flow.

2.3.2 Laboratory Fused Loose Material

Two notable examples of loose material which has been fused to produce a solid are the sintered glass chips between two microscope slides used by Muecke (1979) and the synthetic sandstones created by Bernard (1967). The apparatus used by Muecke allowed the microscopic visualisation of fine particles moving in two-phase (water and oil) flow, which helped to increase the

understanding of the wettability effects on particle mobilisation; this would not have been possible in a 3-dimensional structure. The synthetic sandstones prepared by Bernard allowed the precise control of the constituent parts making up the sandstone to be attained (in the case of this set of experiments, 86% sand, 2% montmorillonite and the remainder Lucite binder). However, the addition of Lucite (Poly(methyl methacrylate)) may have had an effect on the surface properties of the sand and clay. The technique for producing these sandstones was patented by Holbrook and Bernard (1963).

2.3.3 Naturally Fused Loose Material

This term refers to granular material that, through natural processes, has become fused into a solid. In this context, any sandstone which is used as an analogue for a reservoir core may be considered. Outcrop material is most often used an analogue for reservoir core. The outcrop material is most often sourced from large, and seemingly homogeneous outcrops, the most common of which is the Berea sandstone unit, quarried in Amherst, Ohio (Churcher et al., 1991). Others include the Clashach sandstone located in Moray, Scotland and Castlegate sandstone, located in Utah. Berea has advantages over these sandstones as it has a fines content of up to 8% (Kareem et al., 2017), whereas Clashach contains a negligible amount of fines (Ojala, Ngwenya et al. 2004), and is well consolidated whereas Castlegate sandstone is not.

In order to assess the homogeneity of Berea sandstone, a review of 8 sources containing porosity and permeability data measured by MICP was carried out. The porosity vs permeability for each of the cores of Berea used was plotted in Figure 2-25.

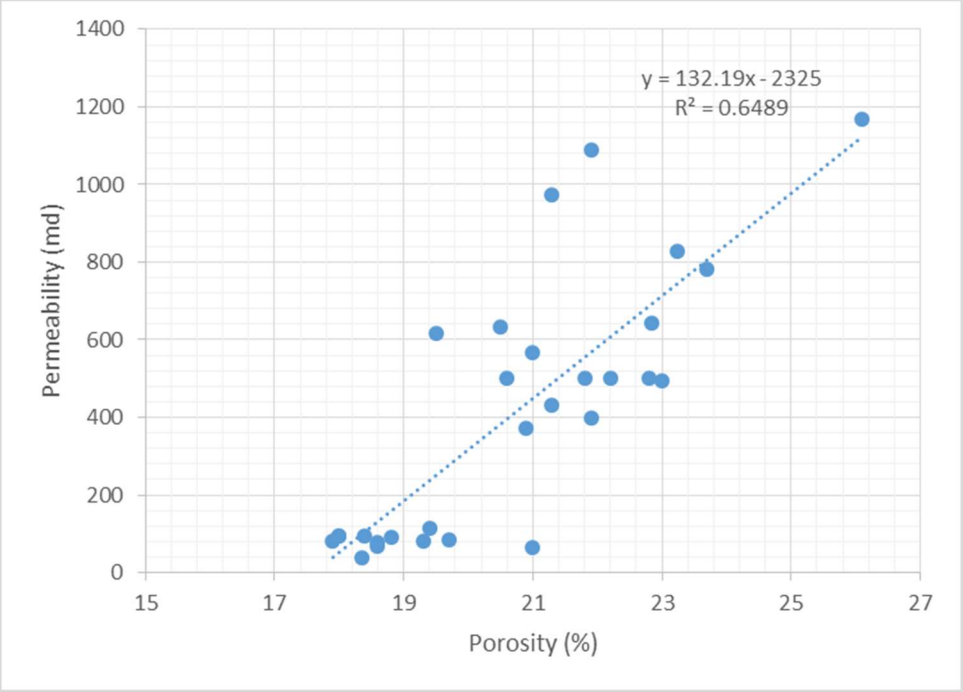

Figure 2-25: Permeability vs porosity data for Berea sandstone from Knight and Nur (1987), Churcher et al. (1991), Malik et al. (1998), Kewen and Abbas (2000), Sbai and Azaroual (2011), Nasralla et al. (2011), Hussain et al. (2013)

It can be seen that, although Berea sandstone is said to be homogeneous, the data points do not overlap (expected for a completely homogeneous system) or lie on a straight line as reported for Berea sandstone by Churcher et al. (1991) in their Figure 13.

When other sandstones are additionally considered, it is clear that a sandstone is firstly not homogeneous in its own unit, but additionally that permeability and porosity of sandstones vary widely, as shown in Figure 2-26.

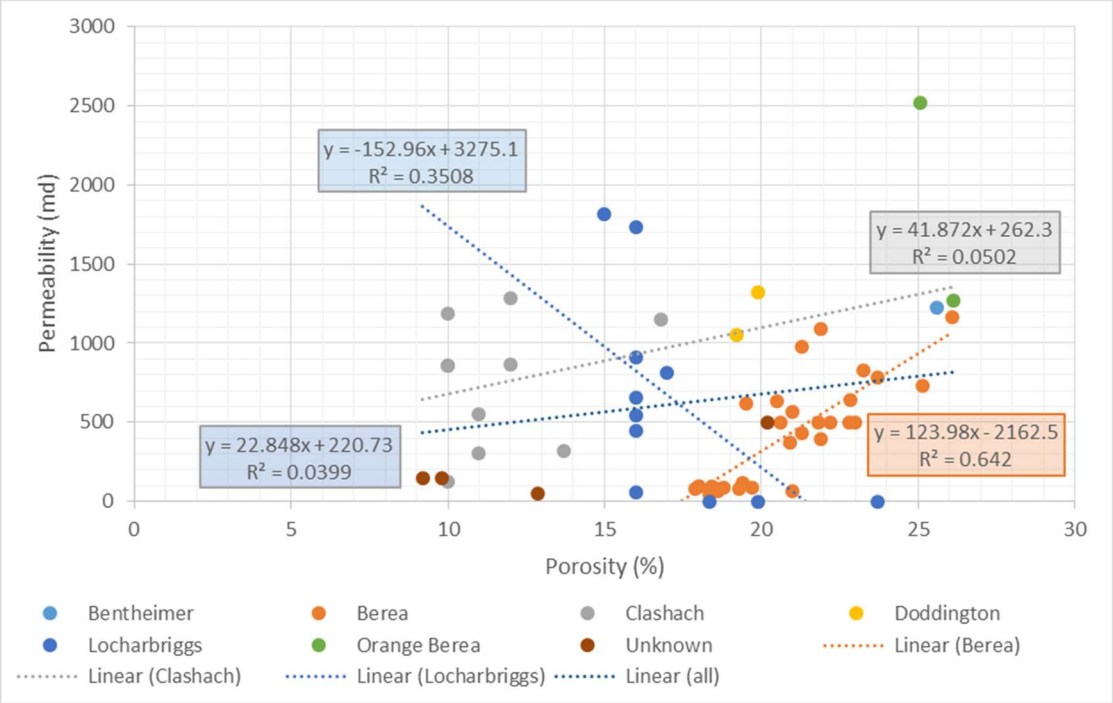

Figure 2-26: Variation of porosity vs permeability for multiple sandstone units. Data from Knight and Nur (1987), Brown et al. (1989), Churcher et al. (1991), Malik et al. (1998), Kewen and Abbas (2000), Ojala et al. (2004), Nasralla et al. (2011), Sbai and Azaroual (2011), Hussain et al. (2013), Alyafei et al. (2016), Ezzat and Shedid (2016)

Figure 2-26 shows that, in order to accurately model a reservoir core, careful and informed selection of an appropriate outcrop core must be made. One cannot select Berea and hope that it will accurately represent the conditions of the reservoir of interest. This analysis also does not consider the composition of the cores; again, careful selection must be made when considering a representative outcrop.

2.3.4 Future Sandstone Analogue Possibilities

Much research has been carried out on fluid flow in different porous networks and network models, but there has been no report of fines migration being studied in such models. Two potential candidate models have been selected as suitable candidates: microfluidics and 3D printing.

2.3.4.1 Microfluidics

Microfluidics is the term used to describe a set of technologies used to precisely control the flow and geometry of flowing fluids by using devices with precisely shaped and sized channels in the micron-scale width. Often these devices are prepared to be transparent, so that flow of fluids can be visualised using a microscope, and recorded using a high speed camera.

Microfluidic devices in have been previously used in the oil and gas industry to monitor the flow of liquids in precisely formed channels. A review by Sinton (2015) looks at the current use of microfluidic devices in the oil and gas industry. Firstly, it is reported that microfluidic devices may be used for faster prediction of the minimum miscibility pressure of water and oil to assist in obtaining parameters for modelling. It is also reported that micromodels (of which the material between microscope slides used by Muecke (1979) and Cerda (1988) may be considered to be a type of) may be used for pore-scale visualisation of fluid movement. Finally, it is reported that nanofluidics may be used as a model for shale pores, and the movement of fluids within these. These applications show that microfluidic devices have the advantage that experiments may be precisely designed and monitored in real time, and many identical replicas can be made so that experiments can be repeated with exactly the same starting conditions.

The movement of fine particles in a microfluidic device in the context of sandstone modelling has not been reported on. Of particular interest would be the movement of fine particles in microfluidic devices of controlled wettability, for example, models as described by Lee et al. (2015), or with wettability modification such as reported by Bashir et al. (2015).

2.3.4.2 3D printed core analogues

A comprehensive review of the application of 3D printing to the oil and gas industry was prepared by Ishutov et al. (2017). To date, 3D printed sandstone cores have been prepared (Ishutov et al., 2015), and used in core flood experiments by the Aramco Research Centre in Houston (Ishutov et al., 2017). More recently, a 0.5 mm cube of Berea sandstone has been reproduced at 1:1 scale by Li et al. (2021). None of these however have been used in fines migration experiments.

2.3.5 Comparison of Current and Future Sandstone Analogue Testing

An overview of the issues raised in this review, along with the analysis techniques described, is shown in Table 2-4. In summary, it is clear that no one technique will be able to answer all possible questions about the movement of fines. Depending on the information required, an informed decision should be made of the most suitable technique for analysis.

*Table 2-4: Comparison between current and future sandstone analogues. *Depending on material*

	Sand or clay-coated particle pack	**Glass sphere pack**	**Sintered glass between two slides**	**Outcrop**	**Microfluidics**	**3D Printing**
3-Dimensional	Yes	Yes	No	Yes	No	Yes
Repeatable (on same sample)	No	No	Yes	No	Yes	Yes
Repeatable (on different sample with same geometry)	No	No	No	No	Yes	Yes
Homogeneous source	No	Yes	No	No	Yes	Yes
Directly viewable	No	Yes	Yes	No	Yes	Yes*
Indirectly viewable (e.g. micro-CT scanning)	Yes	Yes	Yes	Yes	Yes	Yes
Precisely known surface properties	No	Yes	Yes	No	Yes	Yes
True-to-scale	Yes	Yes	Yes	Yes	Yes	No
Sandstone-like pore geometry	Yes	No	No	Yes	No	Yes
Tuneable properties	Yes	Yes	Yes	No	Yes	Yes

2.4 Summary

Over the past 60 years, much work has been done to understand the movement of fines in sandstones under different conditions, and careful experimental models have been built to explore the different properties which influence the movement. However, when considering the different properties which influence fines migration in sandstones, the one which appears to have the least time dedicated to understanding it seems to be how wettability influences fines migration. The study of wettability requires the creation of models with carefully defined and located wettabilities – something which the existing preference for the use of sandstone outcrops wouldn't allow. Considering the more conceptual techniques that have been used to create sandstone models, it would seem that models such as the use of bead packs where the wettability of the beads has been varied (a technique used by Celauro et al. (2014) to analyse multiphase flow, but not yet used for fines migration studies), or microfluidics and 3D printed models where the properties of the model can be carefully controlled may be more applicable. It is therefore the latter technique, the use of 3D printing, that will be used throughout this thesis to help explore fines migration and wettability.

Chapter 3 Experimental Methods

Throughout this work, a number of techniques were used to examine the nature of fines and their movement in pore structures and across surfaces with variable wettability. Rather than the traditional core flood experiments used to examine different contributions to fines migration (see Section 2.2.1), this work gives more of a focus to investigating new techniques which allow the movement of fines to be visualised and tracked, rather than only seeing the end result of fines moving as a function of core permeability. Throughout this work, the theme of wettability and change of salinity from high (1 M) to low (0.001 M) were visited to look at the effects this change of salinity might have in combination with fines movement and wettability, rather than investigating the effects in isolation. The work is divided into three distinct themes, each utilising particular analytical techniques. Firstly, 3D printing (Section 3.1) was used in the preparation of surfaces for wettability analysis (Section 3.2) and characterisation of roughness of the surfaces (Section 3.3). Secondly, the ultrasonic cleaning (Section 3.4) of sandstones was analysed using spectrophotometry (Section 3.5) and scanning electron microscopy (Section 3.6). Finally, the techniques were brought together combining 3D printing with wettability analysis and micro-computer tomography (Section 3.7).

3.1 3D printing

The process of 3D printing an object encompasses many different processes, from 3D model creation to printing preparation, to finally printing as a series of thin layers (and in some cases post processing). The process from model creation to obtaining a usable object is described in detail below.

3.1.1 Obtaining a Digital Model

A digital model is one of the main requirements to be able to create a 3D printed object. There are two main methods which can be used to create a digital model: scanning a physical object and digital creation. In some instances, these methods may be combined, depending on the application.

3.1.1.1 3D Model Creation from Scans

In as early as 1935, photography was used to create contour maps of objects, with the aim of using these contour maps to generate a 3D object (Morioka, 1935). Although this did not give a digital model (digital images were not developed until 1957 (National Institute of Standards and

Technology, 2016)), the methodology of scanning followed by fabricating based on scans is reminiscent of the technology used today. There are numerous methods to create a digital model from a physical object, which can be generally grouped into two categories: those which scan the surface of the object, and those that scan the internal structure of the object.

3.1.1.1.1 Surface Scanning

The simplest form of scanning from a hardware point of view is photogrammetry, where a series of photos from all angles of the object to be scanned are taken, and then stitched together using appropriate software (Luhmann et al., 2014). Photogrammetry may be defined as the science of making measurement from photographs, and has been in use in various forms since the early use of photography. In general, an object will be recreated from a series of photographs by stitching together images which contain a common feature. Often this will be done using cloud-based computing, as a lot of processing is required to carry out the reconstruction. One popular example of photogrammetry software used to scan objects is Autodesk 123D Catch (discontinued by Autodesk in January 2017), a smartphone app which uses the phones camera to take pictures before uploading and processing on the Autodesk servers. The model is then available for clean-up, manipulation and printing (Autodesk, 2016). This method however does not function well with highly symmetrical objects.

A slightly more complex system may make use of a 3D camera, either a stereoscopic arrangement of two cameras or, more commonly, one camera with a depth sensor. A popular example of a camera with a depth sensor is the Xbox Kinect (Andersen et al., 2012, Microsoft, 2017a, Microsoft, 2017b). The Kinect makes use of a pattern of projected infrared dots and an infrared camera, using a technique known as structured light (MacCormick, 2011, Silberman and Fergus, 2011). The dots are positioned in a known pattern and are projected out in front of the camera. The infrared sensor can then pick out the individual patterns and use this to calculate the distance to an object in front of the camera. This is then converted to a depth at a particular pixel, and is fed to the software connected to the Kinect which can then interpret the images and depths and convert them into a 3D object. This often gives a better result than photogrammetry as the depth data does not have to be inferred, but still has problems with highly symmetrical objects (Tzionas and Gall, 2015, Valgma, 2016).

The above techniques will give an object with both shape and material, which in this context refers to the overlay of the photographic images on top of the 3D model. If the material is not important, for example if the model is going to be 3D printed on a monochrome 3D printer,

alternative techniques that make use of either time of flight or triangulation of lasers may be used. The time of flight method times the difference between emitting and receiving a reflection of a pulse of laser light. This method is often used in long-range scanners such as LIDAR, as the accuracy of the timing gives a limit of resolution in the order of centimeters, but a range of up to kilometres (Horaud et al., 2016). The triangulation method on the other hand uses a camera to look for the location of the laser dot on a detector at a known angle to the laser emitter. It has a limited range, in the order of metres, but a much higher accuracy, in the order of micrometers (Blais, 2004).

3.1.1.1.2 Whole-Object Scanning

Non-destructive techniques to look inside physical objects mainly make use of the measurement of carefully controlled electromagnetic radiation passing through the object to a detector. Most commonly used are x-rays, using computer aided topology or computed tomography (CAT or CT) technology, described in more detail in Section 3.7.

3D printing requires a surface topology file to be extracted from the 3D model produced using analysis software. In general, 3D printing requires a STL, OBJ or PLY file, where the surface has been mapped as many connected polygons (for further detail of these file types, see Section 3.1.3). These files may be very large when first produced, as tiny details are reproduced in great detail. It is generally useful therefore to simplify the surface prior to export, so that the file may then be manipulated. Another alternative is to extract a small volume of the original scan file, and carry out manipulation on this file rather than on the whole volume.

3.1.2 Digital 3D model creation

There are numerous different pieces of software available for creation of a digital 3D model; which software is selected will depend on the end use and design considerations of the model.

The simplest 3D modelling software makes use of a library of standard solids, which may then be placed into the 3D design space and resized and combined into new composite objects. Many of these pieces of software may be tablet-based, as there is little need for additional inputs in such a simple modelling environment. Some examples of this type of software include Happy 3D, 3D builder, Tinkercad and Gravity Sketch. This software is designed to be very accessible to people with little 3D design experience, and are often aimed at children. Some of these pieces of software may be designed to work directly with 3D printers, for example Happy 3D for use with FlashForge 3D printers, and will often export STL files for either further manipulation in other design software, or slicing with an appropriate slicer for 3D printing.

A more sophisticated, but still easy to learn, option comes with software that will allow 2D drawings to be created and then extruded to create three-dimensional shapes. Examples include Autodesk Inventor, Autodesk Fusion 360 and Sketchup. These pieces of software allow models to be created with more control over dimensions and shape, and may also include modules for sculpting (Autodesk Fusion 360) or finite element analysis (Autodesk Inventor, Autodesk Fusion 360). These pieces of software may also import and export STL files directly.

Traditionally, 3D designs were made using CAD software (AutoCAD, OpenSCAD), which uses command line input to define shapes. As all properties of a shape are defined, it is often easier to modify models using this software. AutoCAD is marketed as primarily a 2D drafting package, which can, with experience, easily produce plans and drawings for manufacturing or building. OpenSCAD is completely command-line driven, with shapes, dimensions, intersections and cuts all defined in the command line (OpenSCAD, 2017). This can be useful for applying mathematical functions to shapes in order to produce mathematical models, something difficult to achieve using the previously mentioned classes of software.

Software which is more specialised for 3D modelling and the animation industry, rather than printing, includes 3D Studio Max, Maya and Blender. These can be used to create 3D objects in mesh form, and then those objects may be manipulated to produce a finished model. These pieces of software may then add texture, fur, cloth, shadows and lighting effects, and animate the model to give a full 3D animation (not required for 3D printing).

3D scan data may be imported into many of these pieces of software, which gives the option to take the 3D scan data and manipulate and modify it to produce the final model. Another application is the use of the 3D scan as a template for model creation (for example, creating custom foot orthotics (Podfo, 2017)).

All of these pieces of software have the ability to export a 3D model either directly as a surface file, or as a solid object, which can then be converted to a surface file.

3.1.3 Surface file types

As mentioned above, there are three common file types used to describe a surface that will be used to create a 3D printed object. The most commonly used file type for surface mesh files is the STL (**ST**ereo**L**ithography) file type. An STL file divides the surface into a number of triangles (although higher order polygons are possible, in practice they are never used), with the vertices of the triangles defined using Cartesian coordinates, and a surface normal defined for each of

the faces to dictate which face is inside and which is outside the object; the order of the vertices is given using the right-hand rule. In this file type, each triangle is defined separately by each of its vertices, meaning that each vertex may be repeated multiple times in the file. The file does not specify shared edges or vertices, which may in some cases cause problems with gaps being left in the file, particularly for very complex surfaces. 3D printing slicers will check to endure that the mesh file is a closed 3D volume, therefore if the vertices and edges of the STL mesh do not align, this may cause errors. Most slicing software contains ”repair” modules to re-align the edges and vertices, but this may occasionally cause inaccuracies in the surface. The second commonly used format is the PLY (**P**o**LY**gon) file type. The PLY file type may be more compact than the STL file, depending on the object being described. Each vertex is defined, and then the polygons that are used to make up the closed surface are defined by first specifying the number of vertices, then the vertices used; the vertices are numbered from 0 upwards sequentially, with each separate line defining a separate vertex. Finally, the third commonly used format is the OBJ (**OBJ**ect) file type. This file differs from the others in that, in addition to specifying the surface mesh vertices, a material is also associated with the file. This is normally stored in the same directory as the OBJ file, and is specified by the file in the line beginning mtllib.

3.1.4 Slicing Software

Once a surface file of the 3D object to be printed has been obtained, in most cases the object cannot be directly sent to the printer as the surface file. The file must be loaded into a slicer, which divides the mesh file into slices with a given thickness; the thickness is often defined by the user. Following slicing, the slicer produces a file suitable for the printer that is due to be used. There are a number of different slicing software options. Often, the slicing software is specific to the printer that is to be used. Some examples are shown in Table 3-1.

Table 3-1: Printers and associated slicing software

Printer	**Slicing Software**
Flashforge (all printers)	Flashprint
Raise3D (all printers)	Ideamaker
Ultimaker (all printers)	Cura
Lulzbot (all printers)	Cura Lulzbot edition
Form (all printers)	PreForm
Prusa I3	Slic3r Prusa edition
Up! (all printers)	UP Studio
Anycubic Photon	Anycubic photon slicer

There are two commonly used slicers which can output for numerous different printers: Slic3r (opensource) and Simplify3D (commercial). These can produce g-code for a variety of different printers.

3.1.4.1 G-code

A g-code file produced by a slicer consists of a list of commands which tell the printer how to produce the desired object. It is based on the NIST standard for the code sent to CNC milling machines. (Kramer et al., 2000). Different printers may use different commands, hence the variety of slicers available. However, it is possible to modify the g-code designed for a specific printer to work with a different printer if the parameters for both printers are known. It should also be noted that some commands are not included in certain 3D printer firmware versions, for example, M109 does not exist in the Teacup firmware version, and instead M104 followed by M116 is used. Care must therefore be taken when transferring g-code files between printers to ensure that the printer will be able to correctly interpret all commands sent to it and translate them where appropriate.

3.1.5 3D Printer technology

All 3D printers create 3D objects by gradually building up layers of 2D (or, strictly, 3D but with a constant thickness in one dimension, usually defined as the z-direction) shapes, one on top of another. A number of different technologies are used to create the layers; these are summarised in the Table 3-2.

Table 3-2: 3D printing technologies

Type	Technologies	Materials	Resolution (smallest printable object – gap sizes may be smaller)
Extrusion	Fused deposition modeling (FDM) or Fused filament fabrication (FFF)	Thermoplastics, eutectic metals, edible materials, Rubbers, Modeling clay, Plasticine, Metal clay (including Precious Metal Clay)	10 µm z-axis 200 µm x- and y-axes determined by nozzle width (Raise 3D N series)
	Robocasting or Direct Ink Writing (DIW)	Ceramic materials, Metal alloy, cermet, metal matrix composite, ceramic matrix composite	2 µm – resolution determined by nozzle width and therefore viscosity of solution (not commercially available)
Light polymerized	Stereolithography (SLA)	Photopolymer	50 – 150 µm z-axis 140 µm x- and y-axes determined by laser spot size (Form 2) <1 µm (Photonic Professional GT)
	Digital Light Processing (DLP)	Photopolymer	32 µm (M-Jewelry U50)
Powder Bed	Powder bed and inkjet head 3D printing (3DP)	Metal alloys, powdered polymers, Plaster	Metal: 20 µm z-axis 100 µm x- and y-axes Plastic 100 µm z-axis, 500 µm x- and y-axes (3D systems)
	Electron-beam melting (EBM)	Metal alloys including Titanium alloys	140 µm electron beam spot (Arcam Q10)

	Selective laser melting (SLM)	Titanium alloys, Cobalt Chrome alloys, Stainless Steel, Aluminium	20 – 75 µm z-axis 150 µm beam diameter (SLM 500)
	Selective heat sintering (SHS)	Thermoplastic powder	1000 µm z-axis, 100 µm x- and y-axes (blueprinter)
	Selective laser sintering (SLS)	Thermoplastics, metal powders, ceramic powders	80 – 150 µm z-axis (3D systems SLS) 100 µm z-axis (FormLabs Fuse 1)
	Direct metal laser sintering (DMLS)	Almost any metal alloy	200 – 400 µm z-axis 300 µm x- and y-axis
Laminated	Laminated object manufacturing (LOM)	Paper, metal foil, plastic film	100 µm z-axis, 12 µm x- and y-axes (Mcor Iris)
Powder fed	Directed Energy Deposition	Almost any metal alloy	90 – 200 µm z-axis (Insstek MX3)
Wire	Electron beam freeform fabrication (EBF)	Almost any metal alloy	

3.1.5.1 Filament (FDM) Printers

FDM printers use a thermoplastic roll of filament fed into an extruder nozzle, which is then generally moved in the x and y direction while extruding a thin layer of plastic (Figure 3-1). Once a layer has been printed, either the extruder or the print bed is then moved in the z direction to position the nozzle slightly higher (the height set by the layer thickness) than the previous layer, and the next layer is printed on top. The exception to this is when "vase mode" is used as the print method, which continuously extrudes plastic while moving along the perimeter of the object, simultaneously increasing the z height so as to print in a spiral pattern.

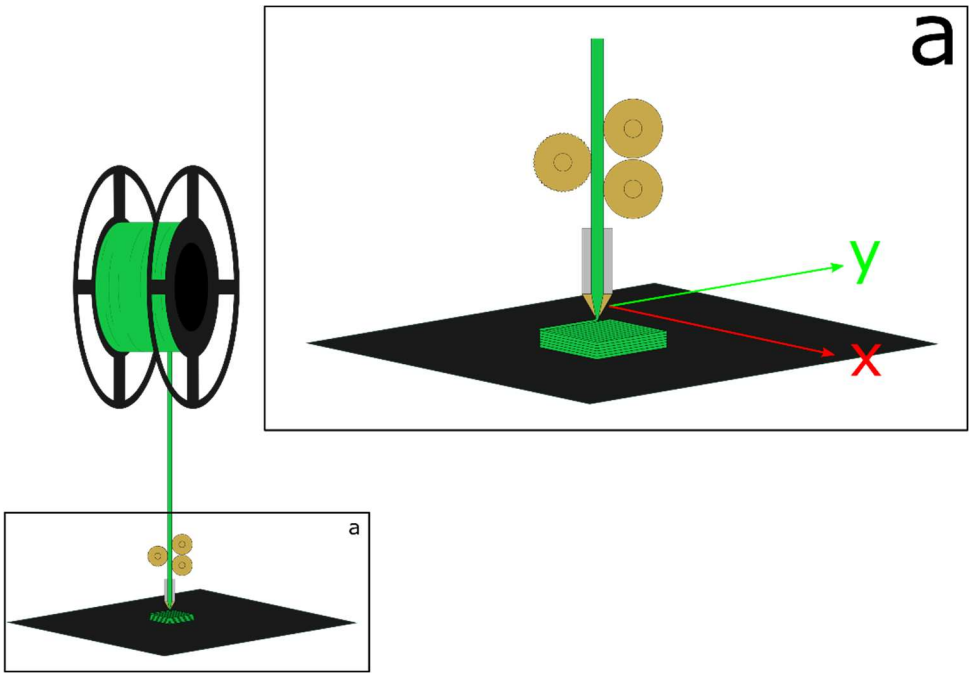

Figure 3-1: Illustration of 3D printing using FDM technology with green filament - movement in the x and y directions.

In general, slicing software divides the object into 4 different parts – the base of the object (the part in contact with the build surface), the walls of the object (the edge surfaces which are supported by edge layers below them), the infill of the object (the fully enclosed inner volume of the object) and the top of the object (the upper layers of the object which may be supported by edges and/or infill). The base is generally printed more slowly than the rest of the object as it is important that the bottom layer adheres well to the build plate. The walls are usually printed at a layer height of around 0.2 mm, and as the filament extrudes from the nozzle in a more cylindrical shape, this leads to a distinct ridged surface texture on the walls of the print. The infill of the object may be printed as a completely filled solid, but it more often reduced to filling 5% - 25% of the volume with a pattern designed to support the object. Finally the top surface is also generally printed more slowly than the majority of the object to ensure the surface is uniform

with no gaps between lines. This surface will have some texture due to the fact that the surface is generally filled by printing parallel lines across the surface. An illustration of the printing directions leading to surface textures is shown in Figure 3-2.

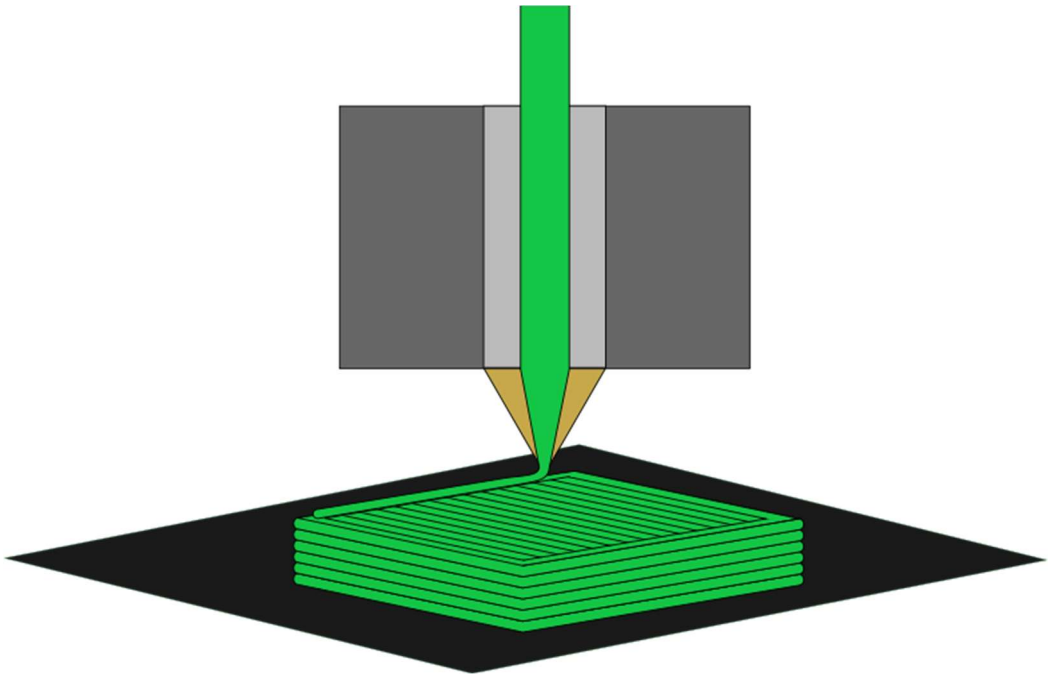

Figure 3-2: Example illustrating the different directions the printing nozzle makes to create a solid object, leading to a variety of surface textures.

Supports may be required for overhanging parts, as there is a limit to how far the plastic can be extruded without sagging or snapping over open space. This limit will be different for each plastic (and, to a lesser extent, each printer) used to print with, and testing should be carried out to obtain the specific data for each plastic used.

Some models may come with two nozzles (often termed “dual extrusion” printers) on the print head, allowing two potentially different plastics to be printed in the same layer of the model. This can be useful, for example, when supports are required, as they can then be printed with a plastic that may be water soluble and then removed with water, or when a model requires materials with different properties, such as rigid and flexible parts, or different surface properties.

3.1.5.1.1 Filament options

Filaments may be divided into two main categories: pure polymeric and composite. Pure polymeric filaments consist of a thermoplastic polymer, which may be a homopolymer, copolymer, grafted polymer etc. This polymer is the only component of the filament, and the

filament will have the properties of this polymer alone. Some common examples are poly (lactic acid) (PLA), amino butyl styrene (ABS), nylon, polyethylene terephthalate (PET), polycarbonate, and poly(methyl methacrylate) (PMMA). Composite filaments contain two or more components, which are mixed, but not bonded, together in a single filament. Composite filaments may therefore have properties not obtainable when pure thermoplastic polymer is used, such as conductivity, magnetism, or functionality such as mineral or metal inclusion. Examples include the addition of wood pulp, lignin, metal powders, carbon fibre, clay, chalk and carbon black.

3.1.5.2 Light Polymerised Resin Printers

3.1.5.2.1 SLA printers

SLA printers use liquid resin cured by a laser to form solid objects. To print a layer, the build platform (or the most recently printed layer) is lowered into a reservoir of resin, and a laser shone to "draw" the 2D image of that layer onto the model and polymerise the resin (Figure 3-3). The model is then moved away from the surface of the resin, the resin is briefly swept to ensure a good flow, and the model is lowered again to print the next layer. Models may be printed either upside-down (where the base of the model is attached to the underside of a platform, which is then gradually raised out of the resin as successive layers are printed), or right-side up (where the model is lowered further into the resin as successive layers are printed).

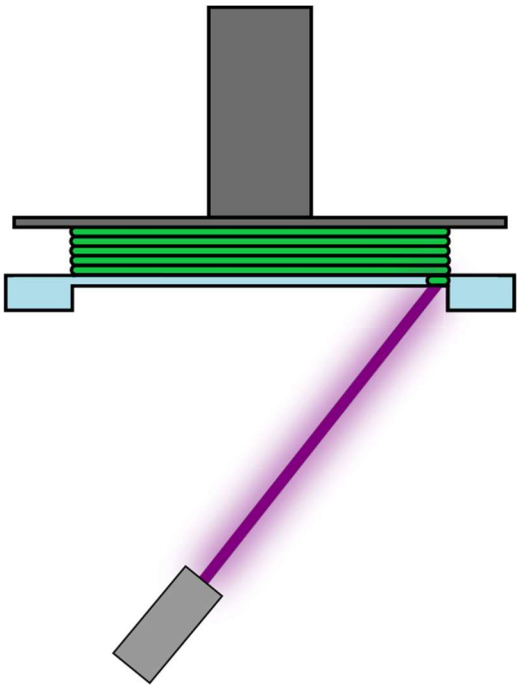

Figure 3-3: Illustration of SLA printing using green resin. A UV laser (purple) is used to cure the resin in successive layers.

As with all other 3D printers, supports are required where there is overhang, but this style of printer may be more capable of printing spanning distances than the FDM printers.

Only one type of resin can be used at any one time in the printer, which means that supports must be removed mechanically and there is no scope for printing different parts of the same model with materials with different propertied without splitting the model into parts to print separately. In addition, hollow objects cannot be printed without drainage holes to ensure excess liquid resin is not trapped inside the prints, and the model may have to be printed at an angle to ensure uncured resin is not retained in hollows in the model, hence printing orientation may be limited which may affect the desired mechanical properties of the printed part. Additionally, post printing finishing is required before the prints can be used. The prints cannot immediately be handled using bare hands. First, the excess resin has to be washed, using isopropyl alcohol (IPA), then left to dry and further cure, usually overnight. The supports added are usually thicker and harder to remove than supports provided in FDM printers, and generally require tools to remove. However, the finish on these prints is usually better than that obtained from FDM printers.

3.1.5.2.2 DLP printers

DLP printers work in a similar manner to SLA printers, except rather than a laser shining through the liquid resin, a projector is used to shine light (or modified to shine UV light) from underneath the model (Figure 3-4). The resolution therefore is controlled by the resolution of the projector attached to the printer, with a variety of projector options available depending on the level of detail required. This printing technique is generally faster than SLA printing as the whole layer is created simultaneously, but the power of the light used is generally lower, so the exposure time of the resin to the light in this instance may need to be higher in order to cure than the time required to cure by the laser.

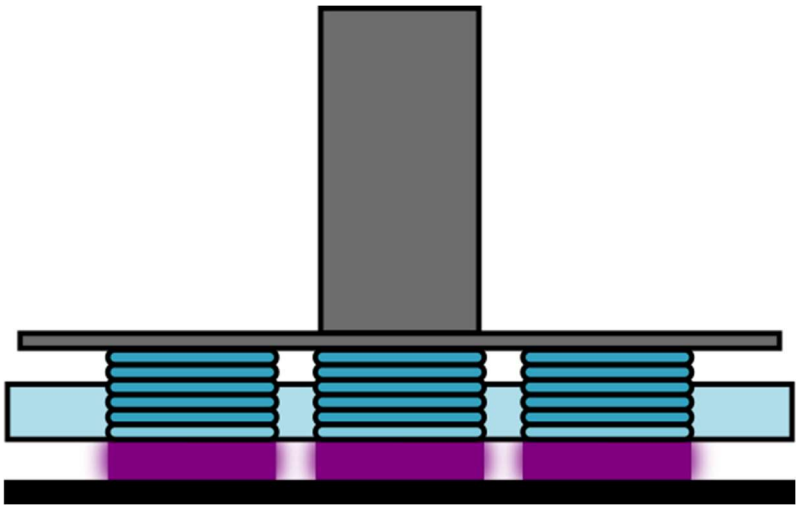

Figure 3-4: Illustration of DLP printing using blue resin cured with UV light, usually 405 nm. In this example, three identical objects are being formed simultaneously.

3.1.5.2.3 Resin Options

Unlike FDM printers, many SLA and DLP printers use proprietary resin and, hence, the variety is limited, and some printers may not be able to use certain types of resin. Most are epoxy- or acrylate-based. The Formlabs resins are based on acrylate chemistry, and are all, in their liquid form, irritating to corrosive. Bio-compatible resins have recently been developed, which allow the printing of objects that, when cured, are non-harmful to biological organisms. This allows objects such as dental moulds and appliances to be printed which then may be directly used in patients, rather than additional casting being carried out. The print resolution may also vary between resins. For example, the Formlabs Black V3 resin can print with a z layer height down to 25 µm, whereas the Durable V1 resin is only capable of 50 µm.

3.1.5.3 Powder Bed Printers

Powder bed printers can be divided into two categories: those which use a binder to fuse the powder particles, and those that directly fuse the powder particles. The printers which use a binder are generally termed “powder bed” printers or, as they utilise more traditional inkjet printing but build up a three-dimensional object, “3D printers”. The printers which fuse the powders directly are known by the method in which they fuse the powders: “selective laser sintering”, “electron-beam melting”, “elective laser melting”, “selective heat sintering”, “selective laser sintering” or “direct metal laser sintering”. All these techniques work with the same principle. Initially, a thin layer of powder (defined by the z-height) is spread across the whole build area. The powder is then fused in the areas which will then become solid, the bed is lowered into the build chamber by another z-height distance, another layer of powder is

spread, and the process is repeated (illustrated using selective laser sintering in Figure 3-5). The print is at all times supported by the powder, as the powder is not removed until the whole build is complete. This is done during post processing; the user must manually remove the powder by a combination of compressed air and vacuum. Finishing may then take place depending on the intended end use.

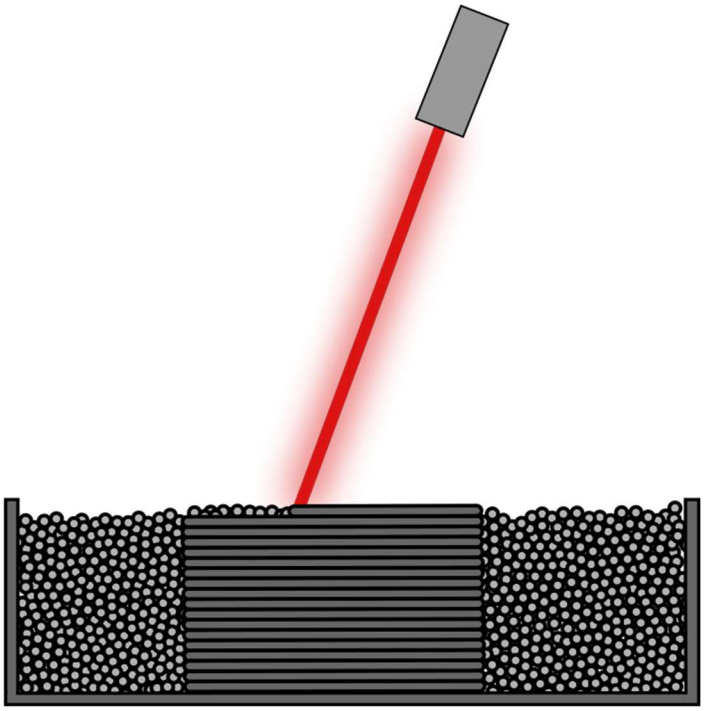

Figure 3-5: Illustration of selective laser sintering using metal powder (grey) fusion by laser (red) melting.

3.1.5.3.1 Binder powder fusion

Originally invented at the Massachusetts Institute of Technology, this technique uses a medium of gypsum and glue-like binder which may contain dye to give full colour printing to bind the powder together. Upon completion of printing, the object is very fragile, and must be treated with either wax, cyanoacrylate or epoxy in order to give a durable print. These prints are often used to produce facsimiles of archaeological or anthropological artefacts as the finish is very stone-like.

3.1.5.3.2 Direct powder fusion

A number of printing techniques can be covered by this category, but all are very similar. The sintering techniques partially melt the particles just enough for them to stick together. The melting techniques fully melt the particles so that they flow into each other and create a solid layer. It has been found that 3D printing with metal has been shown to be as effective, if not more so, than traditional casting methods, with 3D printed parts using a melting technique

typically having a higher density following printing than those using a more traditional casting process (Wysocki et al., 2017).

3.1.5.4 Laminated Printers

From the advent of additive manufacturing (Blanther, 1892), the process of cutting out shapes from material having a known thickness, and stacking these cut pieces of material on top of each other to create a 3D object from a series of 2D shapes has been a useful and convenient process. However, there has been limited application in 3D printing, as the process has always been a manual process, with limited application due to the nature of the material used. The first laminated object manufacturing (LOM) printers were built by Helisys in 1991 (Wohlers and Gornet, 2014), which used a roll of 165 µm thick amber-coloured PVC which is glued using a heated roller and cut layer by layer to give a three-dimensional object.

Figure 3-6: Example print from the SD300 (Cubic Technologies 2004 - 2007, formed from Helisys in 2000 - 2001)

The next innovation in LOM printers came in 2007 when MCor developed the Matrix, a printer which uses A4 paper as the print medium, gluing and cutting the paper layer by layer.

Figure 3-7: Example print from the Mcor Matrix

An interesting innovation came about when Mcor later developed the Mcor Iris, which adds a normal inkjet printer to first print on the paper which is then to be cut, so giving full colour prints.

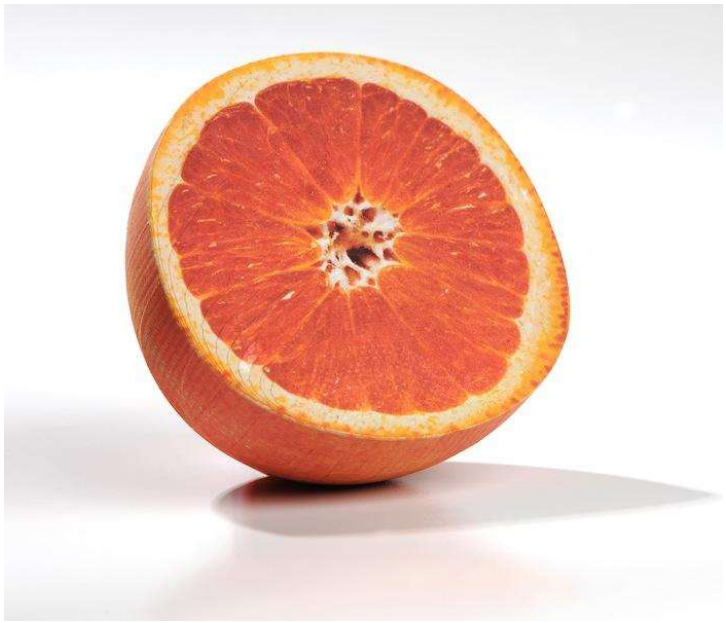

Figure 3-8: Example 3D print from the Mcor Iris

3.1.5.5 Powder Fed Printers

Powder fed printers differ from powder bed printer quite significantly. A powder fed printer deposits molten material from above, and therefore has more in common with FDM printing. A

stream of powder is fed down a nozzle to where an electron beam, laser or plasma arc is located. The powder is melted on contact, and the stream of molten metal is deposited in the pattern predefined by the g-code. The atmosphere in which this takes place therefore is very carefully controlled, oxygen-poor atmosphere. This method is often used to repair or add to existing components as although the technique may be slow, it is highly accurate (Gibson et al., 2010).

3.1.5.6 Wire Printers

Printing with wire melted with an electron beam in a vacuum was developed in the NASA Langley Research Centre, and the technology was patented in 2007 (Taminger et al., 2007). This technique uses an electron beam to melt a metal wire as the wire and electron beam assembly moves in the x-y direction, depositing molten metal which quickly solidifies after deposition, in a similar manner to FDM printing.

3.1.6 3D printing techniques used in this work

In this work, two particular printing techniques were chosen. The first was FDM printing, chosen because of the ease of creating porous media (such as sandstones) and the wide variety of printing materials available, coupled with the low cost, small footprint and easy availability of such printers. The printer selected for the majority of this work was the Raise 3D N1, due to its wide temperature range (up to 300 °C nozzle, 110 °C bed), high resolution (50 µm layer height), easily modified g-code and ability to print with two materials at the same time. The second printer selected was a DLP printer due to the higher resolution prints coupled with the fact that waterproof and transparent objects are much easier to produce. The printer selected was the Anycubic photon due to its high resolution (47 µm pixel size, 25 µm layer height), low cost and small footprint. The availability of materials at the time of purchase was limited to a single 405 nm photosensitive resin, but more recently resins with different properties, such as flexible and casting resins, have been developed.

3.2 Measurement of wettability

Wettability is defined as the attraction of a liquid phase to a solid surface and is controlled by the balance of surface tensions at the liquid-solid, liquid-air and solid-air boundary (where measurements are carried out in air; air may be substituted for any other non-miscible fluid). For further details, see Section 2.2.1.5.

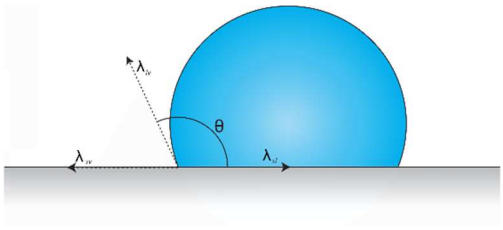

Figure 3-9: Surface tension balance contributing to wettability. Grey: surface, blue: water, white: air, ϑ: contact angle, λ: surface tensions at liquid-solid, liquid-air and solid-air boundaries.

Many techniques have been developed to measure wettability, but the suitability of a particular test depends on the substrate measured (Thyne, 2015). For measuring the wettability of whole rock cores, where the core is rough, heterogeneous and contains many pore spaces, methods which take advantage of this fact such as imbibition by the Amott or Amott-Harvey method, or in a similar but faster method developed by the US Bureau of Mines (USBM) are most appropriate. These methods involve fully saturating the core with one fluid, e.g. oil, and then allowing or forcing (either by flow or by centrifugation in the USBM method) that fluid to be displaced by another non-miscible fluid (e.g. water). By measurement of how much fluid is expelled and imbibed by the rock at each stage, a wettability index can be obtained. Wettability of a formation rather than a core may also be measured using downhole logging tools such as NMR and resistivity by analysing the fluids present in the formation and using this to interpret the formation wettability. These methods however are not particularly useful for measuring the wettability of individual minerals or surfaces. In this case, the most practical method to measure wettability is the measurement of the contact angle. This is the approach to wettability measurement in this thesis and hence the apparatus and measurement method are described in further detail below.

3.2.1 Contact angle measurement technique

The most basic method of contact angle measurement is that of the sessile drop, whereby a drop of liquid, usually water, is placed on a surface, allowed to come to equilibrium and the contact angle the drop makes with the surface is measured (θ in Figure 3-10). If the contact angle is very low however, it may be more accurate to measure the contact angle of a captive bubble, whereby a bubble of air is injected under the surface which has been suspended in a container of the liquid under study. This is illustrated in Figure 3-10.

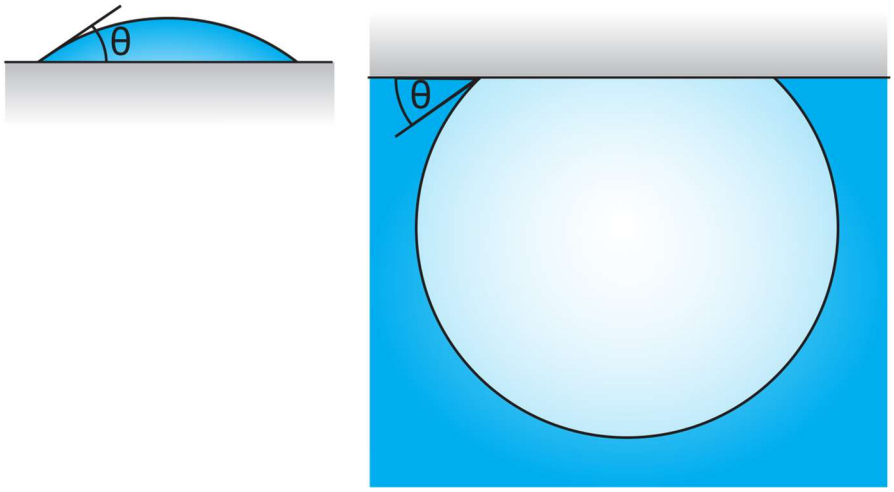

Figure 3-10: Sessile drop (left) vs captive bubble (right) contact angle measurement methods. Grey: surface, blue: water, white/pale blue: air, ϑ:water contact angle for the surface.

Originally, this measurement would take place by the projection of an image of a droplet onto a screen rather than a photograph being taken, and the angle measured manually with a protractor (Chau, 2009). Technology has improved since; now, contact angle measurement is carried out using a contact angle goniometer. This instrument consists of light source and a camera with a platform located in between where the sample is placed (see Figure 3-11 and Figure 3-12).

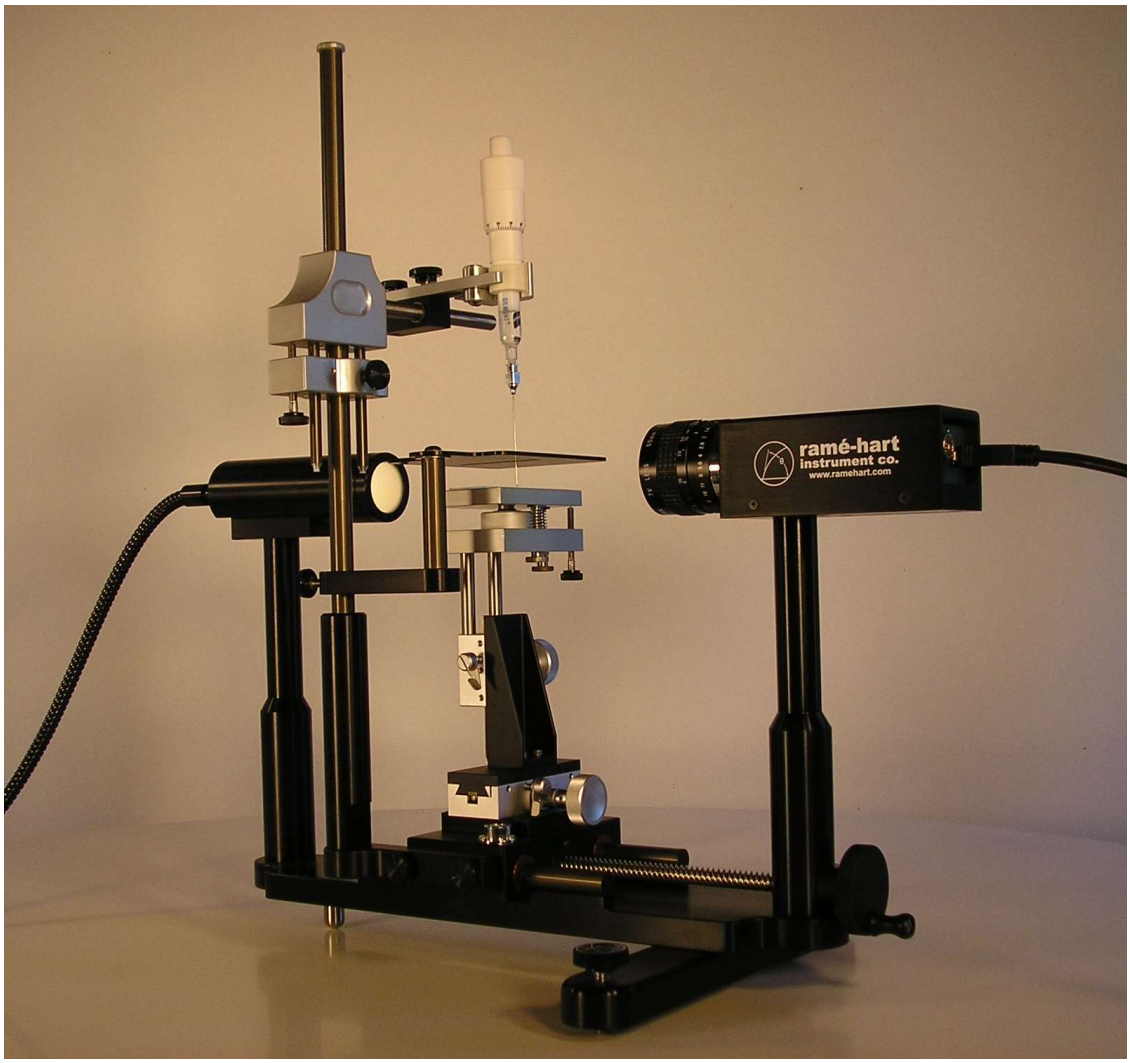

Figure 3-11: ramé-hart contact angle goniometer, model 200, showing left to right light source, dispensing needle and platform, and camera.

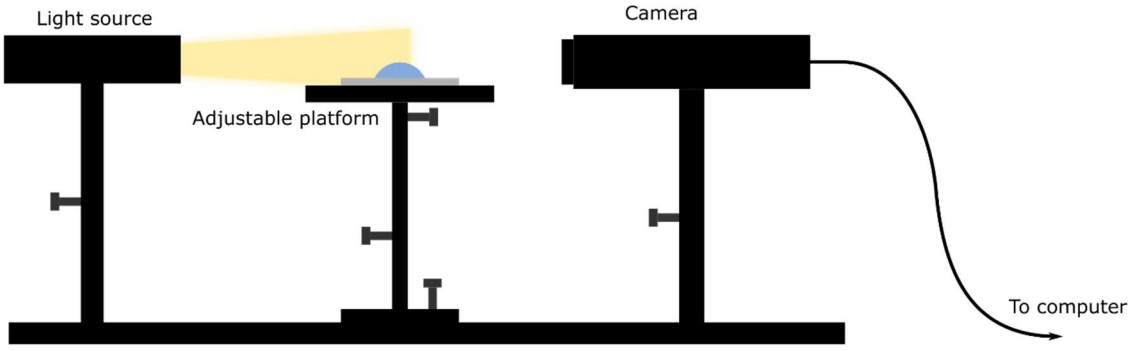

Figure 3-12: Schematic of a typical contact angle goniometer. The light source and camera are fixed, but the sample platform can be adjusted to give a variety of measurement options and the ability to accommodate a number of substrate sizes.

In the case of the ramé-hart goniometer, the software (DropImage) uses a contour fitting algorithm to make multiple different measurements of the droplets in real time on images taken

from the camera connected to the computer (ramé-hart, 2017). The measurements made include the contact angle and the height and width of the drop based on calibration of the software with a ball bearing of known diameter.

The method of drop deposition on a surface to give the most repeatable measurement of contact angle has been developed over time. It has been found that forming a small drop at the tip of a needle and transferring the drop to the surface of interest by lowering the needle until the drop touches and allowing the drop to transfer to the surface from the needle produces the most reliable measurements (ramé-hart, 2017).

3.2.2 Wettability measurement techniques used in this work

In this work, the ramé-hart Model 260 Standard Contact Angle Goniometer / Tensiometer was used for all contact angle measurements, using the sessile drop method. This method was selected as the contact angles that were being measured were generally above 60° and were hence easy to visualize using the sessile drop. The sessile drop method is also quick and easy to carry out as it is carried out in air on an open benchtop. The images were analysed using the contact angle module of the ramé-hart DROPimage software.

3.3 Measurement of Roughness

Roughness is a measurement of surface texture and irregularity over small length scales. It is separate from waviness, which refers to irregularities measured over larger length scales (Black, 2013). These are illustrated in Figure 3-13.

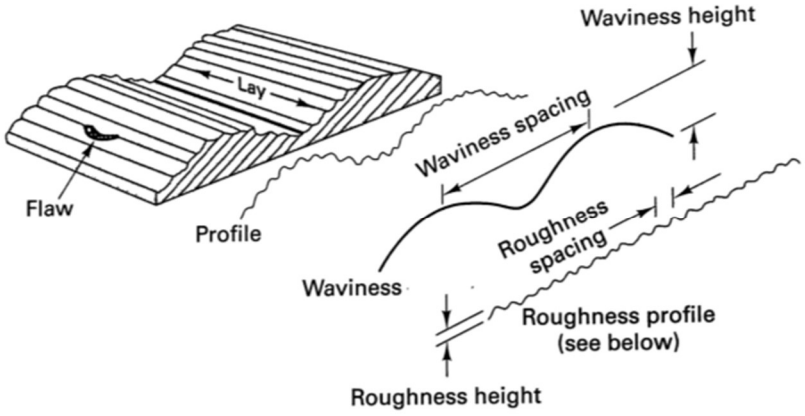

Figure 3-13: Roughness vs waviness illustration. From Black (2013)

Methods used to measure roughness may be either contact measurements or non-contact measurements. These are listed in Table 3-3 and Table 3-4, and described in more detail below.

Table 3-3: Contact measurement of roughness

Technique	Description	Typical scale	2D or 3D profile?
Profilometry	A stylus with tip of defined size moved across the surface. Amplitude of deflection of stylus is measured and recorded	µm	2D
AFM	Atomic-scale probe moved across surface, deflection is recorded	nm	Usually 3D, from a series of 2D lines.

Table 3-4: Non-contact measurement of roughness

Technique	Description	Typical scale	2D or 3D profile?
Micro CT	Use x-ray CT images taken to reconstruct 3D model of surface	µm	3D
Confocal microscopy	Use stack of images from different focal planes to reconstruct 3D image	nm	3D
SEM	Images taken in s Scanning Electron Microscope used to calculate roughness	nm	3D
White light interferometry	Using interference patterns of light to produce a depth map of a surface.	µm to nm	3D

Traditionally roughness measurement was carried out using a profilometer, which uses a contact stylus method, illustrated in Figure 3-14. This method draws a stylus with a diamond tip in a straight line across a surface and records the deflection of the tip along the line. The resolution is therefore limited by the sharpness of the tip. It is also clear that the movement of a diamond tip across a soft surface may damage the surface, therefore limiting the use to surfaces which will not be damaged by the tip.

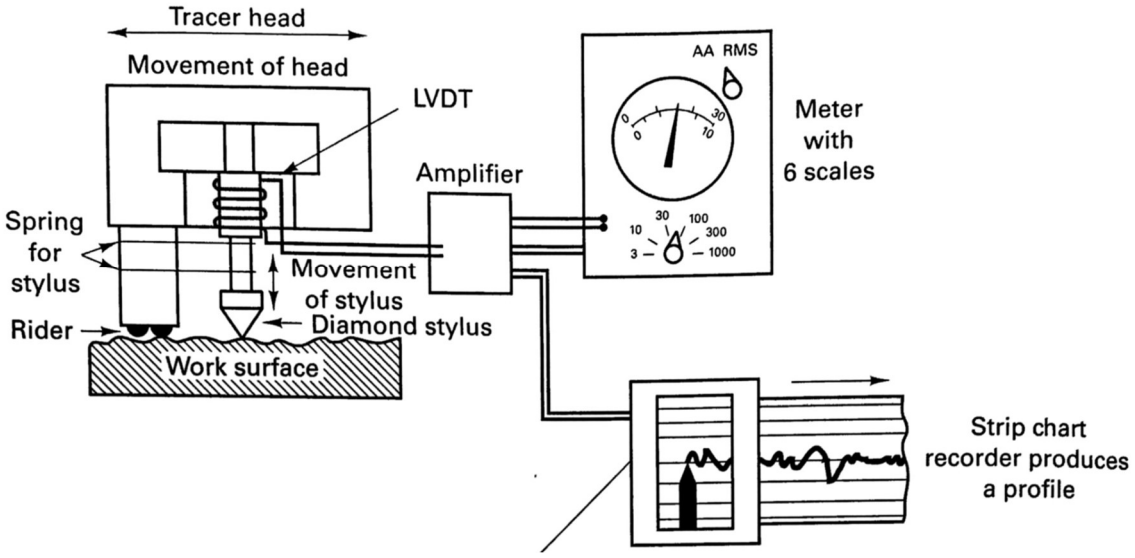

Figure 3-14: Traditional contact measurement of roughness. From Black (2013)

AFM uses a similar principle to profilometry. In this technique, a very sharp probe with a tip with a diameter of a few nanometers is drawn across a surface, usually in both the x and y direction in a raster pattern. The deflection of the tip moves a cantilever onto which a laser light is shone. The deflection of the laser light is recorded on a photodiode, and the position of the laser spot can be converted to a deflection distance with error correction for torsion rather than deflection. This technique can give a namometer scale 3D surface profile. This technique is illustrated in Figure 3-15.

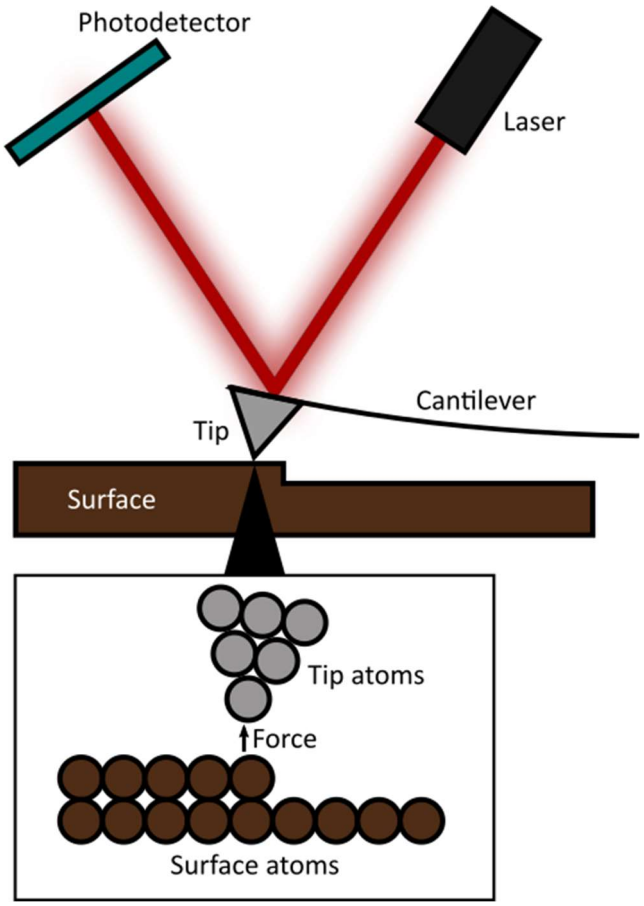

Figure 3-15: AFM principles of operation. Redrawn from Agarwal et al. (2012)

For some surfaces, especially soft surfaces, contact measurement of roughness is not appropriate. To be able to measure soft surfaces, or other surfaces which might not be accessible to profilometry or AFM, a number of non-contact surface profile measurement options are available. Micro-CT is discussed more fully in Section 3.7. Once a scan has been obtained of an object and has been reconstructed into a 3D model, the surface of interest can be extracted and converted into a series of x, y, z coordinates from which roughness parameters can be calculated. Confocal microscopy uses point illumination of a sample with laser light and a pinhole positioned in front of a detector to filter out any unfocused light reaching the detector (Figure 3-16 a). As traditional confocal microscopy looks at an individual point at a time, rastering across the specimen in a similar manner to AFM is used. However, in order to carry out high speed (although lower resolution) scans (Croix et al., 2005), images may be formed using a spinning disk system, as shown in Figure 3-16 b. To form a 3D image, a series of slices at different heights are formed of the object, showing only the parts of the object which were in focus at that height; these can be stacked and interpolated in order to form a 3D surface from which roughness parameters can be obtained. Although normally used for imaging fluorophores of

labelled biological specimens, confocal microscopy used in reflectance mode can produce images of a surface which can be used to obtain roughness parameters. However, the use of confocal microscopy in this mode cannot be used for all materials, and notably may not give good results if specimens with variable reflectivity, opacity or homogeneity are used.

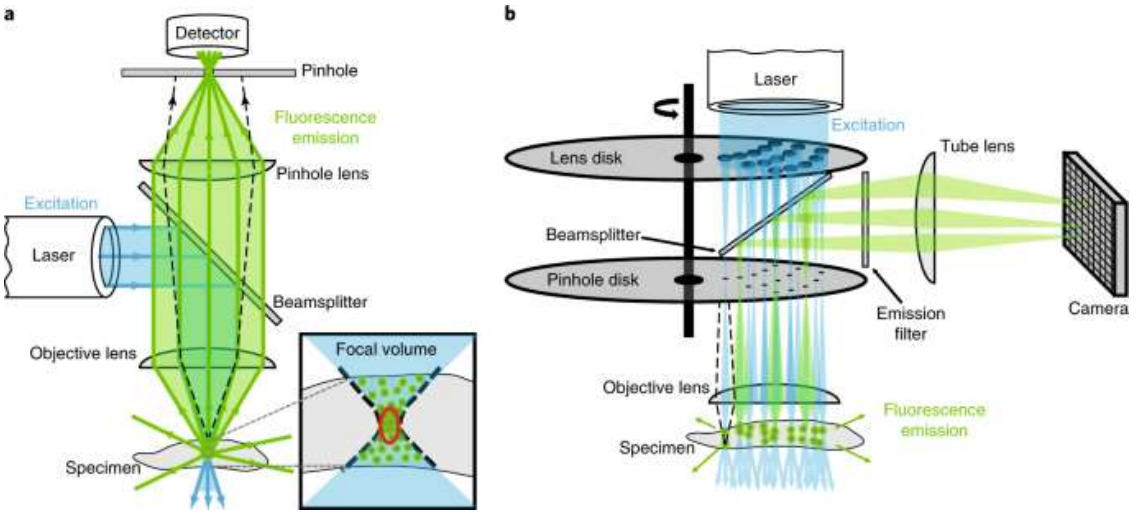

Figure 3-16: a - confocal microscopy operating principle, b - illumination of many points of a specimen at once, removing the requirement to raster across the specimen to produce a whole image thereby decreasing the scan time. From Jonkman et al. (2020).

SEM (discussed in more detail in Section 3.6) can be used for producing a surface profile from which roughness measurements can be obtained by taking two images of a surface at two different tilt angles and using software (e.g. MeX, Alicona software) to reconstruct the surface profile from the images. However, for this measurement the sample needs to be mounted and coated, so, in comparison to the other methods discussed, may not be as convenient if the surface cannot be removed for measurement. White light interferometry is a technique specifically designed for measurement of the texture of surfaces. A collimated light beam is split into a reference beam and a measurement beam at a beam splitter. The reference beam is set to travel the same distance to a mirror as the beam will travel to the sample (or, in the case of a rough sample, approximately the mean height of the sample). The light from the measurement beam is reflected from the sample and meets the reflected reference beam at the detector, usually a camera. Where the height of the sample deviates from the mean height, the light will travel a larger distance to reach the detector than the reference beam; this will cause an interference pattern. By analysing the interference pattern, the software on the computer attached to the detector can reconstruct a height map of the surface. White light is used so that multiple wavelengths hit the sample at one time, therefore forming multiple interference patterns and increasing the accuracy of the measurement, and this also allows for the

reconstruction of the surface with accurate colouring. This technique is non-destructive and does not suffer from the same limitations roughness measurement using confocal microscopy suffers from – many materials are able to be used in a variety of colours, opacities and reflectivities. In addition, unlike the contact measurement techniques, interferometry is non-damaging to soft surfaces. It is however sensitive to surface contamination, unlike AFM where measurements may be made on a surface in air or under liquid.

For all measurement techniques, the aim is to obtain a profile or map of the surface and to then extract roughness parameters from that profile. For a traditional profilometer, a 2D line profile is obtained. A typical profile is illustrated in Figure 3-17, indicating some of the roughness parameters and measurements that can be made. Further values which can easily be extracted from the profile are listed in Figure 3-18. The most commonly used profile roughness parameters are included in BS EN ISO 4287:2000 British standard (identical to the ISO 4287:1997 standard); these are shown in Table 3-5.

In addition to the 2D roughness parameters, 3D surface roughness parameters can be extracted from 3D surface profile datasets. These are very similar to the 2D roughness parameters, but take into account x and y surface movement, and z height variation. 2D roughness parameters can also be extracted from 3D surface profile datasets by selecting the points along a particular line of interest.

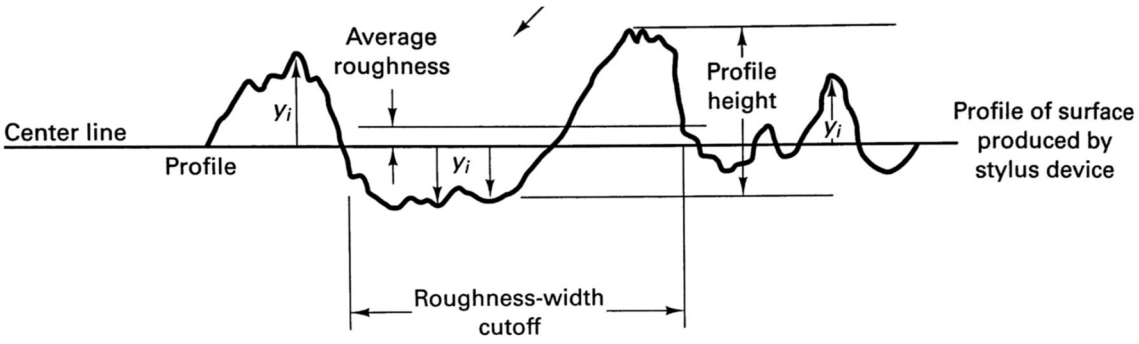

Figure 3-17: Illustration of data recorded from contact roughness. From Black (2013)

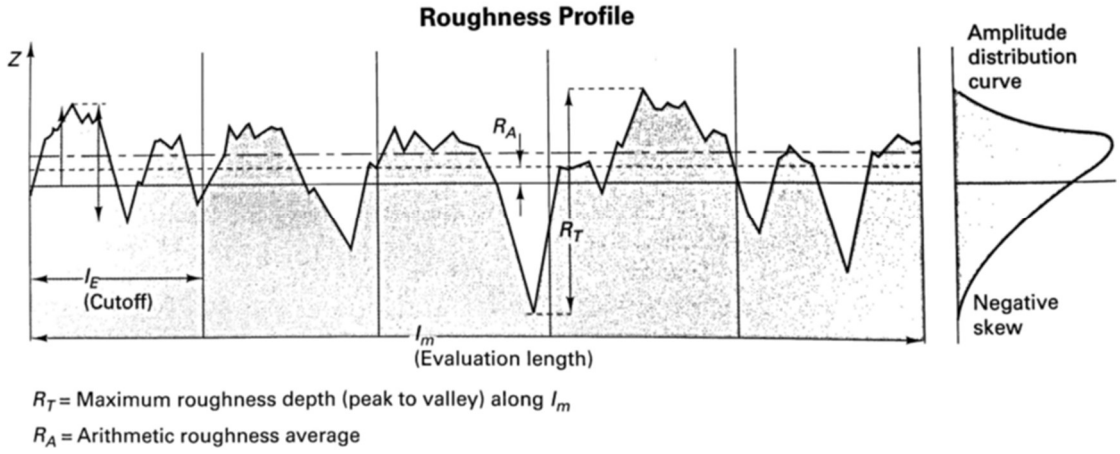

Figure 3-18: Illustration of roughness parameters. From Black (2013)

A number of different measurements may be made in order to give a value to classify the roughness of a surface. Some of the most common are listed in Table 3-5.

Table 3-5: Commonly measured roughness parameters

Parameter	Description	Relevance	Equation
R_A	Arithmetic mean deviation of the profile	No indication of special frequency of irregularities or profile shape	$\frac{\sum_{i=1}^{n}\lvert y_i\rvert}{n}$ $\frac{\int_0^l \lvert Z(x)\rvert dx}{l}$
R_q	Root mean squared deviation of the profile		$\sqrt{\frac{\sum_{i=1}^{n}(y_i)^2}{n}}$
R_v	Maximum valley depth		$\min_i y_i$
R_p	Maximum peak height		$\max_i y_i$
R_t	Maximum roughness depth		$R_p - R_v$
R_{sk}	Skewness	Measure of surface symmetry about a mean line. <0 for peaks, >0 for scratches, 0 for normal	$\frac{\sum_{i=1}^{n} y_i^3}{nR_q^3}$

		distribution about the mean line	
R_k	kurtosis	Measurement of randomness of heights and sharpness of heights. The more random the surface is, the closer the value is to 3. Spiky surfaces also contribute to higher values.	$\frac{\sum_{i=1}^{n} y_i^4}{nR_q^4}$
R_{zDIN}	Average height between the highest peak and the lowest valley for each of the sampled lengths		$\frac{\sum_{i-1}^{s} R_{ti}}{s}$

Where n is the number of evenly spaced segments in the profile assessed, y is the deflection from the centre line and s is a sampled length.

3.3.1 Roughness measurement techniques used in this work

This work required the roughness of a large number of 3D printing materials of varying colour, reflectivity and transparency to be measured. The materials were generally thermoplastic and relatively soft (compared to, say, steel). These properties alone ruled out the use of confocal microscopy (due to the appearance of the materials), SEM (partly due to the thermoplastic nature, but also due to the destructive nature of the testing with the required coating) and profilometry (due to the softness of the plastic compared to the diamond tip). Of the remaining techniques, AFM would have struggled where the surface variation was greater than the nanometre scale it is designed to measure and micro-CT may not have been able to give the required resolution (and would have been extremely time consuming for the number of samples). White light interferometry therefore was the obvious choice of measurement technique. Two different instruments were used – the Taylor Hobson Precision Talysurf CCI,

using Talysurf and Talymap Platinum software at BP Pangborne Formulated products technology (FPT) labs, and the Wyko NT-9300 white light interferometer (WLI) at the Department of Engineering, Swansea University. The Talysurf instrument automatically removed the waviness from the measured profile, leaving only the roughness at a nanometre scale. In order to preserve the waviness, further measurements were taken on the Wyko instrument which preserved both the roughness and waviness and allowed both to be analysed.

3.4 Ultrasonic cleaning

Ultrasonic cleaning involves the use of an ultrasonic transducer in combination with either a water bath or probe. The ultrasonic transducer is made of metal blocks which sandwich a piezoelectric material between them. In the bath configuration, the transducers are attached in an array across the bottom or sides of the bath. When an alternating electric current is applied to the transducers, the piezoelectric material vibrates and the vibrations are transmitted into the water in the bath. The arrangement of the transducers is configured to ensure a fairly uniform distribution of ultrasonic waves throughout the bath; this is shown in Figure 3-19. A more accurate distribution of ultrasonic energy across the bath may be obtained by setting up a test matrix of items to be cleaned in the bath and monitoring the efficiency of cleaning in different areas in a method developed by Kulkarni and Rathod (2014), and illustrated in Figure 3-20.

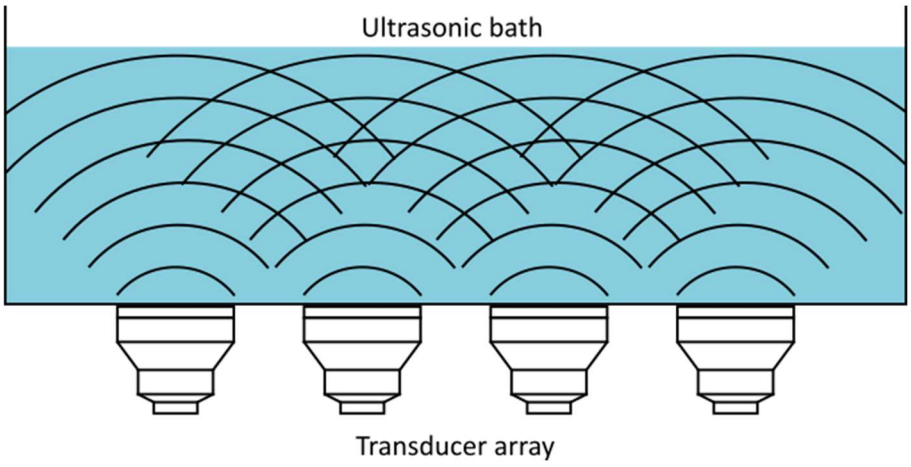

Figure 3-19:Transducer arrangement showing ultrasonic energy waves for ultrasonic bath.

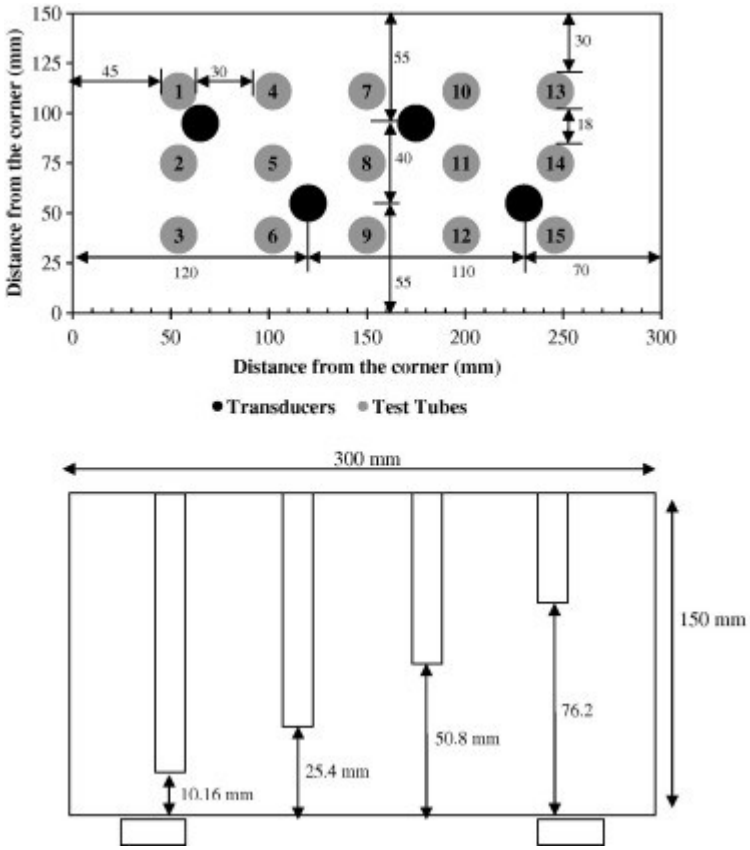

Figure 3-20: Method for mapping ultrasonic power across an ultrasonic bath. From Kulkarni and Rathod (2014).

In the case of the ultrasonic probe, the transducer is mounted above a cylindrical piece of metal (known as the probe or horn) which is submerged in the liquid in which the ultrasonic treatment will take place, illustrated in Figure 3-21. It is the probe itself which vibrates in this configuration rather than the whole bath. An ultrasonic probe generally delivers more energy to the liquid than if the container were placed in an ultrasonic bath.

Figure 3-21: Photograph an ultrasonic probe setup (Fisherbrand™ Model 120 Sonic Dismembrator)

When a fluid is vibrated, whether at ultrasonic frequency or not, compression and rarefaction waves are produced. The rarefaction wave represents a rapid decrease in fluid density, and as a consequence, in a liquid, small bubbles, or cavities, are produced. Through repeated compression and rarefaction cycles, the small bubbles grow until the point where they collapse in a process known as cavitation, illustrated in Figure 3-22. The most common frequency used in ultrasonic cleaning applications is 40 kHz and at this frequency in pure water at 60 °C, cavitation bubbles can reach sizes of up to 100 µm (Mattox, 2010) before imploding at a temperature of up to 5000 °C and pressures of up to 2000 atm. The cavitation bubbles may occur anywhere in the liquid which means that even internal surfaces may encounter the cavitation bubbles.

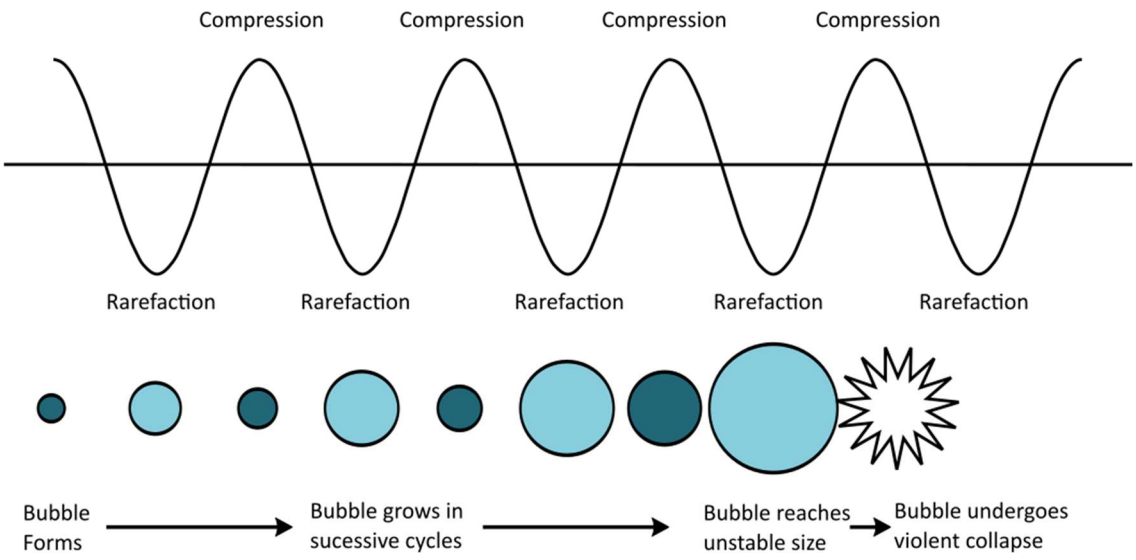

Figure 3-22: Acoustic cavitation - bubble development and collapse.

3.4.1 Ultrasonic application techniques used in this work

Both an ultrasonic probe and an ultrasonic bath were used in this work. The ultrasonic probe used was a Fisherbrand™ Model 120 Sonic Dismembrator, which provides 120 W of power at 20 kHZ via a 3.2 mm probe. The ultrasonic bath was a Ultrawave QS5, which provides 100 W of power at a frequency of 32 to 38 kHz. As the ultrasonic probe provides power directly into the sample, the ultrasonic energy experienced by the sample is much higher than in the ultrasonic bath. However, the ultrasonic bath may be used to treat multiple samples (depending on whether accurate mapping of the bath can ensure equivalent energy being provided to all samples) at once whereas the probe can only treat one. The combination of the two instruments therefore provided the best range of ultrasonic treatment options.

3.5 Spectrophotometry

Spectrophotometry is a qualitative technique that measures the light transmitted through a sample as a function of the wavelength of the light. Spectrophotometers are generally designed to use ultraviolet, visible and infrared wavelengths, although wider wavelengths can be measured by some specialised instruments. In order to measure the absorbance or transmittance of light by a sample, a wavelength is selected and a beam of light is passed through the sample. The light exiting the sample is detected and measured; this is illustrated in Figure 3-23, and an example of an instrument used is shown in Figure 3-24.

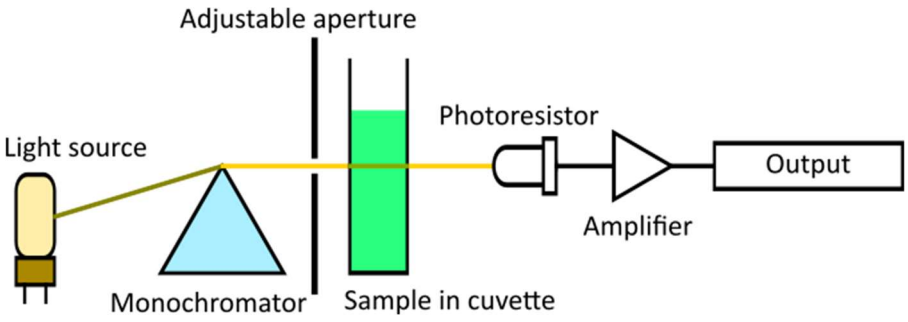

Figure 3-23: Principle of spectrophotometer operation

Figure 3-24: Jenway 6300 spectrophotometer

Spectrophotometry is often used to monitor reaction progress by colour change, as the Beer-Lambert law (Equation (5)) shows a linear relationship between absorbance and concentration for a given molecule and path length (the distance light travels through the sample, given by the particular cuvette used during measurement). In some cases, an instrument is limited to a particular wavelength in order to monitor one particular reaction; in this case the instrument is called a colorimeter. However, in cases where the transmittance of light is reduced not by absorbance of the wavelength of light used by the molecule being used to monitor a reaction and instead is reduced by the presence of particles in the solution blocking the light beam, turbidity is often measured instead of absorbance or transmittance. Turbidity is more often measured using a turbimeter, which uses a single wavelength of light. However, absorbance values can be converted to turbidity values by combining equations (6) and (7).

$$A = \varepsilon c l \quad (5)$$

$$T = -\ln {}^{I_t}/_{I_0} \quad (6)$$

$$A = \log_{10} {}^{I_t}/_{I_0} \quad (7)$$

Where:

T = turbidity (dimensionless)

I_t = intensity of light passing through the sample

I_0 = Intensity of light passing through the reference sample

A = absorbance (dimensionless)

ε = molar absorption coefficient (l mol^{-1} cm^{-1})

c = concentration (mol/l)

l = path length (cm)

3.5.1 Spectrophotometry techniques used in this work

Two instruments were used in this work. The first was the Jenway 6300 spectrophotometer, with a working range of 320 nm to 1000 nm. The second was a single wavelength Hach Pocket Colorimeter at 655nm. The Jenway instrument was used to assess absorbance across a wide variety of wavelengths, whereas the Hach instrument was able to measure a wider range of absorbance values at an appropriate wavelength for the suspension measured.

3.6 Scanning Electron Microscopy (SEM)

Scanning electron microscopy uses a focused beam of electrons rastered across a surface to give information about the elements in and topography of a sample, with a potential resolution of under 1 nm. The instrument produces a highly focused beam of primary electrons (PE) from an electron gun which is directed at the sample (Figure 3-25, Figure 3-26). As the electrons hit the sample, they interact with the atoms in the sample in a small volume controlled by the electron beam energy and the density and atomic number of the sample. Electrons interacting with the most weakly bound electrons in this volume can transfer some of their energy to these electrons allowing them to escape – these electrons are known as secondary electrons (SE). The intensity of the SE are measured as the electron beam is rastered across the sample. The intensity can then be converted to a topology map of the surface. Other interactions with the sample can produce backscattered electrons (BSE) where the PE are reflected by the sample back towards the electron gun, giving information about the atomic number of elements in the area being imaged – heavier elements give more BSE. Finally, information about the atoms present in the

sample can be obtained from x-rays emitted (EDX) when an outer shell electron fills the hole left after the PE knocks an inner shell electron out of a surface atom in the sample.

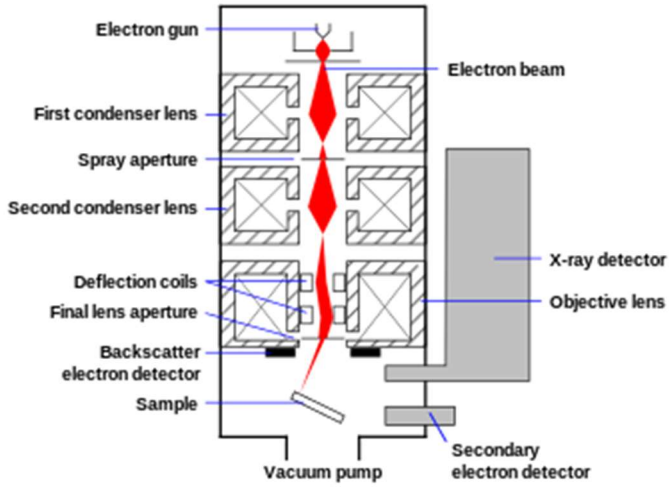

Figure 3-25: Scanning electron microscope diagram

Figure 3-26: Hitachi SU-70 FEG SEM used at Durham University

In order to view samples with conventional SEM, the samples must be conductive. For samples such as sandstone, which are not naturally conductive, a coating must be applied to make the surface conductive. The coating is usually applied using a sputter coater (Figure 3-27) and the sample coated with either gold or carbon (depending on the sample and the resolution required). The coating required is not thick – usually in the order of tens of nanometres. The

coating is required as the beam of electrons is charged, and without being conductive (and grounded) the sample accumulates charge, which leads to imaging artefacts and instability.

Figure 3-27: Cressington 108 auto sputter coater

When scanning an object, there are a number of variables available within the SEM that may improve the resolution or make scanning particular materials easier (Zhou et al., 2006). The electron beam voltage can be varied, with a higher value giving further penetration into the sample but a smaller value giving a smaller interaction volume. The Hitachi SU-70 FEG SEM used at Durham University gives the ability to vary the electron beam voltage from 0.5 kV to 30 kV. 20 kV gives a penetration depth of approximately 1 µm into the sample, whereas 5 kV images the coating applied to the sample. A lower voltage also reduces the chance of charging and damaging the sample where a thin coating has been applied, which may have been done in order to preserve very small details in the sample which might have been covered up by a thicker coating. However, a lower voltage will not give as high a resolution as a higher voltage, and may not be high enough if EDX is required to identify atoms present in the sample as in order to produce the x-rays for EDX analysis, the PE must have a higher energy than the electron that is to be removed to give the EDX signal. Another factor that may change the resolution of the image obtained is the working distance. In the Hitachi SU-70 FEG SEM, the optimal working distance is 15 mm, as at this distance the beam of electrons is most accurately focussed on the sample.

3.7 Micro-Computer Tomography (micro-CT)

Advances in imaging technology have allowed micro- and nano-scale CT scans of objects to be taken, giving extremely high resolution images of the inside of materials which, with the use of data processing algorithms, may be used to generate digital 3D models of the object, which then may be further manipulated, processed or analysed.

CT scans do not differentiate between materials directly; rather, the different materials absorb x-rays with different strengths depending on the atomic number and density of the material (Cnudde et al., 2009), and hence attenuate the x-ray detection at the detector differently. This will produce a greyscale contrast map which then must be interpreted by the user, using data from other sources, such as EDX, thin section analysis, x-ray diffraction etc. to identify which intensity may correspond to which material.

In general, the materials of interest in a clastic digital rock may be the matrix and pore structure, and the relative positions of different mineralogies and their abundance. It is generally relatively straightforward to separate the matrix from the pore spaces, as the pores are generally air filled, so absorb very little of the x-ray energy passing through the sample, and hence are generally visible as dark areas on the resultant scan. In contrast, highly attenuating materials such as quartz, clays and heavier elements produce clearly differentiated bright areas on the scan, and are easily segregated using thresholding methods (Kareem et al., 2017).

A micro-CT scanner works by transmitting x-rays through the sample of interest, recording the x-rays after they have passed through the sample and then rotating the sample by a known angle and repeating. The images formed by the x-rays that have passed through the sample are then processed and reconstructed using a back-projection algorithm from a series of x-y images to a series of x-z slices, or a 3D rendering of the sample. A diagram of the scanner is shown in Figure 3-28, and the XRadia/Zeiss VersaXRM 410 used in Durham University is shown in Figure 3-29.

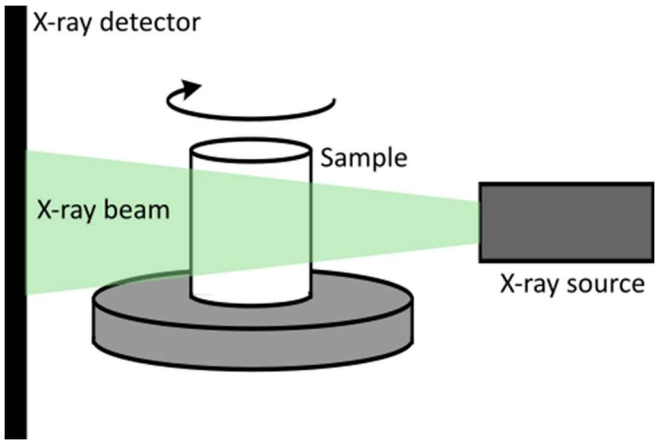

Figure 3-28: Illustration of operation principle of micro-CT

Figure 3-29: Durham University XRadia/Zeiss VersaXRM 410

There are a number of parameters that can be varied while taking a micro-CT scan of a sample. The parameters chosen aim to balance the contrast obtained when scanning the sample with the resolution of the scan, the time taken for the scan and the size of the dataset obtained (du Plessis et al., 2017). The voltage used to produce the x-rays can be varied from 40 kV to 150 kV. If a sample is large or very dense, a higher voltage is required in order for the x-rays to have sufficient energy to pass through the sample to the detector. However, for a small sample of low contrast (for example, plastic), a lower voltage will give a much improved contrast as the lower density materials will be able to attenuate the lower energy x-rays (Orhan and Büyüksungur, 2020). Secondly, the wattage (or amperage) of the x-rays will affect the clarity of the image: a higher wattage will improve the resolution of the image, although in general the

wattage (in W) should not exceed the voxel size (in μm). Thirdly, as in traditional photography, the exposure time will affect the contrast seen in the image. For dynamic processes, reducing the exposure time in order to accurately image the process must be prioritised, and hence imaging large dense samples in a fast dynamic process may not be possible. The best resolution will be obtained from a large number of images taken over a small angle increment from 0 to 360°. However, producing a very large number of images produces a very large file size which may be challenging to reconstruct and manipulate. It is often more common therefore if a high resolution scan is required to image a sub-volume of the whole sample.

Following the acquisition of a scan, the images obtained must be reconstructed to give a stack of horizontal slices through the sample. These can then be combined to give a 3D representation of the sample using software such as imageJ or Avizo. It is common to segment the 3D volume rendering into a series of separate volumes which have the same contrast, in a process known as thresholding. It is assumed that the volumes of the same contrast are formed of the same material, and hence thresholding divides the volume into separate volumes of the same material. These may then be further analysed – for example, a volume of air in a sandstone may define the pore structure and hence a pore network model may be developed. Dynamic processes may also be analysed by using particle tracking algorithms to monitor particle migration or flow.

Chapter 4 Roughness and Wettability of 3D Printed Surfaces

4.1 Background

Additive manufacturing (commonly termed 3-dimensional (3D) printing), since its inception in its current form the 1980s, has provided an alternative method to produce three-dimensional physical objects, built up as a series of layers, from digital models. For a detailed overview, see Section 3.1.

The method chosen for the study presented here is FDM, or Fused Deposition Modelling, as the printer and substrates (in this case, thermoplastic filament) are readily available, affordable and varied. This technology is one where a liquid material is deposited and solidifies, forming objects out of successive layers of melted thermoplastic material, which solidifies shortly after deposition. The filaments used are made of different materials with different additives, which, due to differences in their surface chemistry, have different wettabilities. Filaments dominated by non-polar polymers or additives will tend to be more oil-wet (for example, Acrylonitrile Butadiene Styrene (ABS)), whereas filaments containing more polar polymers or additives tend to be more water-wet (for example, nylon). The formation of three-dimensional objects using FDM technology gives surfaces with varied surface textures as artifacts of the printing method; as described in Section 3.1.5.1, these surface texture variations may also give variations in the wettability of the surface, which is of interest in this study.

Wettability is the tendency of one fluid to spread on, or adhere to, a solid surface in the presence of other immiscible fluids, as described by Young (1805). This may be illustrated by the shape that a water droplet makes on a surface; the precise measurement of the angle which the droplet makes with the surface is a recognised method of measuring the wettability of a surface, and thereby classifying a surface as oil- or water-wet (Yuan and Lee, 2013) depending on the angle. For a water droplet on a surface in air, an angle of < 90° implies a water-wet surface, 90° implies a neutral-wet surface and >90° an oil wet surface. This measurement however requires that the surface be smooth, flat and homogenous. If the surface is rough, a different situation may apply as the measured water contact angle may be larger (in the case of oil-wet surfaces) or smaller (in the case of water-wet surfaces) than if the contact angle were measured on a smooth surface. Wenzel (1949) and Cassie and Baxter (1944) have proposed formulae to correct for the roughness; these, and details on the measurement of wettability can be found in Section 3.2.

The Wenzel and Cassie-Baxter equations require information about the surface on which the drop has been placed, specifically the measured and projected surface areas, and the fraction of the projected surface which is wetted. This information, along with many other parameters describing the texture of the surface, can be obtained from a profilometer (an instrument designed to record the precise texture of a surface). A more detailed description of roughness measurement techniques can be found in Section 3.3.

The objectives of this study are twofold. The first is to assess 3D printing materials to look to quantify the wettability of the different 3D printing materials. The second objective is to vary the roughness of the materials and compare the measured roughness parameters with the wettabilities measured on each material with a different roughness to look for a correlation, both between the parameters themselves and using the Wenzel and Cassie-Baxter approximations.

4.2 Methods

4.2.1 Correlation of FDM 3D printing materials with wettability

4.2.1.1 Creation of 3D printed test chips

A 3D model (termed test chip) was created with Autodesk® Fusion 360® (a cloud-based CAD/CAM/CAE tool) to give a variety of possible surfaces for contact angle measurement, as well as a permanent label to ensure the test substrate was readily identifiable. An example test chip is shown below:

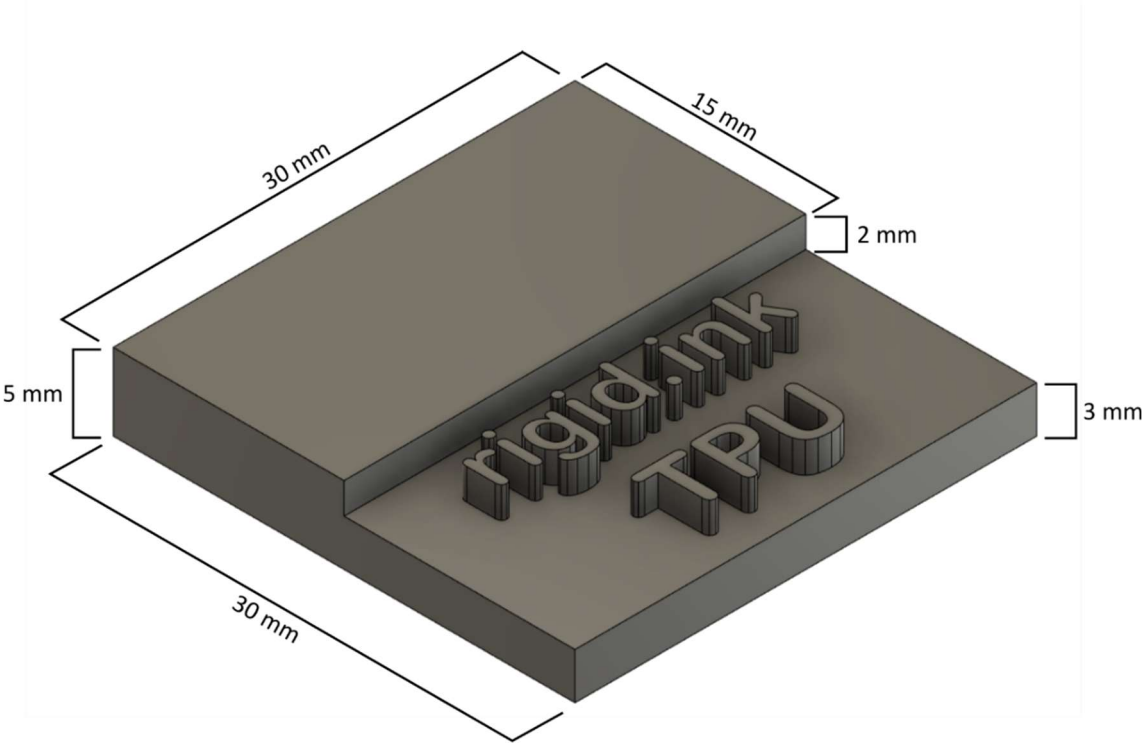

Figure 4-1: 3D print material test chip modelled in Autodesk® Fusion 360®. Chip measures 30 mm × 30 mm × 5 mm.

The test chip was exported from Autodesk® Fusion 360® as a .stl file using the standard 3D print settings included with the software. The .stl file was sliced using Ultimaker Cura 3.0.3 following a custom addition of the Raise3D N1 printer to the printer library. The experimental "ironing" setting (which moves the nozzle of the printer across the top surface of the item printed without depositing further plastic, and which was added in Ultimaker Cura 3.1.0 as a standard feature) was used to produce a more uniform top surface. The test chip was printed using a Raise 3D N1 printer with a V2 hotend. The 46 filaments tested and the precise print settings are listed in Appendix 1.

4.2.1.2 Wettability

Contact angle measurements were carried out using a Ramé-Hart Model 260 Standard Contact Angle Goniometer / Tensiometer using a 10 µl drop of distilled water as the liquid phase. Measurements of the contact angle were made using the contact angle module of the Ramé-Hart DROPimage software. Between three and six drops of water were measured for each material, with 10 contact angle measurements made for each drop, each single measurement made 0.5 seconds apart. The drops were all measured more than 20 seconds after being placed onto the surface (Kubiak et al., 2011). The contact angle of a water drop on the top "ironed" surface and bottom surface of the test chip were tested to assess the effect of printing artifacts

on wettability (Figure 4-2). The contact angle on the side of the print, where visible layering can be seen, was not measured as the size of the printing artifacts compared to the water droplet side would have caused significant difficulty in quantifying the contact angle using the goniometer and software available.

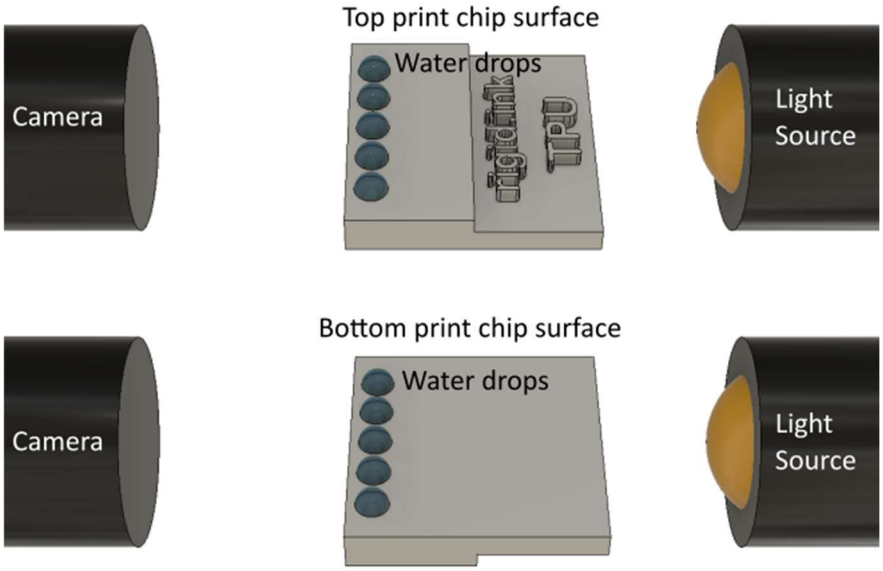

Figure 4-2: Print chip surfaces used for contact angle measurement - top surface, ironed (top) and bottom surface, in contact with build plate (bottom). The same print chip orientation and positioning of water drops was used for each chip.

4.2.2 Correlation of FDM 3D printing material wettability with roughness

4.2.2.1 Creating surfaces with defined roughness

In order to produce a surface with a more tightly controlled roughness, filament was extruded to form a test strip approximately 5 mm by 50 mm on three different commercial print surfaces with different surface textures. Not all filaments could be extruded onto every build surface as some filaments did not adhere to the build surface sufficiently to produce a usable strip. The print surfaces chosen were BuildTak™ (proprietary composition; highest degree of roughness), PEI (polyetherimide; less surface texture than BuildTak™) and Kapton film (poly (4,4'-oxydiphenylene-pyromellitimide; smoothest surface texture). To assess the effect of surface texture and material on wettability, the water droplets were measured in a similar manner to those on the test chips, with the droplets being measured on the surface of the test strip which had been in contact with the print surface. The models were taken to BP Pangborne Formulated products technology (FPT) labs where the roughness of the printed objects was measured suing a Taylor Hobson Precision Talysurf CCI, using Talysurf and Talymap Platinum software. The

models were all measured using the same parameters set in the Talysurf software (xyz mode, low reflectivity and reflectivity mode) and all measured using the 20 × objective lens. An 800 × 800 µm area was scanned at 512 × 512 px into a *.sur file, and text files were extracted containing 262,144 x,y,z coordinate sets. In addition, the single line "strips" were taken to Swansea University Department of Engineering and scanned with a Wyko NT-9300 white light interferometer (WLI) with a 20 × objective lens. A 310 × 232 µm area was scanned at 640 × 480 px into an *.opd file, and text files were extracted as an ASCII data matrix *.csv files. The two different instruments were used to compare the roughness alone and the roughness and waviness parameters, as the Talysurf CCI filtered out the waviness leaving only the roughness, whereas the Wyko instrument retained both the roughness and waviness data, which could be filtered out later.

4.2.3 Data Processing

The Talysurf images were processed in two ways. The first follows the standard method used by the owners of the instrument, and the second was chosen to match the processing method of the Wyko instrument data, and will be explained in more detail below.

In the first method, the text files were pre-processed using a Python script (Appendix A.2.1), then 3D surfaces parameters were extracted using a python script (Appendix A.2.2) and Matutil (a utility by Ricardo Software). 3D plots were produced using Matlab scripts (Appendix A.2.3).

In the second method, the *.sur and *.opd files were opened directly in Gwyddion (Nečas and Klapetek, 2012), the data was levelled by mean plane subtraction using the "Plane Level" function, and the data was then adjusted to put the mean height value at zero, so that the different surfaces could be compared more effectively. This process was required on all .sur files, as these were not levelled and were produced with zero at the lowest value, whereas the .opd files were pre-levelled and were generally only affected by the mean height to zero adjustment. The .opd files also contained some invalid datapoints, visible as the palatinate-coloured "masked" areas in Figure 4-5. Gwyddion offers the option to include these areas in the levelling calculation, but as this data was not used to produce roughness parameters, it was not used when levelling. The process is illustrated in Figure 4-3.

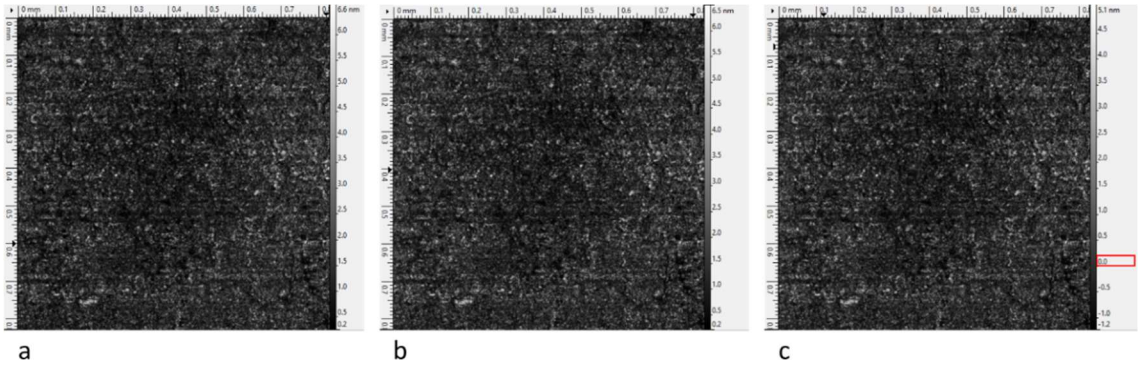

Figure 4-3: Procedure to level and adjust mean of TPE32 Talysurf surface scan. a: original image, b: plane level applied, c: adjusting mean height to zero. The adjusted zero position is highlighted in image c; in images a and b the zero position is not shown.

A line perpendicular to the direction from which the contact angles were measured was drawn, and the roughness and waviness parameters were extracted along this line. This is illustrated in Figure 4-4.

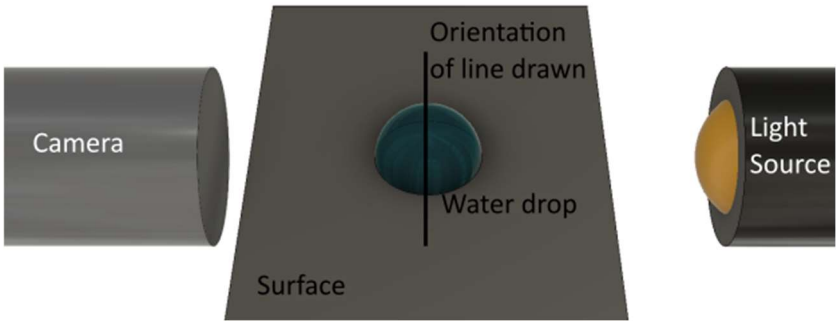

Figure 4-4: Illustration of orientation of line drawn in Gwyddion for roughness and waviness analysis compared to direction of contact angle imaging.

The waviness cut-off value was adjusted for each printing surface by eye in the following manner. Where a scan of the build surface was available, the waviness cut-off value was adjusted to show roughness varying about a horizontal line on the scans of the build surface and this value was used in all print scans. Where a scan of the build surface was not available, the cut-off value was again adjusted by eye and recorded for all the scans; this process is illustrated in Figure 4-5. The median value was obtained and then applied to the scans where a different value had been used and the data was subsequently reprocessed.

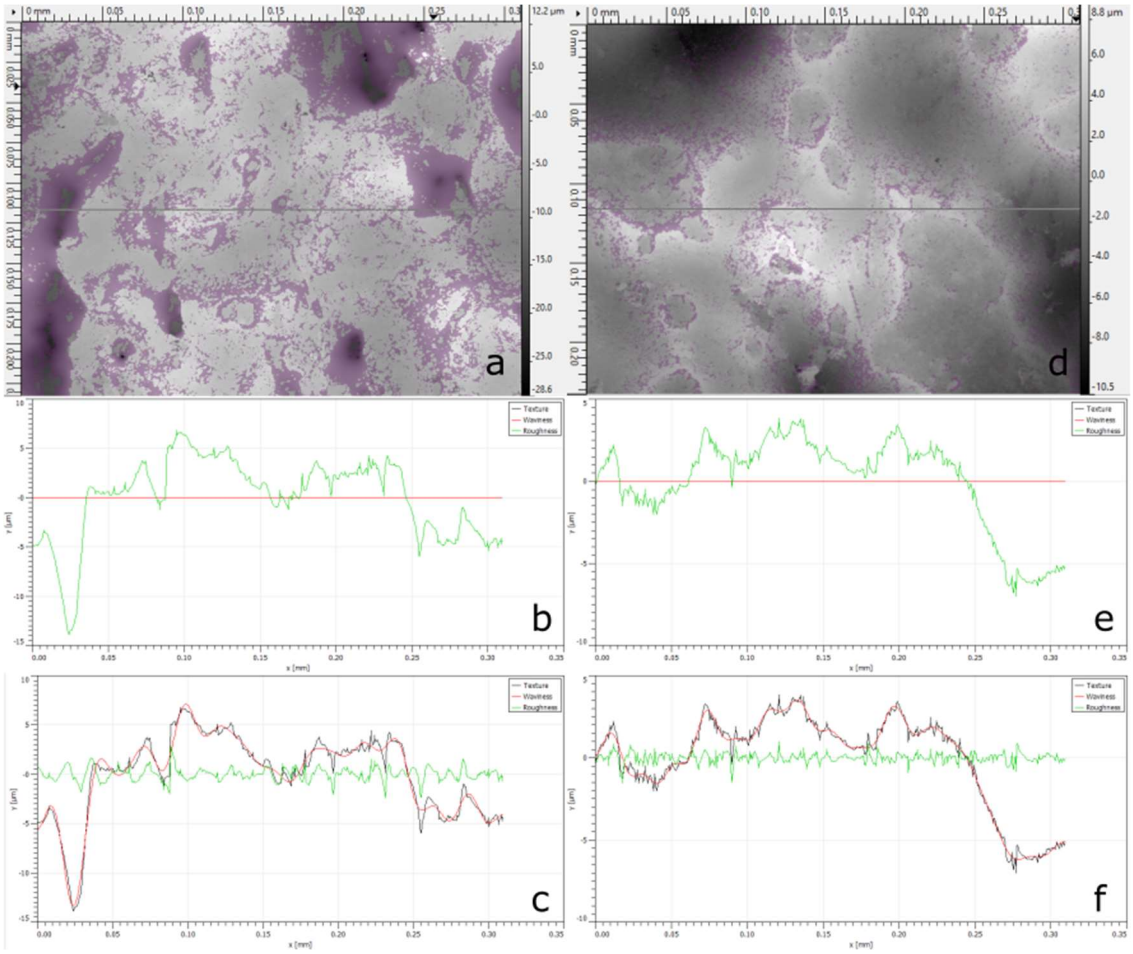

Figure 4-5: Waviness removal from two different materials printed on BuildTak™ build surface. Screenshots from Gwyddion. Scans taken on the Wyko NT2300. Palatinate colouring indicates places where data was interpolated due to invalid datapoints. a - material 1 - PLA with 40% wood fibres, roughness taken along line, d - material 2 – ABS with 2.5% carbon nanotubes, roughness taken along line, b, e - roughness (green) with no waviness (red) subtracted, c, f – waviness cut-off of 0.05 (19.40 µm) applied. For both materials, the same waviness cut-off gave good separation of waviness and roughness.

The waviness was removed from the scans taken by the Talysurf instrument during data processing by the instrument, so the waviness cut-off was set to zero as the waviness had already been removed. The statistical parameters for the whole area were also extracted. Care was taken to ensure that all parameters extracted used the same units, as Gwyddion automatically changes the unit based on the size of the measured value.

In addition to the parameters produced by the software directly, two further parameters required for Equations (3) and (4) were extracted. The r term for both the Wenzel (3) and Cassie-Baxter (4) equations may be obtained from the ratio of the surface area divided by the projected surface area – this will be = 1 for a completely smooth surface, and > 1 for a rough surface. The ϕ_{LS} term can be obtained from R_{mr} *(%)*, which is the relative material ratio measured at 25% of the maximum height of the roughness profile: $\phi_{\mathrm{LS}} = \frac{\mathrm{R_{rmr}}}{100\,\%}$. Both of these terms can be

computed from outputs from Gwyddion. The r term is computed from the "Projected area" and "Surface area" parameters. The $R_{mr}\,(\%)$ term is obtained by firstly levelling the image and setting the minimum value to zero, then saving as a new image. The new levelled image files were then batch analysed by a python script (Appendix A.2.4) to obtain the Rmr (%).

4.3 Results and discussion

4.3.1 Correlation of FDM 3D printing materials with wettability

Figure 4-6 shows the measured contact angles for the top and bottom surfaces of all the 3D print chips produced. The data is categorised into filament types so that different chemistries of filament can be easily compared. In some instances the value could not be measured (due to the bottom surface having either blue tape or glue remaining from the printing process – required for adhesion to the build plate while printing, or the top surface being incompatible with the ironing function), shown as a gap in the data. Figure 4-7 presents this data again overlaid against the average values for each type of filament, as it is assumed that the same filament type should have the same wettability due to having the same plastic chemistry.

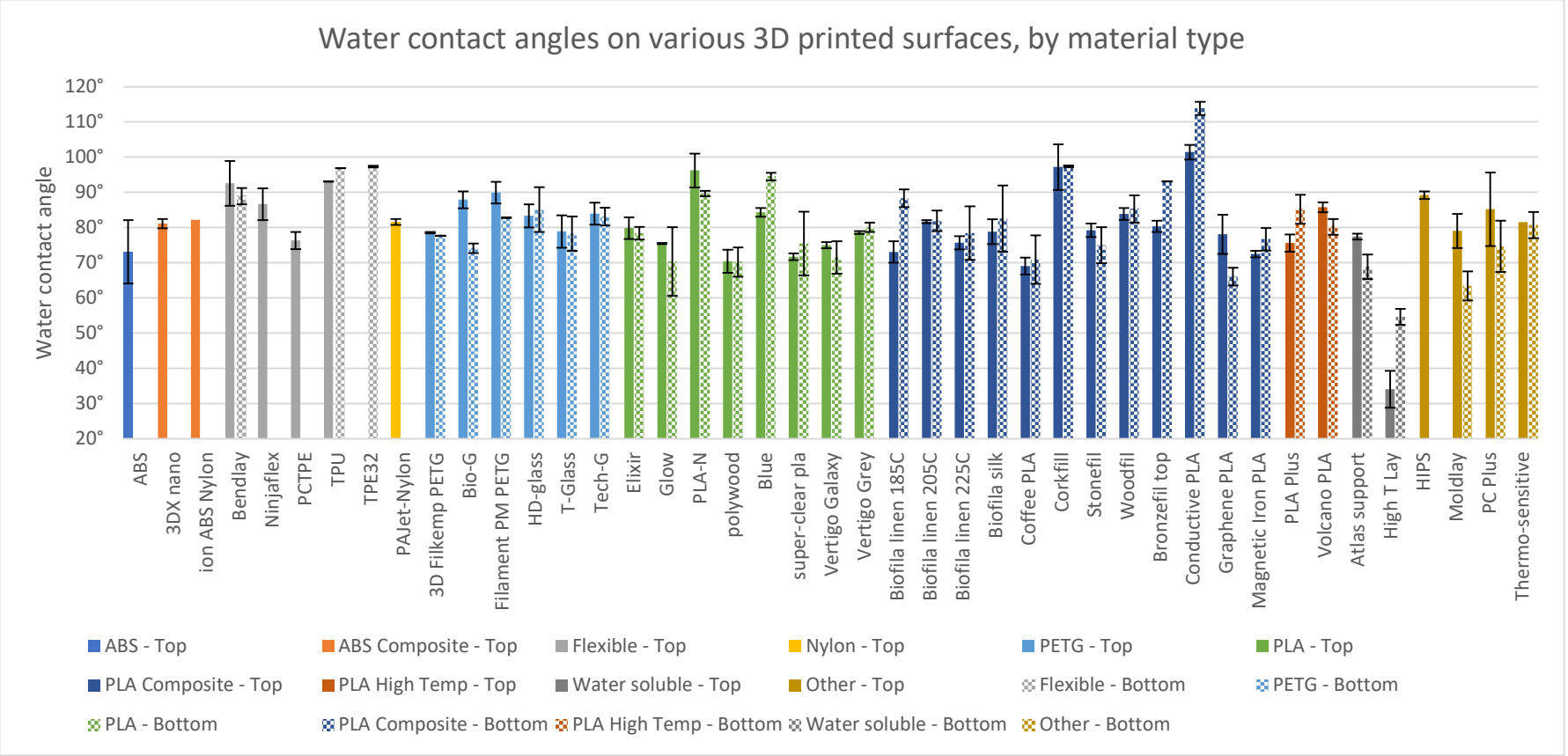

Figure 4-6: Contact angle vs material, for top and bottom surface of 3D printed chip.

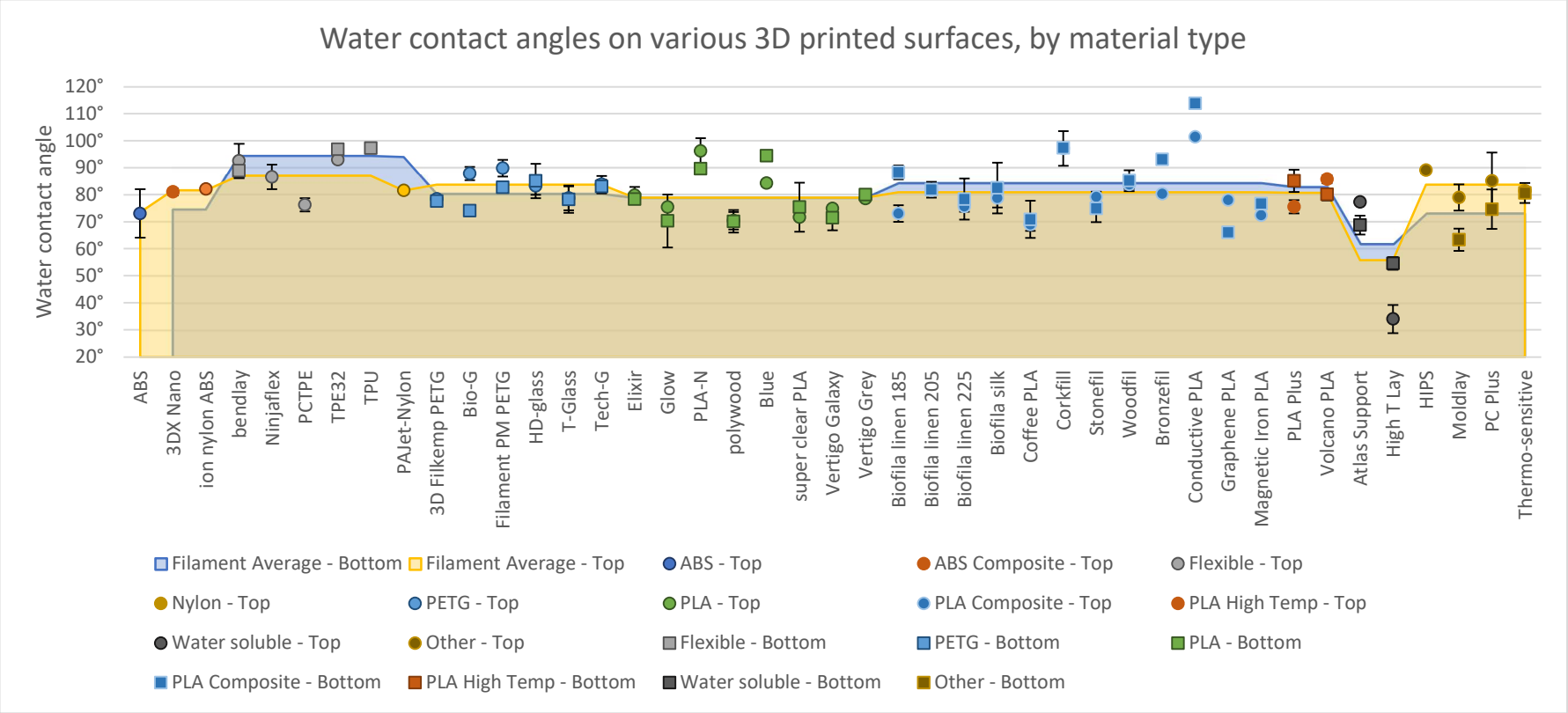

Figure 4-7: Filaments by material type, with indication of average values for those filaments

In general, it can be seen that using a goniometer with a 10 µl drop of water on a 3D printed surface usually gives a wettability of neutral- to water-wet. The average value over all filaments was 81 ±11° for the top surface, and 72 ±12° for the bottom surface. Distinct outliers are seen in the Conductive PLA (PLA with containing carbon black), and the High T Lay (PVA/LDPE) with the conductive PLA having a measured contact angle of 101±2° on the top surface and 114±2° on the bottom surface, and High T Lay having values of 34±5° and 55±2°. The high contact angle of the Conductive PLA may be because carbon black is hydrophobic and so is contributing to the wettability of this material. In contrast, the PVA in High T Lay is water soluble, and therefore hydrophilic. The water-soluble property however makes this material unsuitable for producing lasting items – the material is generally used as a support which is removed following printing.

Published data is available for the wettability of some of the plastics that make up the filaments used in this study. The tables below give details of the published contact angles for each filament chemistry (and where additives are included, the contact angle of the additive where available), along with an average of the published values where there is more than one chemistry in the filament category. A comparison of the published values with the measured values is given in Table 4-3.

Table 4-1: Published contact angles for various filament chemistries

Filament type	Filament	Material	Contact angle	Average Contact Angle
ABS	ABS	ABS (Acrylonitrile butadiene styrene)	92.3° (Hamdi and Poulis, 2021) 59.6° (Win and Liu, 2013) 94.7° (Chlupová et al., 2017) 96° (Lovinčić Milovanović et al., 2020) 75° (Kwiatkowski et al., 2018)	85.7°± 17.4°
ABS Composite	iON ABS Nylon Alloy	ABS and Nylon	No specific data – see Nylon and ABS tables	

Flexible	Bendlay	Modified polybutadiene	92° (Shen et al., 2017)	92.5° ± 0.5°
	Ninjaflex	TPU (Thermoplastic Poly-Urethane)	93° (Jasmee et al., 2018)	
	TPE filaments	No chemistry specified – may be TPU, thermoplastic co-polyester (TCP) or thermoplastic polyamide (TPA)		
Nylon	PAJet Nylon	Nylon 6,6	64° (Sarmah et al., 2021) 49.3° (Waugh and Lawrence, 2008)	56.6° ± 10.4°
PETG	PETG	Polyethylene terephthalate glycol	75° (Bernasconi et al., 2016) 65° (Fedorov, 2017) 75° (Kim et al., 2015)	71.7° ± 5.8°
PLA	PLA	Polylactic acid (PLA)	69° (Bernasconi et al., 2016) 97.9° (Lovinčić Milovanović et al., 2020) 51.25°[a] (Modi and Prakash, 2019) 73° (Yang et al., 2020) 75° - 85° (Baran and Erbil, 2019)	75.2° ± 15.7°
PLA High Temperature	PLA Plus	Engineered PLA	Assumed to be similar to PLA.	

	Volcano PLA	Engineered PLA	Assumed to be similar to PLA.	
Water soluble	Atlas support	Poly vinyl alcohol (PVA)	48° (Musskaya et al., 2016)	
	High T Lay	Low density polyethylene (LDPE)/PVA	No specific data. Contact angle of LDPE: 94° (Kim et al., 2007)	
Other	HIPS	High Impact Polystyrene	90° (Kwiatkowski et al., 2018)	86.4° ± 9.9°
	Moldlay	Not reported. Wax-like.		
	PC-Plus	Polycarbonate	94° (Fedorov, 2017)	
	Thermo-Sensitive PLA	Engineered PLA.	Assumed to be similar to PLA.	

[a] Average of values for surface 1

Table 4-2: Published contact angles for different PLA composite filament additives

Filament	**Filament Additive**	**Contact angle**
Biofila linen	Lignin	56° (Notley and Norgren, 2010)
Biofila silk	Lignin	56° (Notley and Norgren, 2010)
Coffee PLA	Coffee grounds	No specific data. Hydrophilic – likely to be similar to lignin as this is one of the main constituents. (Moustafa et al., 2016)
Corkfill	Cork	84° ± 2° (Gomes et al., 1993)
Stonefil	"Stone" - unspecified	Typically hydrophilic. E.g. 40° ± 8° (Lettieri et al., 2019)
Woodfil	Wood	60° - 74° (Mantanis and Young, 1997)
Bronzefil	Bronze powder	104.6° (Mihelčič et al., 2019)
Conductive PLA	Carbon Black	Hydrophobic (Yan et al., 2006)
Graphene PLA	Graphene	95° - 100° (Taherian et al., 2013)
Magnetic Iron PLA	Iron powder	43° (Kong et al., 2020)

Comparing the reported contact angles to the contact angles measured on the top and bottom of the print chip surface (Table 4-3), it can be seen that the ABS and PLA filament types give results which are in good agreement with the published data. In the case of the nylon and PETG filaments however, the values measured are higher than the published results. Nylon in particular appears anomalously high – nylon is known to be hygroscopic, and therefore would be expected to be hydrophilic. The measured data however suggests that it is neutral-wet to slightly water-wet. This may be due to the fact that as the filament is heated in the nozzle of the 3D printer the water in the filament boils off (audible as crackling sounds during printing if the filament has a high moisture content – this was not observed during printing for these filaments as they had been stored in a sealed low moisture environment with silica gel desiccant) and produces an object which has a lower moisture content that is usual for nylon. In the case of PETG, there are many grades available; the particular grade used in this study may be different to those used in the published results.

Table 4-3: Average contact angle obtained for each filament type, for the top and bottom print surfaces of the print chips. Also included are published contact angles, discussed previously above.

Filament Type	Contact angle on top print surface	Contact angle on bottom print surface	Published contact angles
ABS		73.5°±9.0°	85.7°± 17.4°
ABS Composite	74.4°±1.2°	81.6°±3.9°	N/A
Flexible	94.4°±0.5°	87.1°±1.7°	92.5° ± 0.5°
Nylon	93.9°±19.2°	81.6°±0.8°	56.6° ± 10.4°
PETG	80.2°±1.4°	83.7°±1.3°	71.7° ± 5.8°
PLA	78.8°±1.9°	78.9°±0.8°	75.2° ± 15.7°
PLA Composite	84.1°±1.4°	80.9°±0.9°	N/A
PLA High Temp	82.7°±2.3°	80.7°±1.4°	75.2° ± 15.7°
Water soluble	61.7°±2.1°	55.7°±2.6°	48°
Other	72.9°±2.3°	83.7°±2.9°	86.4° ± 9.9°

Looking at the angles obtained, most lie within the water- to neutral-wet range. Flexible and nylon filaments appear to give a slightly higher contact angle on the top surface being more oil-

wet than the other filaments measured. The flexible filaments also gave the highest contact angle on the bottom surface of the prints, suggesting that the chemistry of the filament might be contributing more to the wettability of the print surface than the texture of the print surface alone.

Previous studies carried out on the wettability of 3D printer filaments have reported a variation of measured water contact angle on PLA depending on printing parameters of 11.07° (91.91° to 102.98° - a further hydrophobic modification process was applied before the contact angle was measured) when varying layer thickness, print speed and filling mode (the method by which the inner portion of the model is printed, as it is not usually filled completely with plastic, rather filled in a pattern which will support the outer using minimal material)(Yang et al., 2020). Direction of contact angle measurement compared to printing direction has also been shown to affect the measured contact angle; Modi and Prakash (2019) show a variation of 21.6° (43.4° to 65°) when varying the angle of measurement from 0° to 90°. In this set of experiments, the printing parameters were kept constant (barring the nozzle and print bed temperature which varied from material to material), and the droplets were all measured at the same position relative to the print direction, so these factors should not contribute to the variation in contact angle between print chips.

4.3.2 Correlation of FDM 3D printing material wettability with roughness

Measurements were made on the following filaments and build surfaces:

Table 4-4: Details of which filaments were extruded onto which build surfaces to give different surface textures.

Filament Type	Filament	Buildtak™ (high roughness)	PEI (medium roughness)	Kapton (low roughness)
ABS	ABS	✓		✓
	ABS-T		✓	
Flexible	Bendlay	✓	✓	✓
	PCTPE	✓	✓	✓
	TPE32		✓	
	TPU		✓	
Nylon	PAJet Nylon	✓	✓	
	Nylon Bridge	✓	✓	✓

PETG	Bio-G		✓	
	PETG	✓	✓	✓
PLA	PLA-N	✓	✓	✓
	Super Clear PLA	✓	✓	✓
Linen	Biofila Linen (185 °C)	✓	✓	✓
	Biofila Linen (205 °C)	✓	✓	✓
	Biofila Linen (225 °C)	✓	✓	✓
PLA Composite	Biofila Silk	✓	✓	✓
	Bronzefil		✓	
	Coffee		✓	
	Conductive	✓	✓	✓
	Copperfil	✓	✓	
	Corkfil		✓	
	Elixir	✓		✓
	Graphene	✓	✓	✓
	Laywood	✓	✓	✓
	Magnetic Iron	✓	✓	✓
	Polywood	✓	✓	✓
	Stonefill		✓	
	Woodfill		✓	
Engineered PLA	PLA+		✓	
	Volcano PLA		✓	
	Thermo-sensitive PLA		✓	
Other	HIPS		✓	
	Moldlay	✓	✓	
	PC-Plus		✓	✓
	3DX Nano	✓	✓	✓
	ABS-T		✓	

	PCABS	✓		✓
	ION ABS-nylon alloy	✓		✓

For most of the filament and build surface combinations, measurements were made with both the Wyko NT-9300 and Talysurf CCI (some were measured with the Wyko only – see Table in Appendix A.4 for number of samples measured with each instrument), and roughness parameters were extracted with Ricardo Matutil and Gwyddion. The full list and description of parameters extracted is given in Appendix A.3. The measurements were separated out into filament types, and the R^2 correlation between each roughness parameter for all the filaments measured in that category and the mean contact angle was calculated. The correlations were also analysed for other contact angle data obtained from the goniometer software, including the measurements for the contact angles on the left and right sides of the droplet and the standard deviation of the measurements. In addition, to assess whether a more complex relationship than a linear correlation existed for any of the parameters and the measured wettability values, further R^2 values were calculated for the square, cube, square root, cube root and natural log of the roughness values, and the cosine of the measured wettability angle and the roughness values. All correlations for each contact angle parameter and each filament type were grouped together, and for each correlation type (linear, square etc.), correlations were colour coded based on the R^2 value obtained – green for 0.8 and above, yellow for 0.6 and above, orange for 0.5 and above and red for 0.4 and above. This allowed a quick visual inspection of the data to assess how well parameters correlated. In addition, an average of correlation coefficients obtained for all the filament types, and for the filament types where the group included only a single chemistry, for each roughness parameter for each type of correlation (linear, square etc.) was calculated and colour coded similarly to above. Any average R^2 greater than 0.4 was noted.

The Wenzel and Cassie Baxter equations ((3) and (4)) were used with the measured contact angles for each filament along with the additional calculated parameters to assess how well the data fit these roughness models. Two calculation methods were used. The first assumed that the measured contact angle was the non-Young angle for both of the formulae, and the formulae were used to calculate the Young angle predicted by the equations. The values obtained for each filament were then compared, as if the models fit the measured data the calculated Young contact angle values should be the same for a single filament with different roughness values. The second assumed that the value obtained for the filament on Kapton was the Young angle (as the Kapton build surface was the smoothest used) and calculated the contact angle that

would have been obtained for the filament on a less smooth surface based on the roughness parameters measured. These values were then compared to the angles obtained on the rougher surfaces – if the data fit the models, the calculated contact angle values for the rougher surfaces should be the same as the measured values.

4.3.2.1 Analysis of correlation of roughness parameter with contact angle

For the filament types which contained a mixture of different chemistries and additives, no single roughness parameter measured (Appendix A.3) consistently correlated with the mean contact angle measured. In particular, the grouping of all PLA composite filaments showed poor correlation over all the parameters measured. This is likely due to the fact that this filament category is very varied, with surface texture given not only by the build surface but also by the additives in some of the filaments. The additives varied from powdered metal to graphene to wood and lignin, and the additives behaved differently as the filament was extruded and produced different surface textures depending on whether or not the additive remained embedded in the filament during extrusion. Two examples are shown in Figure 4-8 below.

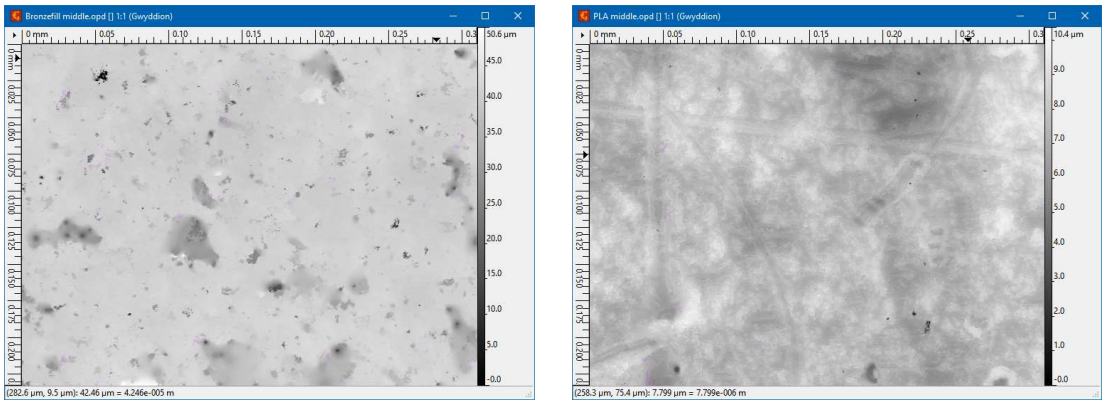

a b

Figure 4-8: a - Bronzefil (height colour scale: 0 – 50 µm), b - PLA (height colour scale: 0 - 10.4 µm), both on PEI, illustrating variation in maximum height between materials.

In the Bronzefil, the bronze particles are clearly visible in the image, as multiple deviations from the standard PEI surface. In comparison, the pure PLA shows little deviation from the PEI surface texture (visible in Figure 4-8 b), as it has no additives embedded in it. The deviation from the expected surface texture however would not be expected to affect the general correlation between results – if the assumption holds that some roughness parameter should predict the mean contact angle observed, then the contribution to roughness from the additives in the filaments would merely create a larger range of roughness parameters to be measured across. It is likely, therefore, that the additives themselves are contributing to the contact angle

observed as the additives, in the example above, bronze, have a different wettability to the PLA in which the bronze has been embedded. The contact angles for this category of materials would therefore be unlikely to be predicted by a roughness correlation measurement. In addition, due to the random heterogeneous nature of the materials, it would be unlikely that a good prediction of contact angle could be obtained using the Cassie approach for heterogeneous surfaces, as the precise percentage of the surface which is encountered by the drop of either the PLA or the additive cannot be easily predicted.

Good correlation was found between the RMS roughness (Sq) and the Mean roughness (Sa) parameters with mean contact angle, for both the measurements made with Talysurf and Wyko instruments. This was interesting to see, as the Talysurf measurements were pre-processed to remove the waviness component of the roughness, whereas the Wyko measurements made for this parameter did not include the subtraction of waviness, nor is there the facility in the Gwyddion software to carry out this subtraction.

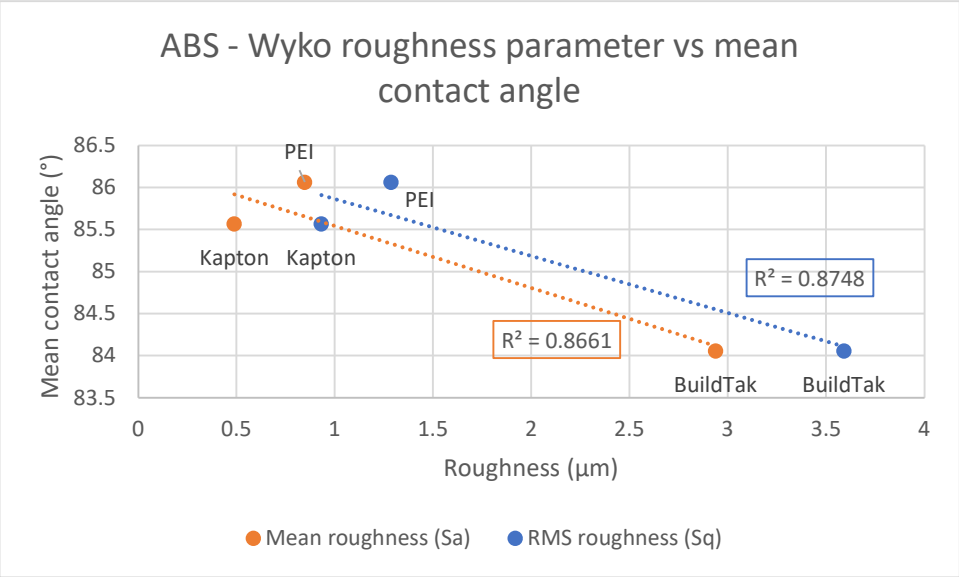

Figure 4-9: ABS Wyko best correlation roughness parameters with mean contact angle

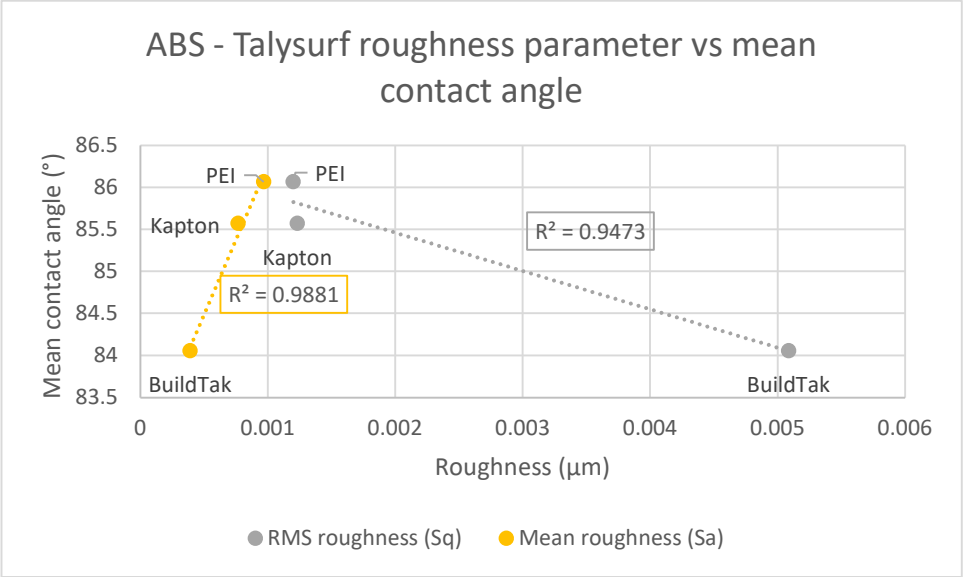

Figure 4-10: ABS Talysurf best correlation roughness parameters with mean contact angle

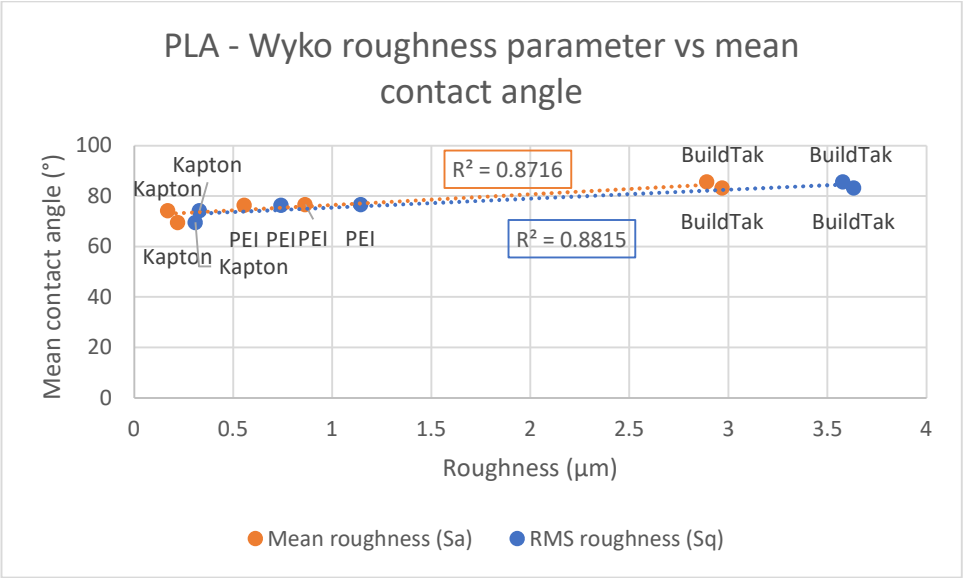

Figure 4-11: PLA Wyko best correlation roughness parameters with mean contact angle

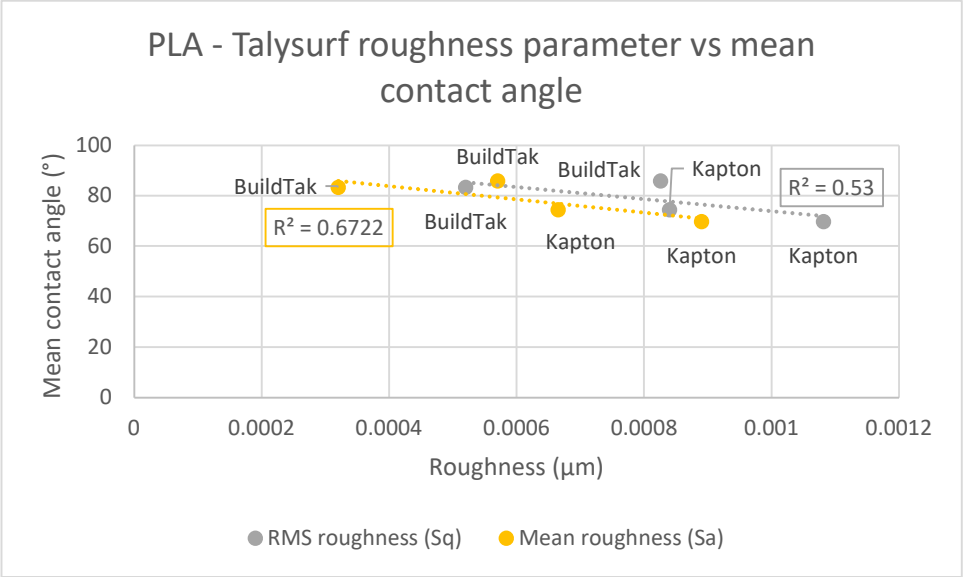

Figure 4-12: PLA Talysurf best correlation roughness parameters with mean contact angle

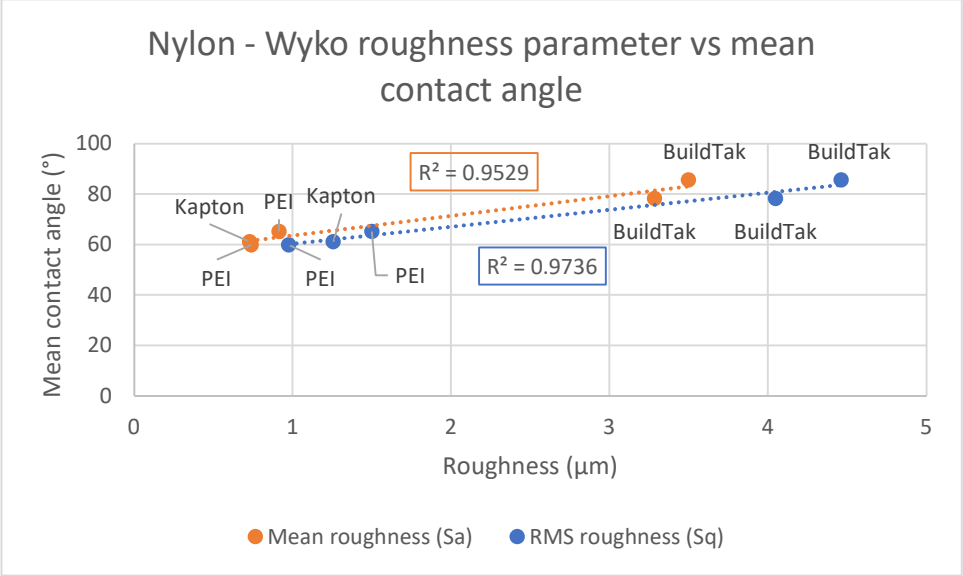

Figure 4-13: Nylon Wyko best correlation roughness parameters with mean contact angle

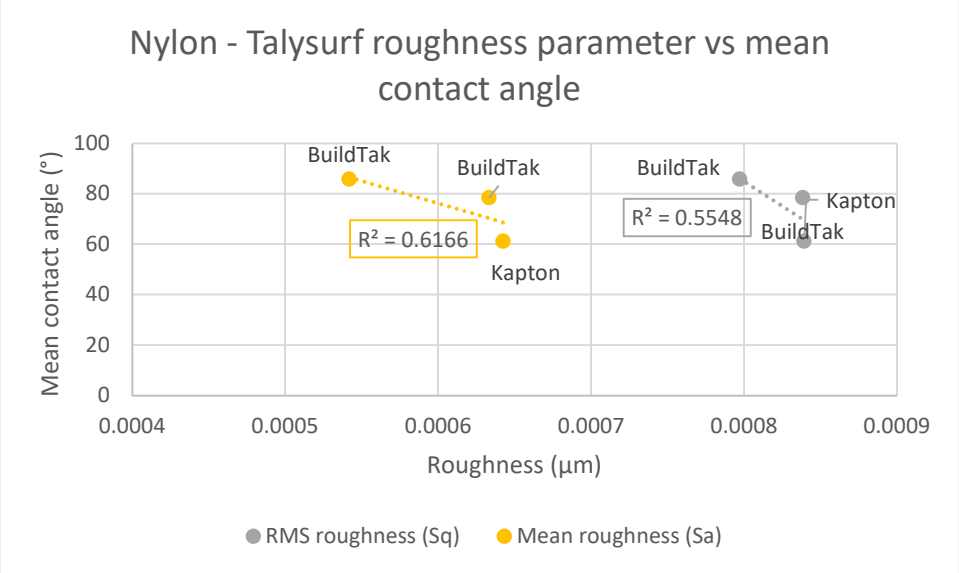

Figure 4-14: Nylon Talysurf best correlation roughness parameters with mean contact angle

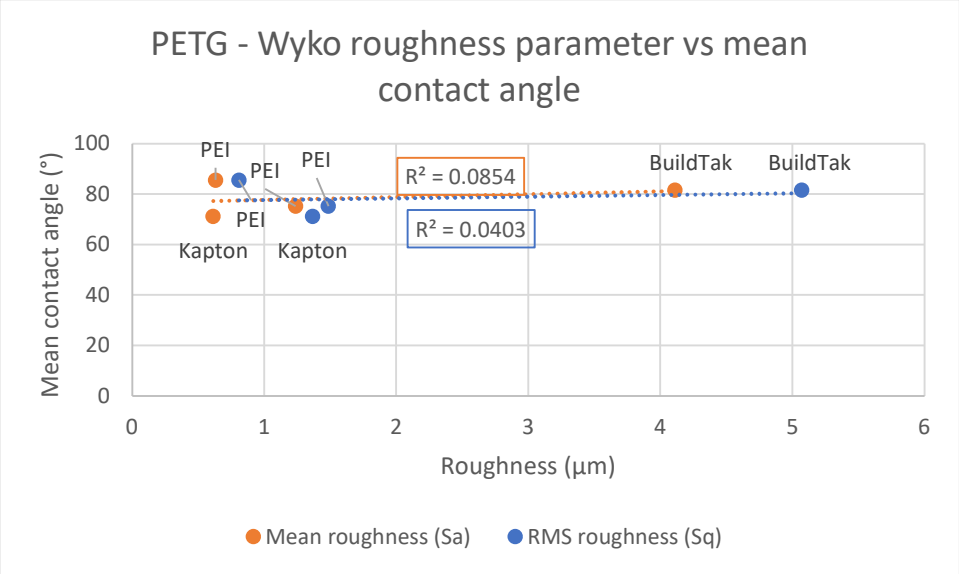

Figure 4-15: PETG Wyko best correlation roughness parameters with mean contact angle

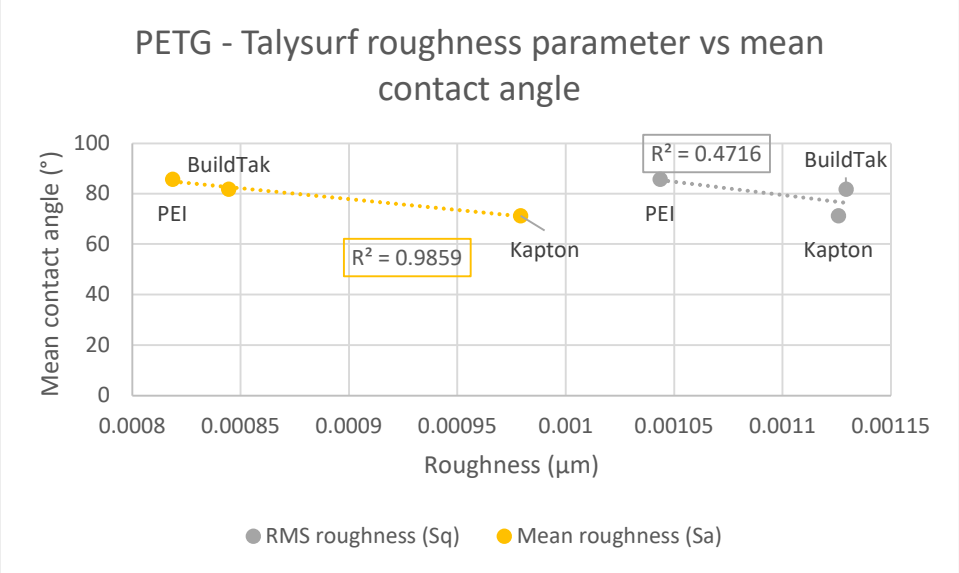

Figure 4-16: PETG Talysurf best correlation roughness parameters with mean contact angle

Looking more closely at the correlations identified, presented in Figure 4-9 to Figure 4-16, there are a number of obvious trends which can be seen. Firstly, the Wyko data shows that material extruded on Buildtak™ was generally rougher than PEI, which was rougher than Kapton. This is the expected trend, as macro scale inspection of the surfaces show an obvious difference in texture between the three – Buildtak™ is rough to the touch, PEI is smooth but has texture, and Kapton is smooth and shiny. This trend of increasing roughness from Kapton to PEI to Buildtak™ was not necessarily seen in the samples extruded onto these build surfaces in the Talysurf data, as the visible and tactile waviness component of the roughness has been filtered out leaving only the nano-scale roughness. In this set of experiments, the droplets measured were under 3 – 5 mm in diameter. The roughness values calculated, however, were in the nanometre scale. It is unlikely therefore that roughness values measured at this small scale would correlate well with droplets measured at a scale 6 orders of magnitude higher. Looking at the data in more detail, it can be seen that the correlations for ABS are only based on three points, and although the data correlates well, the data points for material extruded onto PEI and Kapton in Figure 4-9 do not lie in the predicted order on the line. Similarly for the ABS Talysurf data (Figure 4-10) – the fact that the points form a positive and negative trendline for the data suggest that this correlation may be unreliable. However, when looking at the data for Nylon and PLA (Figure 4-11 to Figure 4-14), the points can be seen to follow the trendline much more closely, giving positive gradients and high correlation coefficients. The Talysurf data also appears to follow a trend of negative gradient and fairly high correlation coefficient, although as discussed above this data may not be as reliable. The Wyko PETG data (Figure 4-15) on the other hand does not have

sufficient variation in measured contact angle to allow a correlation to be seen. This manifests as a lack of correlation for all linear and more complex correlations in the Wyko data. Some correlation may be seen with the Skew and Kurtosis parameters, shown in Figure 4-17 and Figure 4-18, but the clustering of points again suggests a less reliable correlation.

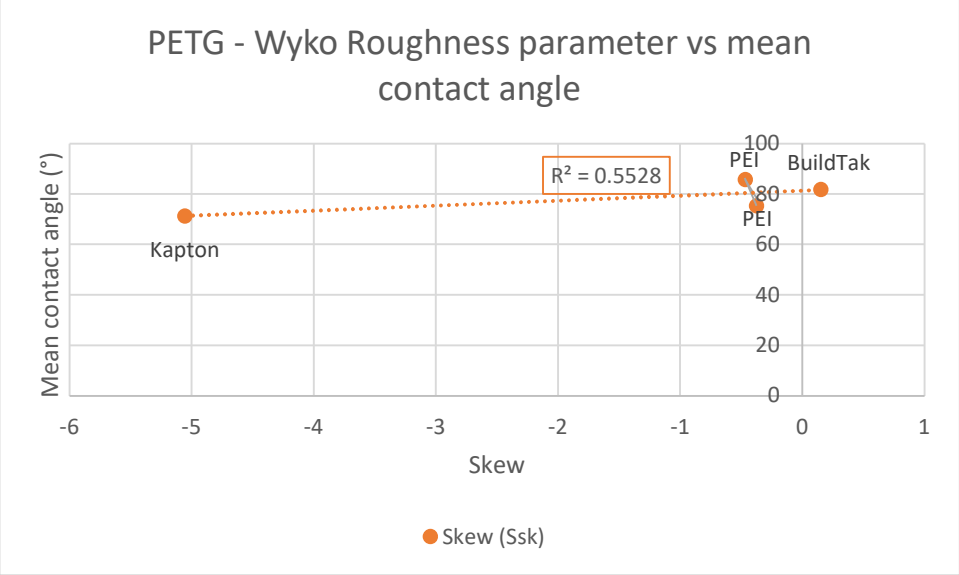

Figure 4-17: PETG Wyko skew correlation with mean contact angle

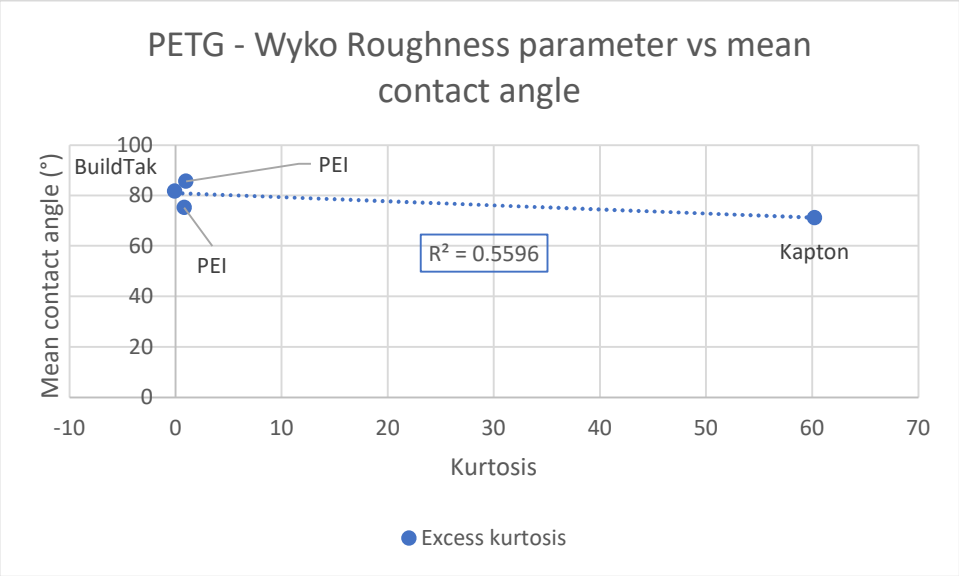

Figure 4-18: PETG Wyko excess kurtosis correlation with mean contact angle

Comparing the simple linear correlations with the more complex power, logarithm and cosine correlations, no benefit can be seen in including these operators in the relationship between roughness parameter and mean contact angle.

4.3.2.2 Modelling contact angle vs roughness

The Wenzel equation predicts that for a surface with a particular Young contact angle, the measured contact angle will vary in the following manner:

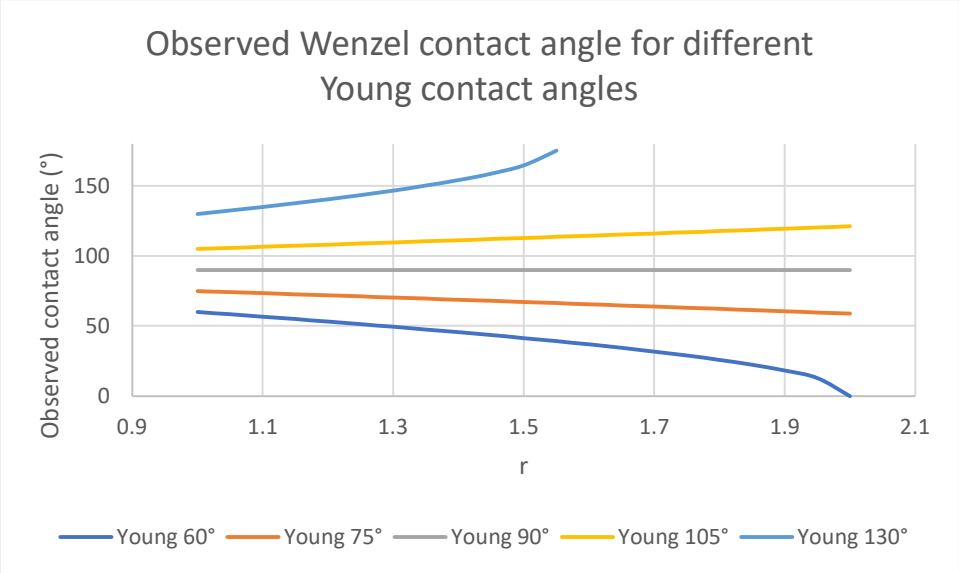

Figure 4-19:Theoretical Wenzel contact angle variation with Young contact angle and r

It can be seen that it would be expected that as the roughness increases (increasing r), the water contact angle will decrease for water-wet substrates, and increase for oil-wet substrates. This analysis would suggest that, given that all the filaments measured are mostly water-wet, as the roughness increases, the contact angle should decrease.

The Cassie-Baxter equation is more challenging to model as the way Φ_{LS} varies with r varies depending on the particular surface texture. It is clear though that Φ_{LS} will vary with r, so choosing three different simple linear functions and assessing the variation of the observed contact angle and r may give some insight into the contact angle variation when using the Cassie-Baxter equation.

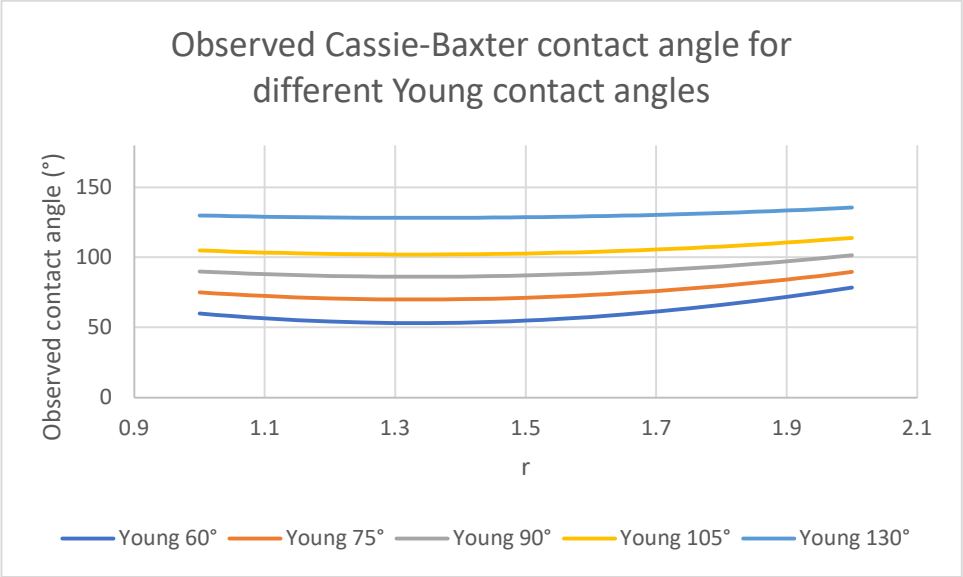

Figure 4-20: Theoretical Cassie-Baxter contact angle variation with Young contact angle and r. Φ_{LS} varied linearly from 1 at r=1 to 0.4 at r=2

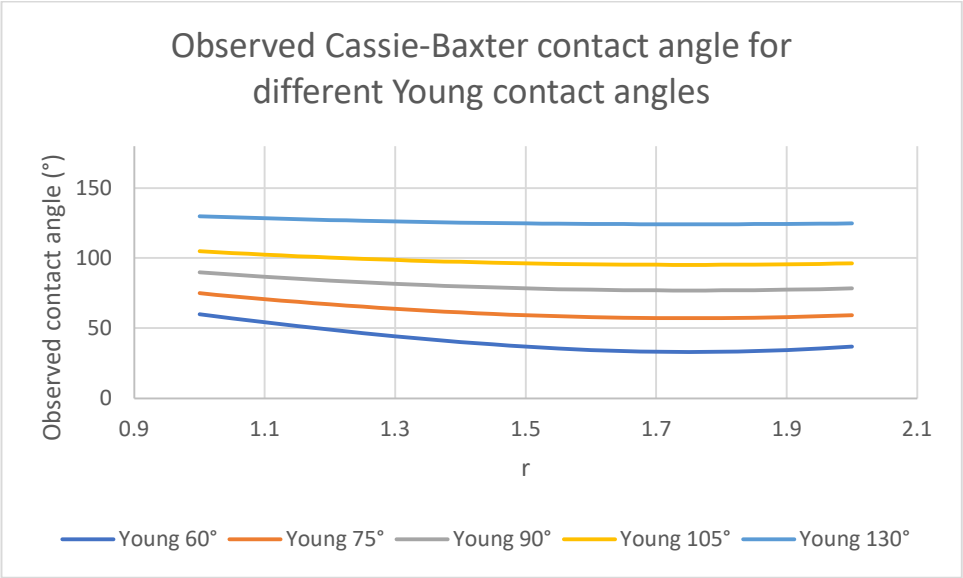

Figure 4-21: Theoretical Cassie-Baxter contact angle variation with Young contact angle and r. Φ_{LS} varied linearly from 1 at r=1 to 0.6 at r=2

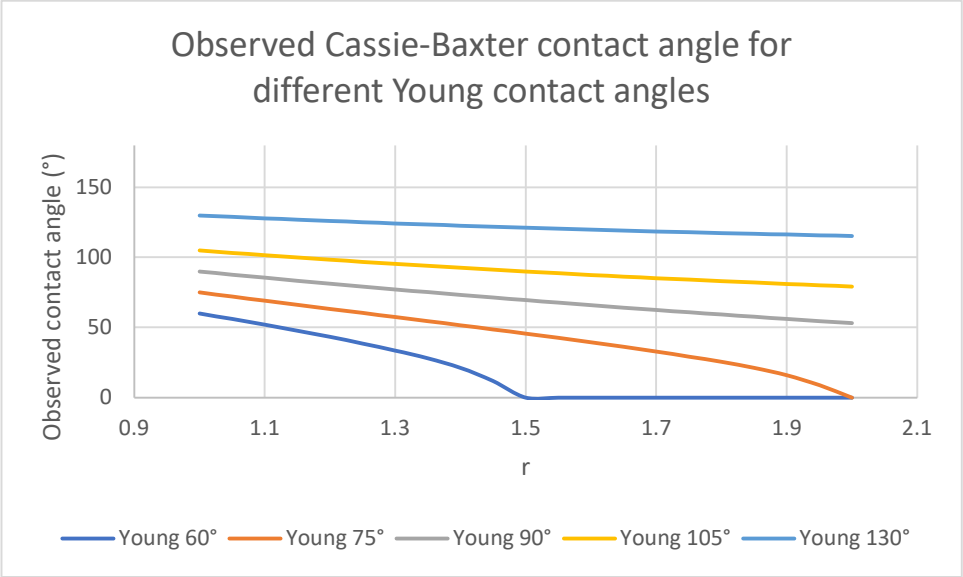

Figure 4-22: Theoretical Cassie-Baxter contact angle variation with Young contact angle and r. Φ_{LS} varied linearly from 1 at r=1 to 0.8 at r=2

The Cassie-Baxter equation shows a more complicated relationship between the observed contact angle and r (and Φ_{LS}). In the first case, a minimum contact angle is reached at around r = 1.35, the second case around r = 1.75 and the third does not reach a minimum over this range. The maximum r encountered in the data in this study is 1.42 (for PCTPE printed on Kapton). All other values are below 1.25. This analysis would therefore be in agreement with the Wenzel contact angle analysis, in that as the roughness increases, the observed contact angle decreases.

Plotting the mean contact angle measured against filament varying from smoothest to roughest (Figure 4-23), it can be seen that these data do not fit this trend, except in the case of ABS. It is therefore unlikely that Wenzel and Cassie-Baxter analysis will yield good results.

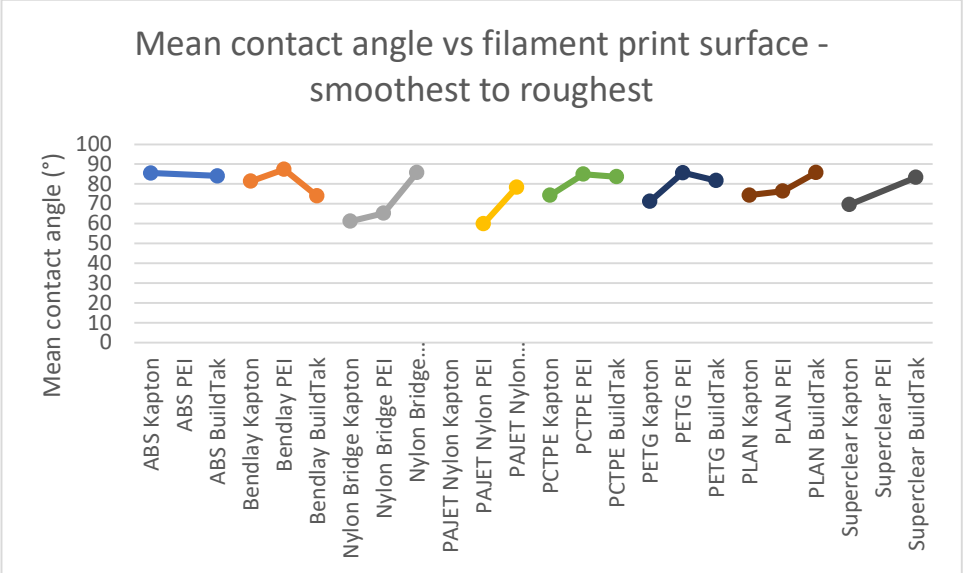

Figure 4-23: Mean contact angle vs filament print surface - smoothest (Kapton) to roughest (Buildtak™)

Calculating the expected Young contact angle using both the Cassie-Baxter (4) and Wenzel (3) equations would be expected to yield a similar value for a single filament regardless of which surface the measurements were made on, as both of these methods should correct for the effect the roughness has on the contact angle. The results for filaments without additives, and where the filament had been extruded onto more than one surface therefore giving more than one roughness, are presented in Figure 4-24 and Figure 4-25. Both equations give a lack of a single Young contact angle being produced from the measured contact angle and roughness parameters, except in the case of ABS which, from the initial analysis above, suggested that this method may be applicable for contact angle calculation.

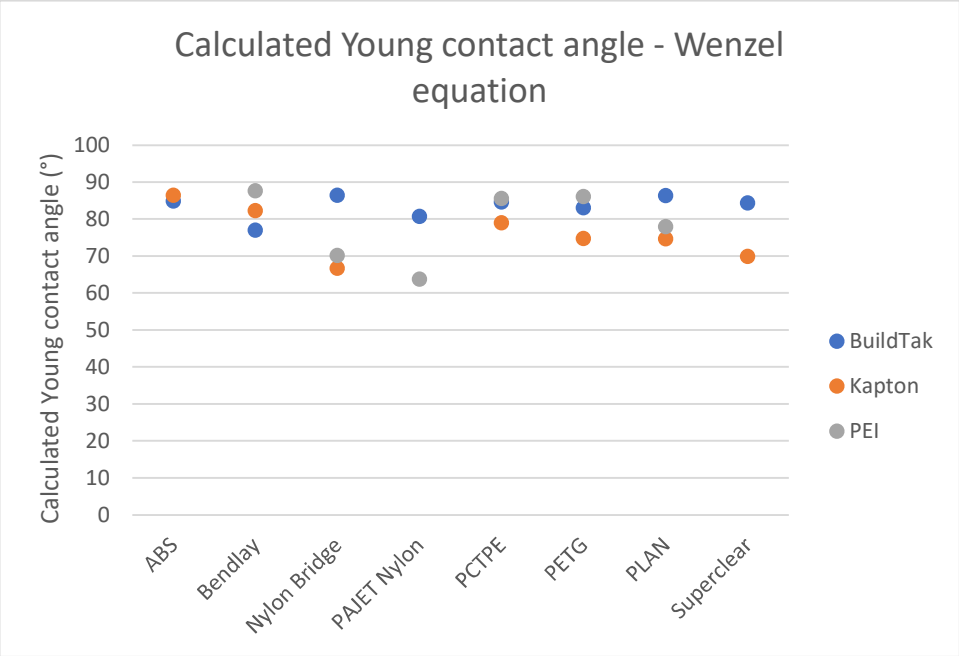

Figure 4-24: Calculated Young contact angle - Wenzel equation

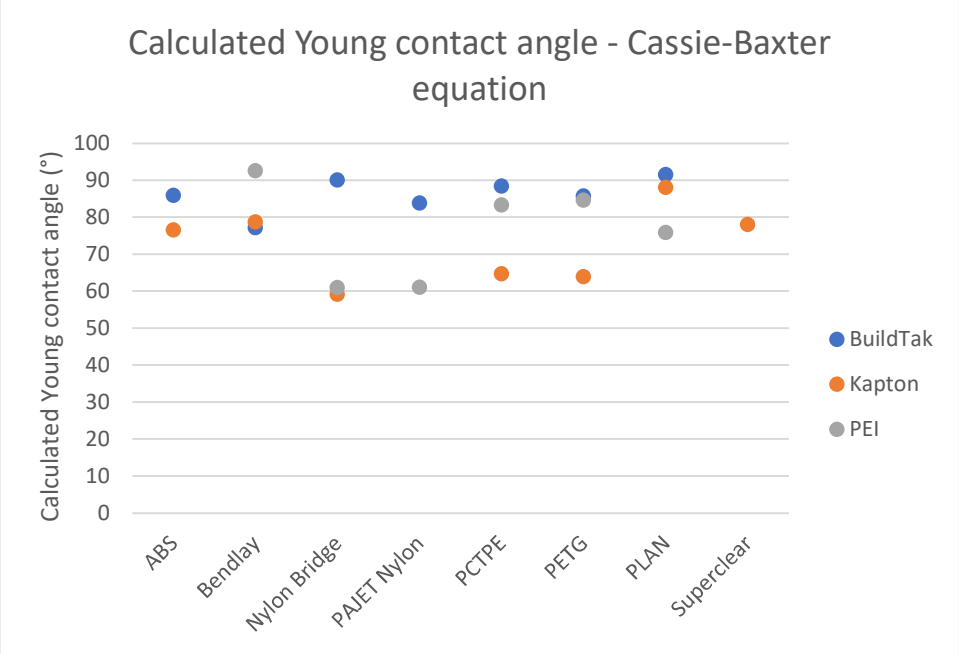

Figure 4-25: Calculated Young contact angle - Cassie-Baxter equation

An alternative approach using the Wenzel and Cassie-Baxter equations to assess the obtained contact angles is to assume that the contact angle obtained on the sample printed on the Kapton surface should be sufficiently smooth to be able to give the Young contact angle. The theoretical contact angle which should be obtained on a surface with the roughness parameters measured for the same material printed on the other build surfaces can then be calculated and compared to the measured contact angle. This data is presented below in Figure 4-26.

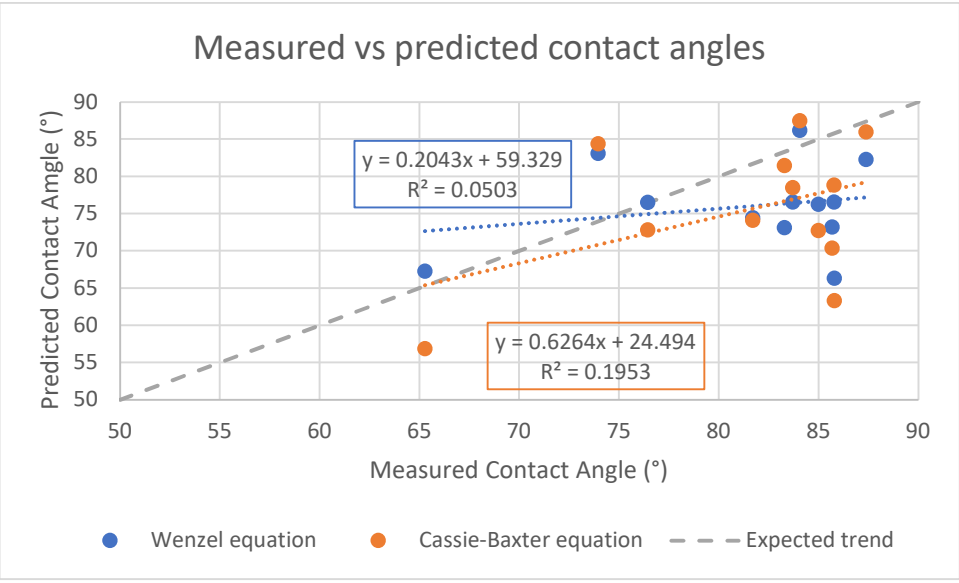

Figure 4-26: Predicted vs measured contact angles using Wenzel and Cassie-Baxter equations, assuming Kapton surface gives Young contact angle.

If the Wenzel or Cassie Baxter equations were to be able to accurately predict the contact angle on surfaces of different roughness, based on the contact angle measured on a surface printed on Kapton, the points would be expected to lie on a straight line of gradient 1 passing through the origin, shown in Figure 4-26. This trend is not seen – the points are generally found below the expected trendline, meaning that both the Wenzel and Cassie-Baxter equations under-predict the contact angle compared to the contact angle that was measured. Looking at the data in particular for ABS (the two points above the gradient 1 line at a measured contact angle of 80°), these again appear to be predicted more reasonably by this analysis.

It is unclear why these data do not behave in the predicted manner when roughness is varied. The roughness was not varied using a mechanical means, which may have produced more predictable roughness variation and hence a clearer sense of how roughness affected the wettability and how it could be predicted. This technique was used by Kubiak et al. (2011), where the roughness was varied by treating the materials analysed with varying grits of sandpaper. This approach, giving much larger-scale roughness variation, may have improved the results seen here. It is likely therefore that the roughness produced by templating onto different build surfaces produced insufficient roughness variability to be able to predict the contact angles based on roughness parameters.

4.4 Conclusions

1. Water contact angle measurements using the sessile drop method give contact angles for non-hygroscopic pure materials that are within the range of contact angles published previously, which suggests that water contact angle measurement may give a good indication of the wettability of 3D printing filaments when printed using typical print settings.
2. Contact angle measurement on composite materials gives varied and unpredictable results, which would be expected based on the criteria to measure the Young contact angle, namely a heterogenous surface.
3. Surface roughness parameters Sa and Sq measured on unfiltered data give the best correlation with contact angle measurements for non-composite materials.
4. The filtering process automatically applied by the Talysurf instrument appeared to remove too much of the surface texture to allow correlation of roughness parameters with contact angle - roughness parameters on the nano-scale did not appear to

accurately represent the surface encountered by milli-scale droplets, and hence correlations were not found in this data.

5. Contact angle measurement cannot be correlated with roughness for composite materials due to heterogeneous nature of the materials, combined with the additional surface texture created by the inclusion of the additives.
6. Contact angle prediction using the Wenzel and Cassie-Baxter equations for this data set does not yield good results. Alternative methods for producing varied roughness (for example, sanding with different grits) or measurement with different water drop sizes (for example, for smaller sized, using an environmental scanning electron microscope) may give improved correlation.

Chapter 5 Controlled Ultrasonic Fines Disruption from Sandstones

5.1 Introduction

The pores in sandstones are known to contain fine loosely bound particles which may, under the correct conditions, move in the pore network. The conditions required for fines mobilisation and migration in the pore network are a complex combination of salinity, temperature, pH, flow velocity and cation composition of the fluid. Khilar and Fogler (1984) have thoroughly investigated the effect of salinity on the migration of fines in Berea sandstones and identified a critical salt concentration (below 4125 ± 125 ppm Na^+) which fines migration will not take place. The effect of temperature was investigated by Schembre and Kovscek (2004), where they found that, for a number of concentrations and pHs of NaCl brine, an increase in temperature consistently promoted the release and migration of fines from the sandstone. The effect of pH on the release of fines has been shown to contribute to two regimes of fines release. Firstly, pH has been shown by Valdya and Fogler (1992) to promote fines release at pHs above 11 for a zero salinity fluid, which was validated using DVLO analysis. In addition, they found that a pH of 2 prevented the release of fines, even in fresh water. Mungan (1965) noted the second effect that an increase of pH may have on sandstone, in particular quartz-cemented sandstones. Mungan showed that the matrix material is seen to dissolve at high pHs, causing release of trapped material in the cement of the matrix. It has been shown that a critical velocity exists, below which fine particles will not be released from the pores of sandstones. Gruesbeck and Collins (1982) first showed this, along with consideration of viscosity and oil:brine ratio. The cations in the fluid play an important role in determining whether or not fines may migrate. Khilar and Fogler (1984), Kia et al. (1987) and Valdya and Fogler (1992) show that the presence of Ca^{2+} ions reduces, or in some cases, prevents, the migration of fines, even at high pH. Bedrikovetsky and Caruso (2014) have modelled these processes and show that fines migration occurs as a balance of drag, lifting, electrostatic and gravity forces. The electrostatic force is a function of salinity and decreases with decreasing salinity, and hence a lower force is required to detach fine particles from the pore surfaces at a low salinity. Some enhanced oil recovery methods (EOR) make use of the fact that oil recovery can in some reservoirs be increased by injection of low salinity brines (under 5,000 ppm). Prevention of fines migration is therefore desirable as it may be problematic when low salinity brines are injected into a reservoir which may be susceptible to fines migration, as the movement of the fines may begin to block the pores in the reservoir and prevent fluid flow. The blocking of pores by fines in a reservoir is one of the known

mechanisms of formation damage, where some process causes a reduction in the porosity or permeability of the reservoir and results in an impairment of the production or injection of the reservoir (Bennion, 2002).

Following formation damage due to fines migration, it is challenging to remove the fines to restore permeability. The most common method involves pumping various acids downhole to dissolve the matrix material rather than removing the fines themselves (Gabriel and Inamdar, 1983, Wong et al., 2003, Galal et al., 2016, Bassir et al., 2017, Ayopo et al., 2018). The acids required will depend on the formation – generally HCl, organic acids or a combination will be used for limestone formations, and HF, possibly in combination with HCl or organic acids, for sandstone formations. Some acid treatments involving a combination of organic acids and hydrofluoric acid may be designed to selectively remove the fines themselves rather than the matrix material (Huang et al., 2002). As chemical approaches can be costly and involve hazardous reagents, alternative approaches have also been studied.

In an experimental method, Venkitaraman et al. (1995) investigated whether the application of an ultrasonic probe would cause a change in permeability of both a sandstone and limestone in which the pores had previously been blocked by fines migration or drilling mud infiltration. It was found that the treatment caused a recovery of the permeability of between 2 and 6 times, although the initial permeability was not recovered. The authors also noted the limited range of the treatment, stating that it would not penetrate more than 1 cm into the rock. The limited range of the ultrasonic treatment is also highlighted by Hamida (2006), who states that by using Biot's theory (Biot, 1956a, Biot, 1956b, Biot, 1962), the attenuation length of ultrasound at 20kHz would be in the range of 2 – 10 cm. Work by Nikolaevskii (1989) and Nikolaevskii and Stepanova (2005) does show however that the use of low energy, low frequency waves in a reservoir will produce high-frequency harmonics upon dispersion, leading to ultrasonic waves being present in the reservoir which could lead to ultrasonic treatments being possible at a greater range. Fines migration due to movement of fines in the pore network is believed to be most problematic in the 30 cm volume surrounding the injection well (Gruesbeck and Collins, 1982), whereas fines migration into the formation from drilling fluid is reported to only occur in the closest 8 cm (Bennion, 1999, Clegg, 2007). Wong et al. (2003) gave an overview of the use of ultrasonic waves for well stimulation, emphasising the clean-up of damaged formations, and showed experimentally that at the laboratory scale, permeability of a Berea sandstone core damaged by fines migration could be successfully recovered. Previous use of ultrasonic treatments to remove the fines from sandstones were first reported in the 1960's, when Porter

(1962) looked at how the fine coating of clays on sandstone particles might be removed and assessed the removal using SEM micrographs. Savage (1969) investigated the use of ultrasound to disaggregate sandstone and siltstone and noted that the clays in the pores were quickly removed, but prolonged treatment may cause rounding of grains of softer minerals, notably lime and larger quartz fragments. A review of how ultrasound has been used to remove particles from surfaces and how ultrasound can be used to separate mixtures of particles which have different sizes or compositions is given by Ranade (1987), who suggests that a collapsing cavitation bubble at the interface of a surface and a particle may be responsible for the removal of the particle.

An explanation of how ultrasonic treatments work, and how they may be applied in cleaning a surface including the surface of a sandstone pore, is given in Section 3.4. The cavitation bubbles produced by the ultrasonic treatment may occur anywhere in the liquid which means that even internal surfaces may encounter the cavitation bubbles. This is important in the field of fines removal from rock pores – as long as there is liquid filling the pores, cavitation may occur in them and as Ranade (1987) noted, it is cavitation that is generally deemed responsible for the activity of ultrasonic treatments. However, in addition, Aarts et al. (1998) note that cavitation and acoustic streaming enhance the flow of liquids in pores, and the increased flow may have an influence on the removal of fine particles from the pore surfaces.

An interesting property may arise when ultrasound is applied to fluid in small pore spaces. The application of ultrasound to a fluid in a capillary is known to increase capillary rise, sometimes by orders of magnitude (Dezhkunov et al., 2003). It is this phenomenon, known as the ultrasonic capillary effect (UCE), which makes ultrasound in porous media an interesting subject to study. Indeed, there have been numerous studies regarding the enhancement of oil production from sandstones upon treatment with ultrasound (Chen, 1969, Fairbanks and Chen, 1970, Fairbanks, 1976, Tu et al., 2007), and of how flow in capillaries may be enhanced by ultrasound (Aarts et al., 1998). In addition, the propagation of the ultrasonic waves may be enhanced in porous media (Mat-Shayuti et al., 2019).

This work aims to investigate the effect of ultrasound on the fine particles contained in Castlegate and Berea sandstones, with a view to assessing whether treating a sandstone with ultrasound can predict the likelihood of fine particles migrating during low-salinity EOR. Two methods of assessing the movement of fines will be used:

1. Measurement of light transmittance through a sample of the solution in which the ultrasonic treatment of the sandstone had taken place immediately following sonication
2. SEM imaging of sandstone and material released from sandstone following sonication

This should allow an assessment to be made as to the effect of ultrasound on the fine particles, and how well the methods correlate, with the aim to be to produce a method that will give an indication of the fines migration potential of a rock without having to undertake full flow experiments.

5.2 Materials

5.2.1 Sandstones

Two sandstones were chosen for the study. Castlegate sandstone, a fluvial sandstone found in Utah (Miall and Arush, 2001), is a relatively poorly cemented sandstone containing approximately 10% clay (predominantly kaolinite and illite-smectite with around 60% swelling capacity). Berea sandstone from Cleveland Quarries, Ohio (Hannibal, 2020) is a widely-used standard for flow studies in the oil and gas industry (Cleveland Quarries, 2021) containing around 11% clay (predominantly kaolinite).

Previous quantitative x-ray diffraction analysis of three separate samples of Castlegate sandstone had been carried out by Prof. Stephen Hillier, James Hutton Institute, Aberdeen (Kareem, 2017). An average of the compositions obtained, along with an average composition of several Berea sandstone samples[a] is shown below in Table 5-1.

Table 5-1: Measured mineral composition of Berea and Castlegate sandstones. Numbers in brackets in the Castlegate column give the composition following washing in 7,000 ppm brine.

Mineral	Castlegate (wt %) (Kareem, 2017)	Berea (wt %)[a]
Quartz	85.6 (88.0)	83.6
Feldspar	4.4 (3.8)	4.4
Dolomite	-	1.1
Kaolinite	2.4 (2.9)	4.4
Illite	-	1.9
Chlorite	-	1
Illite-Smectite	6.6 (3.5)	1.8
Calcite	0.2 (0.1)	1.6
Jarosite	(0.1)	0

Halite	0.5 (0.0)	0
Muscovite	0 (2.9)	0

Note: in this instance, the Castlegate sandstone used for analysis was preserved in 70,000 ppm NaCl brine. It has been shown that removing the brine (shown as halite in the table above) from the dried sandstone affects the concentration of fines. Due to the fact that studies are to be done varying the salt concentration of the brine the rock chip is placed in, the 70,000 ppm salt residue on the dried rock chip will affect the concentration of salt during the test. The Castlegate sample was therefore washed in 7,000 ppm brine before being used. 7,000 ppm brine was chosen as it is above the accepted 5,000 ppm threshold for low salinity enhanced oil recovery.

Studies have additionally been carried out on the fines present in Berea and Castlegate sandstones when separated from the bulk rock. The composition of the fines of each sandstone are shown in Table 5-2, along with the definition used to classify the fines.

Table 5-2: Measured composition of fines in Berea and Castlegate sandstones. Numbers in brackets in the Castlegate column give the composition following washing in 7,000 ppm brine. Definition of fines given in italics in the column header.

Mineral	**Castlegate (%) (Kareem, 2017)** ***< 2 µm fraction***	**Berea (%) (Scheuerman and Bergersen, 1990b)** ***Clays***	**Berea (%) (Kia et al., 1987)** ***Clays***
Kaolinite	55 (57)	46	71
Illite	11 (13)	8	14
Illite + Illite/Smectite Mixed Layer	34 (37)	38	-
Chlorite	-	8	-
Illite-Mica	-	-	15

The Castlegate fines were separated by timed sedimentation from a powdered whole rock sample, which was prepared by spray drying a rock sample initially powdered by McCrone Milling. The method used is discussed further by Kareem et al. (2017). The Berea clay faction was separated from the whole rock by flocculation and dispersion by Scheuerman and Bergersen (1990b), and quoted by Kia et al. (1987).

The sandstones were prepared for use in experiments by breaking them with a hammer and chisel into 0.5 ± 0.15 g chips. The smaller pieces remaining were sieved through a 30 mesh (0.6

mm) sieve and the portion that passed through the sieve used as powdered sandstone in subsequent experiments.

5.2.2 Lab-made model sandstone

Although the sandstones under study have been well characterised, the composition of a small subsample of the sandstone is difficult to obtain without either destructive testing using XRD, requiring a powdered sample, or time consuming scanning and characterising using micro-CT. The nature of the natural material means that there is some variability in the composition of the sandstone at any given point. It was concluded, therefore, that a lab-made model sandstone was required. This lab-made model sandstone consisted of a mixture of pure powdered minerals in proportions representing that of the sandstones under study. It was decided that any components present at <1% would not be included in the mixture, and that the feldspar would also be omitted as it did not occur in any of the fines portion of the sandstones under study. Chlorite was also omitted as it has been found to not be sensitive to changes in salinity and does not generally contribute to formation damage (Scheuerman and Bergersen, 1990a, Wilson et al., 2014). The lab-made model sandstone, although not fully representative of the natural sandstones, should give a good representation of the expected state of a natural sandstone if the sandstone were to be fully broken down into its constituent parts. This should then allow absorbance measurements made to be calibrated to an expected value if the sandstone were fully cleaned of all minerals seen to migrate during a traditional fines migration experiment. The following compositions were decided upon for the standard model sandstone. For the fines portion, all components bar the quartz were used.

Table 5-3: Composition of model sandstones. Details of clay mineralogy are given in Appendix B.

Mineral	**Model Castlegate (%)**	**Model Berea (%)**	**Synthetic component name**
Quartz	90.5%	91.2%	Sand (washed) (Alfa Aesar)
Kaolinite	5.2%	4.8%	Kaolinite (KGa-2, KGa-1b) (Clay Minerals Society)
Illite	1.0%	2.1%	Illite (I-Mt-1) (Clay Minerals Society)
Illite-Smectite	3.2%	2.0%	Illite/Smectite mixed layer (ISCz-1) (Clay Minerals Society)

5.2.3 Salt solution concentrations

Two salts were selected for testing with the sandstones – sodium chloride (Sigma Aldrich ReagentPlus®, ≥99%) and calcium chloride (Sigma Aldrich ReagentPlus®, ≥99%). The concentrations used were as follows:

Table 5-4: Salt concentrations used.

Salt	Concentration (M)	Concentration (ppm)
Calcium chloride	1 M	110980 ppm
	0.001 M	111 ppm
Sodium Chloride	1 M	58440 ppm
	0.1 M	5844 ppm
	0.05 M	2922 ppm
	0.001 M	58.4 ppm
	0.513 M	30,000 ppm
	0.171 M	10,000 ppm
	0.086 M	5,000 ppm
	0.077 M	4,500 ppm
	0.073 M	4,250 ppm
	0.068 M	4,000 ppm

5.3 Instruments

5.3.1 Application of ultrasound

The ultrasonic treatments used were an ultrasonic probe (Fisherbrand™ Model 120 Sonic Dismembrator, hereafter termed “ultrasonic probe”) and an ultrasonic bath (Ultrawave QS5, , hereafter termed “ultrasonic bath”).

5.3.2 Measurement of Absorbance

The absorbance of the samples was measured either using a variable wavelength spectrophotometer (Jenway 6300) (±1%T, ±0.01 Abs at 1.000 Absorbance), or using a Hach Pocket Colorimeter at 655nm (±0.015 precision). The wavelength used with the Jenway spectrophotometer was chosen following analysis of the measurement capability of the instrument and the fluorescence response of the components used. In both machines, a plastic cuvette with a 1 cm pathlength was used, filled to a volume of 2.5 – 4 ml. Zeroing was carried out with deionised (DI) water.

5.3.3 Imaging of fines with Scanning Electron Microscope

Images were obtained using a Hitachi SU-70 High-Resolution Analytical SEM at the G.J. Russell Microscopy Facility, Department of Physics, Durham University. Samples were coated with 40 nm carbon using a Cressington Carbon108/A high vacuum carbon coater, or with 40 nm gold for rock chips and 12 nm gold for powder samples using a Cressington Sputter coater 108 Auto for samples where coating with carbon gave a poor quality image.

5.4 Test methods

5.4.1 Spectrophotometer calibration

Using a variable wavelength spectrophotometer, an optimal wavelength for absorption measurement could be selected. It was important to select a wavelength at which the components in the solution did not fluoresce, so that the absorption is due only to the particles blocking the path of light from the emitter to the detector. Once an appropriate wavelength had been selected, the absorption measured gave a measurement of concentration of particles in the path of the light beam.

5.4.1.1 Variation of measurements with wavelength

The Jenway 6300 spectrophotometer has a quoted accuracy of ±1% T, ±0.01 Abs at 1.000 Absorbance. In order to assess this across the full range (320 – 1000 nm), 14 wavelengths at 50 nm spacing from 350 – 1000 nm were chosen, and 10 repeat measurements of DI water were made after zeroing the machine with the same DI water (removing and replacing the cuvette after each measurement).

5.4.1.2 Variation of absorption of 1M salt solutions with wavelength

Two salt solutions (1 M NaCl and 1 M $CaCl_2$) were screened to confirm that the salt did not fluoresce at any of the possible wavelengths for measurement. An interval of 5 nm between measurements across the whole working range of the Jenway 6300 spectrophotometer (320 – 1000 nm) was chosen. The Jenway 6300 spectrophotometer was adjusted to the selected wavelength, zeroed with DI water (1 cm path length square plastic cuvette), then the absorbance of 1 M $CaCl_2$ and NaCl solutions were measured at that wavelength. The machine was adjusted to the next wavelength, re-zeroed and the procedure was repeated for wavelengths from 320 – 1000 nm. At 100 nm intervals the machine was readjusted to a value 100 nm lower, and the value was re-measured to confirm that the measurements were likely to be reproducible. A measurement within 0.01 of the previous measurement found was deemed acceptable, given the quoted accuracy of the spectrophotometer.

5.4.1.3 Variation of absorption of clay suspensions with wavelength

After initial screening to obtain a suitable concentration, a 10 g/l suspension of each clay proposed to be included in the lab-made model sandstones was prepared. This concentration gave an absorption reading within the measurement range of the spectrophotometer for all wavelengths and clays tested. The clay suspensions were prepared directly in the cuvettes as 0.002 g/4 ml suspensions. The suspensions were treated with the ultrasonic probe for 5 minutes at 39% power, using a 2 s on, 3 s off pattern. Similarly to the salt solutions, the instrument was zeroed with DI water after every change in wavelength, but in addition, as the clays are suspensions and may settle over time, the cuvettes were shaken by hand at 100 nm measurement intervals. The uniformity of the suspension was confirmed during the testing by re-setting the spectrophotometer to a value 100 nm lower at 100 nm intervals and re-measuring the absorbance – a reading within 0.01 was deemed acceptable based on the σ variation obtained in the previous test and the spectrophotometer quoted uncertainty of ±1% T, ± 0.01 Abs at 1.000 Absorbance.

5.4.1.4 Production of clay calibration curves

A calibration curve for fines released from Castlegate and Berea sandstones was prepared in the following manner.

1. 1 g of lab-made model sandstone or powdered real sandstone was placed in a 28 ml glass vial, and 10 ml of salt solution was added
2. The sandstone and brine were treated with the ultrasonic probe in the vial for 16 minutes total ultrasonic treatment time (2 s on, 3 s off) at 39% power.
3. A 2 ml sample of the treated solution was removed and placed into a cuvette, and the absorbance was recorded, both on the Jenway 6300 at the wavelength selected from the previous testing, and with the Hach pocket colorimeter (655 nm).
4. A portion of the remaining solution was removed and placed in another glass vial, and salt solution to make 10 ml total volume was added.
5. The solution was treated with the ultrasonic probe for 2 minutes total ultrasonic treatment time (2 s on 3 s off) at 39% power.
6. Steps 3 – 5 were repeated creating 8 serial dilutions following the table below:

Table 5-5: Table of serial dilutions of model sandstone or fines solution.

Repetition number	Ultrasonic treated solution (ml)	Salt solution (ml)	Dilution factor	Concentration of model sandstone (g/l)

1	5	5	2	50
2	5	5	4	25
3	5	5	8	12.5
4	5	5	16	6.25
5	2.5	7.5	21.3	4.69
6	2.5	7.5	28.4	3.52
7	2.5	7.5	37.9	2.64
8	2.5	7.5	50.6	1.98

5.4.2 Ultrasonic removal of fines from rock chips

5.4.2.1 Assessment of Castlegate sandstone for fines removal potential

Small (~1 g) Castlegate sandstone chips were placed into 50 ml centrifuge tubes with 40 ml 70,000, 35,000, 17,500, 7,000, 3,500 or 1,000 ppm NaCl. The vials were placed on the oscillatory shaker (IKA KS 130 basic orbital shaker) for 1 hour at 400 rpm. The presence or absence of fines released from each of the chips was noted, but not quantified at this stage.

To test whether the ultrasound would be likely to break the Castlegate chips apart, ultrasound was applied to ~1 g chips in a 28 ml vial with 20 ml 70,000 ppm NaCl (the NaCl concentration that the Castlegate sandstone was originally preserved in) with gradually greater power, shown Table 5-6, and the effect on the chip was noted.

Table 5-6: Ultrasonic power sweep for Castlegate sandstone

Power	Time
25%	1 minute
50%	1 minute
99%	2 minutes

The effect of the ultrasound on the Castlegate sandstone was further assessed by imaging the native Castlegate and each of the chips treated by ultrasound, and the material removed from the chip (the “fines”), using SEM.

5.4.2.2 Treating sandstone with ultrasonic using single salinity brines

It has been shown that there exists a critical salt concentration (the CSC) above which fines will not migrate when the brine is pumped through the sandstone. To investigate this effect, individual rock chips were weighed and placed into a 50 ml beaker or 28 ml vial. The salt solution

of interest was added and ultrasound was applied for the desired time with the desired settings. After the application of ultrasound the absorbance of the solution was measured and the rock chip was dried in an oven at 70 °C overnight and re-weighed.

SEM images were taken of the fines and whole rock following treatment with ultrasound. To illustrate the effect of extended ultrasound treatment in a brine which should completely break apart the sandstone (0.001 M NaCl), Castlegate and Berea (100 – 200 mD) were treated (1 g sandstone in 10 ml 0.001 M NaCl in a 28 ml glass vial, 39%, 2 s on 3 s off, 16 minutes, ultrasonic probe). For the imaging of the fines, 0.125 ml of the solution produced following ultrasound containing suspended fines was removed and diluted with 4.875 ml DI water, and a 30 µl drop was placed on an SEM stub and dried. For the whole rock, if a rock chip remained after ultrasonic treatment, the chip was dried, broken in half and the halved mounted on an SEM stub so that the chip surface and the inside of the chip could be imaged. If the rock had been disintegrated by the ultrasonic treatment, or a powder had been used, the solution containing the suspended fines was carefully removed, the remainder dried in an oven then resuspended in 1 ml DI water, shaken for 10 minutes (IKA KS 130 basic orbital shaker), and a 0.125 ml drop of the resulting solution (taken from the bottom of the vial) was placed on the SEM stub and dried. The samples were all gold coated with the Cressington Sputter coater 108 Auto.

5.4.2.3 Treating sandstone with ultrasonic using serial change of salinity

Khilar and Folger (1984) used a serial change in salinity to obtain the CSC for Berea sandstone, with the brine being pumped through the sandstone and the pressure being monitored to look for a decrease in permeability indicating that fines migration was causing formation damage. This sequence of serial application of brines and ultrasound to the same rock chip was designed to find out if application of ultrasound can be used in a similar manner to obtain the same CSC for Berea. Individual rock chips were pre-soaked in 30,000 ppm NaCl for 1 hr and dried in the oven at 70 °C for 3 h. A rock chip was weighed and placed in a vial or beaker, and 30,000 ppm NaCl was added. Care was taken to ensure the volume of brine was greater than 40 pore volumes, which was the volume of brine pumped through the core in the original experiment by Khilar and Fogler (1984). Ultrasound was applied with either the probe or bath for the desired time with the desired settings, the beaker or vial was removed and the absorbance of the brine was measured. The rock chip was placed into a fresh beaker and the following brine was added, ultrasound applied and absorbance measured; this was repeated for all brines in the series. The rock chip was recovered and dried in an oven at 70 °C overnight then re-weighed.

5.5 Results and discussion

5.5.1 Spectrophotometer calibration

The objective of this part of the work was to assess the usefulness of a spectrophotometer or colorimeter for quantifying the concentration of fines released from a sandstone following ultrasonic treatment. Firstly, a wavelength for measurement with the spectrophotometer had to be decided on, based on the likelihood of absorption or fluorescence of the materials at the particular wavelength, and based on the performance of the machine at the particular wavelength. The wavelength of the colorimeter also had to be verified as not posing a problem based on the materials being tested.

5.5.1.1 Variation of measurements with wavelength

The average values obtained following 10 repeated water measurements at each wavelength from 350 – 1000nm is shown in Figure 5-1:

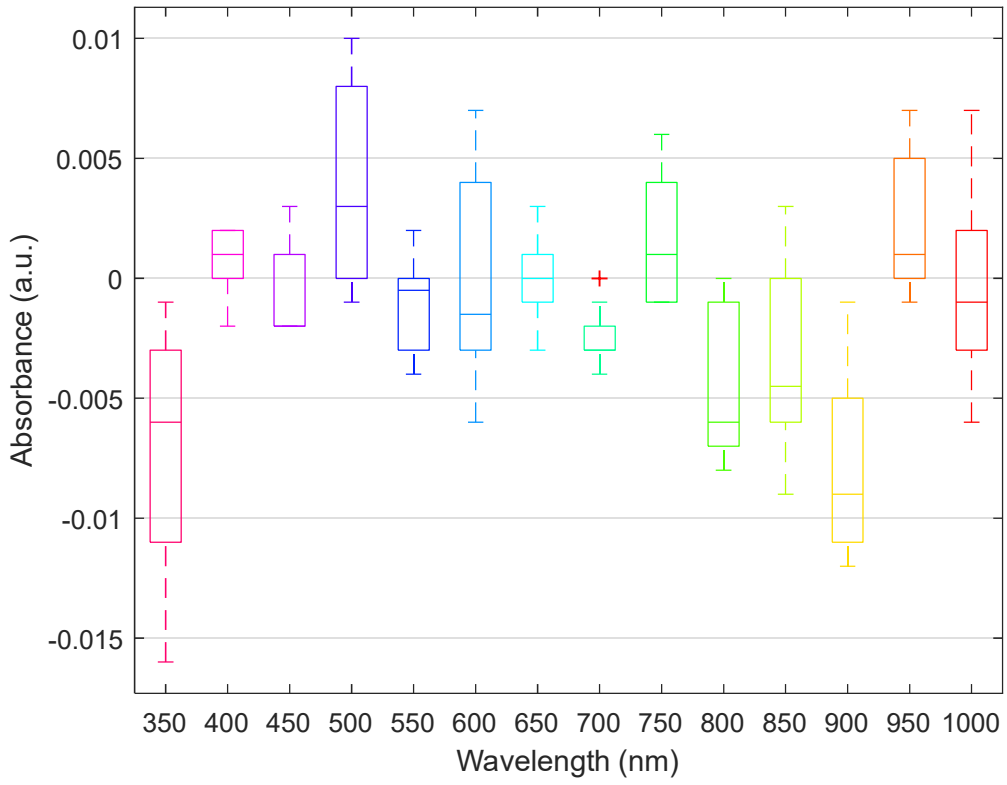

Figure 5-1: Variation of repeated DI water values measured at each wavelength

Another useful way of plotting this data may be to interpolate the values obtained so that the ranges cover the full range of the instrument measurement options; this data, with the average and 1σ and 2σ ranges plotted, is shown in Figure 5-2.

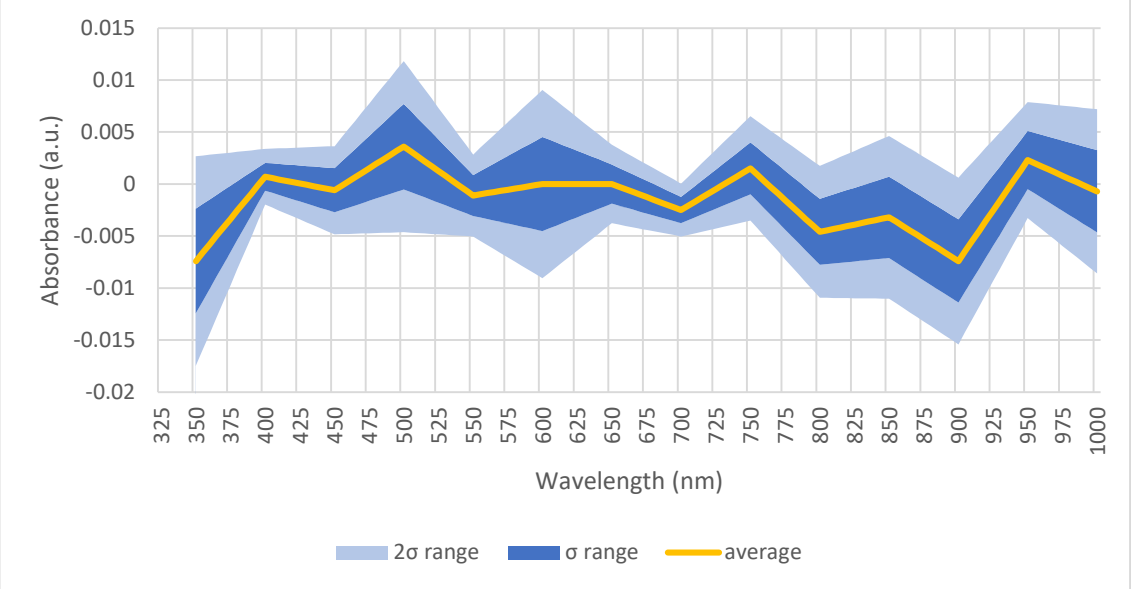

Figure 5-2: Average of 10 repeated water measurements taken at 50 nm intervals, and the σ and 2σ ranges interpolated for all wavelengths.

The variation observed during repeated measurements of water in the Jenway 6300 was generally within the quoted accuracy of the machine (± 1% T, ± 0.01 Abs at 1.000 Absorbance), although the quoted absorbance accuracy was given at 1.000 absorbance rather than the 0.000 absorbance measured in this study. Given the lack of absorbance accuracy data provided across the full range of absorbances, it will be assumed that for all absorbances, a variation of 0.01 is within the accuracy limits of the machine. Considering this data, as the machine was zeroed with the same sample (DI water) that as then subsequently measured 10 times, it should be assumed that the true value of absorbance for this sample is 0.000. Any value therefore in the σ range which falls above 0.01 or below -0.01 should be assumed to be a value outwith the quoted accuracy of the machine. Outlying measurements occurred at 350 nm and 900 nm (Figure 5-2), and when the 2σ range is considered, 500 nm may also be included. As the machine appears to be inaccurate at these wavelengths, the chosen wavelength for measurement going forward should ideally not fall around these wavelengths.

5.5.1.2 Variation of absorption of 1M salt solutions with wavelength

A reading was not possible at 320 nm; the machine produced an error (Err 2 – light level too low), hence the first reading was taken at 325 nm. The temperature was monitored during the measurements and varied between 20 °C and 21 °C. The results obtained are shown in Figure 5-3, and overlaid on top of the results obtained from the previous experiment (Figure 5-4).

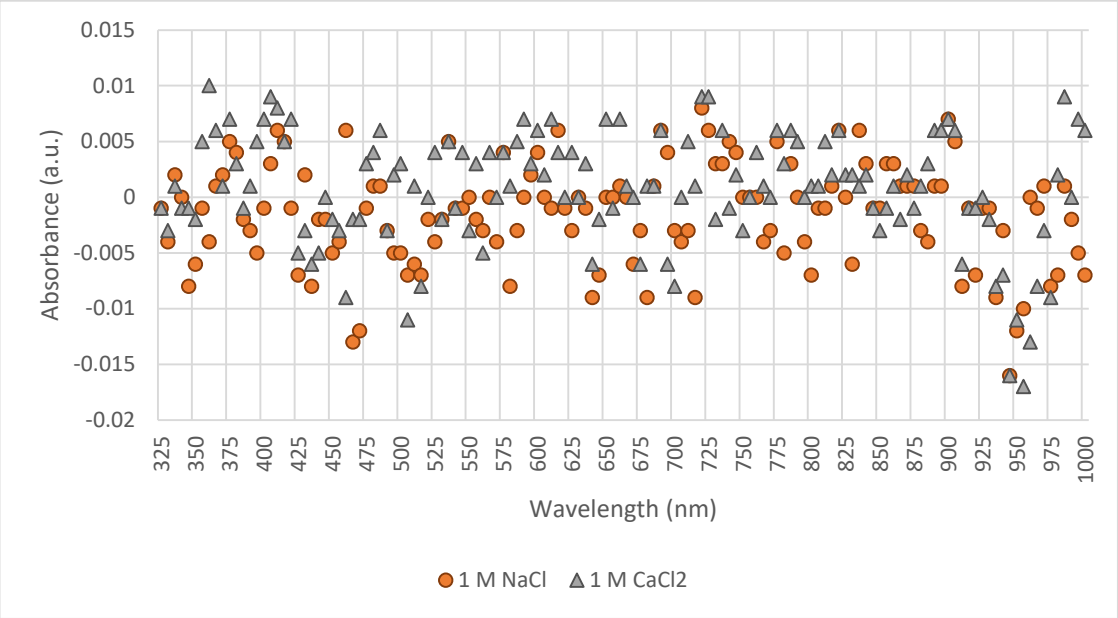

Figure 5-3: Salt solution measurement over full wavelength range of Jenway 6300.

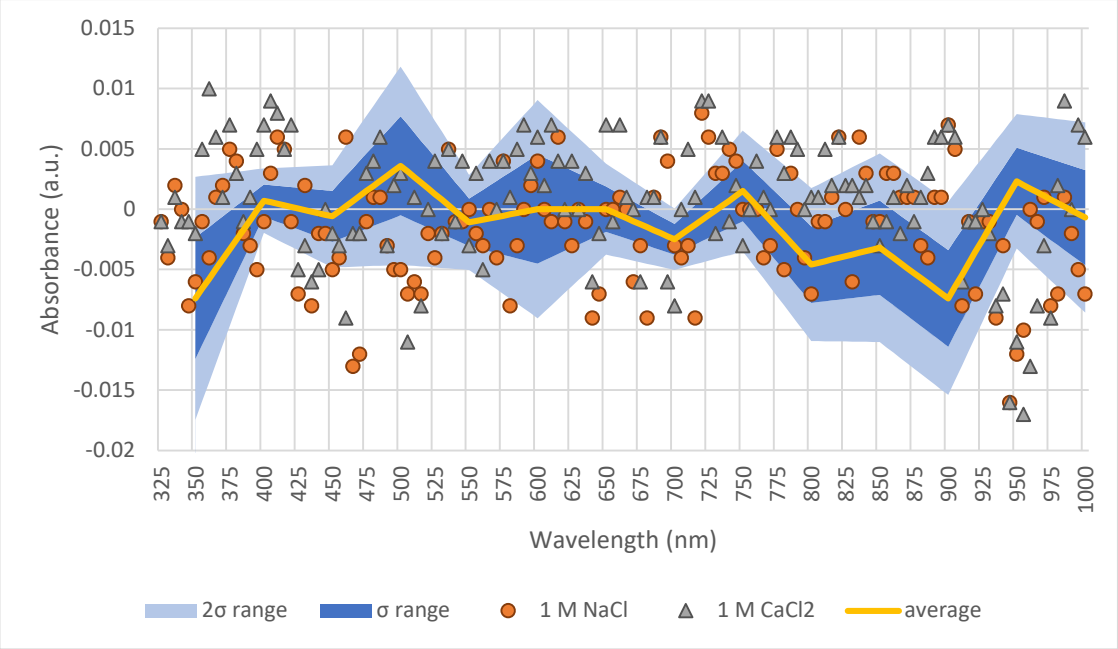

Figure 5-4: Salt solution measurements overlaid on 1σ and 2σ-variations based on repeated measurements of DI water.

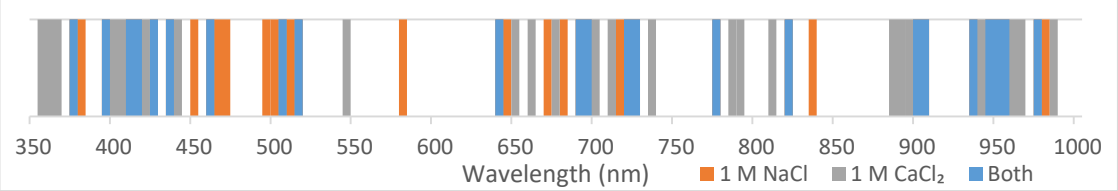

Figure 5-5: Wavelengths at which the 1 M NaCl, 1 M $CaCl_2$ or both the 1 M NaCl and the 1 M $CaCl_2$ measurements were outwith the 2σ range obtained by repeat measurements of DI water.

There is no evidence to suggest that NaCl or $CaCl_2$ in water will show any fluorescence behaviour at 1 M concentration at wavelengths from 320 – 1000 nm (the working range of the Jenway 6300 spectrophotometer used (Chai et al., 2008, Paviet-Hartmann et al., 2001, Kim et al., 2016, Tong et al., 2020)). There may be an absorbance peak below 320 nm (around 270 nm for NaCl (Chai et al., 2008)), but this is outwith the range of operation of this spectrophotometer and should not affect this study. Comparing the range of figures obtained when repeatedly measuring DI water to the measurements obtained by measuring the 1 M salt solutions, it can be seen that 28% of the 1 M NaCl measurements and 36% of the 1 M $CaCl_2$ measurements are outwith the 2σ range (Figure 5-5). However, the 2σ range is smaller than the quoted accuracy of the machine, so most of these may still be assumed to be variation around 0 and not due to absorbance or fluorescence by the salts. Some deviation from 0 absorbance outwith the accuracy of the machine was seen from 945 – 960 nm in both 1 M NaCl and $CaCl_2$, 465 – 470 nm in 1 M NaCl and 505 nm in 1 M CaCl2 (Figure 5-4). The negative absorbance seen at 945 – 960 nm is unlikely to be a feature of the salt solutions; rather this is more likely to be due to the machine. Nevertheless, to ensure that this deviation would not affect the measurements, this wavelength range was avoided going forward. Combining the results from the measurement of salt solution with the repeat measurement of water (Figure 5-4) allows an appropriate wavelength for measurements for the duration of the study to be selected. The wavelength selected was 600 nm, as at this wavelength the measurements made of the salt solutions are within the 2σ range of the water measurements, and the average of the water measurements was 0 implying that measurements may be fairly stable in this range. In addition, the data suggests that measurements at 655 nm appear to be close to zero when measured with the Jenway 6300. 655 nm is the wavelength used by the Hach pocket colorimeter, so this gives confidence that the colorimeter would also be an appropriate device to measure the absorbance.

5.5.1.3 Variation of absorption of clay suspensions with wavelength

Previous work indicates that clays will not fluoresce or absorb strongly in the range of wavelengths under investigation. However, recent work suggests that kaolinite (KGa-1b) will be excited at 517 nm and will weakly fluoresce at 400 nm (Harasawa, 2021) using confocal microscopy. KGa-1b therefore has the potential to show an absorbance peak at 517 nm or a trough at 400 nm, but as the activity is very weak it is not expected to show up in this study. Plotting the absorbance vs wavelength for 10g/l KGa-1b, ISCz-1 and IMt-1 gives the following results:

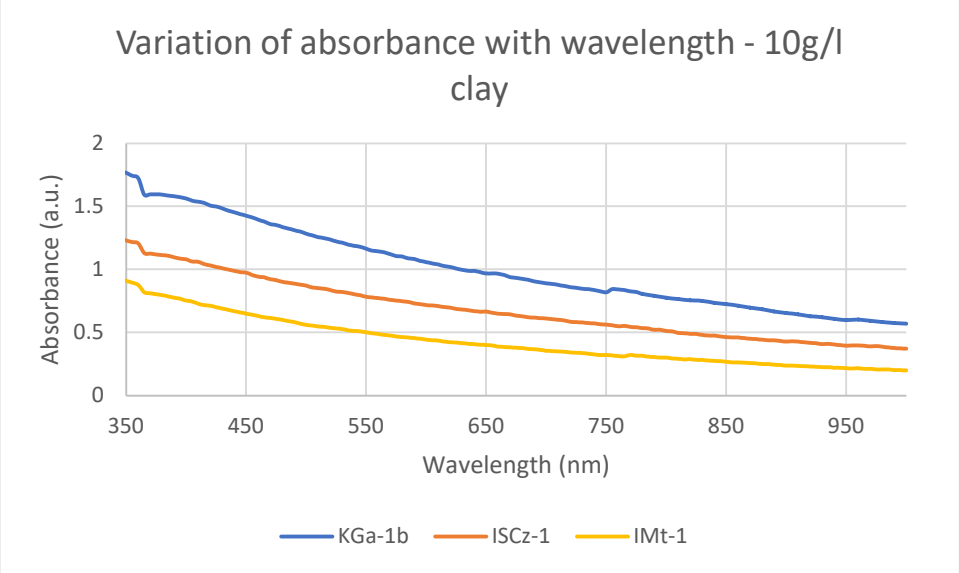

Figure 5-6: Variation of absorbance with wavelength for 10g/l clay suspensions

A small dip can be seen in the absorbance of all clays at approximately 370 nm. As this dip occurs in all clays, this it is unlikely to be due to the chemistry of the clay, rather the instrument. The slight increase in absorbance seen in the KGa-1b (755 nm, 0.025 increase) and IMt-1 (770 nm, 0.011 increase) were as a result of gentle agitation to ensure the clay suspension didn't settle during testing. Again, the results obtained suggest that no absorption or emission of light occurs due to the presence of clay in the solution, confirming that the spectrophotometer or colorimeter would be appropriate choices for measuring the absorbance at any wavelength. In particular, no deviation from the curve is seen at 600 nm or 655 nm, allowing the use of either instrument.

The absorption can be seen to vary with wavelength, with lower absorption being seen at higher wavelengths. This is due to the fact that turbidity measurement relies on particles scattering the light emitted from the spectrophotometer away from the detector. Other work has been done to convert the absorbance (or turbidity measurements) obtained to particle sizes for monodisperse, spherical particles (Dezelic et al., 1963, Melik and Fogler, 1983, Crawley et al., 1997), but the application of this work is beyond the scope of this study.

5.5.1.4 Sandstone fines calibration curve

The measured absorbance values are shown in Table 5-7 for model Castlegate, model Berea and powdered Castlegate and Berea, on both Jenway 6300 at 600 nm and the Hach pocket colorimeter at 655 nm. Concentrations where the absorbance was outwith the readable range of the machine are shown as a dash (-).

Table 5-7: Lab-made model sandstone absorbance table for 1M and 0.001M NaCl and $CaCl_2$, measured on the Jenway 6300 (600nm) and Hach pocket colorimeter (655nm)

	Lab-made model Berea							
	1 M NaCl		1 M $CaCl_2$		0.001 M NaCl		0.001 M $CaCl_2$	
Concentration (g/l)	600 nm	655 nm	600 nm	655 nm	600 nm	655 nm	600 nm	655 nm
100	-	-	-	3.651	-	3.566	-	3.681
50	-	-	-	3.163	-	3.163	-	3.267
25	-	2.652	-	2.557	-	2.384	-	2.693
12.5	-	1.76	-	1.649	1.718	1.379	-	N/A
6.25	1.226	0.971	1.14	0.94	0.913	0.722	1.195	0.951
4.6875	0.935	0.732	0.859	0.679	0.679	0.542	0.9	0.721
3.515625	0.689	0.55	0.655	0.521	0.501	0.407	0.684	0.545
2.636719	0.516	0.399	0.489	0.388	0.373	0.304	0.516	0.409
1.977539	0.376	0.295	0.361	0.297	0.284	0.231	0.38	0.314
	Lab-made model Castlegate							
	1 M NaCl		1 M $CaCl_2$		0.001 M NaCl		0.001 M $CaCl_2$	
Concentration (g/l)	600 nm	655 nm	600 nm	655 nm	600 nm	655 nm	600 nm	655 nm
100	-	3.521	-	3.51	-	3.521	-	3.45
50	-	3.135	-	3.03	-	3.126	-	3.023
25	-	2.542	-	2.338	-	2.504	-	2.254
12.5	-	1.69	1.885	1.537	-	1.664	1.826	1.493
6.25	1.16	0.941	1.062	0.858	1.149	0.935	1.033	0.833
4.6875	0.889	0.722	0.796	0.635	0.881	0.715	0.794	0.643
3.515625	0.676	0.547	0.604	0.492	0.649	0.533	0.606	0.496
2.636719	0.504	0.414	0.456	0.376	0.504	0.417	0.451	0.37
1.977539	0.379	0.311	0.352	0.293	0.378	0.317	0.34	0.29

Plotting the values (Figure 5-7) shows that at concentrations above 12.5 g/l the absorption response is not linear or is not measurable.

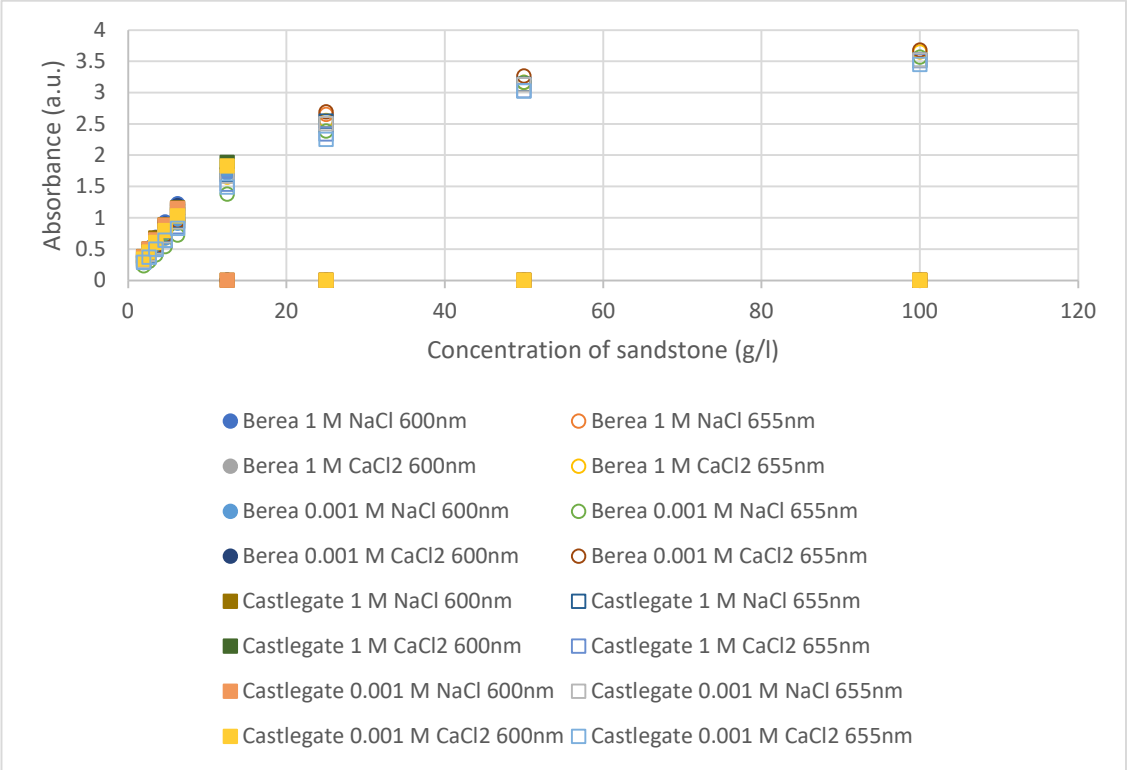

Figure 5-7: Calibration curve for lab-made model sandstones.

Fitting a linear trendline to the data obtained at concentrations lower than 12.5 g/l gives an R^2 value of > 0.99 in all cases (Figure 5-8), suggesting that this concentration range will give data in line with the Beer-Lambert law.

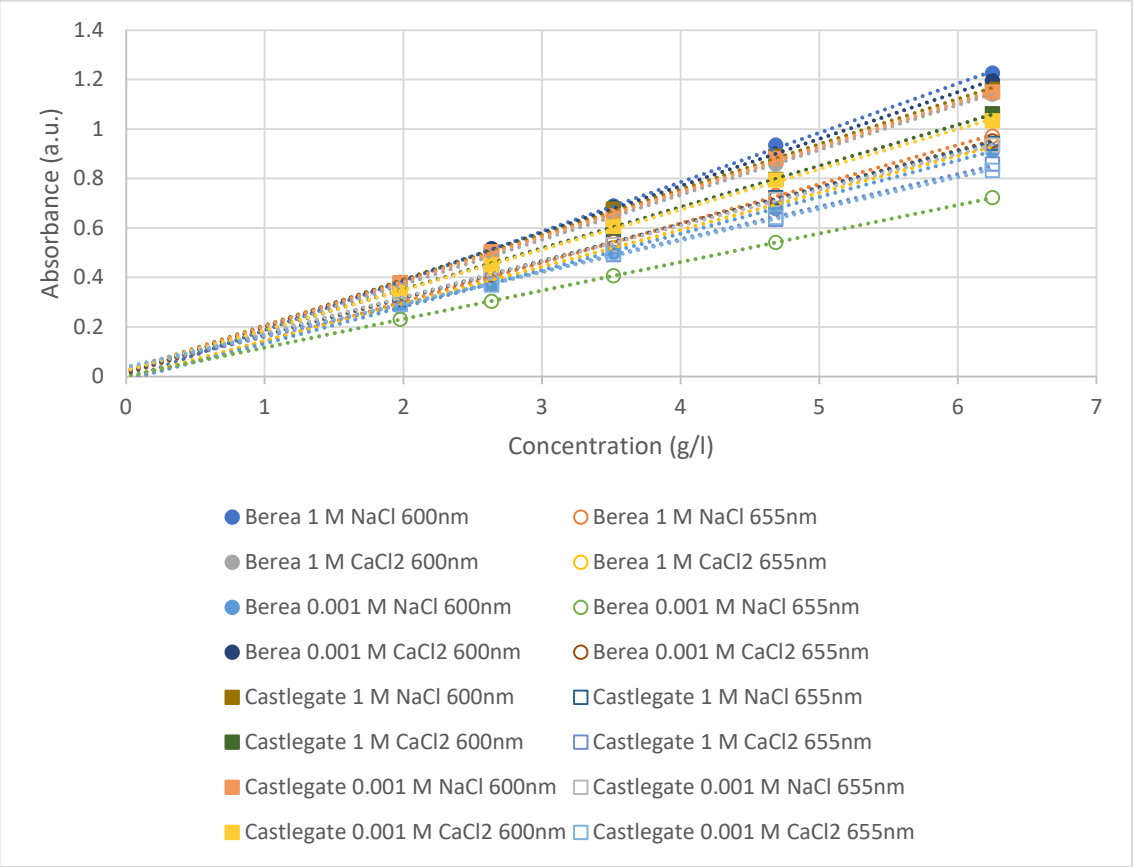

Figure 5-8: Linear region of calibration curve with fitted linear trendlines from serial dilution of lab-made sandstone suspensions

The Hach pocket colorimeter allowed a wider range of absorbances to be recorded than the Jenway 6300, hence the presence of measurements for higher concentrations when using the colorimeter rather than the spectrophotometer. These show the significant deviation from the Beer-Lambert law at higher concentrations and reinforce the fact that high absorbance measurements cannot be translated to concentration using the linear fit.

These calibration curves are designed to convert the absorbance measurement obtained after a piece of sandstone has been treated with ultrasound into the concentration of sandstone, in g/l, which would give that concentration of fines if all of the fines were removed from that sandstone. Given that the concentration of sandstone (i.e. weight of sandstone chip or powder with volume of brine added) for each subsequent experiment is known, the % of total fines removed may be calculated. However, the method used to prepare the calibration curves used a serial dilution by volume method, whereas subsequent experiments added a known volume of brine to a sandstone chip or powder. The volume of the sandstone chip or powder may be estimated by assuming a density of 2.65 g/ml for the sandstone (Manger (1963) suggests a bulk density of 2.06 – 2.24 g/ml; this gives a particle density of 2.58 g/ml using the measured

porosities but generally a value of 2.65 g/ml may be assumed) and should be accounted for in order to ensure the calibration curve can be used correctly.

5.5.2 Ultrasonic removal of fines from rock chips

This series of experiments utilises sandstone chips or powder prepared by breaking with a hammer and chisel. The sandstone chips prepared had a somewhat irregular dimensions but were sized to 0.5 ± 0.15 g pieces. It would be expected, from Biot Theory, that an ultrasonic wave of 20 kHz would penetrate into a rock between 2 and 10 cm (Hamida, 2006). The sandstone chips in this experiment had a maximum length of 1 cm (the average chip, prepared as a cube, had a side length of approximately 6 mm) so the ultrasonic waves in this experiment therefore are expected to penetrate the samples fully, and hence should be fully treated with ultrasound.

In a traditional fines migration experiment (for example, those described by Gruesbeck and Collins (1982), Tang and Morrow (1999), Ashraf et al. (2010)) fines migration will only occur at salinities lower than the critical salt concentration (CSC) of the brine flooding the core, and at a flowing velocity greater than the critical velocity (CV) determined for the core in question. In these experiments there was no direct flow velocity, but there were small, localised areas where the velocity of the fluid increased beyond the CV due to the implosion of the cavitation bubbles produced by the ultrasound treatment applied. In addition, the continued application of ultrasound has been shown to induce flow in porous media (Aarts et al., 1998).

The method chosen to break apart the sandstone cores was used to try to ensure that the fines on the sandstone remained present and in their original position. Cutting the sandstone in the conventional manner often involves the addition of water to aid the cutting process. The addition of water may have caused the fines to migrate from their initial positions before the experiment began. SEM images were taken of the <30 mesh powder which was produced during the production of the Berea and Castlegate chips (Figure 5-9). It is clear from these images that the surface fines (including large kaolinite booklets) are still present on the surfaces of the grains. This would suggest that this method of sandstone chip preparation should preserve the fines present in the pore spaces. However, the use of a hammer and chisel may reduce the strength of the sandstone by introducing fractures into the chip, which then may promote the breakdown of the chip when ultrasonic power is applied – this was not seen in the case of the Berea sandstone but may have contributed to the results seen with the Castlegate sandstone.

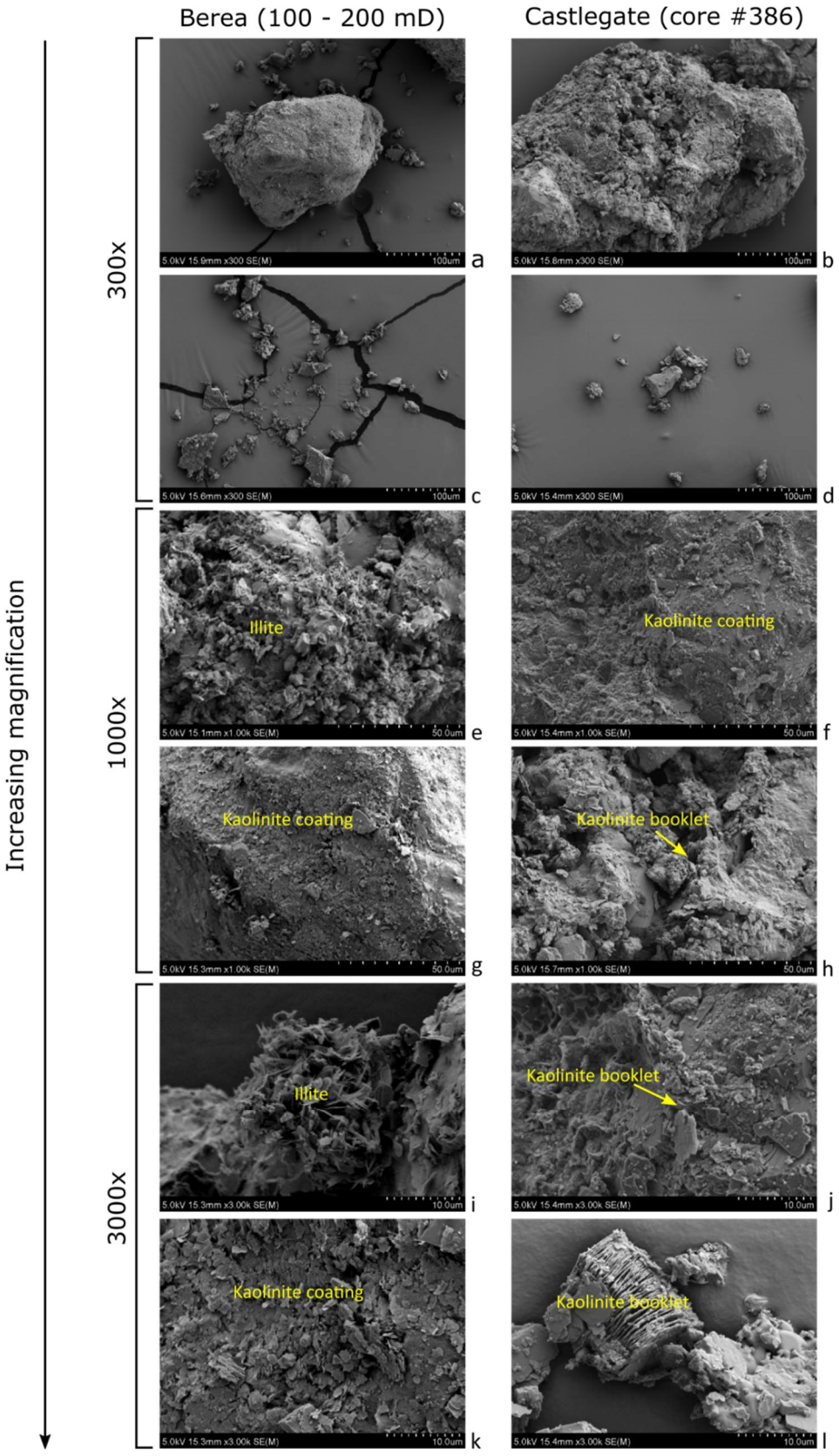

Figure 5-9: Powdered sandstone SEM images. a, c, e, g, i, k: Berea (100-200 mD), b, d, f, h, j, l: Castlegate. a-d : 300 x magnification, e-h: 1000 x magnification, i-l: 3000 x magnification

5.5.2.1 Assessment of Castlegate sandstone for fines removal potential

Visual inspection of the presence or absence of fines clouding the NaCl solution in the centrifuge tube following agitation was carried out; the results are presented in Table 5-8.

Table 5-8: Brine concentrations for Castlegate chips

	Castlegate (core #387)		**Castlegate (core #388)**	
NaCl (ppm)	mass of chip (g)	Fines released?	mass of chip (g)	Fines released?
70000	0.9237	yes	0.9773	yes
35000	1.0175	yes	1.222	yes
17500	0.8898	yes	0.7542	yes
7000	0.6943	yes	0.8304	yes
3500	0.9393	yes	0.9549	yes
1000	0.724	yes	0.8111	yes

It is clear that the Castlegate sandstone readily releases fines even under gentle agitation. However, it is not clear whether the fines represent poorly adhered detrital material, material present as an artefact of the core retrieval process or matrix material, which can break apart easily.

The Castlegate sandstone used in this study was poorly cemented and easily broken. When 99% ultrasonic power was applied using the probe, the sandstone disintegrated within 10 seconds. Even following treatment for 1 minute at 25% power, there was a noticeable change in the surface of the sandstone chip, from smooth cut lines to rough and pitted. There was also a noticeable number of sand grains present in the released fines suggesting that the chip may be breaking apart.

Looking at the images taken of the native Castlegate and chips and fines (the material released following treatment with the ultrasonic probe – in this case a mixture of clay and sand grains due to the poor cementation of the sandstone) following treatment with the ultrasonic probe (Figure 5-10) there is a clear change in the material present on the surface of the grains. In the native Castlegate, kaolinite booklets are readily found throughout the matrix. Kaolinite is known to migrate readily in a traditional fines migration experiment (Sharma et al., 1985), so assessing the clay surface for the presence of absence of kaolinite booklets may give some indication if fines migration is likely to take place. Kaolinite is clearly present in the chips and fines treated with 25% power ultrasound (images h and o), and also on the chip treated with 50% power

ultrasound (image j). No kaolinite is visible on the fines arising from treating the chip with 50% power ultrasound, nor on the fines present after treating the chip with 99% power ultrasound. Sharma et al. (1985) also state that illite is known to migrate during a traditional fines migration experiment. Assessing the SEM images, there appears to be illite present in image k (50% power ultrasound), suggesting that illite may not migrate as readily as kaolinite. Looking at the fines resulting from treatment of the chip with 99% ultrasound (no chip remained after the treatment; it had fully broken down into fines), the grains present in the fines appear clean and smooth, with only occasional finer particles seen on the surface of the grains. These likely resulted from settling during evaporation of the 70,000 ppm NaCl in the sample preparation.

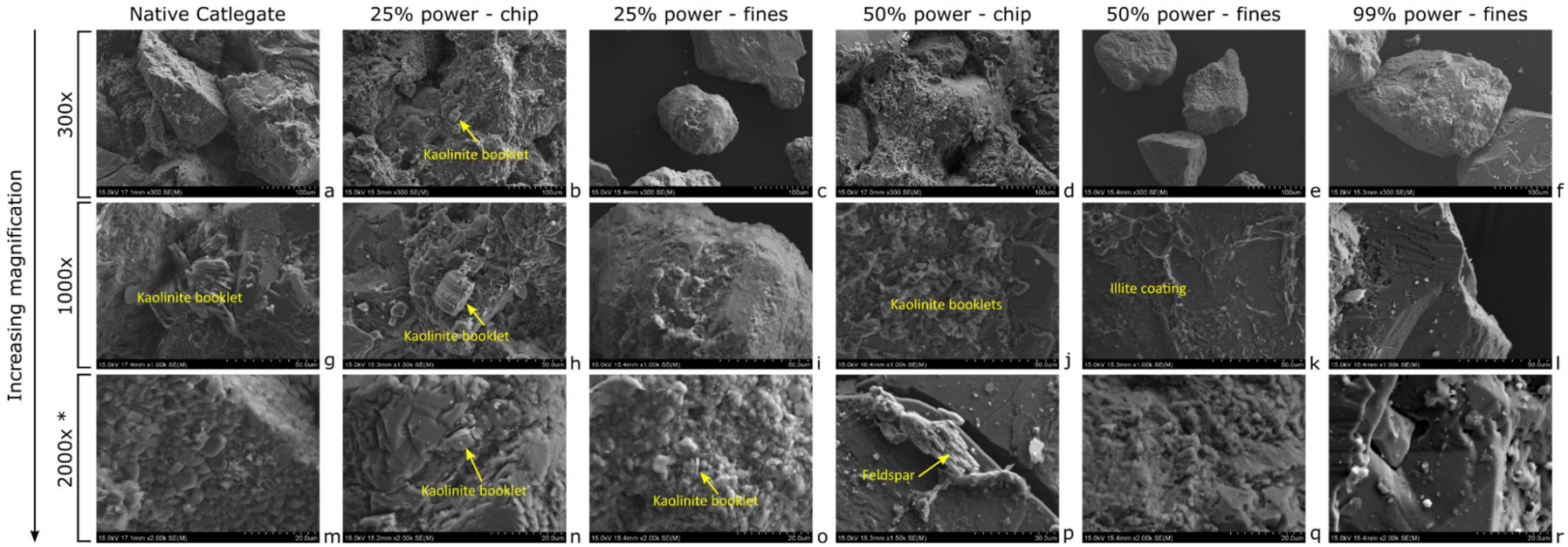

*Figure 5-10: SEM (15 kV, gold coated) images of Castlegate sandstone following ultrasonic treatment in 70,000 ppm NaCl. a-f: 300 x magnification, g-l: 1000 x magnification, m-r: higher magnification2000x magnification. * p: 1500x magnification*

5.5.2.2 Treating sandstone with ultrasonic using single salinity brines

Initially, brines were selected to be significantly above and below the CSC of Berea sandstone. A series of different power and time settings were chosen to look for the energy applied (recorded by the ultrasonic probe) which separated the absorption measured at high and low brine concentration. Further refinement was made by introducing brine concentrations closer to the CSC. Castlegate sandstone was used in both chip and powder form, whereas Berea was used only as chips.

Assessing the data, no combination of ultrasonic power and time settings seemed to repeatedly separate the amount of fines released based on the salinity of the salt solution the chip or powder was placed in. In order to compare the data over the variety of different initial sandstone masses and ultrasonic treatment powers, the absorbances obtained were normalised to absorbance per gram of sandstone per joule of ultrasonic energy applied. The results obtained for Castlegate sandstone chips and powder can be seen in Figure 5-11 and Figure 5-12, and for Berea sandstone chips in Figure 5-13. The CSC has been indicated on the figures – the CSC for Castlegate sandstone has not been measured but based on the results for Berea and the similarities between the sandstones, it is assumed to be of a similar value and therefore to fall between the brine concentrations tested.

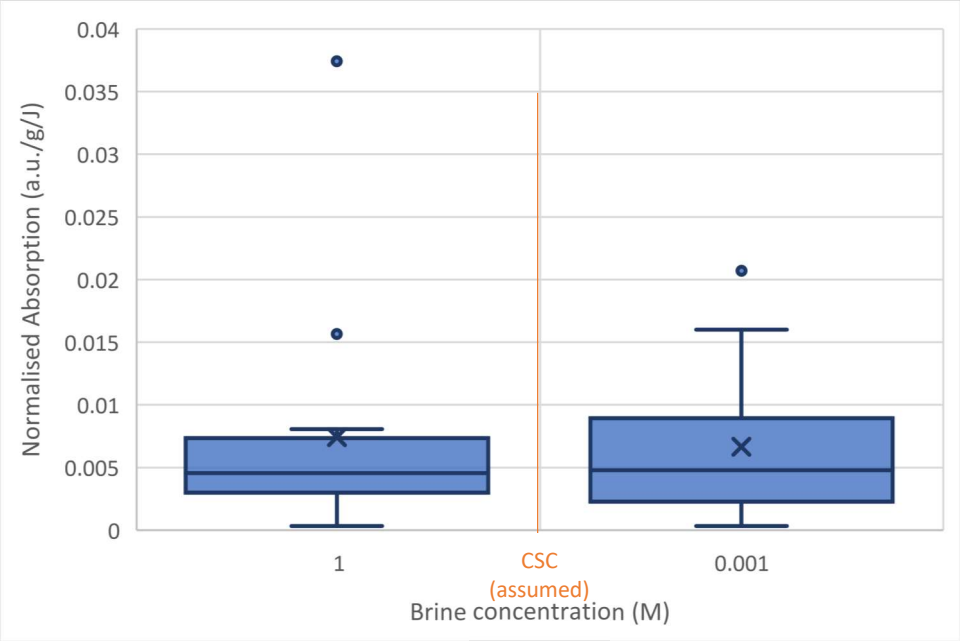

Figure 5-11: Normalised absorbance of solution obtained for Castlegate chips treated with ultrasound in brines of different salinities. Cross point: mean dot points: outliers.

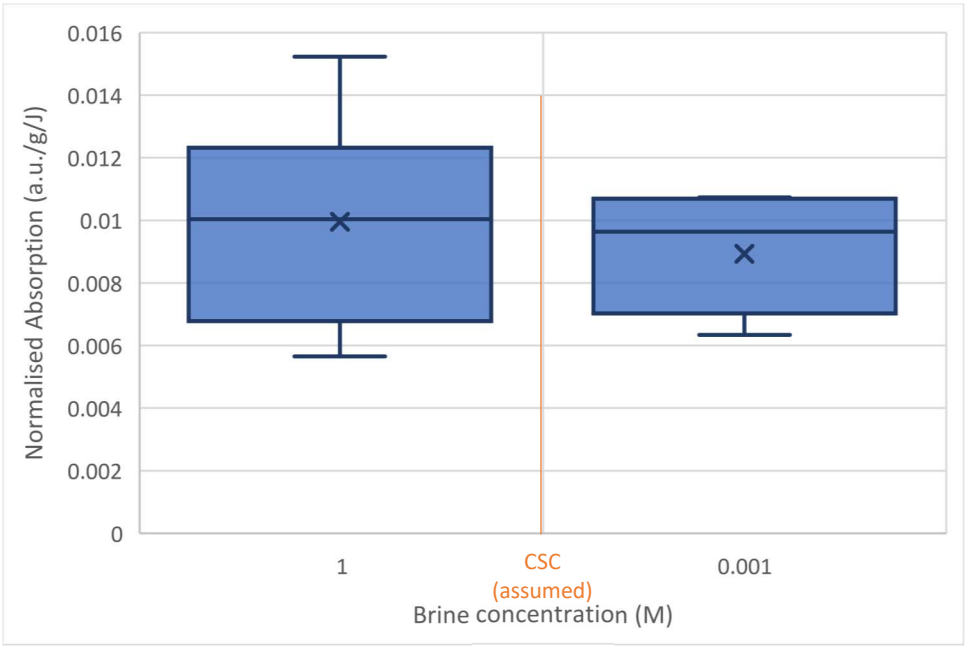

Figure 5-12: Normalised absorbance of solution obtained for Castlegate powder treated with ultrasound in brines of different salinities. Cross point: mean, dot points: outliers.

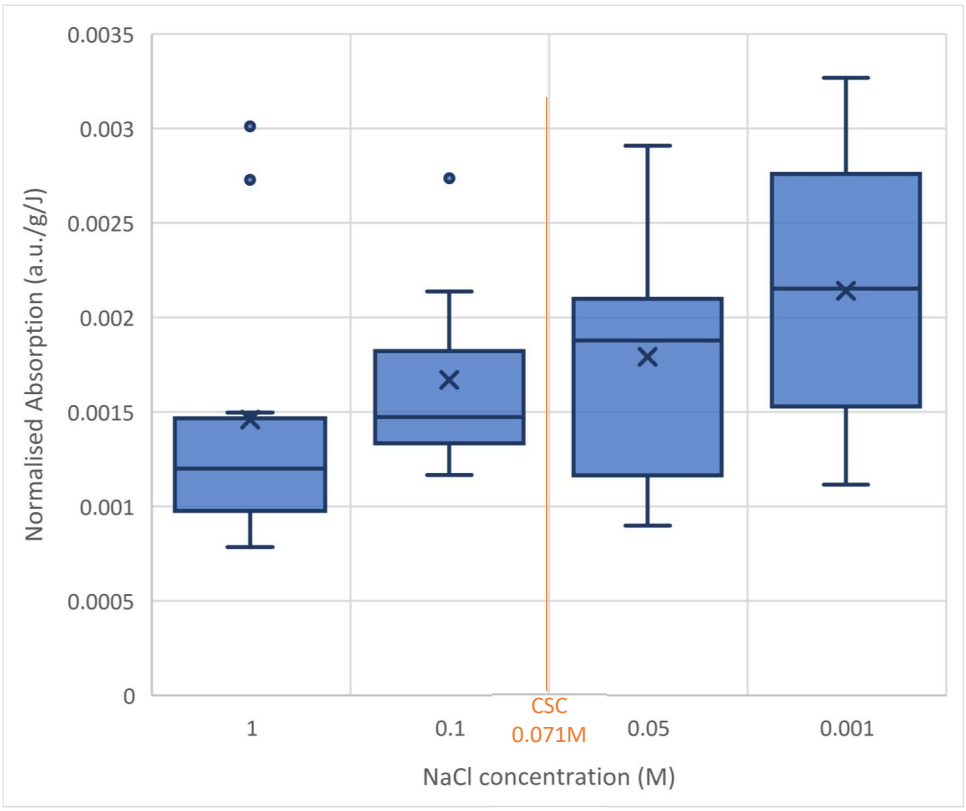

Figure 5-13: Normalised absorbance of solution obtained for Berea chips treated with ultrasound in brines of different salinities Cross point: mean, dot points: outliers.

The results obtained for Berea sandstone suggested that there may be a trend between decreasing concentration leading to increased absorption. However, the overlap between the

results obtained for each concentration cannot confirm this trend. Considering the statistical power of the results, in order to separate the 1 M and 0.001 M results, approximately 50 individual measurements at each concentration would be required. Selecting a power of 39% for 2 minutes, with 2 s on, 3 s off, in a 28 ml vial with 10 ml brine, the following results were obtained:

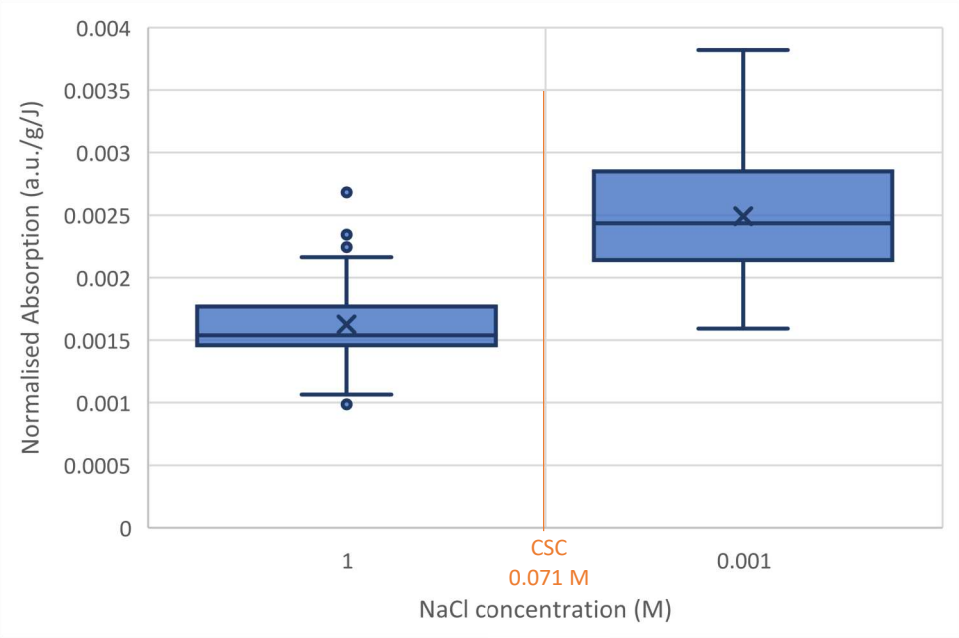

Figure 5-14: Normalised absorbance of solution obtained for Berea chips treated with ultrasound in brines of different salinities (1 M and 0.001 M) - repeats to show statistical significance of separation. Cross point: mean, dot points: outliers.

Repeating the 0.1M NaCl and 0.05M NaCl tests an additional 50 times each in a similar manner did not yield a separation in the absorbances measured (Figure 5-15).

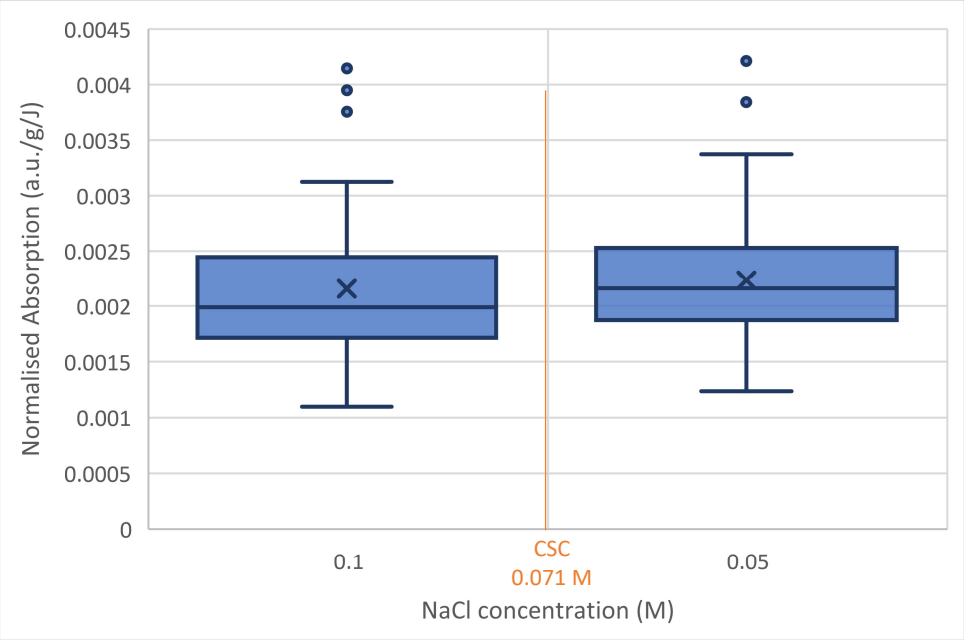

Figure 5-15: Normalised absorbance of solution obtained for Berea chips treated with ultrasound in brines of different salinities (0.1M and 0.05M) - repeats to show statistical significance of separation. Cross point: mean, dot points: outliers.

Looking at the statistical power of the 0.1 M and 0.05 M results (from Figure 5-13), it would be expected that if a separation were to be seen, 20 individual measurements at each salinity should separate the results. As no separation is seen, it can be concluded that this test is not appropriate for refining a CSC to the value obtained by Khilar and Fogler (1984), although it does show that the salinity of the brine may contribute to the effectiveness of sandstone cleaning.

The absorbance data can also be used to calculate the % of fines removed using the calibration curve created. Using the calibration curve, the absorbance data can be converted to a concentration of sandstone which would give the measured absorbance. Dividing this sandstone concentration by the initial sandstone concentration will give the % fines released (Figure 5-16).

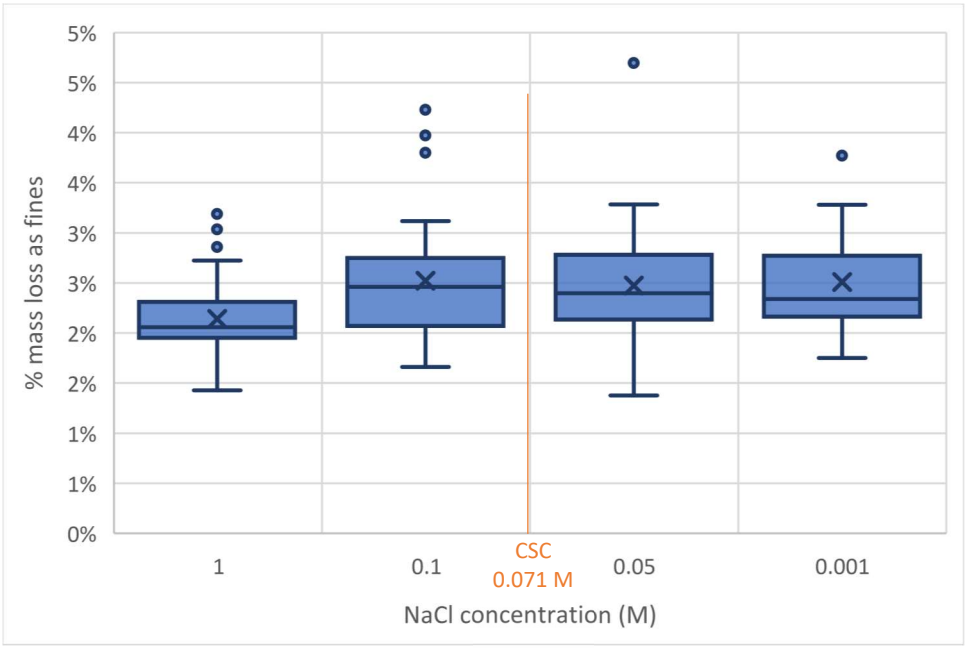

Figure 5-16: Fines released as a percentage of total mass of Berea sandstone chip following ultrasonic treatment – calculated from absorbance data. Cross point: mean, dot points: outliers.

Another method of analysing this data is to look at the mass loss from the sandstone chip. In the case of the 1 M NaCl, it was found that the mass loss due to fines removal was less than the mass increase due to the NaCl, which filled the pores and subsequently crystallised during drying (resulting in a chip with a higher mass after treatment and drying than when initially weighed). The results are shown in Figure 5-17. There appears to be no distinct trend in the change in mass of chips which had been treated in solutions with a concentration of NaCl lower than 1 M either.

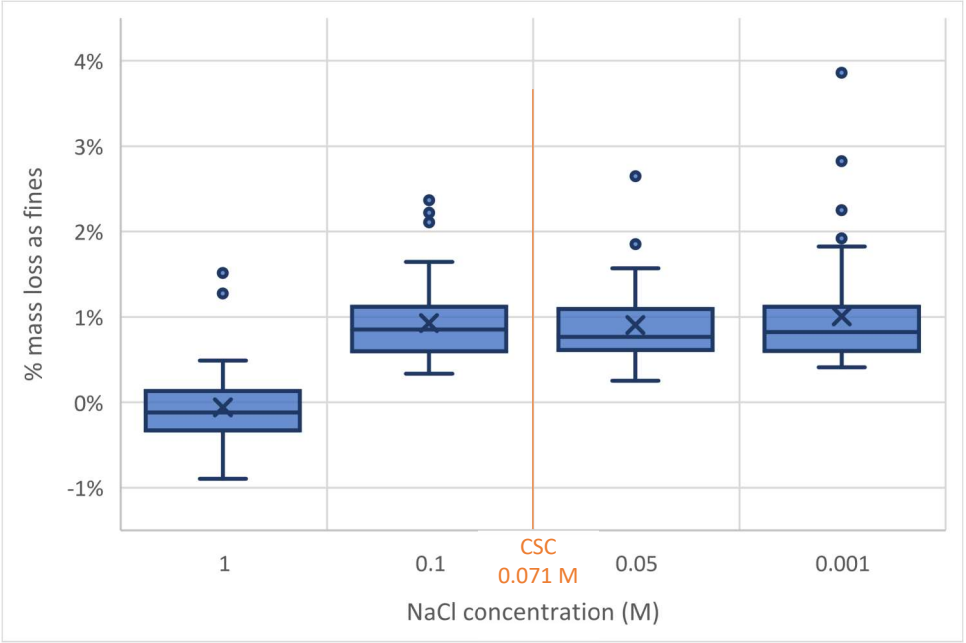

Figure 5-17: Mass change of Berea chip following treatment with ultrasound in solutions with different NaCl concentration. Cross point: mean, dot points: outliers.

The mass of salt that would be left in the pores following evaporation was calculated, using a porosity value of 21.1% (an average of porosities from Kareem et al. (2017)). Plotting the data from the 200 repeat tests shows a slight trend of lower fines released from lower salt concentrations. This is not the expected trend – it is expected that lower salt concentrations (below the CSC of Berea sandstone) should cause the release of a higher percentage of fines.

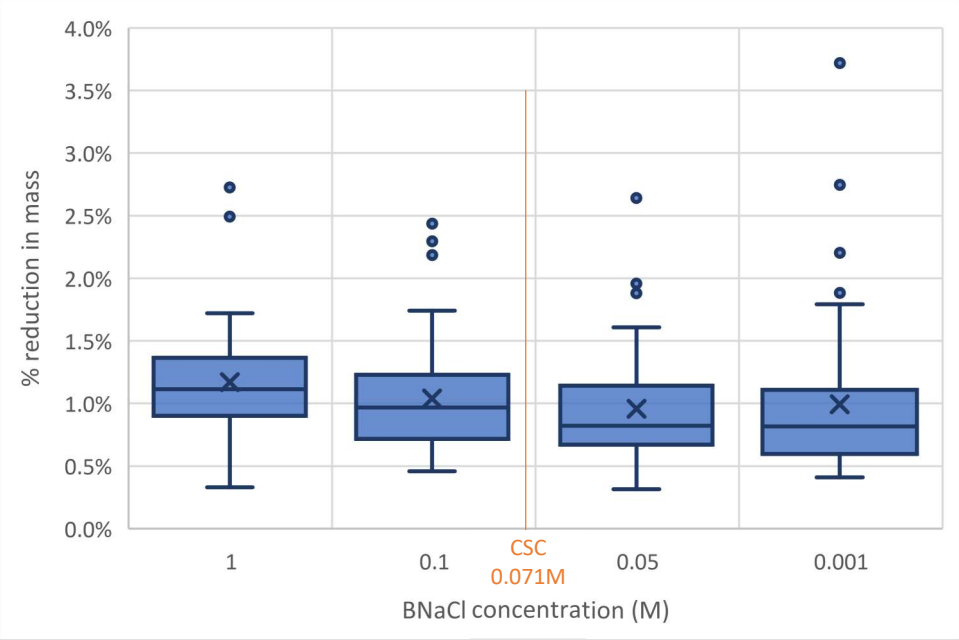

Figure 5-18: % reduction in mass of sandstone chip following ultrasonic treatment in various NaCl concentrations, accounting for mass of salt in pore spaces. Cross point: mean, dot points: outliers.

Figure 5-19 and Figure 5-20 contain the results of the sandstones and lab-made synthetic sandstones treated with ultrasound with sufficient power to completely break apart the sandstone and remove the fines from the sand grain surfaces. Considering Figure 5-19, images j and l show fines, likely kaolinite, still present on the grain surfaces. Comparing this to image r in Figure 5-10, it is clear that the grains have been cleaned more poorly than treatment with ultrasound for 2 minutes at 100% power. A typical treatment for 10 minutes at 2% power would provide 2486 J from the ultrasonic probe to the solution, whereas a typical treatment at 39%, 2 s on 3 s off for 16 minutes total ultrasound treatment time (or 40 minutes total time) provides 2908 J (although the figures may vary from test to test by up to 100 J). It would appear therefore a continuous treatment may provide a more effective cleaning of the sandstone grains than a pulsed treatment, or that a higher power for a shorter time may provide a more effective cleaning. Looking at the fines produced by the Castlegate and Berea following ultrasonic treatment, they appear well dispersed and fairly highly broken.

Comparing the natural Castlegate and Berea sandstone with the synthetic lab-made versions (Figure 5-20), it is clear that there are morphological differences in the sand grains that have been used – the sand grains used in the lab-made version are much more rounded and do not have the covering of kaolinite visible frequently seen on grains from the natural sandstones, which would be expected as this sand is a washed sand so would be expected to appear clean. Indeed, images taken of the sand grains alone show the clean and rounded nature of the grains (Figure 5-21, image a), but also show the presence of smaller broken pieces of quartz (image b). Looking at the whole rock images, Figure 5-20 image j shows the presence of some grain coating similar to that of Figure 5-19 image l, suggesting that during ultrasonic treatment, it may be possible for the fines in solution to bind in some way to the sand grains. This may be promoted by the lower power and pulse settings, as the grains from the fully broken down Castlegate sandstone Figure 5-10) do not show any of this fine grain coating. Looking at the fines, there are obvious kaolinite booklets present Figure 5-20 images i and k), which have not been broken by the ultrasonic treatment. These were not obvious in the images taken of the Castlegate and Berea samples (Figure 5-19).

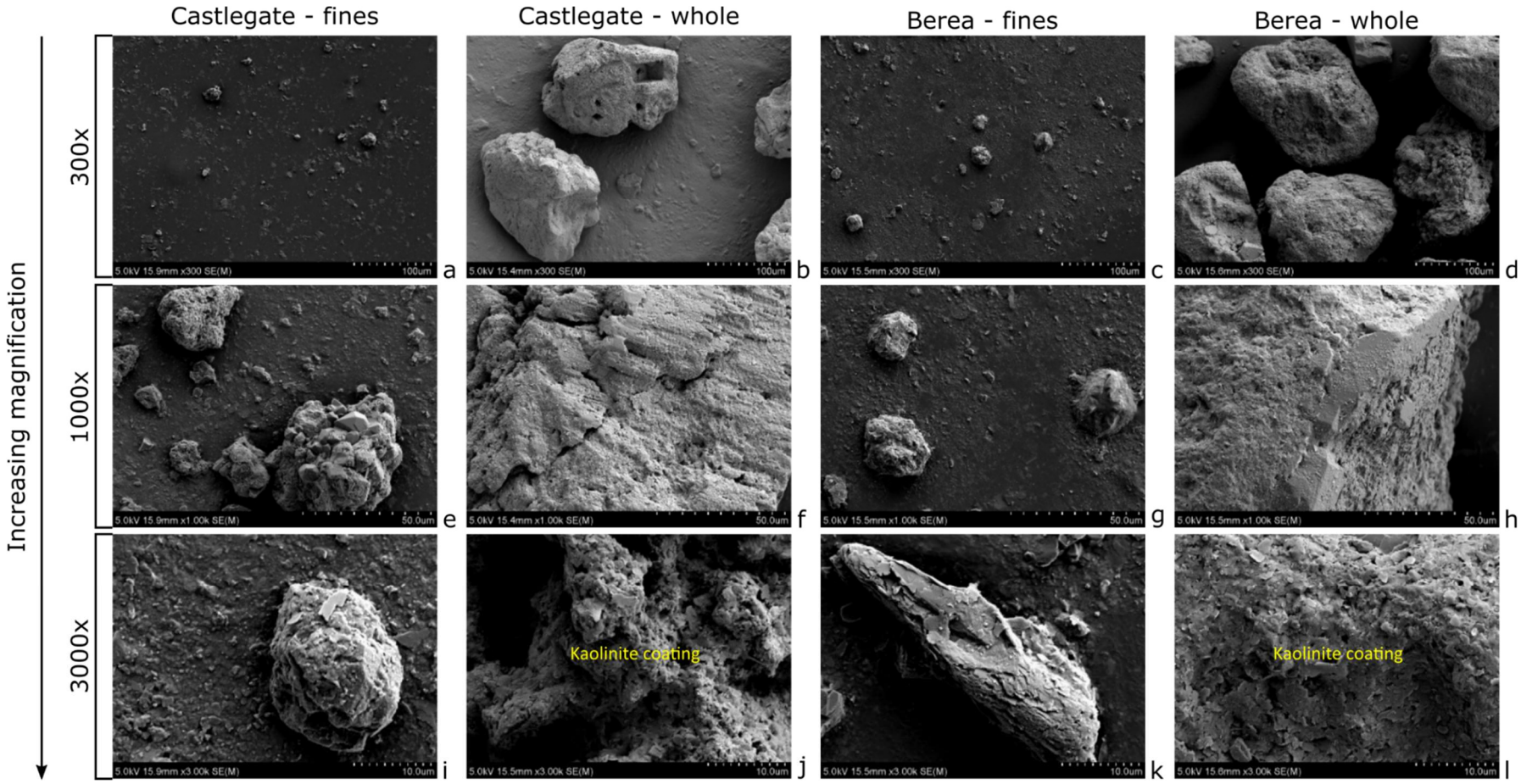

Figure 5-19: Castlegate and Berea sandstones treated with ultrasound to break apart the sandstone and remove the fines from the sand grains. a-d: 300x magnification, e-h: 1000x magnification, i-l: 3000x magnification.

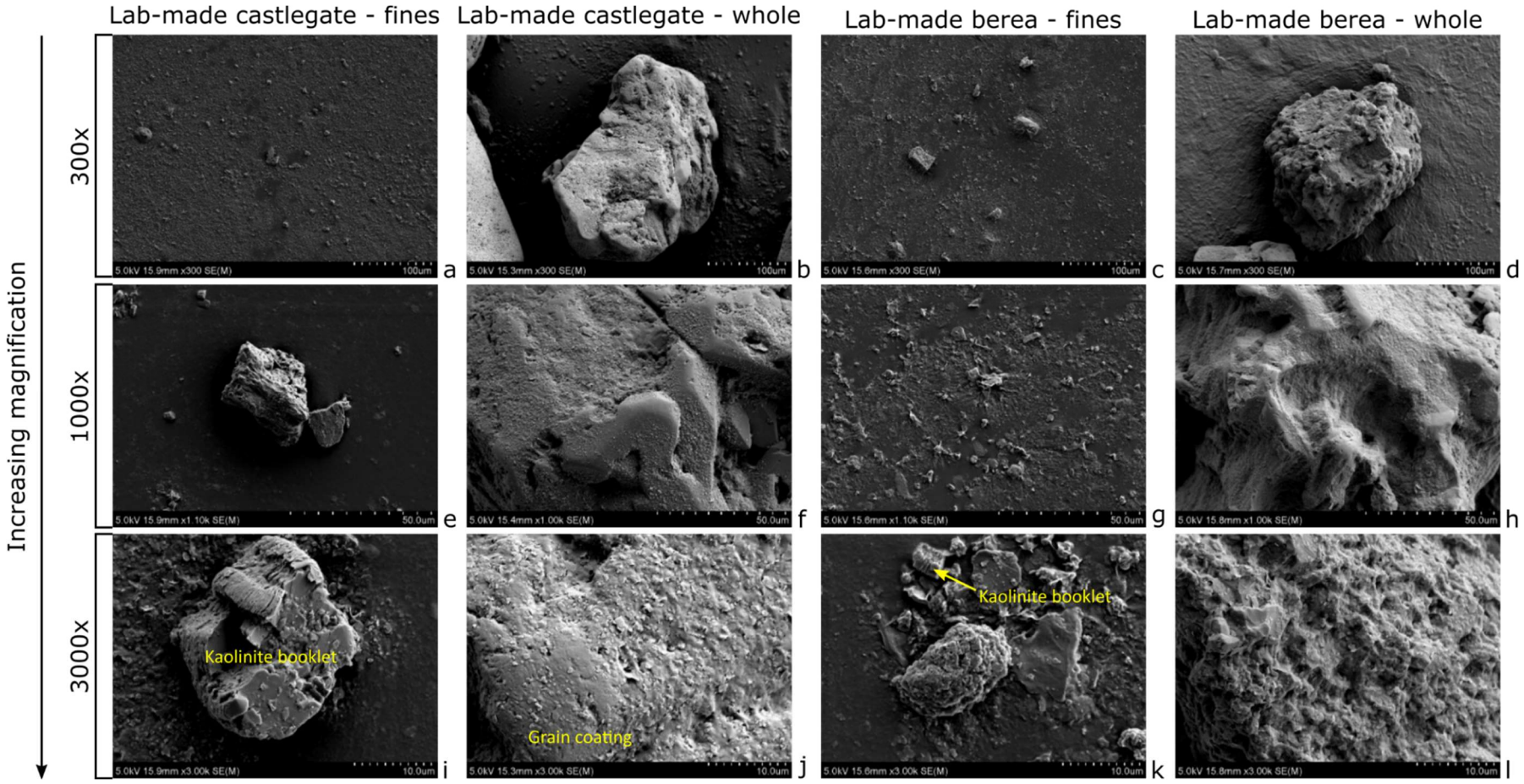

Figure 5-20: Lab-made synthetic Castlegate and Berea treated with ultrasound to break apart the sandstone and remove the fines from the sand grains. a-d: 300x magnification, e-h: 1000x magnification, i-l: 3000x magnification

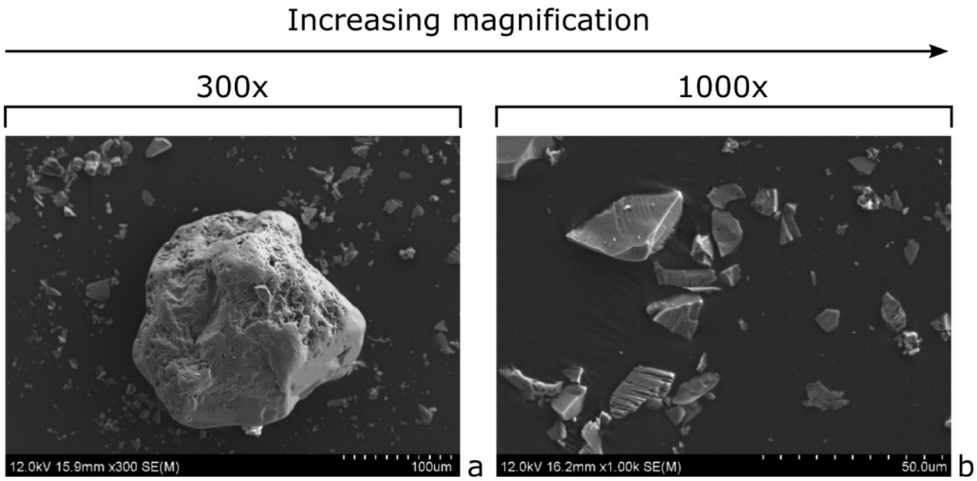

Figure 5-21: SEM images of washed sand used for lab-made synthetic sandstones. a: 300x magnification, b: 1000x magnification.

SEM Images were taken of the fines (the material suspended in the brine) and the inner and outer surfaces of the Berea sandstone chip after treatment in 1 M NaCl (Figure 5-22), 0.05 M NaCl (Figure 5-23) and 0.001 M NaCl (Figure 5-24). Firstly, comparing the fines present on the chip outer surface with the chip inner surface for the 1 M NaCl (Figure 5-22, images b, c, e, f, h and i) it is clear that there are fines present on both the outer and inner surfaces. In addition to the grain coating fines similar to those seen in Figure 5-19 image l, there is a considerable coating of larger platey fines seen in Figure 5-22 image i. These were not seen on the chips that had been completely broken down by ultrasound, suggesting these may be more likely to be disrupted by ultrasound, but require more time in order to become detached. There seems to be some indication of fines similar to these in Figure 5-23 image g, further suggesting that full detachment of these fines may be more time dependant. Considering now the inner and outer chip surface for the Berea chips treated in 0.05M NaCl, a greater difference is seen between the fines present on the outer and inner surface (Figure 5-23 images b, c, e, f, h and i). There are clear kaolinite booklets seen in image e, on the inner surface, but no evidence of such fines on the outer surface. A similar pattern is seen in Figure 5-24, where the outer surfaces on the chip have noticeably less fines present on the outer surface than the inner surface. It is interesting to note the visible kaolinite booklets in Figure 5-24 image i. These look to have been covered by an additional coating, which may have protected the clay minerals from being disrupted during ultrasonic treatment, providing an explanation for their continued presence on the outer surface. Comparing the chip which had been treated in the 1 M NaCl (above the CSC for Berea) with those treated in 0.05 M and 0.001 M (below the CSC), a difference can be seen in the fines present on the outer surface of the chip. It appears that the 1 M NaCl brine had a somewhat

protective effect, meaning that more fines were present on the outer surface of the chip following treatment than in the brines below the CSC.

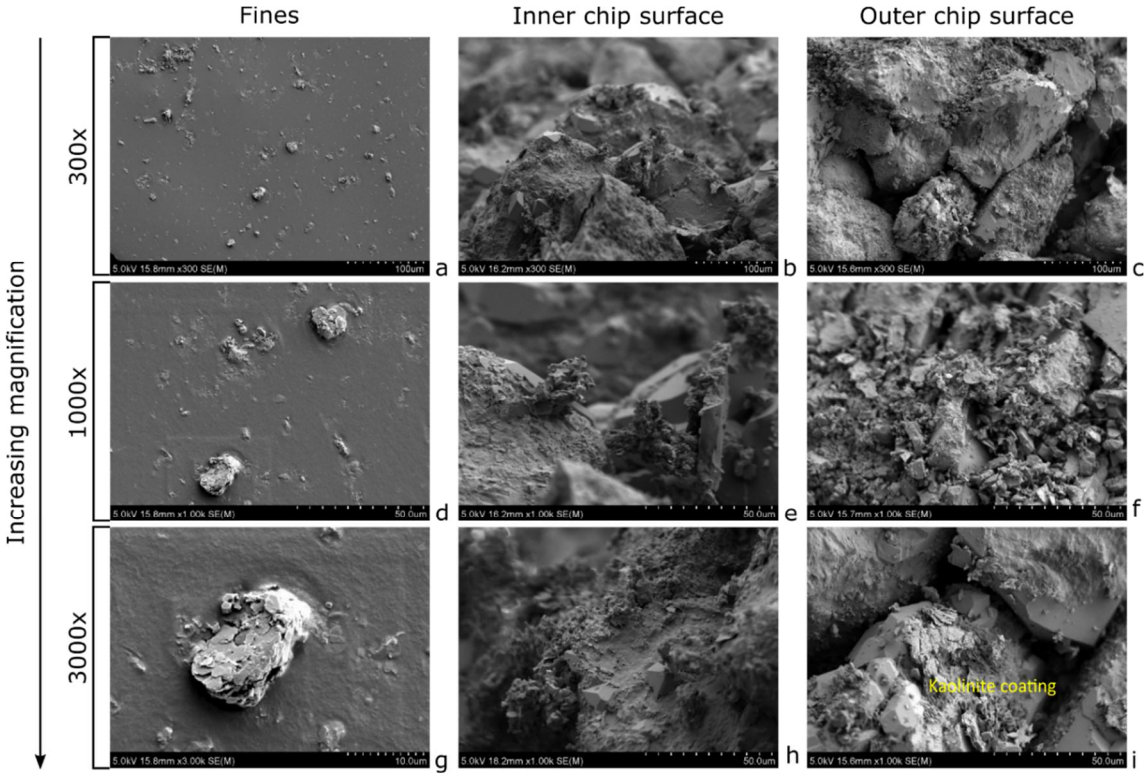

Figure 5-22: Berea chip treated with ultrasound (2s on 3s off, 2 minutes, 39%) in 1M NaCl (above CSC). a-c: 300x magnification, d-f,h,i: 1000x magnification, g: 3000x magnification

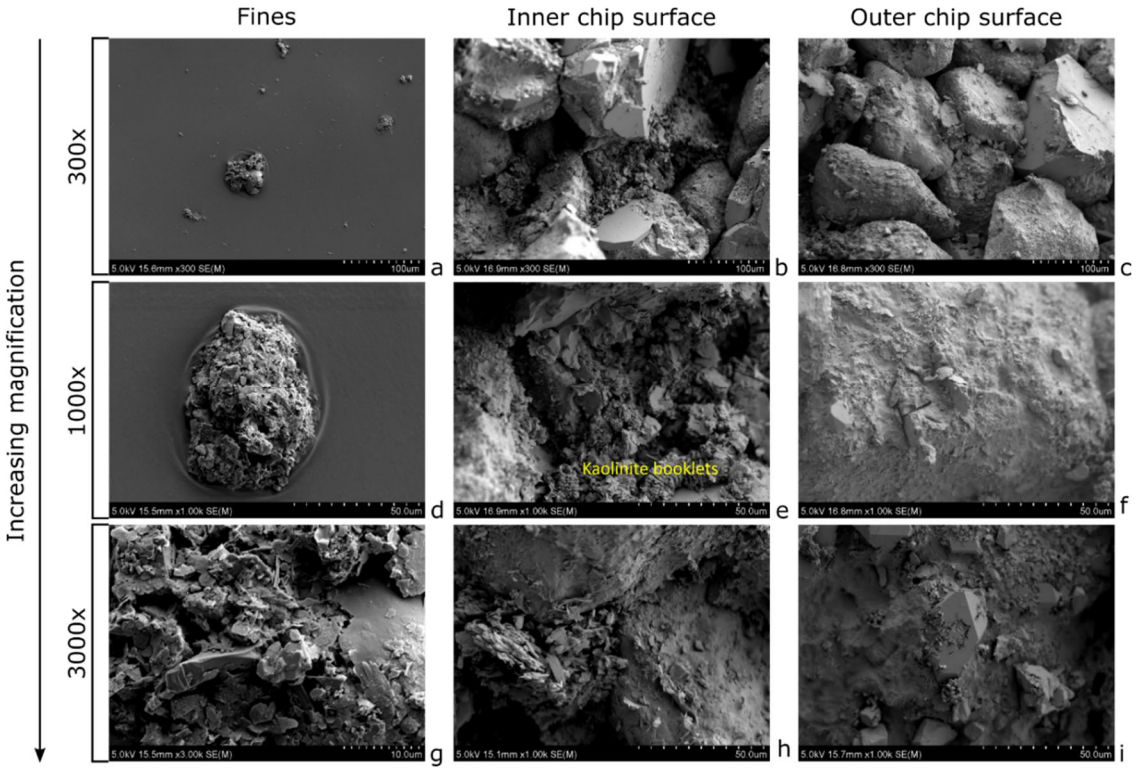

Figure 5-23: Berea chip treated with ultrasound (2s on 3s off, 2 minutes, 39%) in 0.05M NaCl (below CSC). a-c: 300x magnification, d-f,h,i: 1000x magnification, g: 3000x magnification

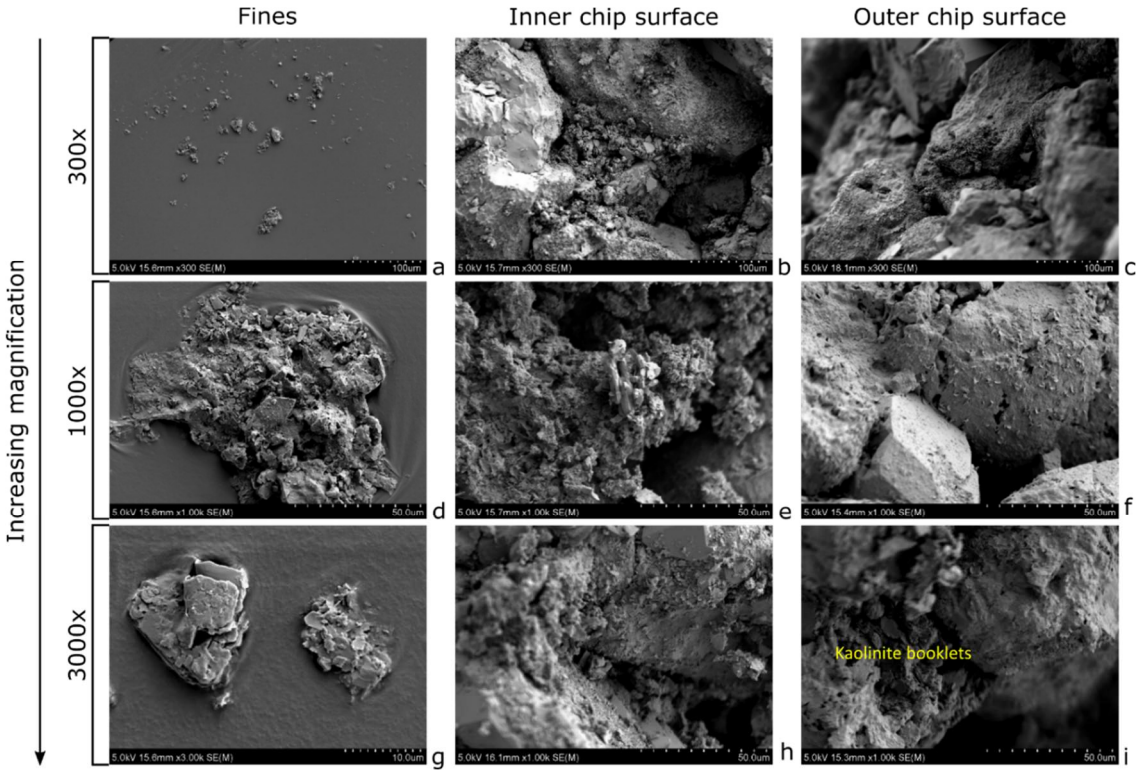

Figure 5-24: Berea chip treated with ultrasound (2 s on 3 s off, 2 minutes, 39%) in 0.001M NaCl (well below CSC). a-c: 300x magnification, d-f,h,i: 1000x magnification, g: 3000x magnification

5.5.2.3 Treating sandstone with ultrasonic using serial change of salinity

In order to attempt to replicate the results of Khilar and Fogler (1984) where a critical salt concentration of below 4125 ± 125 ppm Na^+ was identified by the flowing of a series of brines through Berea cores, a similar series of brines were selected and a single rock chip was treated repeatedly with the ultrasonic probe. Two separate series of brines were used. The first used a reduced number of brines (Table 5-9); the results are shown in Figure 5-25 and Figure 5-26.

Table 5-9: Reduced brine treatments

Treatment number	Serial Concentrations	Same Concentration
1	30,000 ppm NaCl	30,000 ppm NaCl
2	5,000 ppm NaCl	30,000 ppm NaCl
3	4,000 ppm NaCl	30,000 ppm NaCl

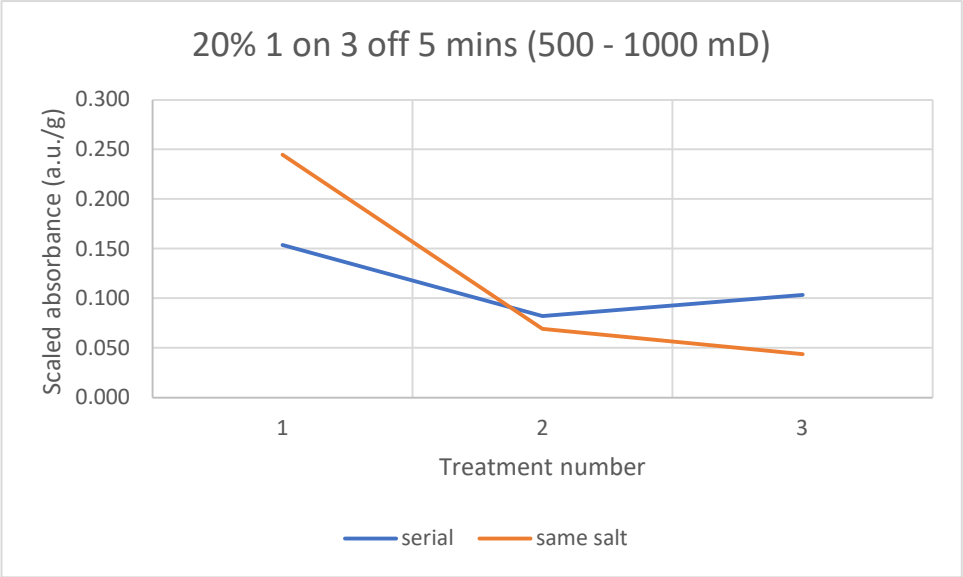

Figure 5-25: Serial brine treatments. 500-1000 mD Berea, 20% power, 1 s on 3 s off, 10 minutes

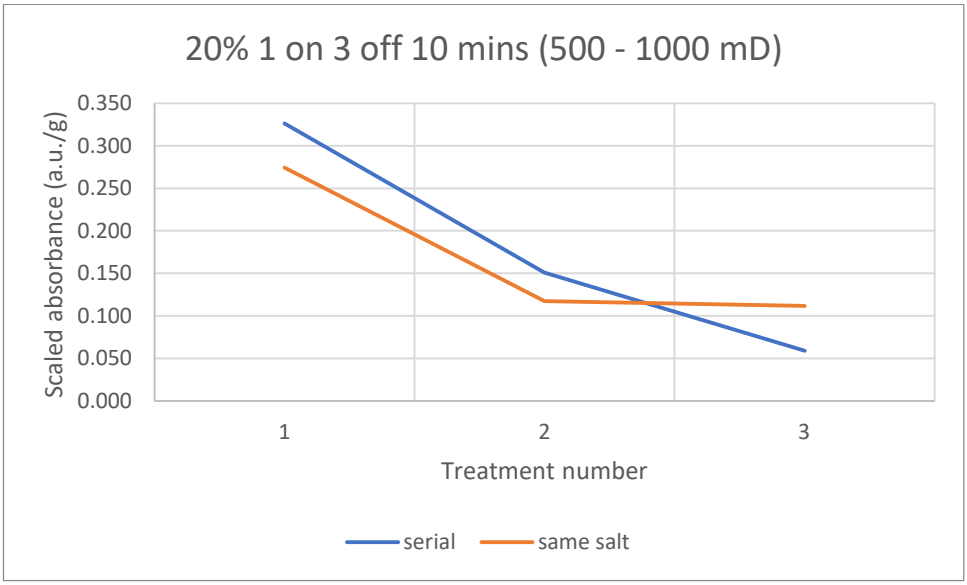

Figure 5-26: Serial brine treatments. 500-1000 mD Berea, 20% power, 1 s on 3 s off, 5 minutes

Based on the results of Khilar and Fogler (1984) for this brine series it would be expected that there would be an enhancement in the release of fines (and hence absorbance) at the third treatment for the serial salt test compared to the same salt test, as this concentration is below the CSC. This is seen in Figure 5-26, but the opposite is seen in Figure 5-25. The fact that these single tests do not show a conclusive trend suggests that a statistical approach similar to that of the individual salinity tests may be more appropriate.

The second used a series of brines replicating the experiment of Khilar and Fogler (1984) (Table 5-10).

Table 5-10: Full series of brine treatments

Treatment number	Serial Concentrations	Same Concentration
1	30,000 ppm NaCl	30,000 ppm NaCl
2	10,000 ppm NaCl	30,000 ppm NaCl
3	5,000 ppm NaCl	30,000 ppm NaCl
4	4,500 ppm NaCl	30,000 ppm NaCl
5	4,250 ppm NaCl	30,000 ppm NaCl
6	4,000 ppm NaCl	30,000 ppm NaCl

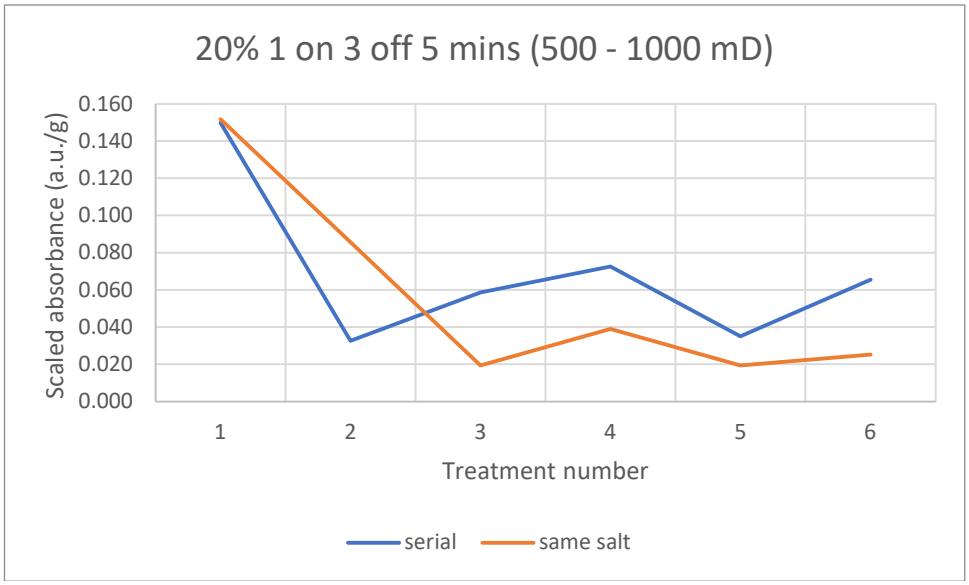

Figure 5-27: Serial brine treatments. 500-1000mD Berea, 20% power, 1s on 3s off, 5 minutes

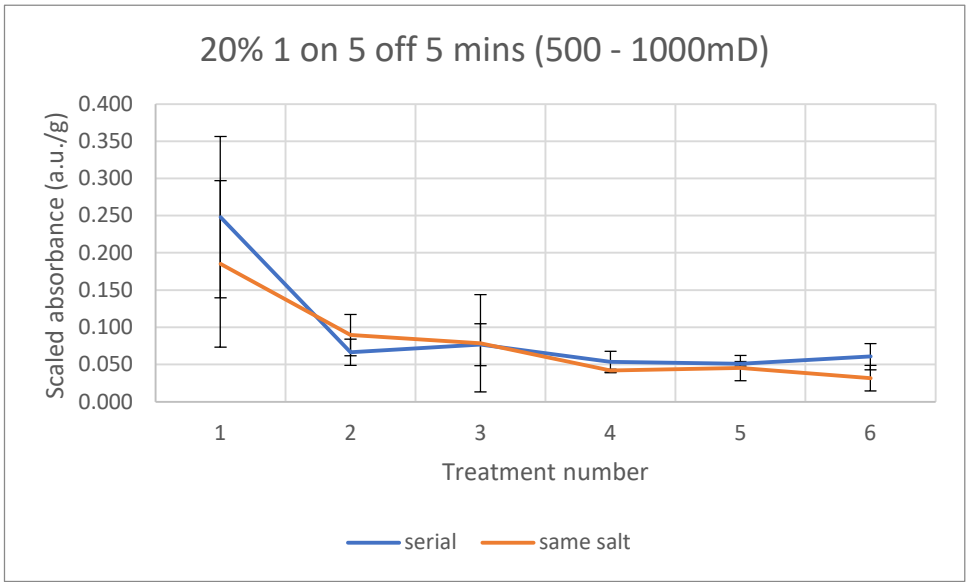

Figure 5-28: Serial brine treatments. 500-1000mD Berea, 20% power, 1s on 5s off, 5 minutes

If these results were to replicate the results reported by Khilar and Fogler (1984), the absorbance would be expected to increase in the serial salt test relative to the same salt test at 4,250 - 4,000 ppm. Figure 5-27 shows an enhancement at 5,000 ppm and below, whereas Figure 5-28 only shows an enhancement at 4,000 ppm. Again, it would appear that a statistical approach might show whether a trend exists or not.

5.5.2.4 Overall discussion

The precise mechanism by which the fines migrate out of the rock chip into the free solution is not currently known. In general, particles will become detached by the pressure waves produced by the implosion of the cavitation bubbles which form preferentially on surfaces (Fuchs, 2015) due to the reduced strength of the bond between the surface of the particle and the liquid. During cavitation, if the bubble is close to a solid surface, the energy of the implosion will be directed towards the surface, and hence if it is close the boundary of a fine particle and the surface which it is adhered to, the energy would be directed towards the join promoting particle detachment (Brennen, 1995). The energy involved in such implosion events is greater than the energy required for particle detachment (Brennen, 1995, Rosenbrand et al., 2015) so it is assumed that the application of ultrasound will mobilise the fines, and indeed this is seen in the experiments undertaken and in previous work. Once a particle becomes detached but is still present in the pores of the sandstone, in the absence of further ultrasound treatment it is likely to reattach to the side of the pore, either simply due to gravity settling or in the case of 1 M NaCl, due to the attractive interaction energy between the fines and the grain surfaces (Rosenbrand et al., 2015). In this case, it is unlikely that the strength of the interaction between the fine particle and the pore surface is as great as the original interaction, due in part to the heterogenous nature of the pore surface and the non-uniform geometry. This process is illustrated in Figure 5-29.

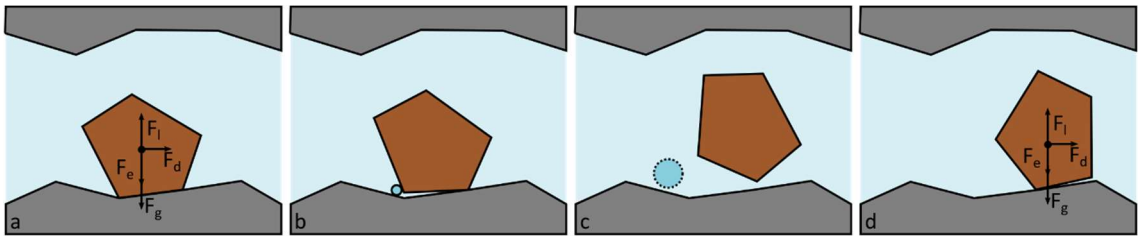

Figure 5-29: Force balance and particle detachment during ultrasonic cavitation. a - initial particle force balance, b - formation of cavitation bubble at particle/pore surface junction, c - implosion of bubble causing particle movement, d - re-attachment of particle to pore surface with lower F_e.Force balance from Bedrikovetsky and Caruso (2014)

However, if ultrasound is then reapplied, the fine particle will likely become detached again and move again in the pore. It is known that application of ultrasound to a fluid saturated porous medium will cause flow in the pore system (Aarts et al., 1998), and has been recorded as up to 7 mm/s for a 0.15 mm capillary, or 0.3 mm/s for oil flow in a soft sandstone. It would appear then that the flow velocity possible in the pore system of a Berea sandstone provided solely by the application of ultrasound could be greater than the critical flow velocity (the velocity below which fines migration will not happen) which has been reported as 0.007 cm/s (0.07 mm/s) by Gabriel and Inamdar (1983) for 2% KCl and fresh water. Khilar and Fogler (1984) however do not report a critical flow velocity for NaCl solutions in Berea sandstone, only that flow was required at 3.4 cm/hr – 570 cm/hr (0.01 mm/s – 1.5 mm/s), suggesting that any flow set up by the ultrasonic treatment will contribute to fines migration.

5.6 Conclusions

1. NaCl, $CaCl_2$, Kaolinite (KGa-1b), Illite (IMt-1) and Illite-smectite mixed layer (ISCz-1) do not show any absorbance or fluorescence peaks between 320 nm and 1000 nm.
2. Absorbance measurements will give an indication of the removal of fines from a rock chip following ultrasonic treatment. Using a calibration curve of serial dilutions of sandstone vs absorbance will allow the mass of fines removed to be calculated, and hence the % removal of fines from the rock. This method produces better results than a simple mass difference as the salt remaining in the sandstone pores following treatment with 1 M brine causes an increase in the chip mass after drying and the mass of salt cannot be calculated from the pore volume.
3. Sandstones treated with an ultrasonic probe or bath will behave differently depending on how much ultrasonic power is applied and for how much time the treatment is applied for. Castlegate sandstone is poorly cemented and will break apart much more readily than Berea sandstone, but both sandstones will be completely broken down after approximately 2500 J applied by the ultrasonic probe. This process removes the majority of the grain coating fines, although some still appear attached. Kaolinite fines become detached and removed during this process.
4. Treating Berea sandstone with ultrasonic in 1 M NaCl vs 0.1 M NaCl, 0.05 M NaCl or 0.001 M NaCl results in the % of fines released increasing from an average of 2.2% in 1 M NaCl to 3% in the lower concentration NaCl. The reduction in fines is seen more on the inside of the chip than the outer chip surface.

5. Treating a single Berea chip with a series of brines with reducing concentration may show an enhancement of fines removal at NaCl concentrations lower than the CSC. However, the prolonged application of ultrasound to the Berea chip causes progressively more fines to be removed with every treatment, which may not only be removing fines which would normally migrate during a traditional fines migration experiment. As shown in in the single brine treatment experiments, prolonged exposure to ultrasound can cause disintegration of the rock chip so unless a significantly lower power ultrasonic transducer can be used, this method is not likely to yield results replicating a traditional fines migration experiment.

Chapter 6 Monitoring Particle Flow on Surfaces and in 3D prints

6.1 Background

It is thought that fines migration may be problematic during low salinity (< 5000 ppm) EOR (enhanced oil recovery) operations (Vaidya and Fogler, 1990, Katende and Sagala, 2019) as the lower salinities and relatively high velocities (Bedrikovetsky and Caruso, 2014) near the injection well may promote fines detachment and migration (Jones, 1964, Mungan, 1965, Gray and Rex, 1966, Gruesbeck and Collins, 1982, Gabriel and Inamdar, 1983, Khilar and Fogler, 1984, Sharma et al., 1985, Khilar and Fogler, 1987b, Valdya and Fogler, 1992, Ochi and Vernoux, 1998, Schembre and Kovscek, 2004, Howard et al., 2012), discussed in detail in Section 2.2.

Fines migration may be defined as the movement of small particles that exist within the formation, or that may have been introduced during drilling operations (Bennion, 1999, Faergestad, 2016). The fines are typically less than 2 µm (Sharma et al., 1985), and move in the pore spaces during a fluid flow operation. Of interest here is the movement of fines, native to a sandstone, moving in the sandstone pores during a fluid injection operation, particularly when the injected brine is of a lower salinity than the brine found naturally in the sandstone.

It has been shown many times that fines migration may occur in a sandstone during a fluid injection operation when the salinity of the fluids injected is lower than the salinity of the pore fluids (Johnston and Beeson, 1945, Gray and Rex, 1966, Jones, 1964, Mungan, 1965, Khilar and Fogler, 1984, Ochi and Vernoux, 1998, Schembre and Kovscek, 2004, Morrow and Buckley, 2011), as long as the fluids are injected with sufficient velocity to cause movement (Gruesbeck and Collins, 1982, Gabriel and Inamdar, 1983, Sharma et al., 1985, Khilar and Fogler, 1987b, Howard et al., 2012). A critical salt concentration for Berea sandstone, above which fines migration will not take place, has been obtained experimentally by Khilar and Fogler (1984) and modelled for other systems by Schembre and Kovscek (2004); it is generally in the region of 5000 ppm, similar to the upper limit of salinity of injected fluids during a low salinity EOR operation (Morrow and Buckley, 2011). These conditions are generally most likely to be met in the first 30 cm or so from the injection well (Gruesbeck and Collins (1982), and hence this area is most at risk from formation damage due to fines migration (Bennion, 1999, Clegg, 2007).

Sandstones are comprised of several different minerals. Generally the matrix grains of a sandstone will be composed of quartz particles, along with other minerals such as feldspars, bound together with a quartz cement with clays coating the pore spaces (Churcher et al., 1991, Kareem, 2016). The clays lining the pore spaces may not be tightly bound to the surface of the pores, and if conditions occur where the fluid flowing past the clays has a velocity higher than the critical velocity, and a salt concentration higher than the critical salt concentration, the clay particles are likely to detach and move in the pore spaces.

It is assumed that the clay particles will move in the pore spaces until there is a form of mechanical trapping, causing the particle to stop moving (Khilar and Fogler, 1983, Han et al., 2020). It is also assumed that the pore surface may be rough, but the chemistry of the pore surface in unimportant. This work aims to investigate whether a change in chemistry of the pore surface, causing a change in wettability, will influence the movement of fine particles.

The wettability of a surface may be defined as "…the tendency of one fluid to spread on or adhere to a solid surface in the presence of other immiscible fluids." (Craig, 1971). A convenient quantitative measurement of this statement comes from looking at the contact angle a droplet of fluid makes on the surface, most commonly a drop of distilled water in air. Surfaces may then be classified as follows:

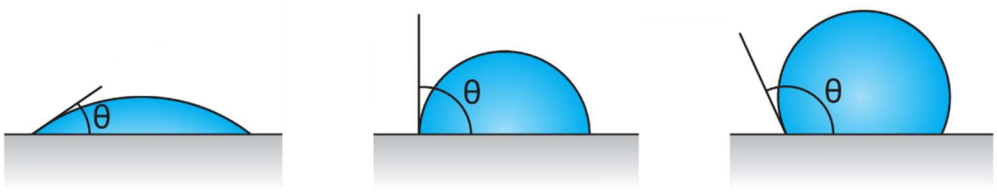

Figure 6-1: Illustration of contact angles vs surface wettability. Left to right: water-wet, neutral-wet, oil-wet.

In a sandstone, there are several minerals exposed in the pore. In general, the minerals will have similar wettabilities (usually 0 - 50°, strongly water wet), but differences will exist. For example, in Berea sandstone, the minerals present, and their wettabilities, are shown in Table 6-1. Note the hydrophobicity of chlorite, one of the few naturally hydrophobic minerals.

Table 6-1: Wettability of different minerals present in Berea sandstone

Mineral	**Berea (wt %)** [a]	**Wettability**
Quartz	83.6	0 – 54° (Jańczuk et al., 1986) 26.8° (Janczuk and Zdziennicka, 1994) 41.0° – 53.8° (Suzuki et al., 2007)

Feldspar	4.4	28.9° ± 4.8° and 28.0° ± 3.7° (different cleavage planes) (Rao et al., 2021) 45° ± 2° (Han et al., 2020) 26.8° - 38.6° (Deng et al., 2018)
Dolomite	1.1	51.7° ± 0.8° (Wu et al., 1996) 6.6° ± 0.7° (Gence, 2006) 36° - 53° (Wang and Zhang, 2020)
Kaolinite	4.4	75° (Borysenko et al., 2009) 17.5° (Jańczuk et al., 1989) 46.1° (KGa-1b), 42.0° (KGa-2) (Wu, 2001) 27.8° ± 0.4° (KGa-1b) (Shang et al., 2008) 5° - 20° (pH dependant) (Hu et al., 2003)
Illite	1.9	43.3° ± 1.4° (Shang et al., 2008) 10° - 20° (Hu et al., 2003)
Chlorite	1	114.6° (Yin et al., 2017)
Illite-Smectite	1.8	Not reported.
Calcite	1.6	55.6° ± 1.8° (Wu et al., 1996)

It should be noted that wettability measurement requires the surface to be homogeneous, smooth, inert, insoluble, non-reactive, non-porous and non-deformable (Chau, 2009). A sandstone pore surface, or sandstone surface, will not fulfil all of these criteria, so a measurement of contact angle on this surface will be merely a measure of contact angle of the droplet on that particular part of that particular sandstone surface, and should not be generalised to the whole sandstone. A model with controlled wettability variation is therefore needed to look at if, and how, wettability influences fine particle movement. The results from this model may then give some insight into how particles move across surfaces where the wettability varies.

In their natural buried state, sandstones are not dry, in comparison with the laboratory outcrop samples which may be received dry. Instead, the sandstone pores are full of a brine (often termed formation water), which tends to be high salinity (Bazin et al., 1994, Robertson, 2007, Aghaeifar et al., 2015, Katende and Sagala, 2019). During an injection operation, the salinity of the injected fluid tends to be lower, often either fresh water or a <5,000 ppm brine. This

presence of this low salinity brine flowing in the pores is likely to promote the detachment of fine particles and hence carry the fine particles in the low salinity brine as it moves through the higher salinity pore structure. This contrast in salinity also needs to be modelled with a suitable experimental setup in order to analyse the effect of the particle movement and brine salinity contrast.

The simplest way of introducing a suspension of fines into another fluid is to drip the suspension in a single drop at a time. The shape that a drop makes when introduced into another fluid has been the subject of many studies previously. Thomson and Newall (1886) first described and illustrated the underwater ring shapes that drops of ink make when introduced into water, termed vortex rings. Their work goes on to discuss the importance of the liquids being miscible when the droplets are introduced, and that the viscosity of the liquids will play a part in how the drop liquid behaves when dropped into the bulk liquid. A description is not given though of the shape of the splash that the drop makes when it enters the water. Worthington (1895) however described, photographed and illustrated the effect at the liquid surface of drops of various liquids, notably a milk and water mixture, falling into a deep container of the same liquid, or in some cases onto a flat surface and spreading. No comment is made as to the mechanism of the formation of the shapes seen, merely the description of them and the experiments which lead to their formation. One such illustration (in this case, an engraving of a photograph) is shown in Figure 6-2.

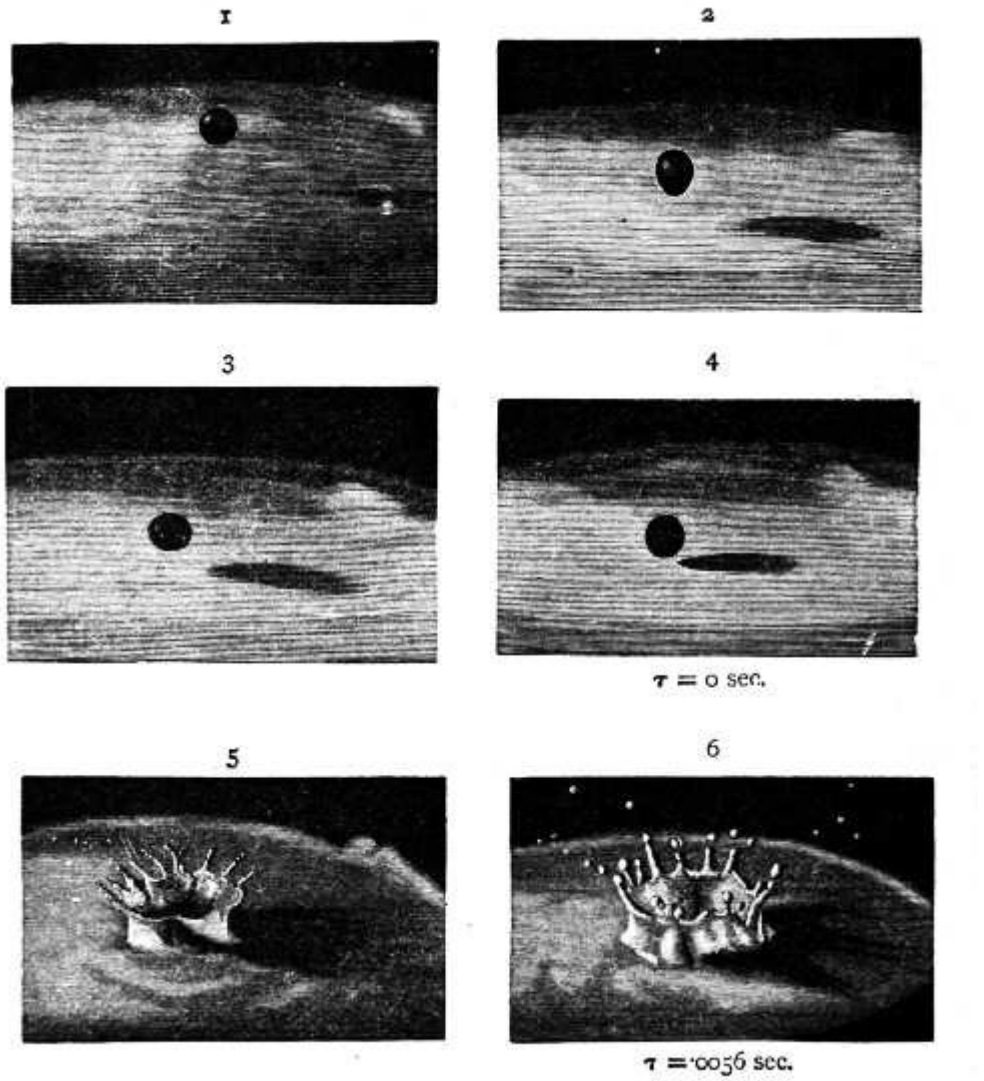

Figure 6-2: Engravings of Instantaneous Photographs of the Splash of a Drop of Water falling 40 cm into Milk. From Worthington (1895).

The effects of a droplet falling into a shallow container of liquid are however different than falling into a bulk container. The hard surface beneath the drop starts to have an effect on the shapes formed. Hobbs and Osheroff (1967) describe the effects on the surface of the liquid when droplets of milk are dripped into shallow dishes of water. The description is concentrated on the height of the ejected Rayleigh jet and in the crown, and considers the effect of the vortex ring produced by the droplet on the height of the Rayleigh jet and crown breakup. Consideration is not however given to the top-down spread of the droplet. Yu and Hopkins (2018) expand on this by dropping droplets of water with a 2 mm or 4.5 mm diameter into water with a depth ranging from 0 mm to 10 mm at various velocities up to terminal velocity, and measuring the force

produced by the impact. Empirical models were developed to describe the force, as complications of the system did not give good agreement with existing prediction models.

The shape of drops as they hit surfaces of variable roughness or wettability has been the subject of more recent study. For fluids hitting dry surfaces of variable wettability, de Goede et al. (2018) show that the impact velocity beyond which a drop will splash and cause smaller droplets to be ejected from the original drop is independent of the wettability of the surface the drop impacts, both for water and other Newtonian fluids. Latka et al. (2018) similarly show that splashing of droplets into numerous smaller droplets is independent of the wetting of the surface hit by the droplet. This relationship was seen to hold for surfaces where the contact angle made by the drop (without splashing) was below 100°; other work has shown that for higher contact angles this relationship changes and results in a lower splashing velocity (Quetzeri-Santiago et al., 2019a, Quetzeri-Santiago et al., 2019b). In a similar manner, de Goede et al. (2021) describe the impact of Newtonian fluids on surfaces of variable roughness and show that the impact velocity beyond which a drop will splash is independent of roughness provided that the roughness is not sufficient to disrupt the lamella of the droplet impacting the surface.

Combining the phenomena of water droplets splashing in shallow water, and surfaces of variable wettability, Zhu et al. (2021) show that a hydrophobic surface under a thin film (depth less than the diameter of the falling drop) of liquid may slow the spread of the droplet crown after impact compared to a neutral-wet or hydrophilic surface. This is similar to the previous results found by Pan and Hung (2010) when a droplet of water falling onto a thin film of water covering an aluminium (neutral-wet) plate vs an acrylic (water-wet) plate was seen to change the formation regime of secondary droplets, although no firm conclusions were drawn as to the mechanism.

Increasing in complexity from a single drop to a flowing system of clay suspension in various brines, models have been used to assess the effect of wettability in a flowing system, most notably to model oil displacement from reservoirs. 2D micromodels have been used. Zulfiqar et al. (2020) use silicon micromodels of different wettabilities and morphologies produced by chemically altering the surface of the silicone to assess the efficiency of gas displacement by flowing water dyed with the fluorescent dye Uranin. Li and Zhang (2019) produced 3D printed microchannels (using micro-stereolithography (μ-SLA) printing technology) at 2 μm resolution from a CT scan of a rock and modified the rock surface using a silane coating to produce models of different wettabilities. The fluid flow was visualised using a confocal microscope equipped with a high-speed camera. This model gave insight into the trapping of the wetting or non-

wetting fluid in the different natural rock morphological features. These models however do not consider how particles flowing through the network may be affected by the different wettabilities of the surfaces.

Considering the flow of particles in micromodels, one of the first reported uses of a micromodel to look at how wettability affects the flow of particles was by Muecke (1979), who looked at both a sintered glass pack and an unconsolidated sand pack between two glass slides, and assessed the movement of calcium carbonate fines in both single- and multiphase (oil and water) flow. It was shown here that fines were only mobilised if they were wetted by the flowing fluid. This apparatus, however, did not allow for the careful designing of pore geometries to give defined shapes to be studies. In contrast, Razavi Bazaz et al. (2020) specifically designed microchannel networks and 3D printed them in order to direct a flow of particles (in this case cells) through the microchannels, which can be used to separate particles of different sizes. In particular, a spiral design was trialled, the dimensions of which were not possible using traditional microchannel fabrication methods.

Utilising microchannels to monitor the effects of wettability on fluid flow or to monitor particle migration requires that the microchannel, or the substrate that the microchannel is bonded to, is sufficiently optically transparent to monitor the flow using an optical or confocal microscope. This can be challenging to achieve using fused deposition modelling (FDM) 3D printing, as this printing method does not generally produce objects which are optically transparent as the method of laying down subsequent layers of material leaves some air gaps, disrupting the path of light through the object. However, careful selection of print settings, reported by Morgan et al. (2016), allowed a modular 3D printed microchannel system to be fabricated with sufficient optical clarity to monitor the flow of coloured fluids forming individual alginate droplets. This technique is limited to particular transparent materials and specific printing processes, so using alternative techniques, such as micro-CT, to monitor flow through 3D prints or other structures reduces the need for optical clarity and widens the scope of materials that are able to be used to form such channels. The challenge then becomes one of how to obtain sufficient contrast in the flowing fluids and particles for them to become visible.

An issue which may be encountered when attempting to image clays in detail using micro-CT is that the contrast of the clays may not be sufficient to show up clearly, either in the CT scan itself when in low concentration (such as individual clay particles), or against the matrix material of a sandstone being imaged. Cation exchange has been used to enhance the contrast of clays in

sand pack or sandstone matrices when viewed in micro CT (Nadeev et al., 2013). Here, the samples were of frozen porous rocks to investigate the distribution of air pockets in the sample; something which is hard to see without enhanced contrast as the air and water in the pores show as the same density in the CT image. The clay was allowed to exchange for a day in lead nitrate solution (or a solution of barium ions) then the clay was pumped into the matrix; an enhanced contrast was seen. Cation exchange has also been seen to enhance the contrast of clays in a sandstone by Sakellariou et al. (2004). A sandstone was imaged dry, then saturated with a solution of caesium ions, followed by draining and re-imaging; a difference contrast map was obtained showing the areas which had absorbed the Cs ions (assumed to be cation-exchangeable clays). Another method of increasing the contrast in micro-CT is to use a high-contrast flowing brine during a flow experiment. CsI was used as a component in the flowing brine by Lebedeva and Fogden (2011) when looking at a sand pack surrounded by kaolinite and saturated in oil to look at low salinity oil recovery. In this case, the position of the brine was seen as a lighter coloured area compared to the dark oil-filled areas, and the sand grains appeared lightest. A similar technique, using CsI to improve contrast, was used by Bultreys et al. (2015) to visualise the real-time wetting of a Bentheimer sandstone in a gantry-based micro-CT scanner, allowing the real-time displacement of the CsI with kerosene, and the Haines jumps associated with the process, to be visualised.

A potential downfall of using micro-CT rather than optical or confocal microscopy to image particle movement is that the length of time to complete a scan of the object may be relatively long, depending on the instrument used. Some instruments may take hours to days to complete a scan, whereas synchrotron sources may produce upwards of 208 full scans per second at 4.9 µm voxel size giving a spatcial resolution of < 15 µm (García-Moreno et al., 2019). Synchrotron access is however limited, and hence often alternative techniques to obtain the high special resolution desired for particle tracking must be employed. One often-used technique is to take scans at discrete points during the process being monitored and infer the way that the process evolves between these points. Another is to monitor processes that evolve very slowly over time, or adjust the process being monitored so that it happens over a longer timescale. Allman et al. (2020) give an example of the use of scanning at discrete points in a micro-CT scanning and 3D printing process which takes a CT scan of an aneurism, reproduces the aneurism using 3D printing, conducts a flow experiment then analyses the resultant 3D print with micro-CT. However, some high-speed micro-CT scanners have been developed. The most common setup involves the sample being held static, and the source and detector moving around it to acquire

images. Using such a set-up has allowed Dewanckele et al. (2020) to study real-time muffin baking (11.3 s/scan, 72 µm voxel size) and beer foam evolution (9.4 – 15 s/scan, 150 - 160 µm voxel size).

Radiography (imaging in 2D using ionising radiation, usually x-rays) may be used in a similar manner to CT scanning, but as it is a 2D technique rather than a 3D technique, requiring only one image to represent the system rather than a series of potentially thousands of images, it gives the possibility to image at a much higher time resolution. Lappan et al. (2020) have used radiography to monitor foam flow by imaging the flow in the presence of small, custom-shaped 3D printed items. Looking at the shape and orientation of these tracers allowed the authors to accurately track the foam flow through a curved channel with a rectangular cross section. Guillard et al. (2017) used radiography to monitor bulk particle during flow conditions, and developed algorithms to define the individual particle orientations to analyse how particle orientation was related to flow.

6.2 Aims

The main aim of this work is to determine if the movement of fine particles is influenced by the change in wettability when moving from a surface with one wettability to a surface with a different wettability. There is a large scope for experimental design when looking at the influence of wettability on particle movement. A number of experiments were therefore devised in order to test the advantages and limitations of various ideas, and to provide a good baseline from which to progress. These experiments are now summarised below.

6.2.1 Contact angle of clay suspensions on surfaces

Many studies have been carried out looking at the flow of particle-containing fluids in porous media of varying wettabilities (Sarkar and Sharma, 1990, Bennion et al., 1998, Huang et al., 2002, Schembre and Kovscek, 2004, Ashraf et al., 2010). Does the presence of particles in the fluid change the apparent wettability of the surface (either hydrophobic or hydrophilic) by causing a change in contact angle when compared to distilled water?

6.2.2 Immersed drop spread shape

During a water injection or low salinity EOR operation, low salinity fluids being injected encounter generally high salinity fluids in the rock pores (Bernard, 1967, Nasralla et al., 2011, Hussain et al., 2013, Kareem, 2016, Katende and Sagala, 2019). If the low salinity fluids cause fines migration, they will then carry in them fine particles, which have become detached from

the pore walls. In order to gain a greater understanding of fines migration around areas where the wettability or roughness changes, a simple experiment was devised to assess the potential migration pathways. The complication of the sandstone pore geometry was removed by considering the motion of a fluid over a submerged flat surface where the wettability or roughness varied. Singular drops of fluid containing a dye were introduced to the system, and the pattern of spread of the drops was observed from overhead, noting the spreading pattern of the dyed fluid. The shape that the drop made could then be likened to the spreading potential of that fluid over a surface of that wettability.

6.2.3 Fluorescent flow in 3D prints

Following from the drop shape analysis, can dyed low salinity clay suspensions flowing through a 3D printed cell with or without variable wettability or patterning be monitored to give an idea of how changes of wettability and flow path influence flow? Would this cell be suitable for use in a micro-CT scanner to better track individual particle flow?

6.2.4 Micro-CT flow in 3D prints

The previous experiments were carried out on a macro-scale, using coloured fluid flow to approximate the movement of particles. Can individual particles be tracked through a 3D printed cell using micro-CT, either in 2D or 3D?

6.2.4.1 Cation exchanging bentonite

Individual clay particles (aggregates or platelets) have insufficient contrast to easily be tracked individually in micro-CT. Will exchanging the exchangeable sodium ion in Wyoming bentonite for heavier ions give an improved contrast for fine particle tracking either in sandstone or in 3D printed parts?

6.2.4.2 Particle tracking in 3D prints

Given that a particle with sufficient contrast can be found, can a method be developed to track individual particles in real time flowing through a 3D printed model?

6.2.5 Simulation of flow in flow cells

3D models have been made for all the flow cells used in physical experiments. Can the 3D models produced be used in simulation software to show flow patterns similar to those found experimentally?

6.3 Methods

6.3.1 Contact angle of clay suspensions on surfaces

Four different clays were chosen to look at the effect of the presence of clay in suspension on the contact angle of water or salt solution on hydrophobic, intermediate-wet (60° - 120°) or hydrophilic surfaces. The first set of experiments looked at the effect of clay concentration in deionised (DI) water on the contact angle on hydrophobic and hydrophilic surfaces. The clays selected were Wyoming bentonite (ex Steetly, majority montmorillonite) and LAPONITE XLS (Byk, synthetic hectorite). 0.2 g of each clay was placed into a 28 ml glass vial and 25 ml distilled water was added. The vials were shaken on a shaker plate (IKA KS 130 basic orbital shaker) at 720 rpm for 15 minutes, and three 2× serial dilutions were made, with 2 minutes shaking after each dilution, to give the following clay suspensions:

Table 6-2: Clay concentrations used for the first set of clay suspension contact angle studies

Clay	**Concentration (g/l)**
Bentonite	8 g/l
Bentonite	4 g/l
Bentonite	2 g/l
Bentonite	1 g/l
LAPONITE XLS	8 g/l
LAPONITE XLS	4 g/l
LAPONITE XLS	2 g/l
LAPONITE XLS	1 g/l

In order to assess the contact angle of the clay suspensions on hydrophobic surfaces, a method of modifying a glass slide to become hydrophobic was sought. A number of approaches were assessed to give a hydrophobic coating using beeswax on the glass slides. In the first method, a clean slide was rubbed with solid beeswax to leave a thin layer on the slide, and the slide was either used directly or the slide was placed on a hotplate at 70 °C to melt the beeswax into a smooth layer. In the second method, beeswax was applied by first dispersing 0.2 g beeswax in 100 ml acetone and then applying the resulting emulsion to another clean slide, in a method inspired by Wang et al. (2016). The acetone was left to evaporate at room temperature, then the slide was either used directly, or beeswax was melted as before. Finally, the slide surface was first activated by immersion in a 1:1 mixture of concentrated HCl/methanol, rinsing in DI

water, immersion in concentrated sulfuric acid, and again rinsing in DI water (Dressick et al., 2014). The beeswax in acetone emulsion was then applied as for the second method, with again one slide being used directly and the other having the beeswax melted before use.

Five drops of either clay solution or DI water were placed onto the slide using a Gilson pipette by allowing the drop to form at the tip of the pipette and then touching the drop onto the slide. The droplets were measured using a ramé-hart Model 260 Standard Contact Angle Goniometer / Tensiometer using the contact angle module of the ramé-hart DROPimage software set to measure the left and right contact angles of the droplets 10 times over 5 seconds. Droplets on the glass slide were 3 µl to ensure the droplet was fully visible to the software; the droplets on the hydrophobically modified slides were 10 µl.

It was noted during the first set of experiments that the contact angle on the glass slide was rather variable. There was a concern that this may have contributed to the variability of the results obtained in the first set of experiments. A new cleaning protocol was therefore developed, and a larger number of clays were analysed on hydrophilic and neutral-wet surfaces. The clays used were as follows:

Table 6-3: Clay concentrations used for the second set of clay suspension contact angle studies. Details of clay mineralogy are given in Appendix B.

Clay	**Concentration (g/l)**
Bentonite	2.5 g/l
LAPONITE XLS	2.5 g/l
Kaolinite (KGa-2)	2.5 g/l
Illite (IMt-1)	2.5 g/l

Each of the clays was prepared as a suspension in the following salt solutions:

Table 6-4: Salt solutions used to suspend clays

Salt	**Concentration (M)**
NaCl	0.001M
NaCl	0.01M
NaCl	1M
$CaCl_2$	0.001M
$CaCl_2$	0.01M

$CaCl_2$	1M
DI water	-

The surfaces used for contact angle measurement in this test were uncoated glass slides and 3D printed PLA strips (similar to those previously used in Chapter 4). The 3D printed PLA strips were produced by a Raise 3D N1 printer using a custom-made script (see Appendix B). The 3D printed strips were cleaned in DI water in the ultrasonic bath for 5 minutes (Ultrawave QS5, 100% power, no heating, frequency leap on). The strips were used twice (one measurement on each end), then discarded to ensure as little contamination as possible, and to also ensure that the surface was not changed by repeated cleaning cycles. An illustration of the measurement process is shown in Figure 6-3.

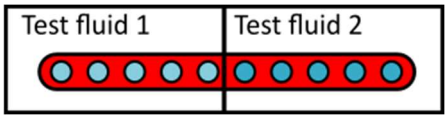

Figure 6-3: 3D print strip (red) used in two different sets of contact angle measurements for two different fluids. The piece was discarded after to prevent cross-contamination.

A thorough washing procedure was developed for the glass slides:

1. Clean with washing up liquid and tap water, rubbing slide with fingers; rinse washing up liquid off with tap water (removes either the factory coating from the slide, or the dirt/contamination from a used slide)
2. Place in ultrasonic bath (Ultrawave QW5, 100% power, no heating, frequency leap on) in beaker of DI water for 5 minutes
3. Dry with clean paper towel, place in ultrasonic bath (as previous) in beaker of acetone for 5 minutes (removes organic contamination)
4. Dry with clean paper towel, place in ultrasonic bath (as previous) in new beaker of DI water for 5 minutes
5. Dry with clean paper towel, place in ultrasonic bath (as previous) in beaker of ethanol for 5 minutes (removes biological contamination)
6. Store in ethanol until use
7. Dry on clean paper towel before use

Five, 5 µl drops of each clay suspension or salt solution without clay were placed onto the slide using a Gilson pipette by allowing the drop to form at the tip of the pipette and then touching

the drop onto the slide. The droplets were measured using a ramé-hart Model 260 Standard Contact Angle Goniometer / Tensiometer using the contact angle module of the ramé-hart DROPimage software, set to measure the left and right contact angles of the droplets 10 times over 5 seconds. In order to confirm that the slides had been adequately cleaned, after every drop of clay suspension or salt solution, the contact angle of a drop of water of the same size was also measured. All measurements were repeated once more.

6.3.2 Immersed drop spread shape

Two different methods were used to produce patterns on glass slides so that the direction on spreading of drops could be analysed. One glass slide was patterned with a series of parallel lines etched into the glass using a HPC LS6840 Laserscript laser cutter with a 60 W tube, 400 mm/s, 18 W 0.05 mm. Others were patterned with an intermediate-wet paint (nail varnish) to change the surface wettability. Four slide patterns were used. The first was a clean glass slide, the second with 2 mm parallel lines 3 mm apart etched as above, the third 3 mm lines 2 mm apart painted, and the fourth 1.5cm squares, either glass inside, paint outside or paint inside, glass outside.

The patterns are shown in Figure 6-4.

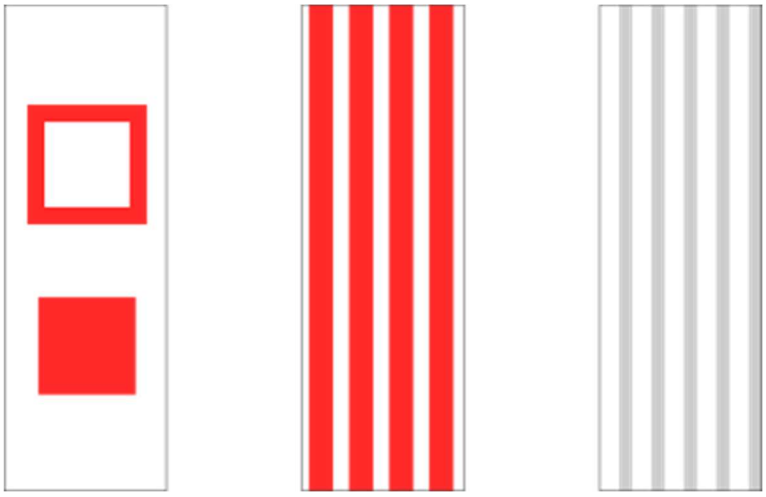

Figure 6-4: Patterns on slides for drop spread shape analysis. Red: intermediate-wet paint, grey: laser etching

In the first set of experiments, the slides were placed in the bottom of a glass petri dish and 20 ml or 30 ml of DI water was syringed on top of the slide in the dish. One drop of fluorescently dyed clay suspension was dropped from 3.5 cm above the dish from a 3 ml plastic pipette into the water. The experiment was performed in relative darkness, with the petri dish being

illuminated by a UV torch. The process was recorded as a video using a Logitech C950 webcam and Logi Capture software. The dyed clay suspensions are listed below:

Table 6-5: Drop shape drop solutions - water test. Details of clay mineralogy are given in Appendix B.

Fluorescent dye	**Clay**
0.002 M (0.8 g/l) fluorescein sodium salt (Sigma Aldrich, for use as fluorescent tracer)	20 g/l bentonite (SWy-2)
0.002 M (0.8 g/l) fluorescein sodium salt (Sigma Aldrich, for use as fluorescent tracer)	5 g/l kaolinite (KGa-2)
0.002 M (0.8 g/l) fluorescein sodium salt (Sigma Aldrich, for use as fluorescent tracer)	none
0.2 mM (0.1 g/l) Rhodamine B (Sigma Aldrich, for fluorescence)	20 g/l bentonite (SWy-2)
0.2 mM (0.1 g/l) Rhodamine B (Sigma Aldrich, for fluorescence)	5 g/l kaolinite (KGa-2)
0.2 mM (0.1 g/l) Rhodamine B (Sigma Aldrich, for fluorescence)	none

At least two drops of each solution were recorded on the slides; the experimental process is illustrated in Figure 6-5. Three images were captured from the recorded video – the point before the drop was released from the syringe, the drop initially hitting the surface of the bulk solution in the petri dish and the point at which the drop stopped spreading and began to disperse. The images were then loaded into Inkscape (Harrington, 2019) and the three images were aligned on top of each other. The non-glass area of the slide was traced around using the image with no drops present as a guide. This area was then subtracted from a larger box drawn which covered the extent of the droplet spread to give a mask which covered the unchanged glass areas. This image was then removed, and the second image was used to mark the point at which the drop first hit the bulk solution; it was noted here whether the droplet hit above the normal glass, coated or etched surface. This image was removed, then the spread drop was traced around. The area of the spread drop was measured using the measuring tools in illustrator, and then the spread drop shape was intersected with the mask – this gave the area which spread on the glass. It is assumed that if the drop were not affected by the patterned surface it would spread out in a circular fashion. A circle with an area equal to that of the spread drop was therefore placed with its centre in the location of the point where the drop entered the bulk solution, and the circle was intersected with the mask to give the area which would have spread on glass had the drop spread in a circular fashion.

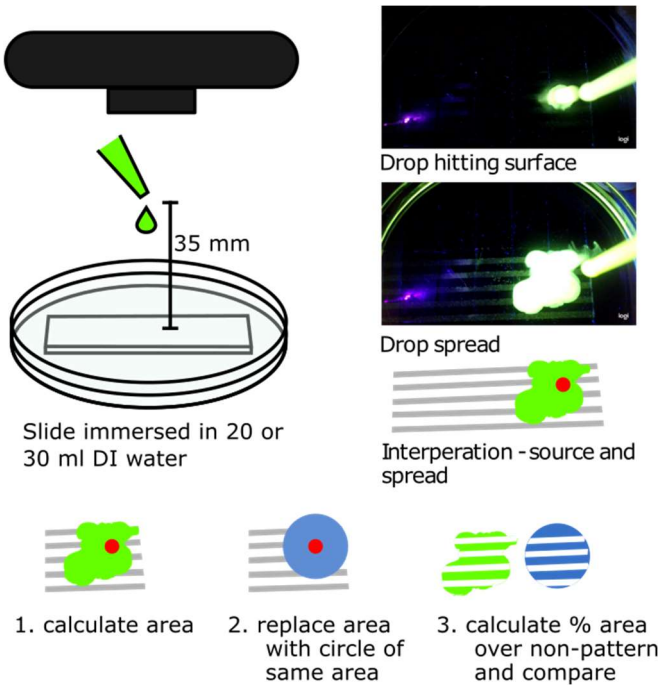

Figure 6-5: Process of drop spread calculation

In the second set of experiments, the slides were placed into the bottom of a glass petri dish, and 25 ml of bulk solution was syringed onto the slide in the dish to ensure the slide was uniformly covered. One drop of the low salinity, fluorescently dyed solution was dropped from a plastic 3 ml pipette 3.5 cm above the dish, illuminated by a UV torch. The process was recorded as a video. The solutions used are detailed below:

Table 6-6: Drop shape bulk solutions – salinity test

Bulk solutions
1 M NaCl (Sigma Aldrich ReagentPlus, >99%)
1 M $CaCl_2$ (as calcium chloride hexahydrate, Sigma Aldrich 98%)
0.5M NaCl/0.5M $CaCl_2$ mixture (1:1 ratio of the above solutions)

Table 6-7: Drop shape drop solutions - salinity test. Details of clay mineralogy are given in Appendix B.

Salt	**Fluorescent dye**	**Clay**
0.001 M NaCl (Sigma Aldrich ReagentPlus, >99%)	0.002 M (0.8 g/l) fluorescein sodium salt (Sigma Aldrich, for use as fluorescent tracer)	20 g/l bentonite (SWy-2)

0.001 M NaCl (Sigma Aldrich ReagentPlus, >99%)	0.002 M (0.8 g/l) fluorescein sodium salt (Sigma Aldrich, for use as fluorescent tracer)	5 g/l kaolinite (KGa-2)
0.001 M NaCl (Sigma Aldrich ReagentPlus, >99%)	0.002 M (0.8 g/l) fluorescein sodium salt (Sigma Aldrich, for use as fluorescent tracer)	none
0.001M $CaCl_2$ (Sigma Aldrich ReagentPlus, >99%)	0.002 M (0.8 g/l) fluorescein sodium salt (Sigma Aldrich, for use as fluorescent tracer)	20 g/l bentonite (SWy-2)
0.001M $CaCl_2$ (Sigma Aldrich ReagentPlus, >99%)	0.002 M (0.8 g/l) fluorescein sodium salt (Sigma Aldrich, for use as fluorescent tracer)	5 g/l kaolinite (KGa-2)
0.001M $CaCl_2$ (Sigma Aldrich ReagentPlus, >99%)	0.002 M (0.8 g/l) fluorescein sodium salt (Sigma Aldrich, for use as fluorescent tracer)	none

The drop spread was analysed in a similar manner to the first set of experiments (see Figure 6-5). The contact angle of DI water on the etched glass and neutral-wet paint was also measured following the previous method.

6.3.3 Fluorescent flow in 3D prints

3D printed flow cells were designed in Autodesk Fusion 360 and printed with an Anycubic Photon DLP 3D printer (see Section 3.1.6) using standard resin in either clear green, clear or yellow. The flow cells were designed to hold two glass slides parallel to each other with a variable gap between the slides, and to use aquarium airline tubing to introduce the fluids to the cell. The design is illustrated in Figure 6-6, and a 3D rendering of the design is shown in Figure 6-7.

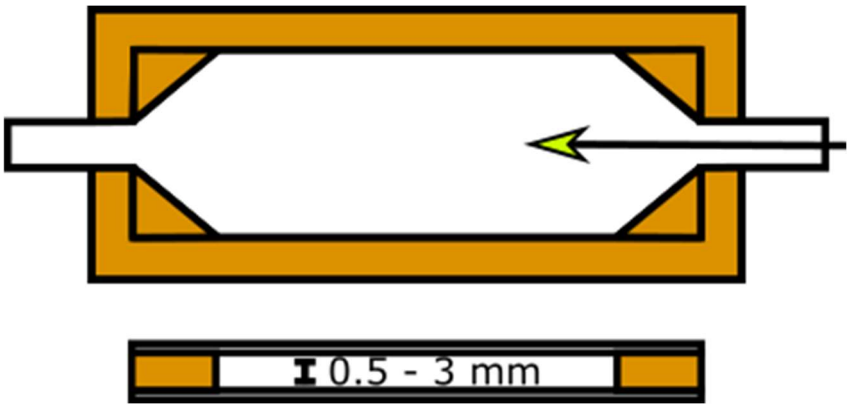

Figure 6-6: Parallel slide flow cell design for fluorescent flow studies

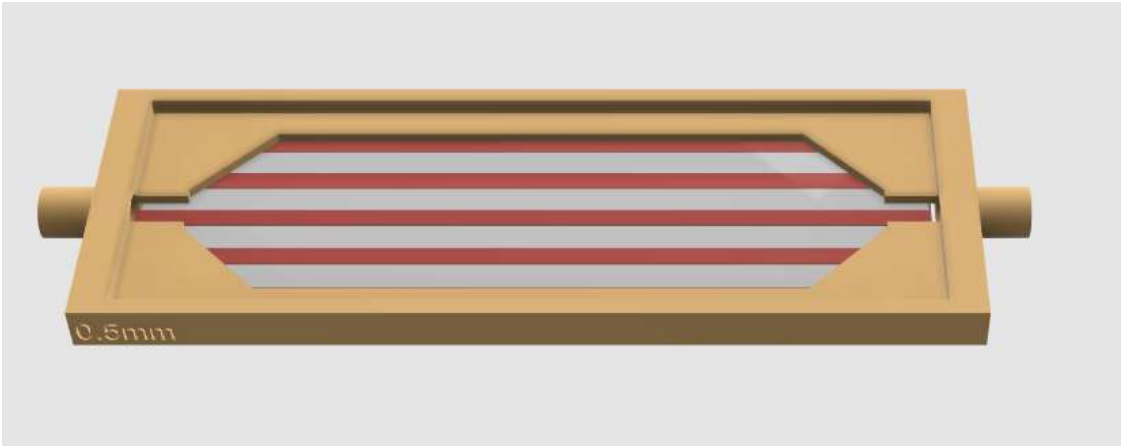

Figure 6-7: Rendering of 3D model of flow cell, illustrating intermediate-wet paint line patterned and clear slides in place. Each slide holder is marked to denote the gap width between slides.

The slides were held in place with two-part rubber (Flexbar reprorubber thin pour rubber replica casting system) which gives a watertight bond but is easy to remove completely from the surface, making all components easily reusable. The top slide in every case was a cleaned clear glass slide, whereas the bottom slide was either clear, a pink parallel lined pattern or a red parallel lined pattern (3 mm lines 2 mm apart, running parallel to the long edge of the slide; see Figure 6-7). The clear and pink lined slides were prepared with the 1 mm spacing, whereas the red lined slides were prepared as a 0.5 mm spacing. Aquarium airline tubing was attached to the inlet and outlet of the slide flow cell and the cell was placed in a dark box illuminated with a UV light only. A Logitech C950 webcam was positioned above the cell looking vertically down onto the cell (using a 3D printed mount). The outlet tube was placed in a secure waste bottle. The inlet tube was attached to a T-junction connector, and two further short lengths of tubing were attached. The short tubing was attached to two 20 ml syringes – one containing the fluorescently dyed solution, the other containing DI water. The syringes were loaded into two Chemyx OEM syringe pumps. The syringe pumps were connected to a laptop via USB and controlled using

TeraTerm through the serial interface (Baud Rate: 38400, Data Bits: 8, Parity: None, Stop Bits: 1, Flow Control: None). The flow rate was set to 5 ml/minute, and the procedure for running a flow experiment was then as follows:

1. 1.5 ml dyed solution was pumped into the tubing and clamped at the T-junction (1.5 ml solution filled the short tubing attached between the syringe and the T-junction)
2. 10 ml DI water was pumped into the tubing and slide flow cell and the tubing was clamped at the T-junction.
3. The webcam was set to record using Logi Capture software.
4. The clamp on the dyed solution side of the T-junction was unclamped and 15 ml dyed solution was pumped into the apparatus. The tubing was re-clamped.
5. The clamp on the DI water side of the T-junction was unclamped and 10 ml DI water was pumped into the apparatus.
6. The recording was stopped and the apparatus was cleaned.

The dyed solutions used were as follows:

Table 6-8: Fluorescently dyed flow solutions. Details of clay mineralogy are given in Appendix B.

Fluorescent dye	**Clay**
0.002 M (0.8 g/l) fluorescein sodium salt (Sigma Aldrich, for use as fluorescent tracer)	20 g/l bentonite (SWy-2)
0.002 M (0.8 g/l) fluorescein sodium salt (Sigma Aldrich, for use as fluorescent tracer)	5 g/l kaolinite (KGa-2)
0.002 M (0.8 g/l) fluorescein sodium salt (Sigma Aldrich, for use as fluorescent tracer)	none
0.0002 M (0.1 g/l) Rhodamine B (Sigma Aldrich, for fluorescence)	5 g/l kaolinite (KGa-2)
0.0002 M (0.1 g/l) Rhodamine B (Sigma Aldrich, for fluorescence)	none

Cells with a patterned flow path were designed to look at the effect of different flow paths on the movement of dyed clay suspensions in the flow cell. A number of different designs were prepared; these are shown in Figure 6-8. The Voronoi patterns were prepared using the Voronoi plugin in Autodesk Fusion 360, using both the curved and straight options and setting the number of objects to 30, then adjusting the spacing to give narrow but printable channels

between the objects. These cells were designed to be printed in once piece in clear resin rather than to have a slide attached to the top surface, as there was concern that having to adhere the slide to each individual feature in the pattern may give rise to leakage of the flowing fluid between the upper side of the feature and the slide rather than flowing in the channels as designed.

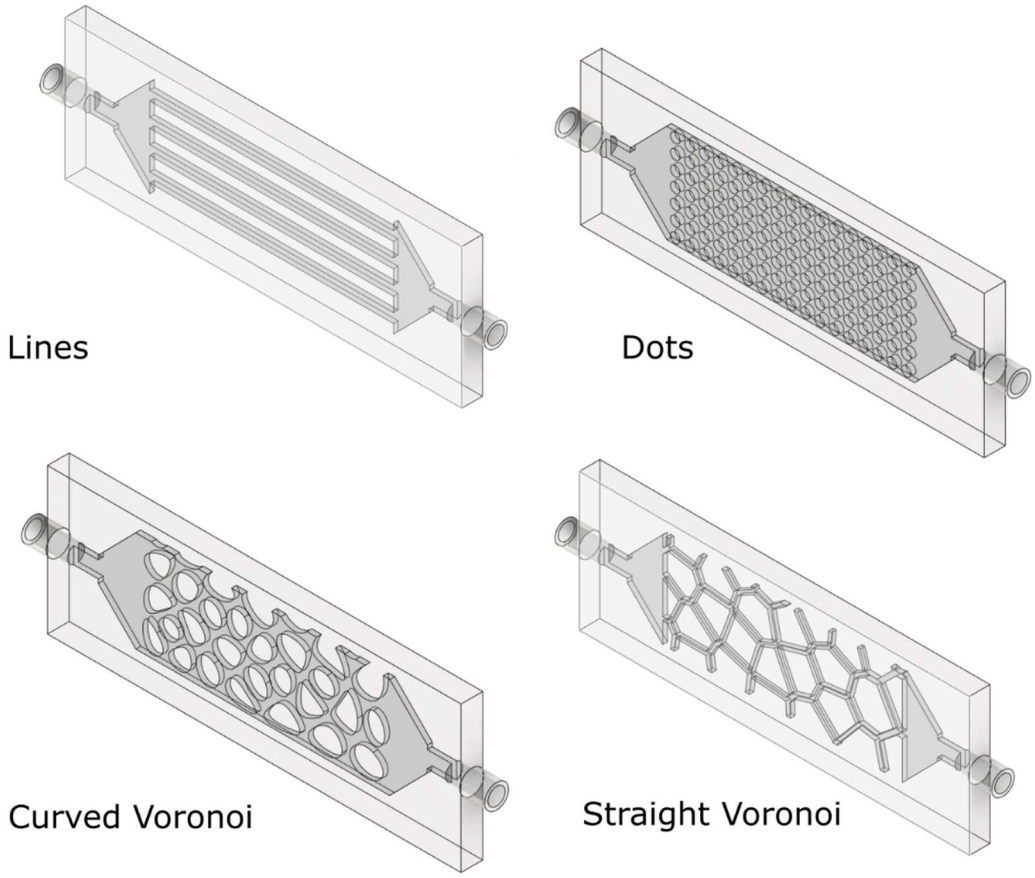

Figure 6-8: 3D printed solid slide designs - linear channels, dotted grid, curved Voronoi features, straight Voronoi features.

6.3.4 Cation exchanging bentonite

1 M solutions of lead acetate, caesium iodide and potassium iodide were prepared. 1 g Wyoming bentonite (ex Steetly) was added to a 25 ml centrifuge tube and 25 ml of one salt solution was added. Two tubes containing clay and KI and one tube containing clay and Pb acetate were shaken overnight at 480 rpm (IKA KS 130 basic). The suspensions were centrifuged for 3 minutes at 3000 rpm (Grant-bio LMC-3000) and the supernatant was decanted off. This was repeated, and then repeated a second time with the suspensions left shaking over the weekend. Four tubes containing clay and CsI were shaken over the weekend in the first instance, and then two

of the solutions were shaken overnight a further two times, with the suspensions being centrifuged, the supernatant decanted and then replaced twice, similar to the protocol above. Deionised water was added to one of the pellets obtained from KI, the pellet obtained from Pb Acetate and one pellet from CsI from each protocol and they were shaken for 1hr, centrifuged for 15 minutes at 3000 rpm, the water decanted off and all pellets were dried in an oven overnight. The resulting dried pellets were placed one at a time into the micro-CT scanner (XRadia/Zeiss VersaXRM 410) and a single image taken at each of 70, 100 and 150 kV accelerating voltage and saved as a *.gif file. The images were analysed using imageJ (Schneider et al., 2012).

6.3.5 Particle tracking in 3D prints

3D printed flow cells were prepared with different channel patterns to monitor the movement of particles through different pathways. The flow cells were initially designed in a similar manner to the flow cells for the previous experiment, using a glass slide as one of the surfaces and the 3D printed pathway as the other, so that the progress of the experiment could be monitored visually as well as with CT (XRadia/Zeiss VersaXRM 410). However, it was found that the height of the flow cell using a glass slide did not allow the top part of the flow cell to be monitored in the CT scanner due to limitations in the y range of the scanner. The cell was therefore redesigned using a shorter length, and clear 3D printed panels were glued in place using silicone sealant instead of the glass slides as the reprorubber used previously was difficult to cure in the presence of the resin prints and the bond was not strong enough for extended test times in the CT scanner. The redesigned cell is shown in Figure 6-9; the original design was based on the cells shown in Figure 6-8.

Upon initial testing, it was found that the doped clays did not give sufficient contrast against the 3D print for particle tracking. In order therefore to carry out individual particle tracking, a system of viscous fluid and high density ground and sized minerals was developed. The viscous fluids tested were a 50:50 mix of golden syrup and water, a 75:25 mix of golden syrup and water, a 90:10 mix of golden syrup and water, golden syrup and 6.25 g/l xanthan gum (DUO-VIS). The sized minerals tested were API barite ($BaSO_4$, max 3% w/w >75 µm, max 30% w/w <6 µm), ultra-fine grind barite (lower proportion of larger sized particles than API barite), hematite (Fe_2O_3, similar but narrower size distribution to API barite), Micromax (Mn_3O_4, smaller particle size than API barite) and Microdense (Ilmenite, FeTiO, <1.5% w/w ≥ 45 µm).

The viscous fluids were tested for their ability to suspend API barite when flow had stopped, and carry the barite in suspension when flow was started. To carry out this test, approximately 1 g barite was added to the viscous fluids and mixed thoroughly. For the xanthan gum and 50% syrup fluids, the barite was incorporated with a Hamilton beach mixer at high speed. In the case of the 75% and higher syrup concentrations, the dispersion was carried out in an OFITE rolling oven at room temperature overnight so as not to introduce too much air into the fluid. Airline tubing was fed out of the labyrinth of the scanner and was filled with the viscous fluid/barite mixture, and a 20 ml syringe filled with the same fluid was attached to the tubing. The syringe was loaded into a Chemyx OEM syringe pump, which was controlled via USB connection to a laptop. The tubing was mounted on a 3D printed flow cell holder and a further 20 ml syringe without a plunger was attached to the open end of the tubing and suspended above the tubing to receive the fluid as it passed out of the tubing. In order to scan quickly enough to monitor individual particle movement, it was decided to use the CT scanner in a 2D radiography mode. The tubing was scanned at 100 kV, 10 W with a 1 s interval between each of the 500 scans and binning of 2, giving a total scan time of approximately 30 minutes, at pixel size of 13.18 µm. The XRadia/Zeiss VersaXRM 410 will not scan without a change in angle between subsequent scans. The angle was therefore set to vary between 0° and 1° over the 1000 scans; this made the scans as close to radiography as the machine would allow, and sufficiently close for continuous particle tracking. If the particles did not fall rapidly through the viscous fluid during the initial part of the test, a flow test was carried out to check whether the fluid was able to flow in the system and carry the particles. To do this, the syringe pump was started at 0.02 ml/minute approximately 5 minutes after the scan had started, and was stopped 5 minutes before the end of the scan. The pump speed was set so that individual particles could be seen clearly and did not move too far from one scan to the next.

The different sized minerals were tested in a simplified testing regime. A 15 ml centrifuge tube was filled with 90% golden syrup and placed in the scanner. A small amount (the tip of a small spatula) of the sized mineral was added on top of the syrup and the scanner was started, using the same settings as the previous set of tests. The sized mineral was monitored as it fell through the syrup.

After a sized mineral and a viscous fluid had been identified as giving the optimal suspension and contrast characteristics, the test could be carried out in the flow cells in a similar manner to the previous tests. A series of flow and pause steps were programmed into the syringe pump and the flow of particles was recorded at different points in the flow cell in a series of scans.

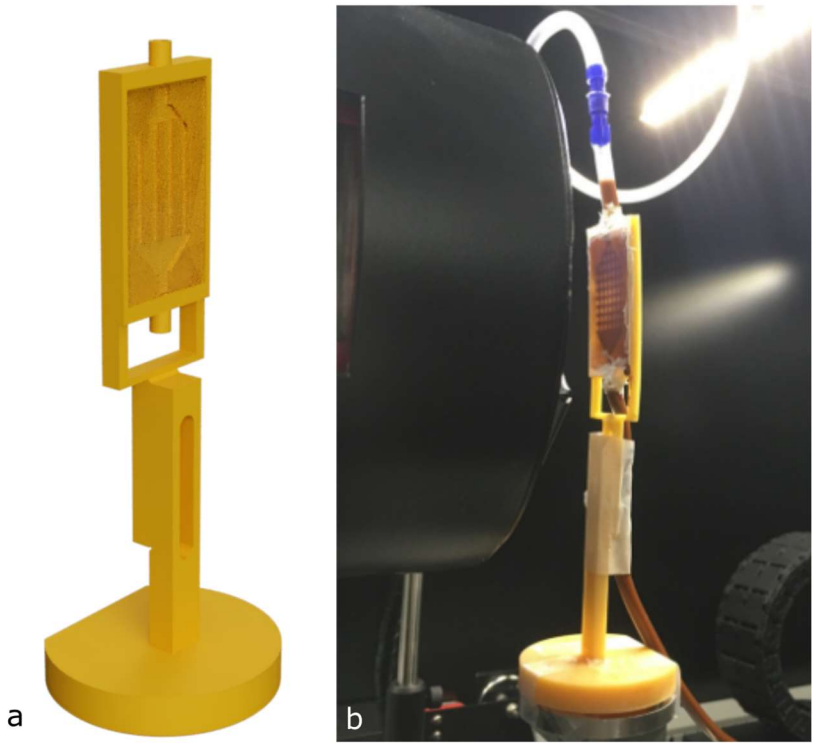

Figure 6-9: The flow cell design (a) and the flow cell in place in the micro-CT scanner (b).

The .txrm files produced by the XRadia/Zeiss VersaXRM 410 were imported into imageJ. For particle tracking, the background was subtracted, the images was inverted and filtered and the filtered images were processed with the Particle Tracking (Sbalzarini and Koumoutsakos, 2005) module of the MosaicSuite plugin for imageJ.

6.3.6 Simulation of flow in flow cells

The 3D models used for the flow experiments exported from Autodesk Fusion 360 into Autodesk CFD, which is a commercially available Computational Fluid Dynamics (CFD) simulation software package. Where a viscosity profile did not exist for the fluid used, a viscosity profile was obtained using a HAAKE Viscotester iQ Air. The 3D models were modelled as ABS (polycarbonate), as this material available in the default database should be sufficiently similar to 3D printed resin for the model to be representative. A transient ramp-step model was used for the flow rate, increasing to the desired flow rate over the first second of the simulation for low flow rates, and over the first 5 s of the simulation for high flow rates. An automatic mesh was applied, and the simulation was set to run over 50 s with a 0.5 s time step and 10 iterations per step for the slow flow rates, saving every 10 time steps, and 180 s with a 1 s time step and 10 iterations per step

saving every 10 time steps for high flow rates. During the simulation the convergence plot was observed to check for model instability (discontinuities between subsequent time steps). The results were plotted as a plane and traces.

6.4 Results and discussion

6.4.1 Contact angle of clay suspensions on surfaces

The contact angle of water on a glass slide has been reported as 9.0° ± 1.3° by Wu et al. (1996) (measured on precleaned glass slides as received), 55° (Mohsin et al., 2016), 0° (Menawat et al., 1984), 22° (Damchan et al., 2008). Although all show glass to be highly water-wet, the variation suggests that the glass surface preparation may be a significant factor in the contact angle obtained. Iglauer et al. (2014) give a review of glass slide cleaning methods, which range from washing in acetone or ethanol to use of piranha solution. Piranha solution is usually composed of a 3:1 mixture of concentrated (98%) sulphuric acid to 30% hydrogen peroxide and is often used to hydroxylate glass prior to surface reaction, giving a highly hydrophilic surface. However, piranha solution is known to be explosive, so a safer method to reproducibly clean a glass slide was desired. The method developed for this set of experiments has produced sufficiently reproducible results and is considerably safer. The results obtained for individual water droplet measurement on glass slides with and without using the developed cleaning procedure are shown in Figure 6-10 and Figure 6-11. The average contact angle measured on the uncleaned surface was 28.0° ± 9.3°, and the average variation between the angle measured on the left and right side of the droplet was 2.3° ± 2.9°. The cleaned surface showed an improvement in these measurements, giving an average contact angle of 28.9° ± 5.5°, and an average variation between the left and right side of the droplet of 0.2° ± 2.1°. It may appear that the reduction in error could be due to the increase in the number of measurements from 15 to 155; however, considering the F-test for variances, and assuming that the variance of the values for the cleaned glass slide is less than that for the uncleaned glass slide, looking at a 95% confidence interval it would appear that this result is due to the improved cleaning process rather than an increase in number of measurements.

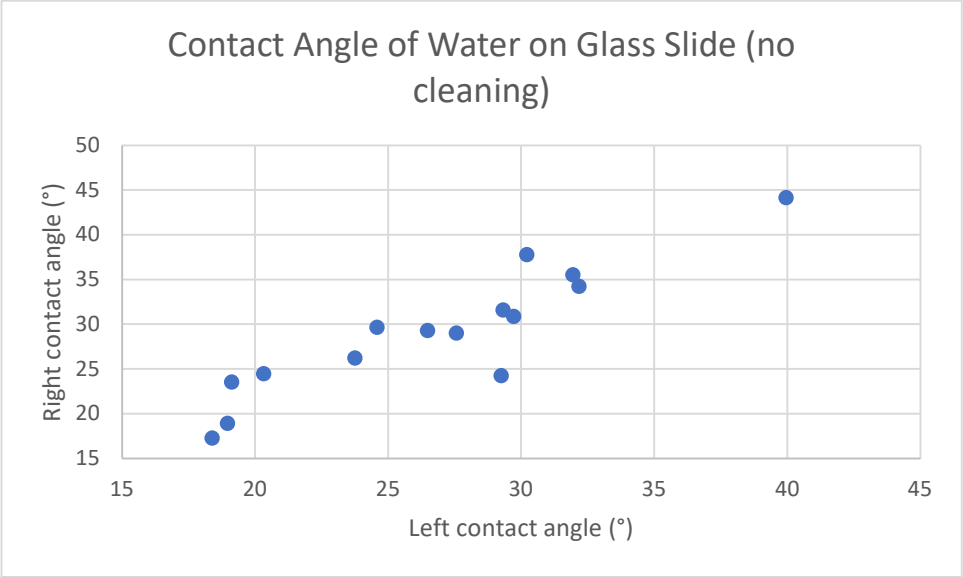

Figure 6-10: Left vs right contact angles measured on individual DI water droplets on uncleaned glass slides.

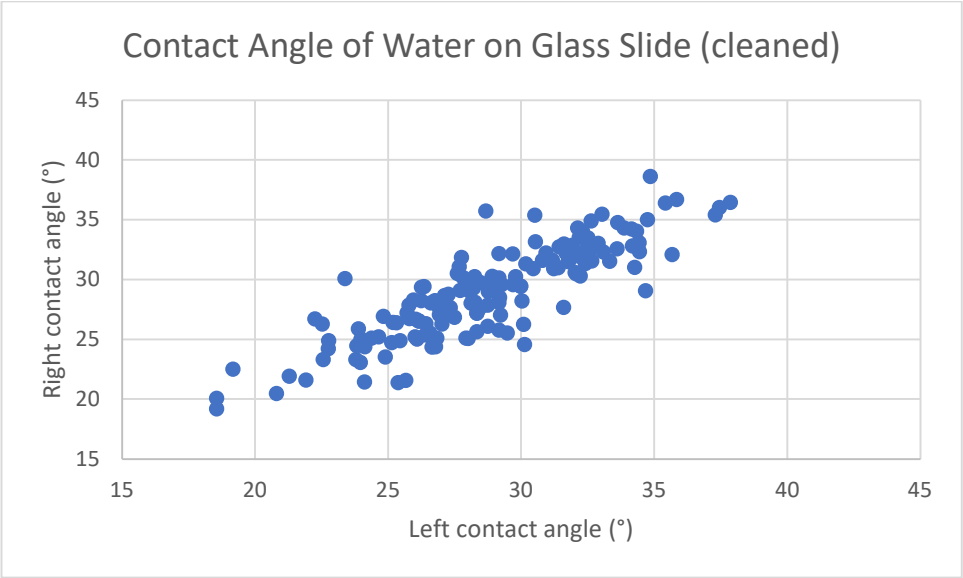

Figure 6-11: Left vs right contact angles measured on individual DI water droplets on cleaned glass slides

A comparison was made of the different beeswax application methods to the glass slide by measuring the contact angle of DI water on each slide; the results are shown in Figure 6-12. It is clear that any method of application increases the contact angle of the water drop. Considering the standard deviation in the measurements, it appears that the method whereby beeswax is applied from an emulsion then melted produces the coating which gives the most reproducible measurements. This method was therefore used in future testing. Activating the slide before beeswax application in these experiments didn't appear to have any benefit. The coating wasn't any more firmly adhered, nor was the coating any more even. The contact angle change increase

was also less than for the non-activated slide; as the aim was to give a distinctly more hydrophobic coating, this result was not desirable. It was therefore concluded that the additional risk associated with activating the slide was not necessary. Rubbing beeswax on the slide gave the roughest coating; this is reflected in the highest contact angle and the largest standard deviation in contact angle measurement. Subsequent melting of the beeswax reduced the contact angle to within the range of the emulsion applied beeswax. However, given that this method of application is less easily controllable, this method was also not used in further testing.

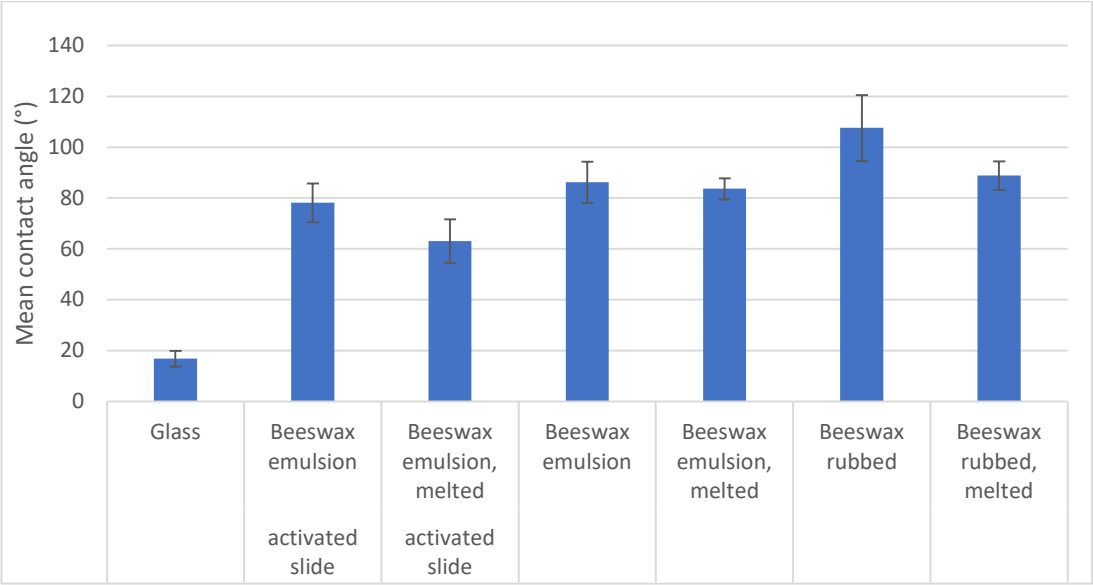

Figure 6-12: Contact angle of DI water on glass slide and different applications of beeswax on glass slide.

Figure 6-13 shows the effect of varying the concentration of two clays on the contact angle on glass and beeswax on glass (applied from an acetone emulsion, then melted). There would appear to be little effect on the contact angle measured on the beeswax coated surface when clays were added compared to the values measured with DI water alone. The measurement errors were quite large, which was probably due to the fact that the beeswax coating wasn't very uniform. The method used by Wang et al. (2016) sprayed the beeswax acetone emulsion onto the surfaces to be made superhydrophobic in order to create an additional texture to increase the hydrophobicity. Spraying the coating onto the slide is likely to give a more uniform coating, but a superhydrophobic coating was not desired, and hence this method may not have been appropriate. In contrast, the drops placed on the uncoated glass showed a smaller variation in the measurements, and the higher concentrations of LAPONITE appear to decrease the contact angle compared to the contact angle of water alone on glass. LAPONITE is a hydrophilic nano-sized synthetic layered silicate, incorporating an inorganic polyphosphate

dispersing agent. It is thought to have a majority hectorite-like structure (Christidis et al., 2018). It was chosen for this study as it has a known composition, will disperse well in water or saline solutions and will produce a solution with optical transparency. LAPONITE is known to stabilise oil-in-water Pickering emulsions (Ashby and Binks, 2000, Brunier et al., 2016), and hence is known to be surface active. In a water droplet on a surface, the water at the surface will be slowly evaporating. The evaporation of water leaves a higher concentration of particles at the droplet edges, and a flow of water from the centre of the droplet will bring further particles to the edge, in a process often termed the "coffee-ring effect" (Deegan et al., 1997). The accumulation of hydrophilic particles at the edge of the water droplet might therefore account for the decrease in contact angle at higher LAPONITE concentrations, shown schematically in Figure 6-14. This scheme, whereby particles at accumulate at the edge of a drop during evaporation, has shown to be enhanced where surface active particles are present (Li et al., 2013) due to the edges of the droplet being "pinned" in place and the apparent contact angle reducing as the experiment proceeds. However, in this experiment, measurements were taken rapidly without excess heat present, and hence evaporation would have been negligible during the duration of the measurement process (approximately 20 s between the droplet being placed and a contact angle measurement being completed). The effect then may be a combination of slight evaporation causing accumulation of particles at the surface combined with spreading to ensure all the particles are water-wet.

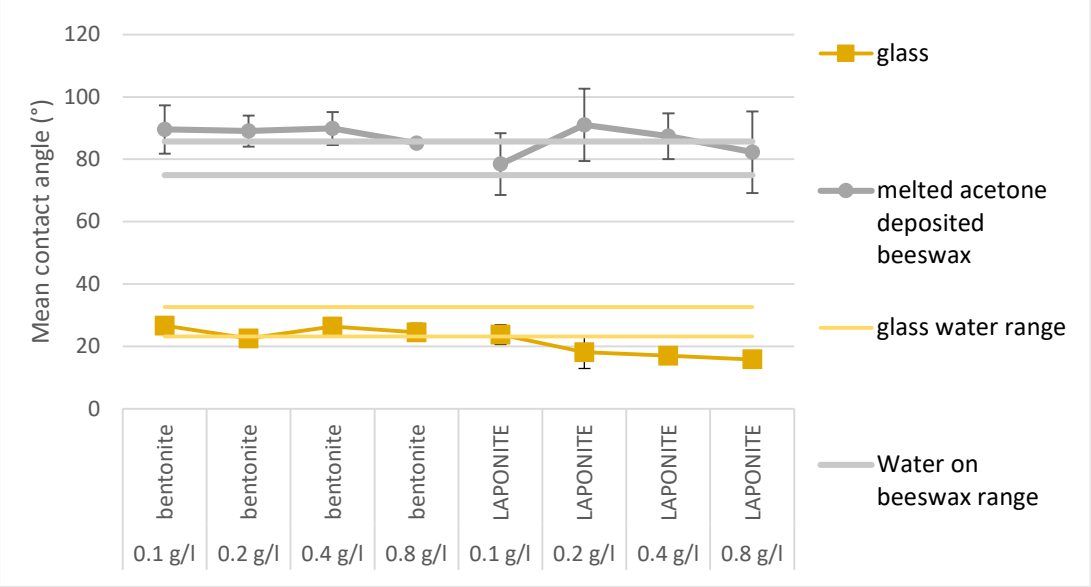

Figure 6-13: Variable concentrations of clays on glass and beeswax coated glass. The ranges shown by horizontal lines are a 95% confidence interval for water on the surface.

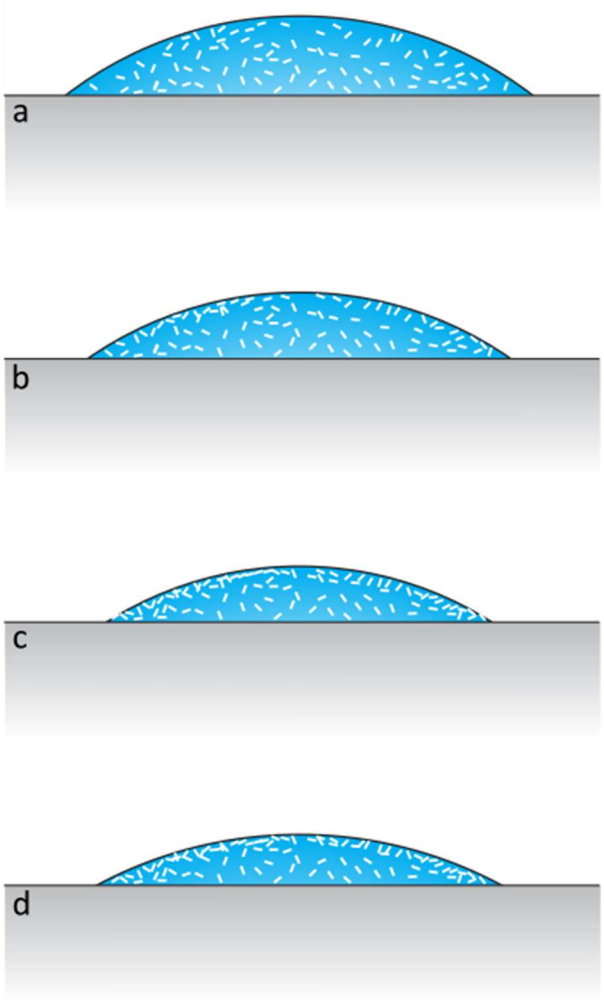

Figure 6-14: Proposed schematic of LAPONITE influencing the contact angle of water on glass. a – initial drop, b – initial evaporation, c – further evaporation leading to lack of wetting of LAPONITE at corners, d – spread of drop to wet LAPONITE in corners.

Looking now at additional clays at 2.5 g/l and the effect of their presence on the contact angle that the droplets containing clays make on either glass or 3D printing PLA surfaces, it can be seen from Figure 6-15 that bentonite and illite may affect the contact angle. LAPONITE does not continue the previously seen trend of higher concentration leading to decreased contact angle, although the contact angle is reduced compared to the contact angle of DI water on cleaned glass. Figure 6-16 shows the contact angle of salt solutions at various concentrations without clay on the cleaned glass and 3D print surfaces. These data show that the presence of salt in solution does not affect the contact angle measured. Figure 6-17, Figure 6-18 and Figure 6-19 show the effect of clays in various concentrations of salt solution on the contact angle of a drop on cleaned glass or 3D print surfaces. In 0.001 M $CaCl_2$ and NaCl, the clays have no significant effect on the contact angle measured compared to DI water alone. In contrast, in 1 M $CaCl_2$

(Figure 6-17) bentonite appears to increase the contact angle on both cleaned glass and 3d print surface, and in 0.01M NaCl, illite appears to decrease the contact angle measured on cleaned glass. It is not clear why these combinations of clay and salt cause a change in the observed contact angle which was not observed with other combinations. It is likely that a further, more detailed study may be required to confirm and explain these results. It is also possible that due to the variable nature of the sessile drop contact angle measurement technique that further repeated measurements may produce results which do not show these outliers.

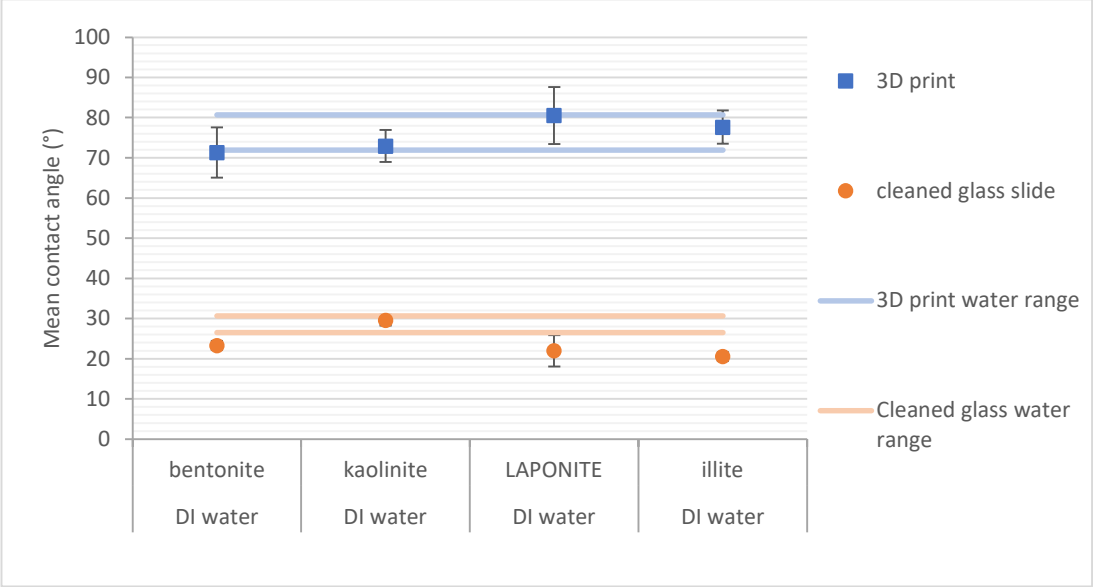

Figure 6-15: Contact angle of DI water with various clays at 2.5 g/l measured on 3D print surface and cleaned glass. The ranges shown by horizontal lines are a 95% confidence interval for water on the surface.

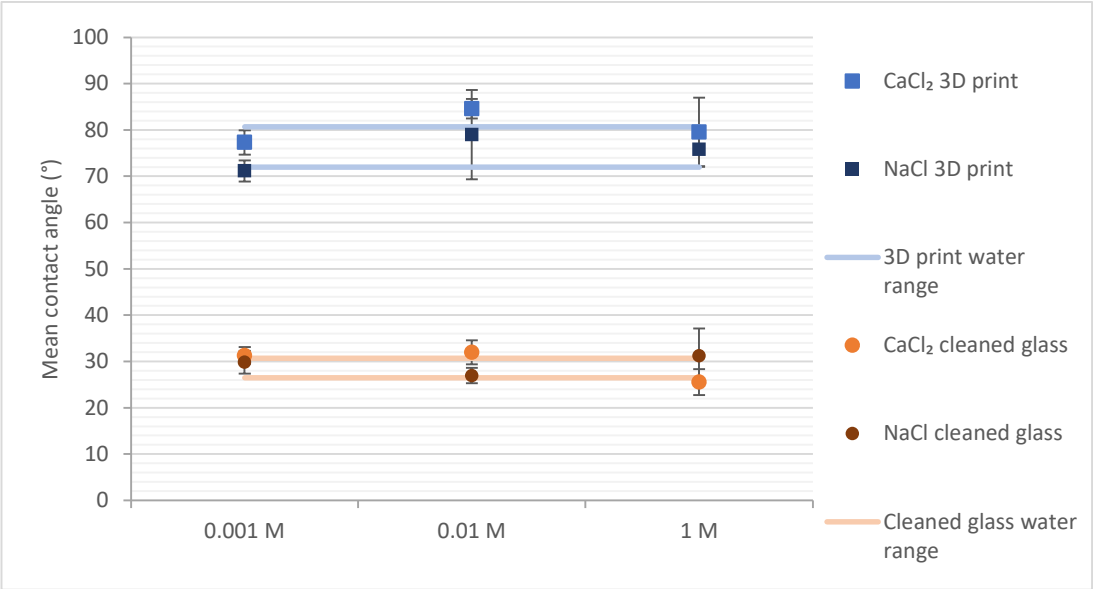

Figure 6-16: Contact angle of NaCl and $CaCl_2$ solutions without clays at 1 M, 0.01 M and 0.001 M measured on 3D print surface and cleaned glass. The ranges shown by horizontal lines are a 95% confidence interval for water on the surface.

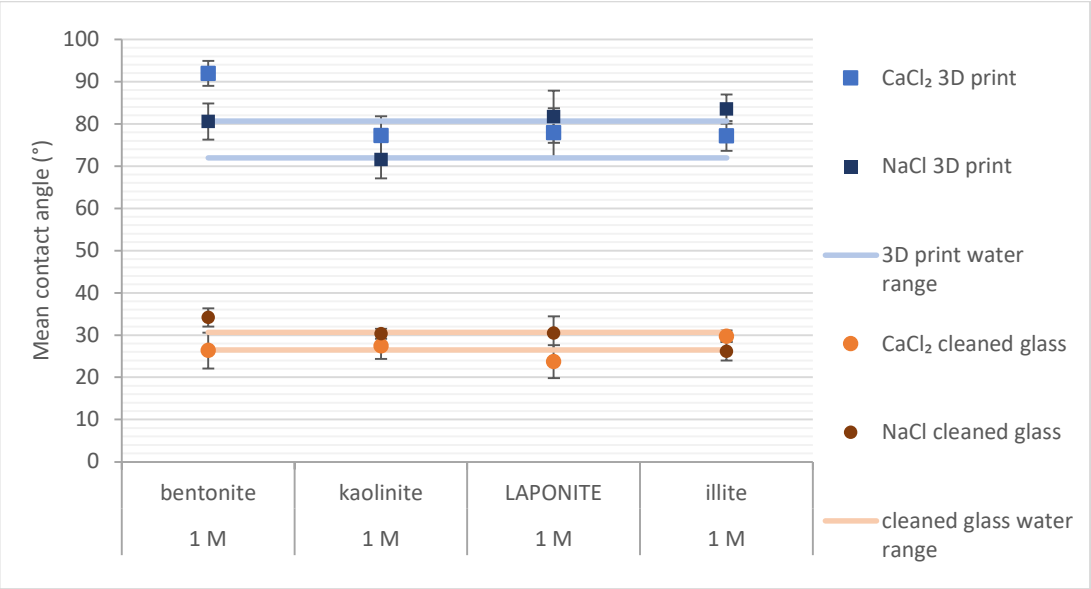

Figure 6-17: Contact angle of 1M salt solutions with various clays at 2.5 g/l measured on 3D print surface and cleaned glass. The ranges shown by horizontal lines are a 95% confidence interval for water on the surface.

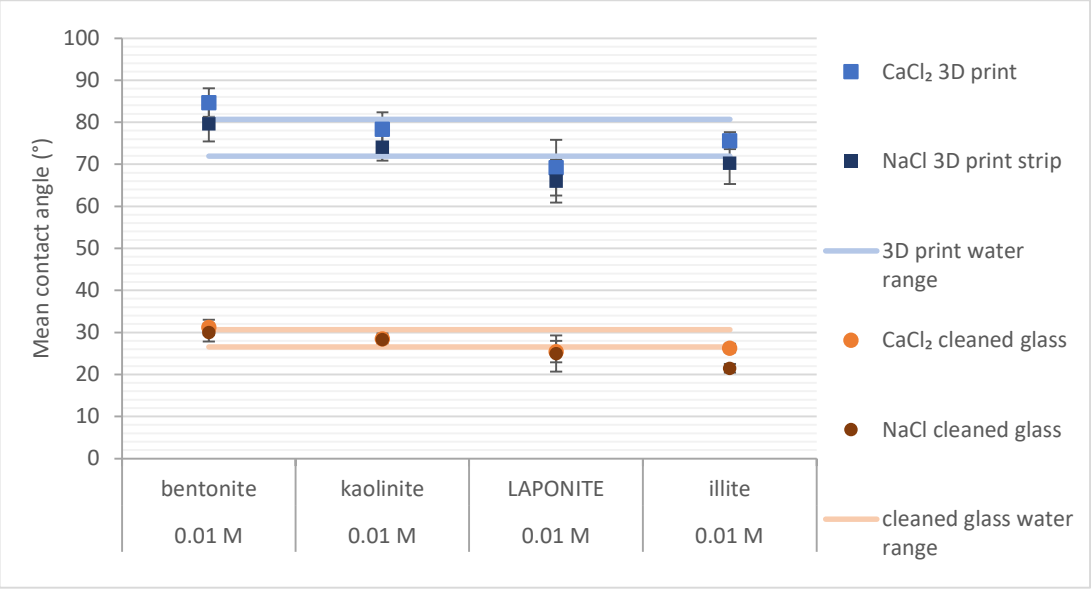

Figure 6-18: Contact angle of 0.01 M salt solutions with various clays at 2.5 g/l measured on 3D print surface and cleaned glass. The ranges shown by horizontal lines are a 95% confidence interval for water on the surface.

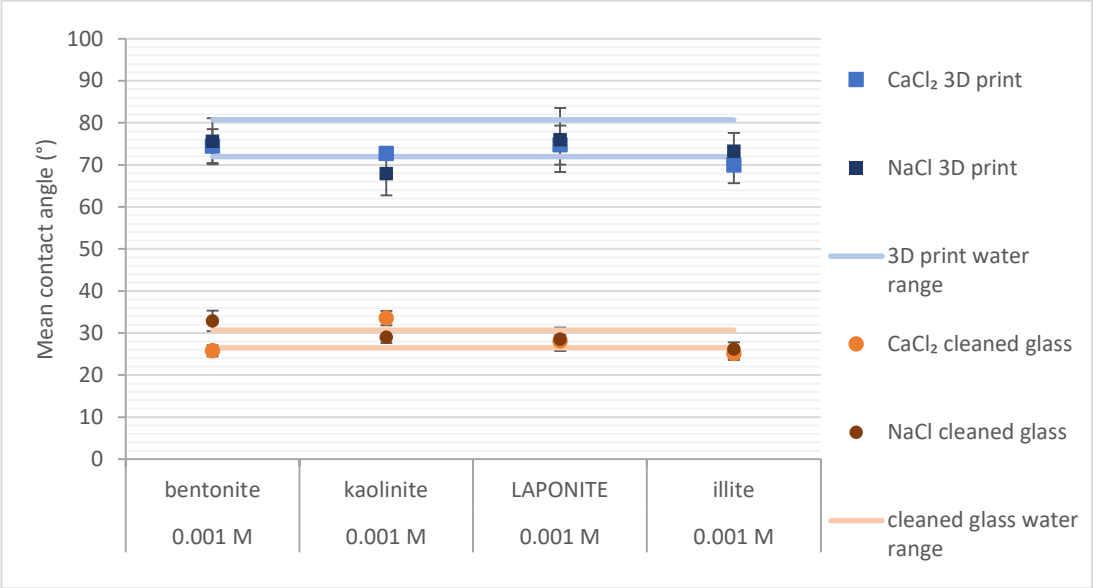

Figure 6-19: Contact angle of 0.001 M salt solutions with various clays at 2.5 g/l measured on 3D print surface and cleaned glass. The ranges shown by horizontal lines are a 95% confidence interval for water on the surface.

6.4.2 Immersed drop spread shape

The contact angles made by a drop of DI water on etched glass and intermediate-wet paint are shown in Figure 6-20 and Figure 6-21, compared to the contact angle made by a drop of DI water on cleaned glass (following the cleaning procedure described in Section 6.3.2). The etched glass was expected to produce a lower contact angle, as a rougher surface has been shown by Wenzel (1949) and Cassie and Baxter (1944) to produce a lower contact angle than a smoother surface for a hydrophilic substrate (see also analysis in Section 4.3.2.2); this was confirmed by contact angle measurement. The paint was expected to produce a surface with higher wettability (following initial screening of a number of candidate coatings). It is designed to produce a smooth surface when applied, adheres to glass without any additional treatments and is cheap and readily available. It is also easy to use with masking materials (such as Sellotape or masking tape) to produce a defined pattern.

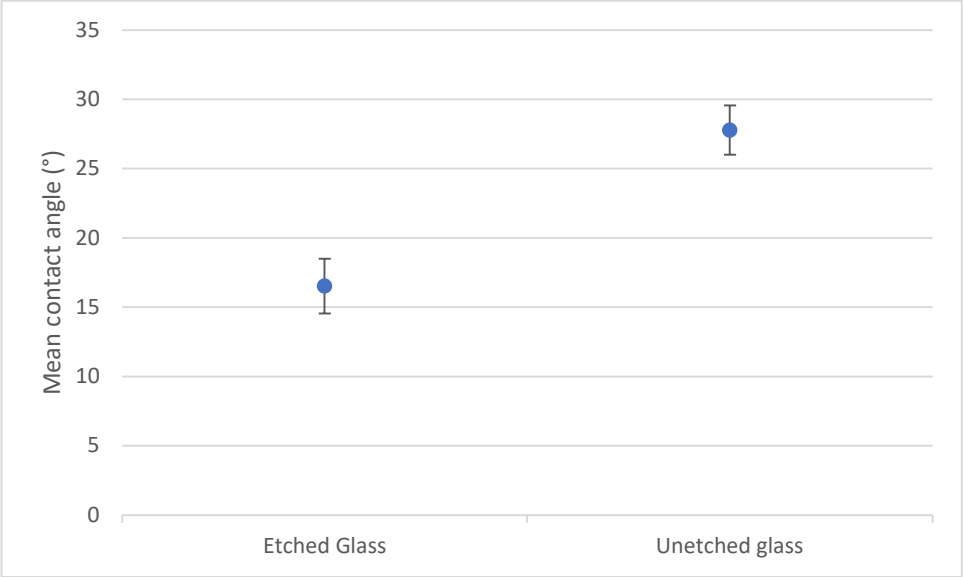

Figure 6-20: Contact angle of DI water on etched glass and unetched glass

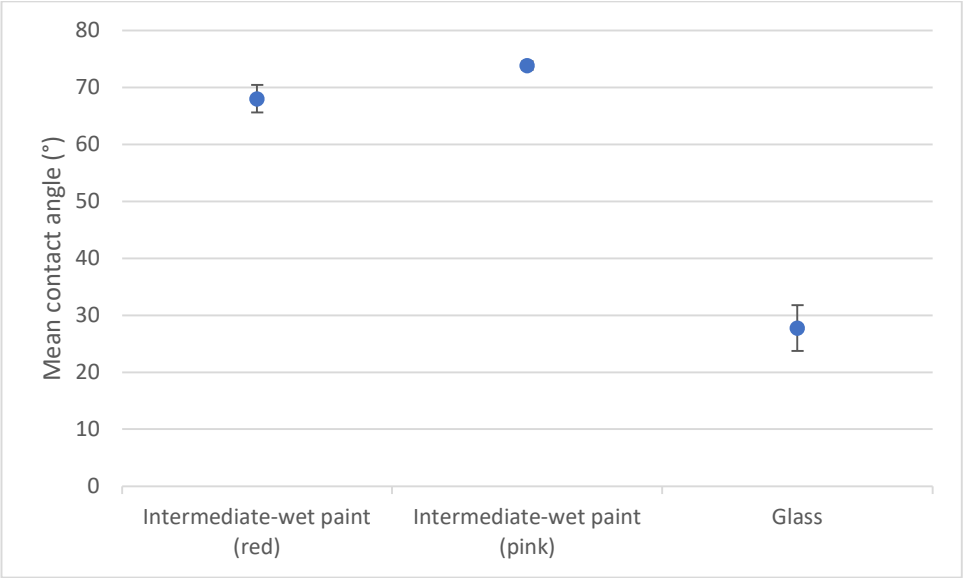

Figure 6-21: Contact angle of DI water on intermediate-wet paint and glass

During preparation of the solutions to carry out the drop spread analysis, an interesting interaction was found when bentonite was added to rhodamine B. It was found that the fluorescence of rhodamine B was dramatically reduced in the presence of bentonite (see Figure 6-22). Rhodamine B is a cationic dye and was selected for use as it was though that it would bind to the bentonite and fluorescently mark the clay particles rather than simply dying the free solution. Selvam et al. (2008) have shown that rhodamine B is absorbed onto montmorillonite, with peak absorbance happening at pH 7. Fang, Zhou et al. (2018) have studied the absorption isotherms of binding of rhodamine B to montmorillonite, and have proposed that it binds to the

edge of the montmorillonite platelets. Baranyaiová and Bujdák (2018) propose that rhodamine 123 forms complexes on the clay surface during binding, and that the nature of the complexes may affect the fluorescence. Baranyaiová and Bujdák (2018) also propose that the nature of the complex formation may be modified by changing the ionic strength. However, in this experiment, all clays were used at unaltered pH and at controlled salinity and hence it was not possible to modify the fluorescence of the rhodamine B/bentonite suspension to give a colour visible under UV light. This combination of dye and clay was therefore not used.

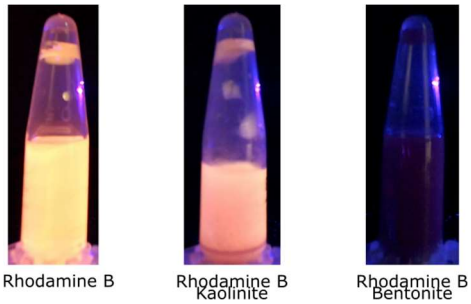

Figure 6-22: Effect of bentonite on the fluorescence of rhodamine B, at unaltered pH. Note the presence of kaolinite produces a cloudy suspension hence the change in appearance, but fluorescence appears unaltered.

There would appear to be little significant effect on the preference of a drop containing clay and/or fluorescent dye on the spread of the drop over a surface of variable wettability when the drop and the liquid it is dropped into are both comprised of DI water (Figure 6-23 and Figure 6-24). A preference for spreading on glass in this instance would be seen as a positive percentage, whereas a preference for spreading on the non-glass surface would be seen as a negative percentage. The error bars for these data, where given, span between positive and negative percentages giving no confidence in any apparent spreading preference.

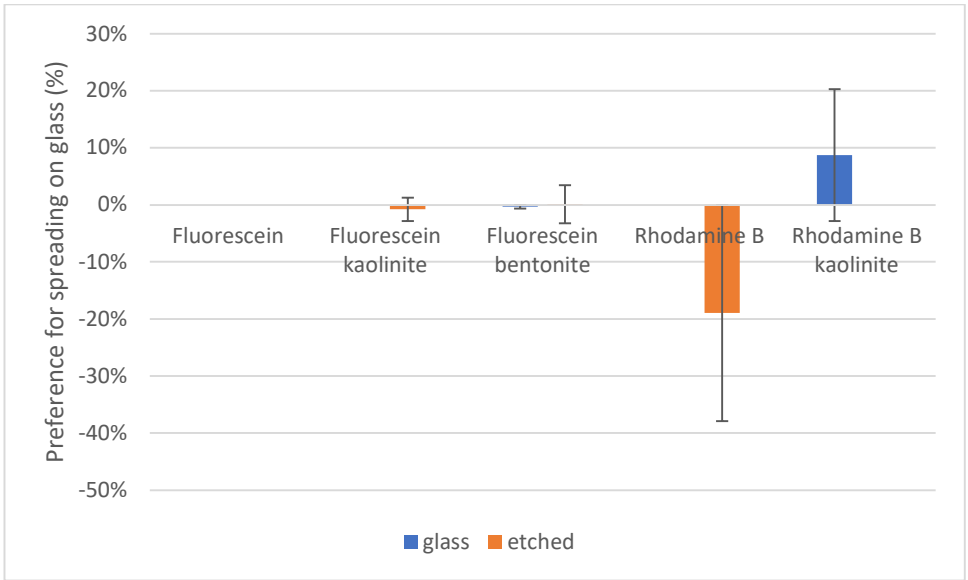

Figure 6-23: Same salinity drop spread on etched slide. Series names denote whether drop spread initiated from unetched glass or etched glass surface.

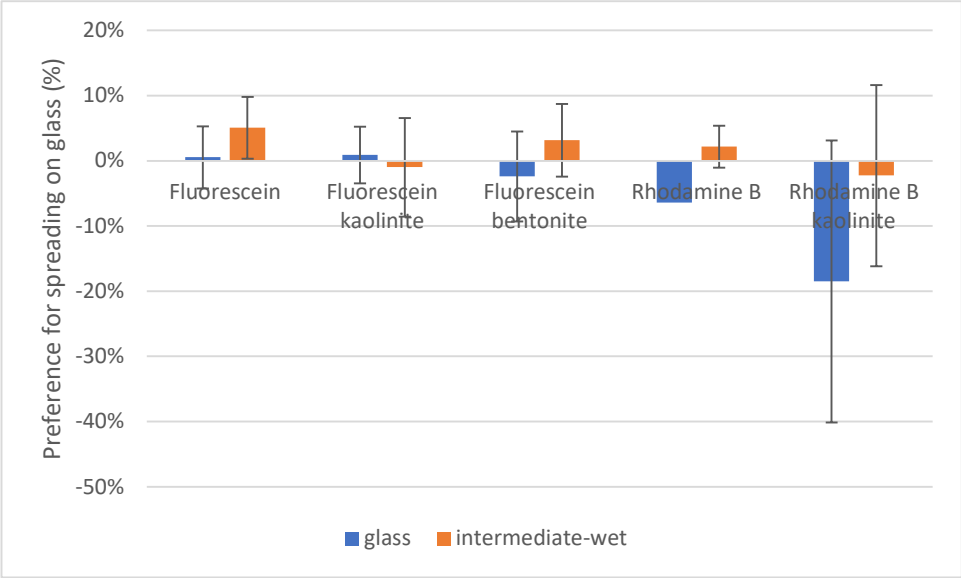

Figure 6-24: Same salinity drop spread on intermediate wet patterned slide. Series names denote whether drop spread initiated from glass or intermediate-wet surface.

In contrast to the same-salinity experiment, it appears (from Figure 6-25, Figure 6-26, Figure 6-27, Figure 6-28, Figure 6-29 and Figure 6-30) that the presence of a high salinity bulk solution with a low salinity drop solution causes the drop to spread more readily on the glass surface than on either the etched or on the intermediate-wet surface, regardless of which surface the drop spread was initiated from. Given that de Goede et al. (2018) and de Goede et al. (2021) have shown that wettability and roughness variation under a dry droplet do not change the spread characteristics, and Zhu et al. (2021) and Pan and Hung (2010) have shown that a hydrophobic surface under a thin film of water onto which a drop is dropped only affects the formation of secondary droplets, this result would seem surprising. It might be supposed that the etching and intermediate-wet paint form a slightly raised surface, which the dyed fluid flows off and onto the glass during drop spread; this slight difference in height may also account for the preference for spreading on glass when the drop hits the glass initially rather than the modified surface as it would be flowing in slightly lower channels (but this effect was not seen in the same-salinity experiments so may not be the cause). However, density considerations of the two fluids might suggest that the bulk fluid would have a higher density and therefore the dyed drop fluid would not preferentially sink. It may then be interesting to repeat this experiment with a carefully milled slide with variable wettability so that any slight height variations can be discounted as causing this effect.

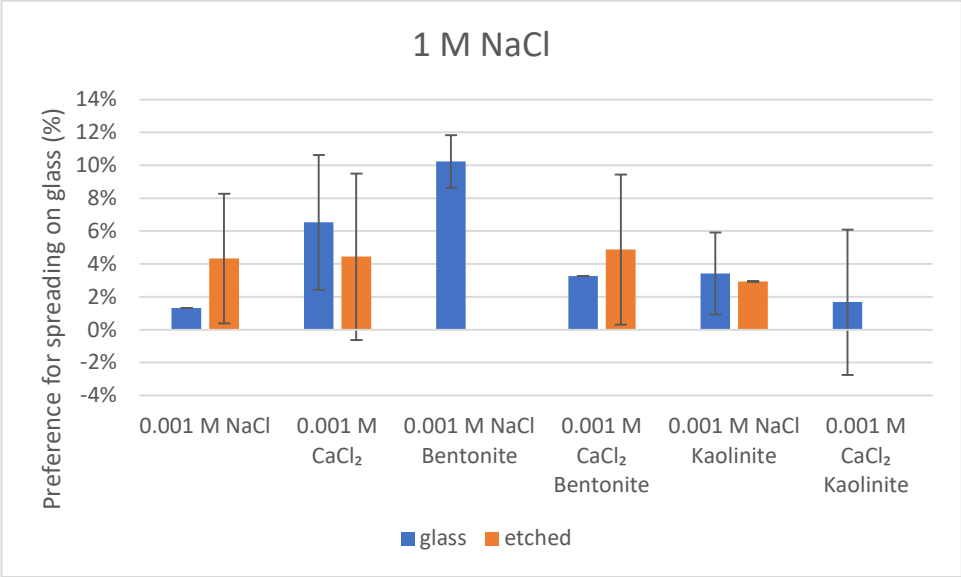

Figure 6-25: Salinity contrast drop spread on etched glass slide - 1 M NaCl bulk solution. Series names denote whether drop spread initiated from unetched glass or etched glass surface.

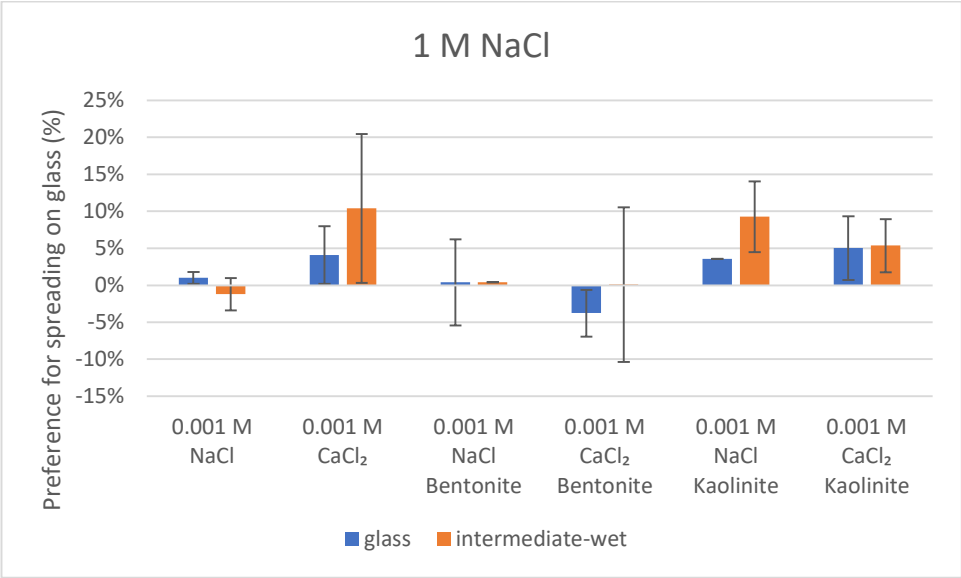

Figure 6-26: Salinity contrast drop spread on intermediate wet patterned slide – 1 M NaCl bulk solution. Series names denote whether drop spread initiated from glass or intermediate-wet surface.

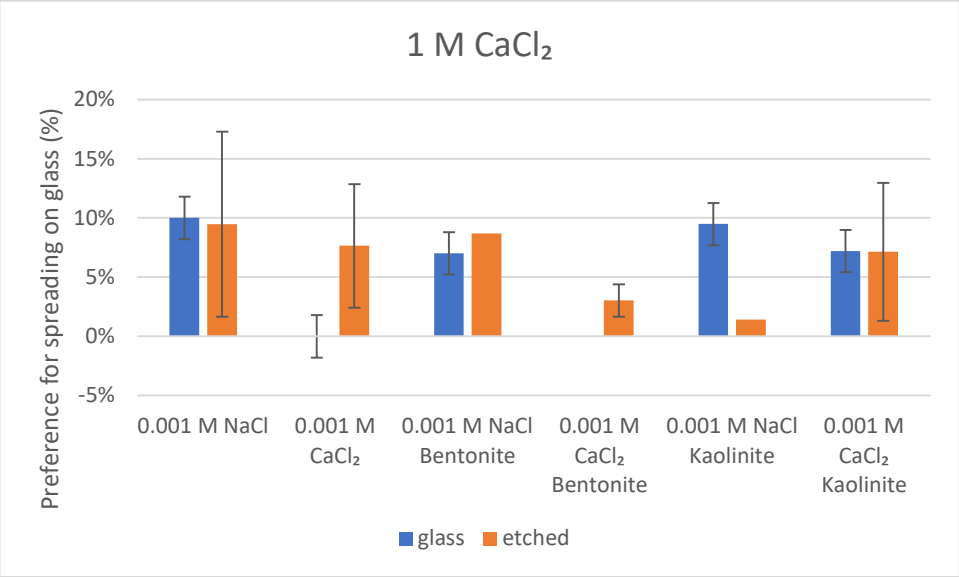

Figure 6-27: Salinity contrast drop spread on etched glass slide - 1 M $CaCl_2$ bulk solution. Series names denote whether drop spread initiated from unetched glass or etched glass surface.

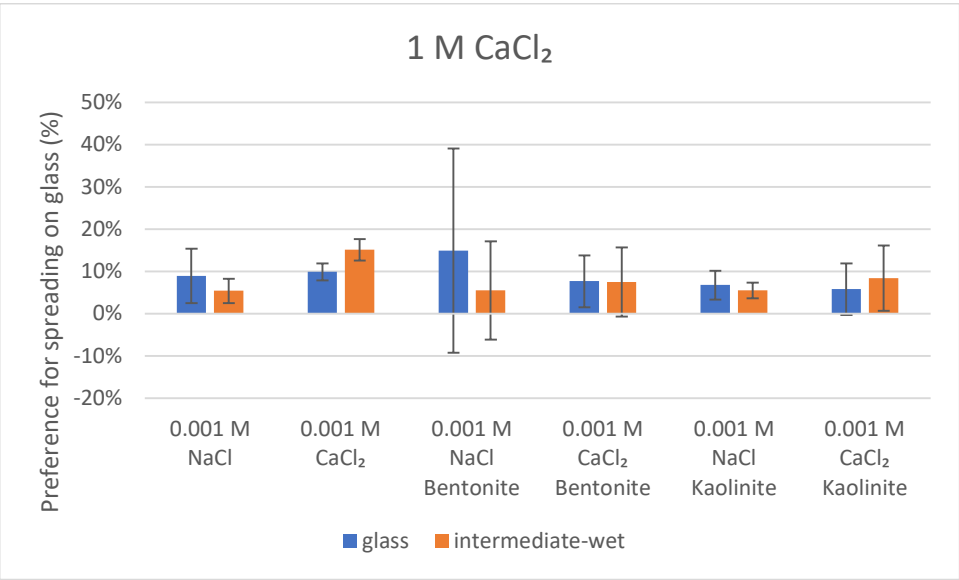

Figure 6-28: Salinity contrast drop spread on intermediate wet patterned slide – 1 M $CaCl_2$ bulk solution. Series names denote whether drop spread initiated from glass or intermediate-wet surface.

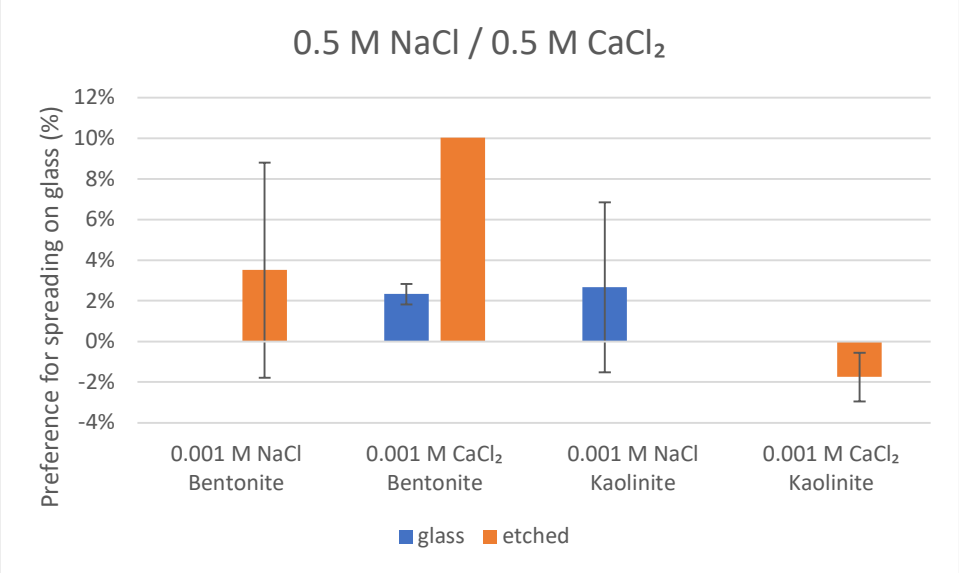

Figure 6-29: Salinity contrast drop spread on etched glass slide – 0.5 M NaCl/0.5 M $CaCl_2$ bulk solution. Series names denote whether drop spread initiated from unetched glass or etched glass surface.

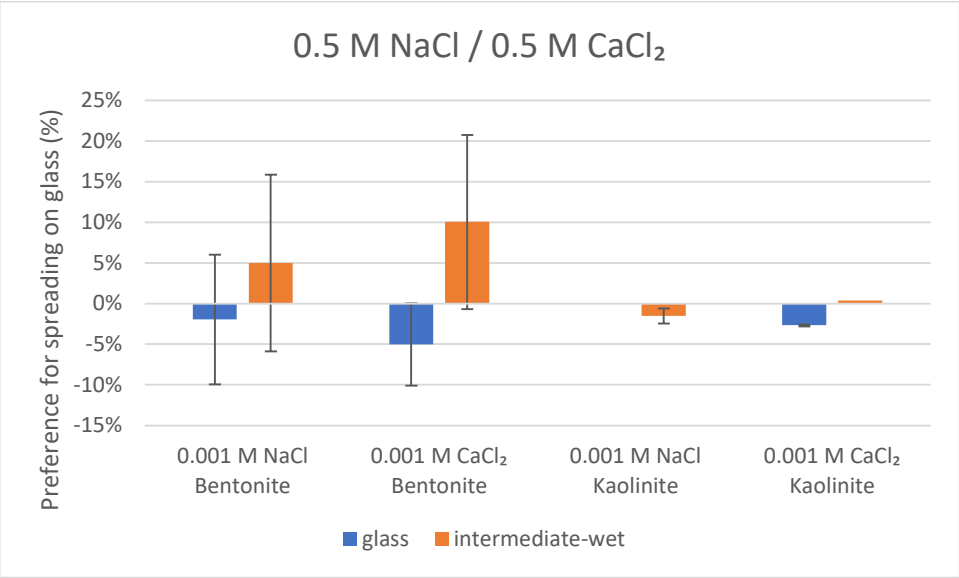

Figure 6-30: Salinity contrast drop spread on intermediate wet patterned slide – 0.5 M NaCl/0.5 M $CaCl_2$ bulk solution. Series names denote whether drop spread initiated from glass or intermediate-wet surface.

6.4.3 Fluorescent flow in 3D prints

Figure 6-31 shows the fluorescent flow development at different time steps. When the flow contained clay, at 60 s for the clear and pink striped cells, and at 30 s for the thinner red lines flow cell, the flow pattern became separated into individual linear flow lines; these are outlined in red in Figure 6-31, and shown more clearly in Figure 6-32 for fluorescein/bentonite at 60 s. The lines were transient, disappearing within 60 s. The flow lines appear to be related to the presence of clay in suspension, as when fluorescein alone is used as the flowing fluid, no flow

lines are seen. In addition, no flow lines are seen when rhodamine B is used; this may be due to the fact that the fluorescence was less intense when using the rhodamine B, and hence the lines could not be seen. The presence of the flow lines shows a strong association between the fluorescein and the clays; this was not expected for fluorescein as it is an anionic dye and as such would not be expected to associate with the anionic clay sheets. The partitioning however shows this association. The flow pattern is unlikely to be due to viscous fingering (Homsy, 1987), as this has been shown to only occur when a less viscous fluid flows into a region where a more viscous fluid resides; in this case, although the viscosity of the clay containing fluids have not been measured directly, it may be assumed that the viscosity may be slightly higher than the DI water initially filling the cell, and therefore the pattern is unlikely due to this effect. It is possible that the flow may be partitioning the clay particles into different size bands in a manner similar to that described by Razavi Bazaz et al. (2020) due to the variation of fluid velocity throughout the cell during this time. It is also interesting to note that these patterns only occur at the outlet end of the flow cell; possibly then there may be some contribution of the glass slides forming the walls of the cell slowing the fluid non-uniformly along the length of the cell. It is not clear at this point what this effect may be caused by, and careful further experimentation and modelling may be useful to help explain the phenomenon.

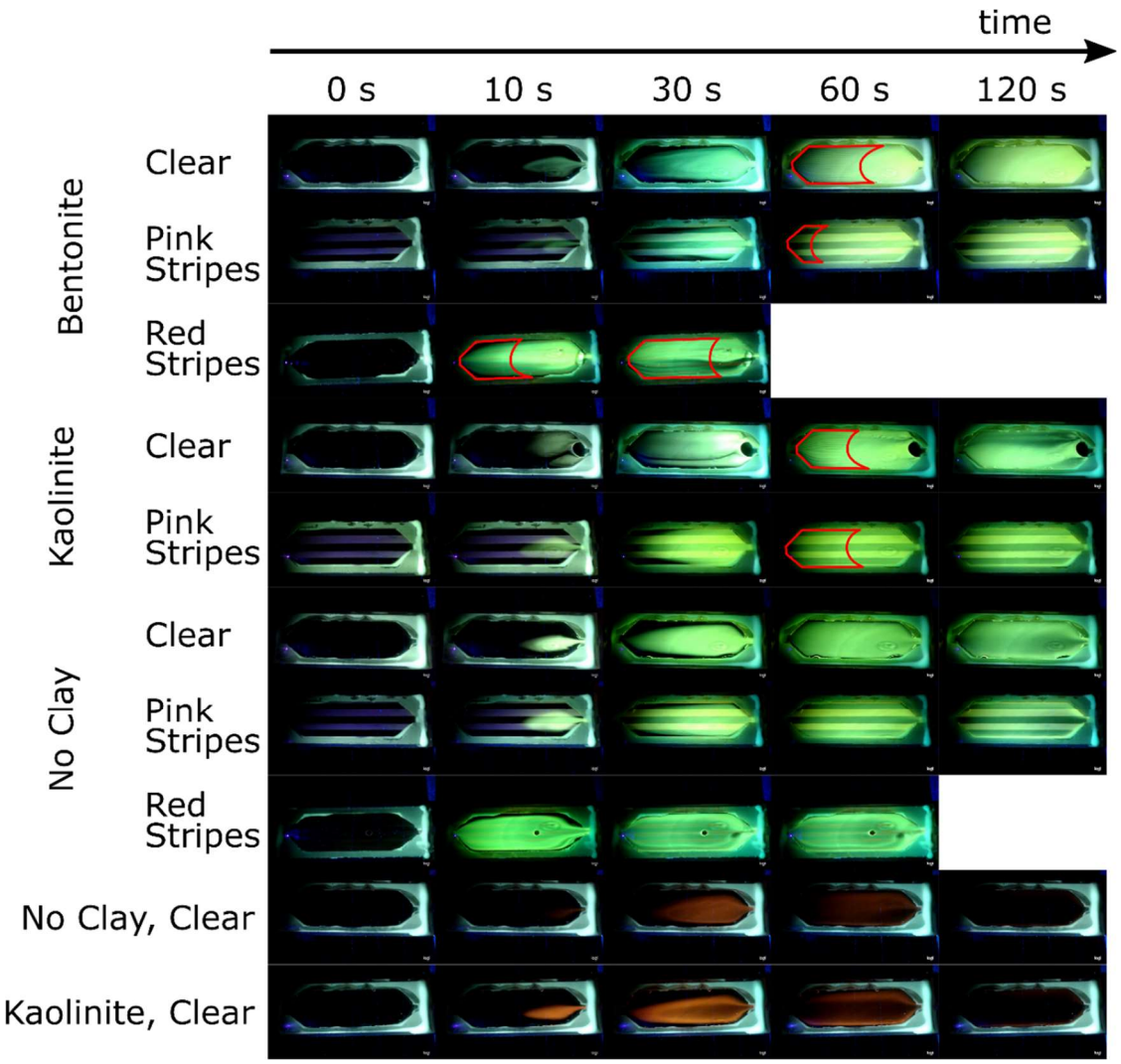

Figure 6-31: Time steps of all fluorescent clay flow experiments. Red outlined sections indicate presence of linearly separated flow patterns. Air bubbles are visible in fluorescein/kaolinite/clear and fluorescein/no clay/red stripes.

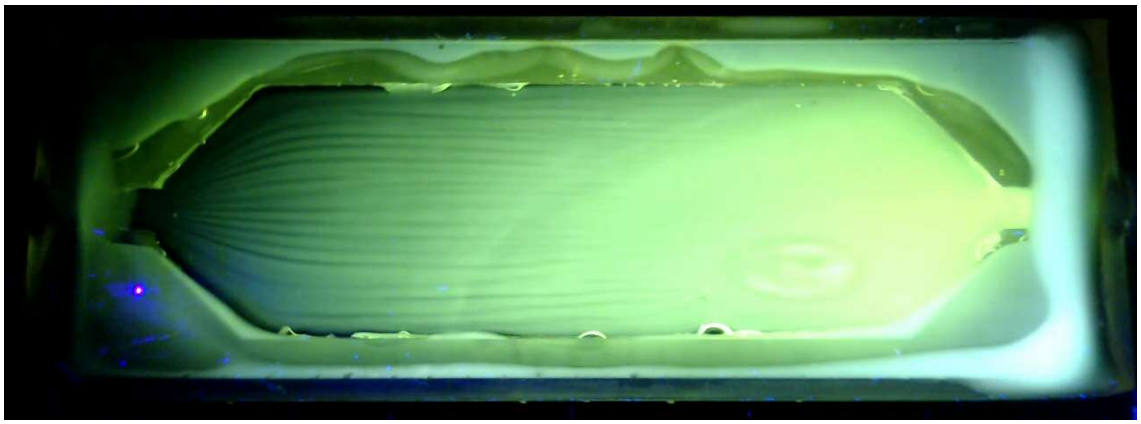

Figure 6-32: Linearly separated flow pattern seen at 60 s in fluorescein/bentonite flow conditions.

When the cells which were printed in one piece were tested with the fluorescent flow, the fluorescence was not seen, and hence the fluid flow pattern could not be monitored. This is

likely due to the fact that the resin curing is catalysed by UV, and although the resin was cured thoroughly following printing, it is likely that some of the resin remained able to further absorb the UV light and prevent the dyes fluorescing. These tests were therefore not continued, as the planned CT flow experiments were designed to use a very similar flow cell setup and therefore would provide a way of monitoring particle and fluid flow which was not dependent on UV light penetrating the cells.

6.4.4 Cation exchanging bentonite

The images obtained are shown below:

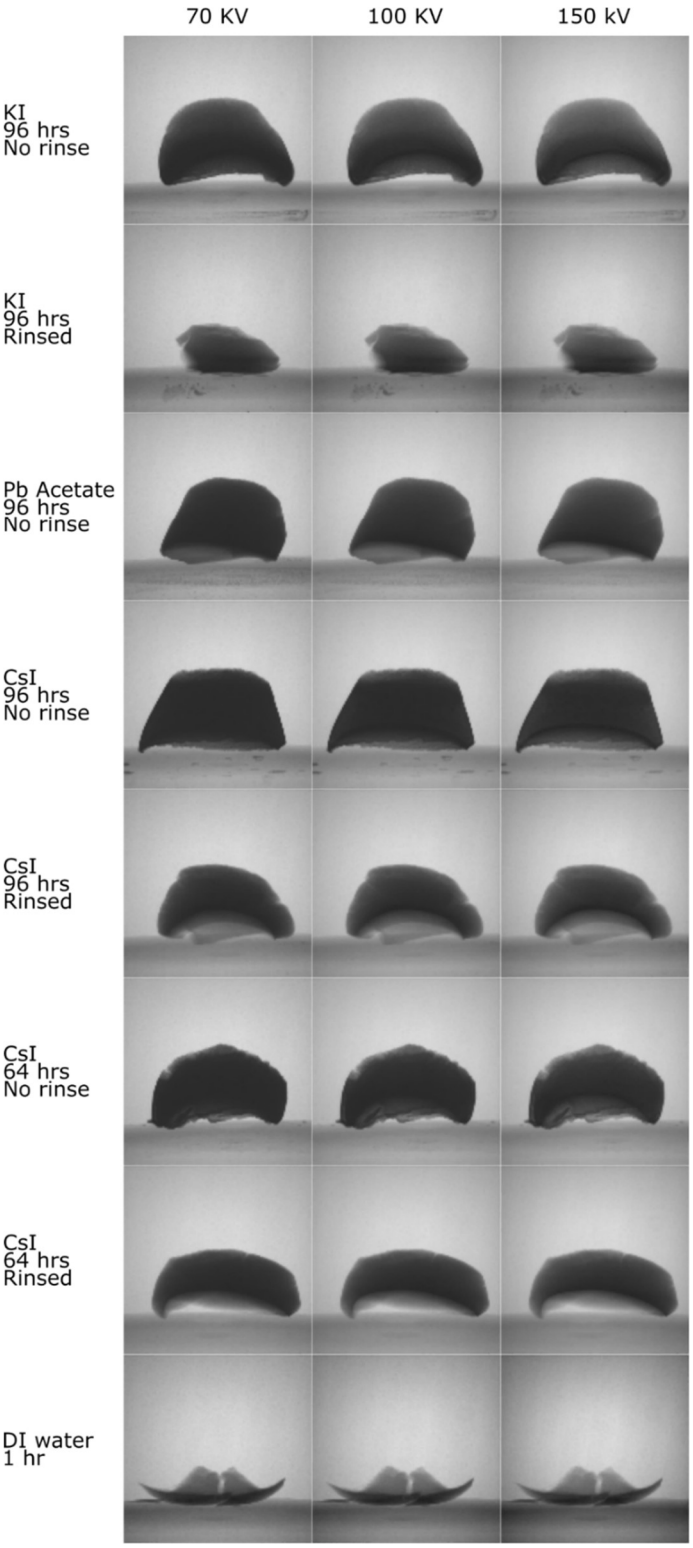

Figure 6-33: Micro-CT images of clay doped with various heavy metal salts.

The images were opened with imageJ and a histogram of the whole image, and a plot profile of the pellet at approximately ¼ of the pellet's height from the top of the pellet was taken. A cut-

off at a grey value of 100 (black = 0, white = 255) was taken – this selects the pellet from the background of the image. A further cut-off was taken at 50 grey value, and the percentage of the count at values below 100 which were also below 50 was calculated. This shows which pellet images contain a higher proportion of darker pixels, and hence give higher contrast (Figure 6-34). This analysis gives a good assessment of the effectiveness of the heavy metal cation exchange – it can be seen that all pellets give a higher contrast than the untreated pellet, that rinsing gives a lower contrast, and that longer treatment time is more effective than shorter. It can also be seen that a lower voltage gives a higher contrast, and hence for good contrast for these experiments, the lowest possible voltage should be selected.

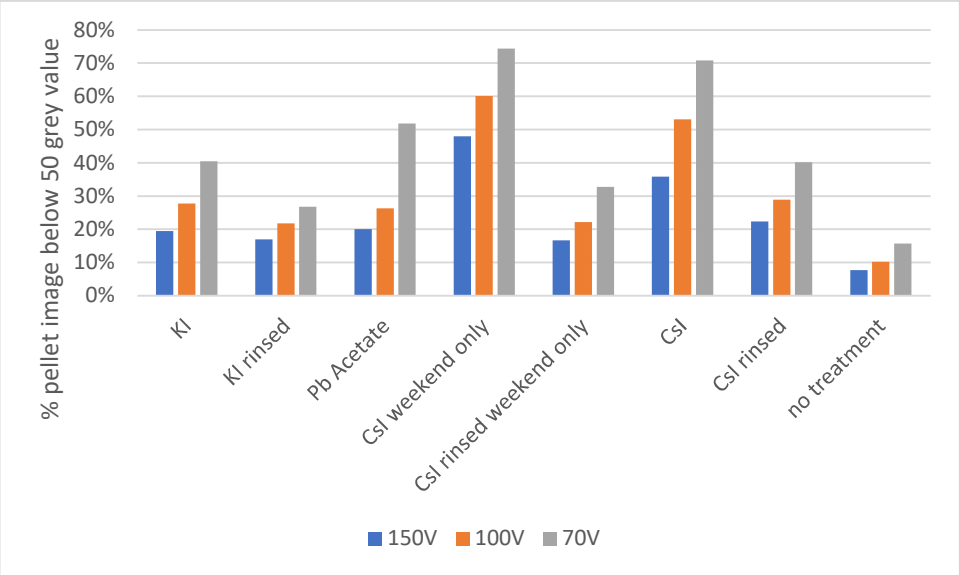

Figure 6-34: Percentage of pellet image below 50 grey value.

To assess the plot profiles, an average was taken of the centre 40 pixels (in the case of the pellets with no treatment, which cracked in the centre, and average was taken of the 40 pixels to the left of the crack). These are plotted in Figure 6-35. This analysis suggests that CsI may be the most appropriate salt to use to dope the clay as it consistently gives the highest contrast, and also gives consistently high contrast across the range of voltages scanned, giving the potential for a higher or lower voltage to be used while still giving good contrast.

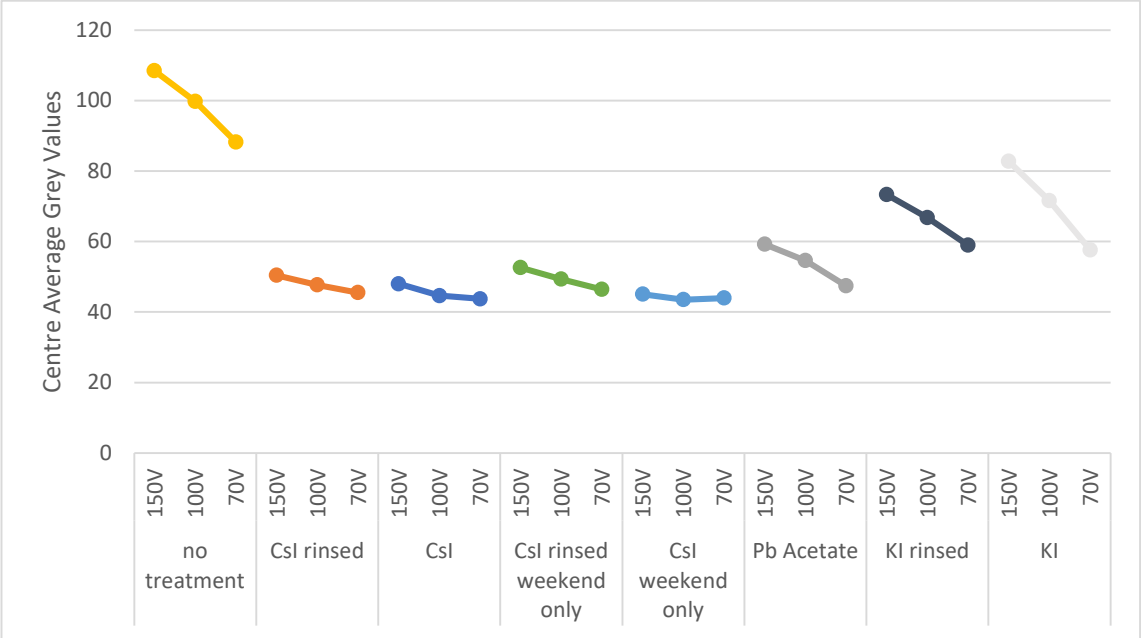

Figure 6-35: Grey values averaged over the centre of the top 1/4 of clay pellet images.

When used for a flow test, the particles will be suspended in either deionised water or a salt solution; if rinsing the particles in deionised water following suspension repeatedly overnight in heavy salt solution had resulted in the heavy salt becoming leached from the clay, the salt would have not been appropriate for use in this test. The salt in all cases remained bound to the clay, suggesting that all salts tested with rinsing should be effective in producing high contrast.

6.4.5 Particle tracking in 3D prints

Despite being able to dope bentonite with CsI to give a higher contrast, when the doped bentonite was dispersed in water and introduced to the 3D print, no particles, or flow, could be seen. An alternative naturally high-density mineral was therefore sought, which would give sufficient individual particle contrast to show up easily in the scans, and that ideally had a known particle size distribution so as to aid tracking. The oil industry regularly uses high density particles of a known size distribution to increase the density of drilling fluids, and so a selection of industry standard sized minerals were obtained and tested. Initial tests were carried out with 25 g/l API barite and 6.25 g/l xanthan gum (DUO-VIS) in water, at 100 KV, 10W with binning set to 2 and angle varying from 0° to 1° over the duration of the scan. The following images, at a flow rate of 0.1 ml/minute, were obtained:

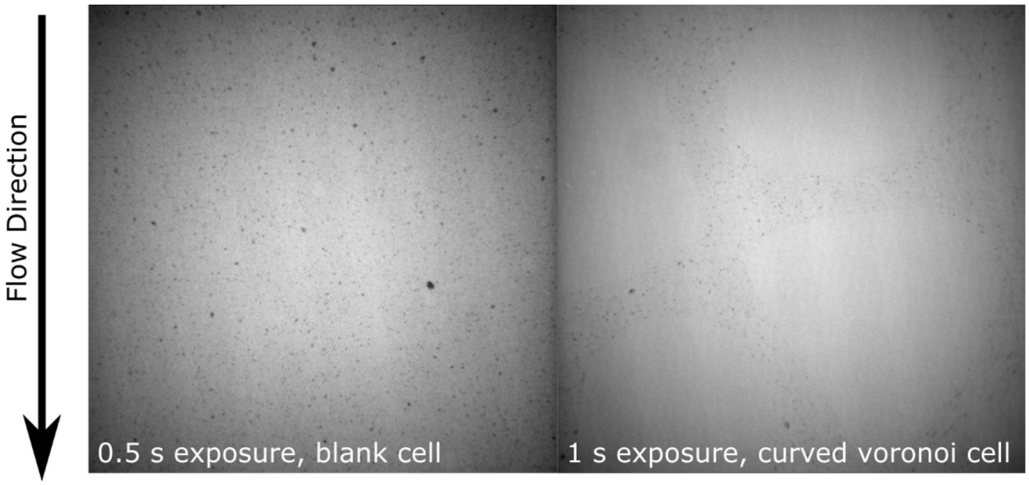

Figure 6-36: 25 g/l API barite and6.25 g/l xanthan gum in water, micro-CT flow test. Different exposure times showing definition of particles. 12.35 µm/pixel blank cell, 10.95 µm/pixel curved Voronoi cell.

Individual particles are clearly visible in the images obtained, and upon processing the blank cell scan with the particle tracking module in the MosaicSuite plugin in imageJ, individual particles were also able to be tracked:

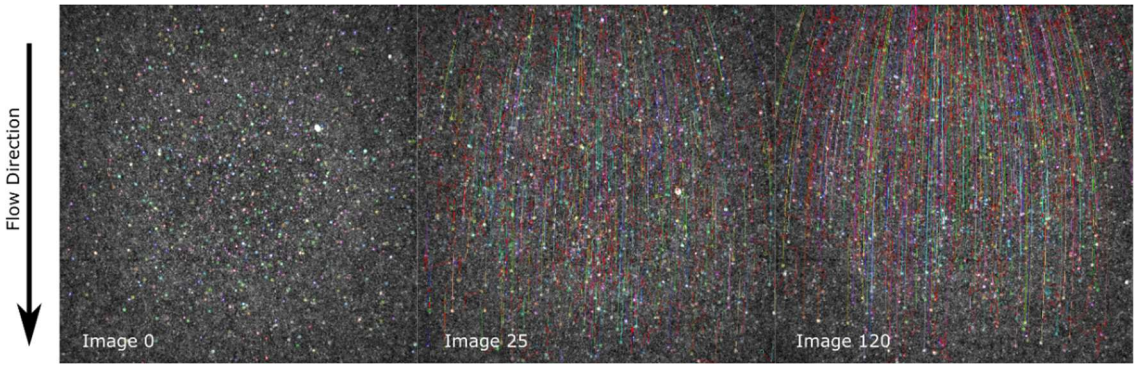

Figure 6-37: Individual particle traces tracking particle movement from one image to the next. Images require inversion for use in the particle tracking plugin.

The alternative sized minerals were scanned using the same parameters as above, with the scan duration set to 1 second per image. The magnification for all minerals was 9.72 µm/pixel (Figure 6-38). Comparing the clarity of the individual particles of these minerals to the clarity of the API barite particles, it is clear that these minerals do not give as high a contrast. Fe_2O_3 may allow individual particle tracking, but this mineral is more difficult to use than barite as it has a tendency to stain and is difficult to clean. Comparing the fine grade barite to the API barite, it is also clear that the particles are less distinct due to the smaller size. There may be an advantage to using this material where smaller flow pathways are being investigated, and where a higher resolution is possible, but API barite was found to be the optimum mineral for use in the XRadia/Zeiss VersaXRM 410 for the particular conditions under study.

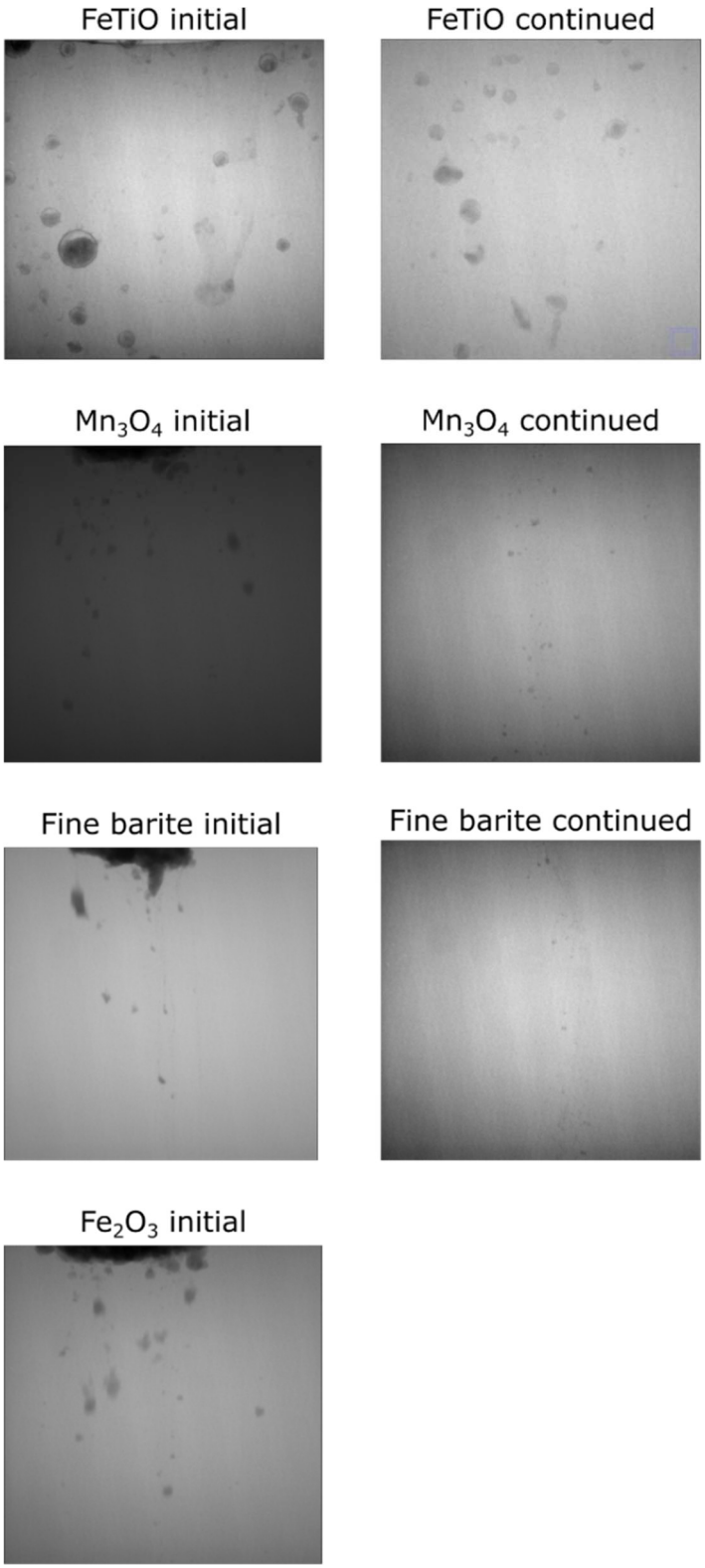

Figure 6-38: Alternative sized minerals imaged after addition of sized mineral and 10 - 15 minutes after addition, where mineral was still settling.

Initial testing was carried out with a xanthan gum solution. The xanthan gum gives a non-Newtonian flow with a relatively high yield stress which allows suspension of the barite particles

in static flow, but gives a relatively low viscosity under flow conditions and is commonly used in the preparation of water-based drilling fluids. These properties make it an ideal candidate for a suitable fluid for flow experiments. However, it was found that initiating the flow, to overcome the yield stress along approximately 2 m of tubing from the outside of the scanner to the flow cell, that the flow was not initiated at the flow cell at the rate and at the time intended. The fluid started flowing sometime after the syringe pump had started, and the flow was visibly faster initially, then slowed after a time. As the time for flow to initiate and the speed at which flow progressed initially was not repeatable an alternative was sought. Golden syrup is a Newtonian fluid, commonly used to simulate lava flow in experimental volcanology (Bagdassarov and Pinkerton, 2004) and hence has well characterised rheology at a variety of dilutions. API barite in various golden syrup dilutions was recorded in the micro-CT scanner. It was found that 50% and 75% w/w golden syrup/water did not suspend barite sufficiently for the barite to be held at the level of the x-ray source for long enough to be imaged. 90% golden syrup gave some suspension, but it was insufficient to keep all particles stationary when flow ceased. It was also noted that a particle size gradient developed in the tubing as the flow experiments proceeded, and that during cessation of flow, the larger particles sank but the smaller particles rose. It is assumed then that the sinking particles induce flow conditions in the tubing and as, at this point, the volume in the tubing is fixed, the volume containing particles sufficiently small to be suspended by the syrup begins to flow in the opposite direction – this is shown in Figure 6-39. Golden syrup was also found to be denser than the xanthan gum solution, and hence reduced the contrast between it and the sized mineral particles making particle tracking more difficult; a comparison between API barite in xanthan gum vs golden syrup is shown in Figure 6-40.

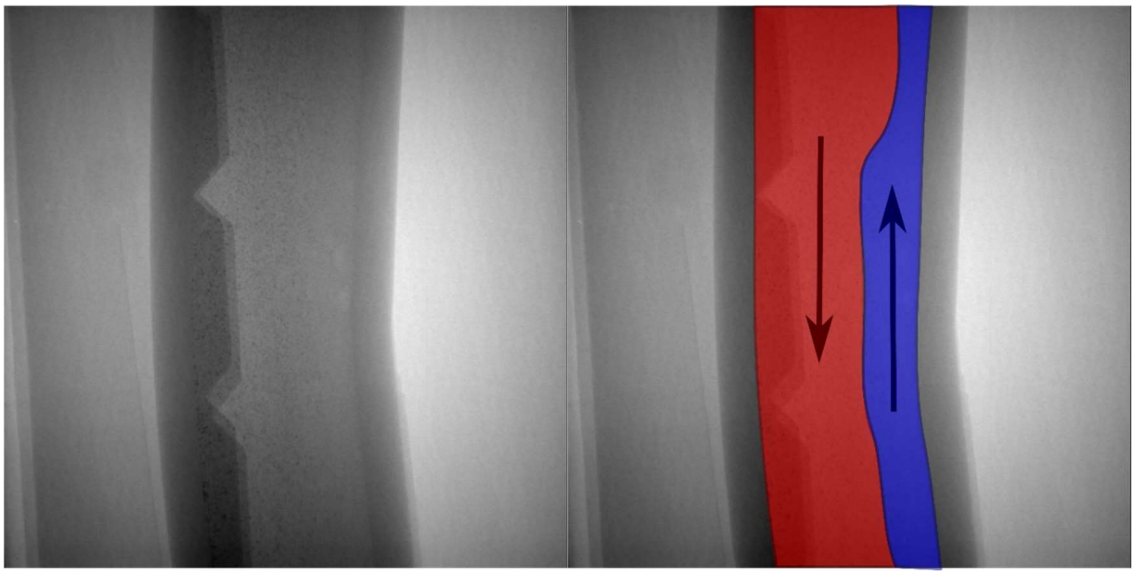

Figure 6-39: Induced flow due to gravity settling of larger barite particles in tubing in micro-CT. Larger barite inducing downwards flow (red), smaller particles experiencing upward flow (blue). 100 KV, 10 W, 1 s/image with binning set to 2 and angle varying from 0° to 1° over the duration of the scan. 13.18 µm/pixel.

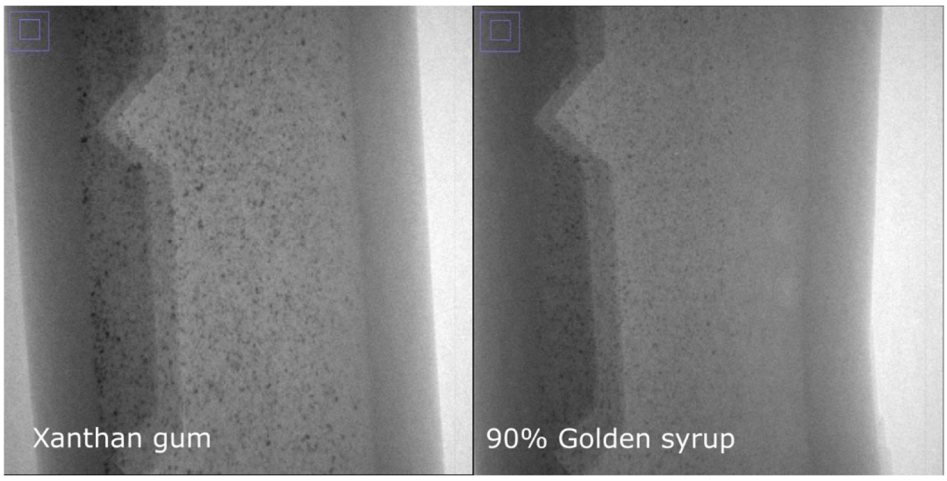

Figure 6-40: API barite in 6.25 g/l xanthan gum and 90% w/w golden syrup/water. 100 KV, 10 W, 1 s/image with binning set to 2 and angle varying from 0° to 1° over the duration of the scan. 13.18 µm/pixel.

Following this testing, it was concluded that API barite in xanthan gum solution may be the optimal combination for particle tracking, although for quantitative tracking the syringe pump should be placed as close to the flow cell as possible to reduce the initial stress required to initiate flow.

Particle tracking was carried out with API barite in xanthan gum solution for the lines and the curved Voronoi cell. The regions of these cells which were scanned are shown in Figure 6-41.

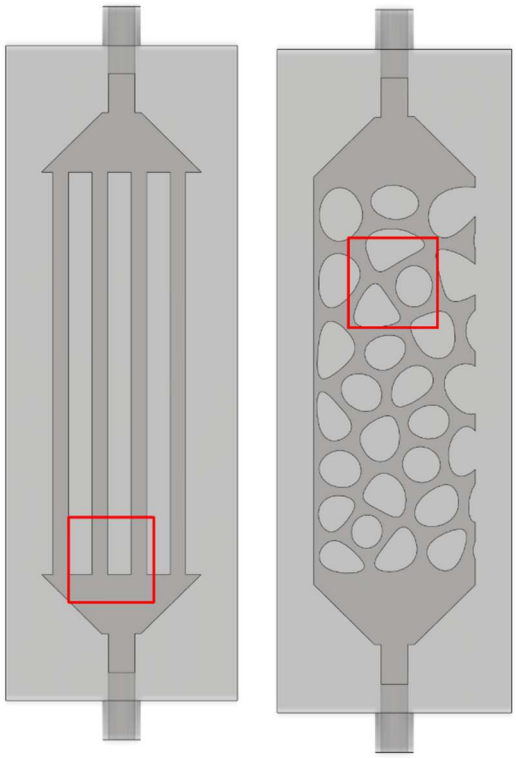

Figure 6-41: Scanned regions of interest (red boxes) for straight and curved Voronoi cells.

The cells were pre-filled with the xanthan gum solution without API barite, to allow initial flow to be visualised. The scans were carried out at 100 kV, 10 W at 1 s per image, binning of 2 and resolution 10.95 µm/pixel. The flow rate was set to 0.01 cm^3/min. During the lines cell scanning, air bubbles were present in the cell. However, this gave rise to interesting flow patterns during the test, shown in Figure 6-42 and Figure 6-43. The air bubbles are shown in Figure 6-44. It can be seen that the flow through the left channel was prevented by the presence of the bubble in that channel. The bubble began moving in image 80, but flow was not seen in the particle movement until image 250 due to the pre-filling of the cell. However, clear flow preference for the middle two channels at this point of the flow test was noted. This test however demonstrates some limitations of the particle tracking software. Firstly, the absence of particles in the initial image (image 0, Figure 6-42) caused the particle tracking software to artificially create particles. The software looks for areas in the image that are brighter than a percentage brightness threshold set by the user. This threshold set is applied to all images in the scan. In order to track the fast-moving particles in images 300+, the threshold needed to be set sufficiently low so that these particles could be detected. However, in the initial images, where there are few bright particles, the software created artificial particles. This caused artificial particle traces to be formed in the first 150 images, even though the threshold was set to

minimise such traces. Secondly, very few of the fast-moving particles highlighted in image 400, Figure 6-43 are visible as particle traces in Figure 6-42. The software does not track these particles effectively as the contrast is not sufficiently high to detect these particles in the presence of slower moving, and therefore higher contrast, particles. This analysis of flow patterns also shows that although xanthan gum suspends particles very effectively, the flow may again be affected in a non-predictable manner under low flow rate conditions when there are barriers to the flow such as air bubbles.

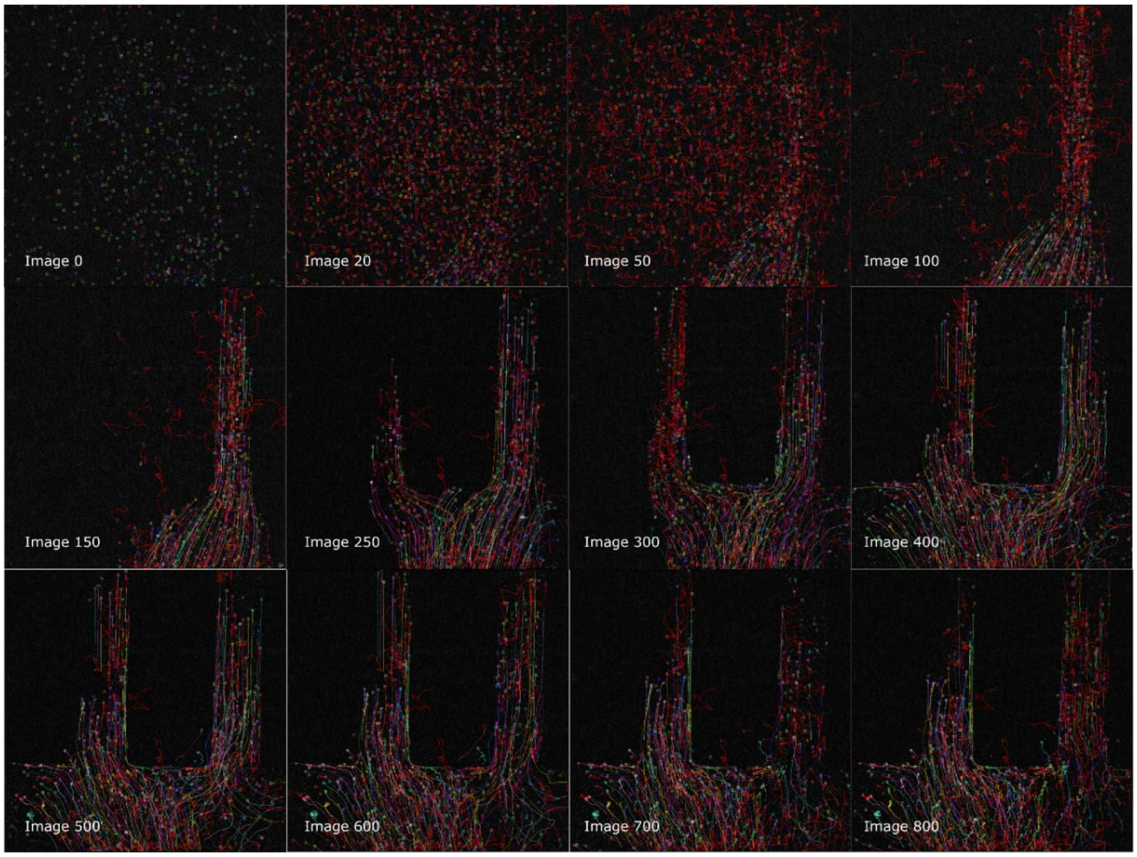

Figure 6-42: Particle tracking from micro-CT scans in lines cell. Images are taken from 1000 image scan. Coloured lines indicate tracked particle movement.

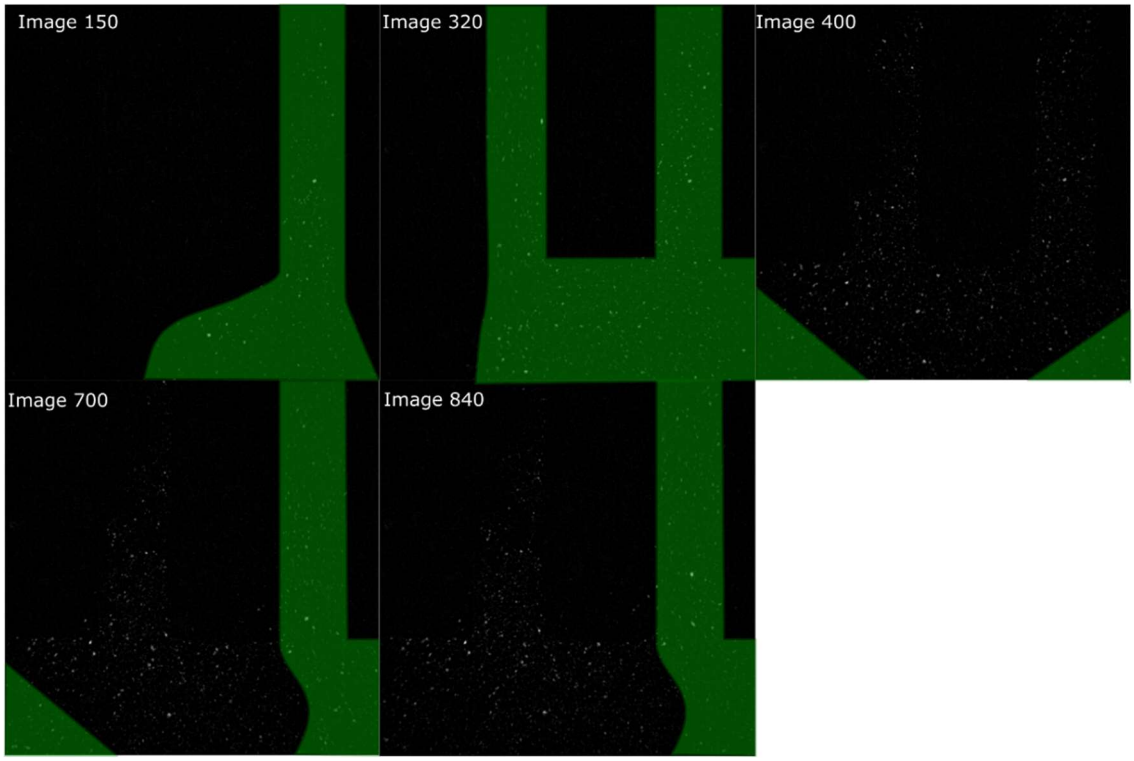

Figure 6-43: Micro-CT scans of particle flow in lines cell. Green areas indicate areas in the images which show particle movement between that image and the next shown.

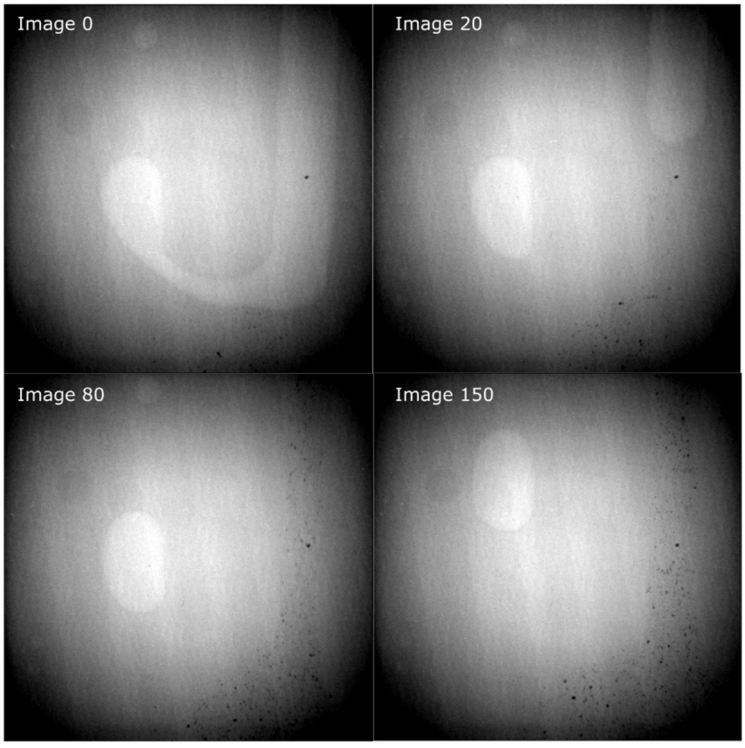

Figure 6-44: Bubble flow in lines flow cell.

Considering now the flow in the curved Voronoi cell, the particle tracking can be seen to be much improved (Figure 6-45). Multiple images are not given as the particle flow remained stable throughout the test, and this image was representative of the whole flow. Again however, the very fast moving particles (at the left side of the image) were not as well tracked due to similar contrast issues. The slowest moving particles are shown in the areas with a lack of long smooth particle traces; these were assumed to be areas of lowest flow.

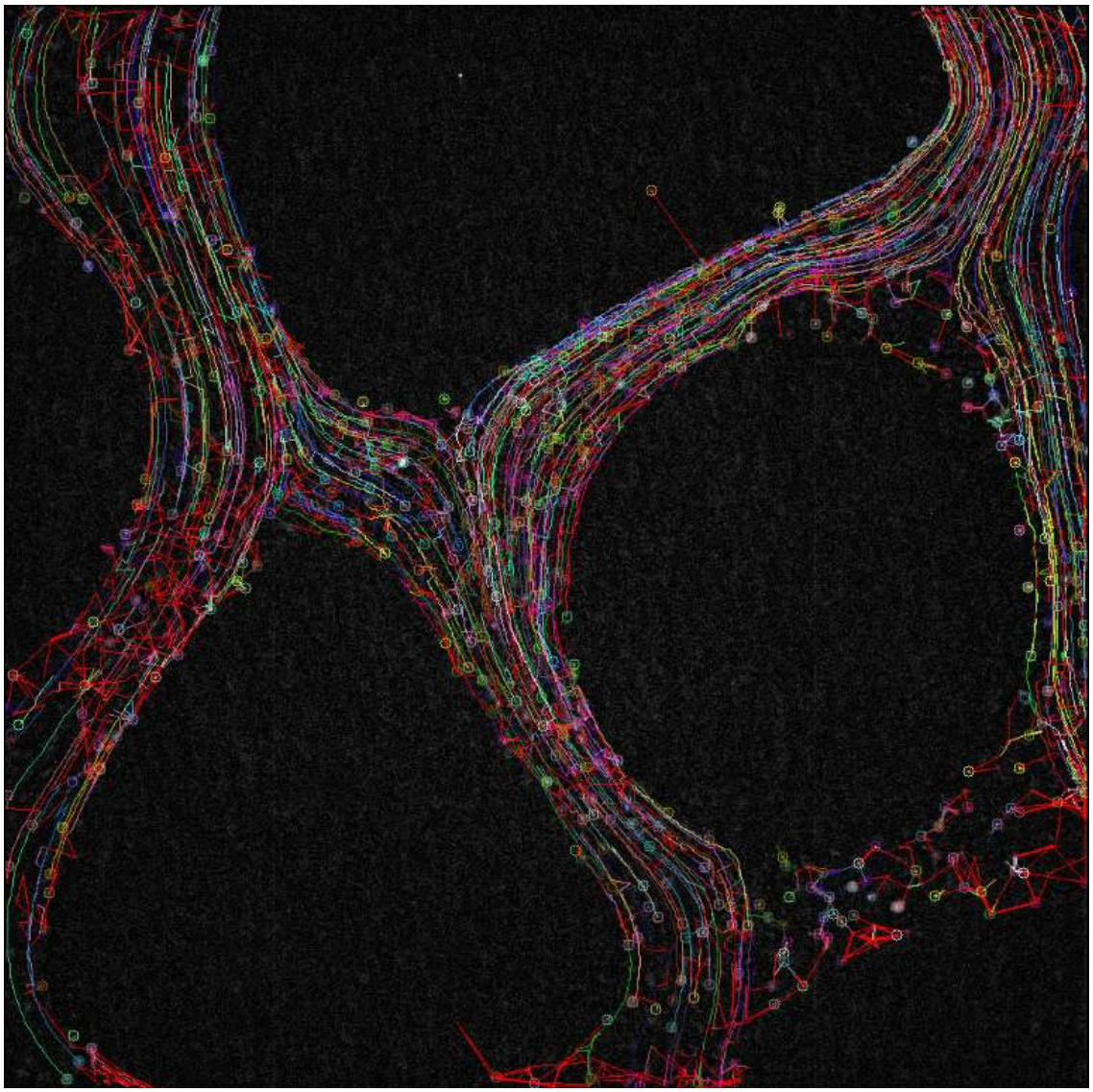

Figure 6-45: Micro-CT particle flow with particle tracking in curved Voronoi cell. Coloured lines represent individual particle tracks.

6.4.6 Simulation of flow in 3D prints

Simulations were run with Autodesk CFD 2021 on flow in various flow cells, looking at water, 90% w/w golden syrup/water and 6.25 g/l xanthan gum in DI water. In order to accurately model the flow, the viscosity of the fluids to be modelled were required. Water was available in the

fluid library of the software. Viscosity testing with the HAAKE Viscotester iQ Air gave a dynamic viscosity for 90% golden syrup of 1.40 Pa.s, which is similar to that found by Jones (2018). This, along with the density of the syrup from Jones (2018) was input as a new material into the software. Other parameters were taken as the values for glycerin (a fluid already present in the software fluid library). Xanthan gum solution is however non-Newtonian, so a shear rate vs viscosity table was taken from the viscosity testing and added as a piecewise linear model to the software, shown below. It should be noted that the viscometer used was not a low shear viscometer, and as such the low shear rates display some instability in the readings. As the tests occur over low flow rates, the shear rates encountered by the fluid are also likely to be low and may not accurately model some aspects of the flow. In order to more accurately model the fluid movement, measurement with a low shear viscometer would be needed.

Table 6-9: Shear rate vs viscosity table for 6.25 g/l xanthan gum.

Shear rate (1/s)	**Viscosity (Pa.s)**
0.013092	1.633859
0.024328	0.347564
0.045186	2.936372
0.085371	4.208371
0.159458	2.187387
0.298458	2.439387
0.559077	1.841482
1.045056	1.148517
1.957332	0.776931
3.661893	0.540317
6.852463	0.371644
12.82404	0.256944
24.00095	0.179365
44.91769	0.127206
84.06346	0.091773
157.3249	0.066807
294.4335	0.048969
551.0333	0.035541
1031.26	0.025943

1930.003	0.019362

The flow was modelled over 180 s for water, to recreate the flow seen in the fluorescent flow tests. Experimental results have only been shown for the clear cell, but simulation was carried out for all cell geometries created. In this instance, the modelled flow shows some similarities to the experimental flow results, in that a higher velocity is seen close to the inlet of the cell. However, attempts to model the spread of fluid in the patterns seen in experimental flow were not able to be obtained at the flow rates used experimentally. Additional modelling looking at the mixing of fluids flowing into the cell with fluids already present in the cell (Figure 6-47) also did not yield data which resembled the experimental data, although a gradient of mixing can be curving in a similar fashion to the solid flow/linearly separated flow seen in flow with solutions containing clay, suggesting that this sort of gradient may be seen in the cell.

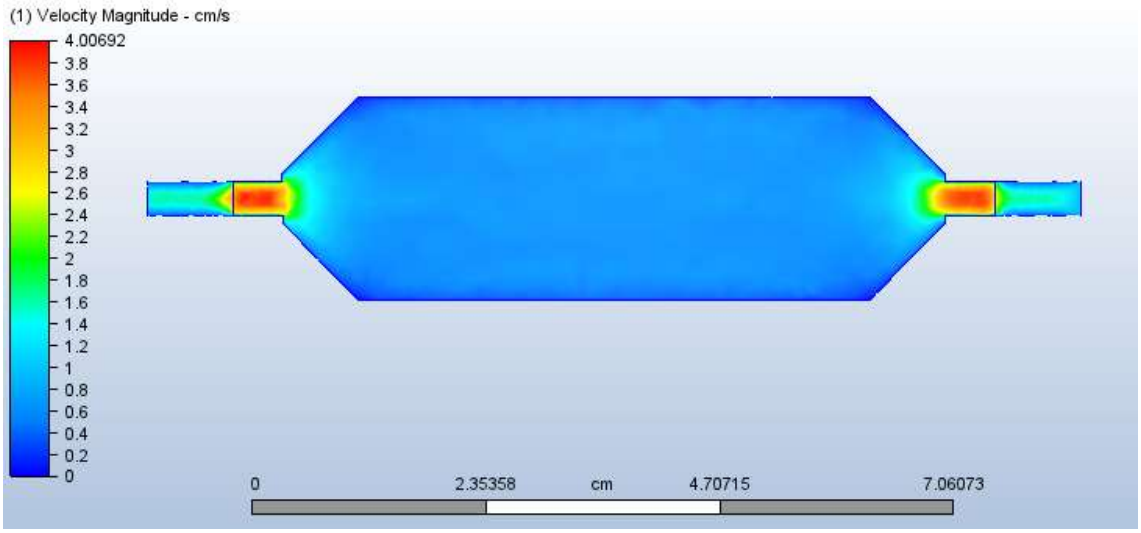

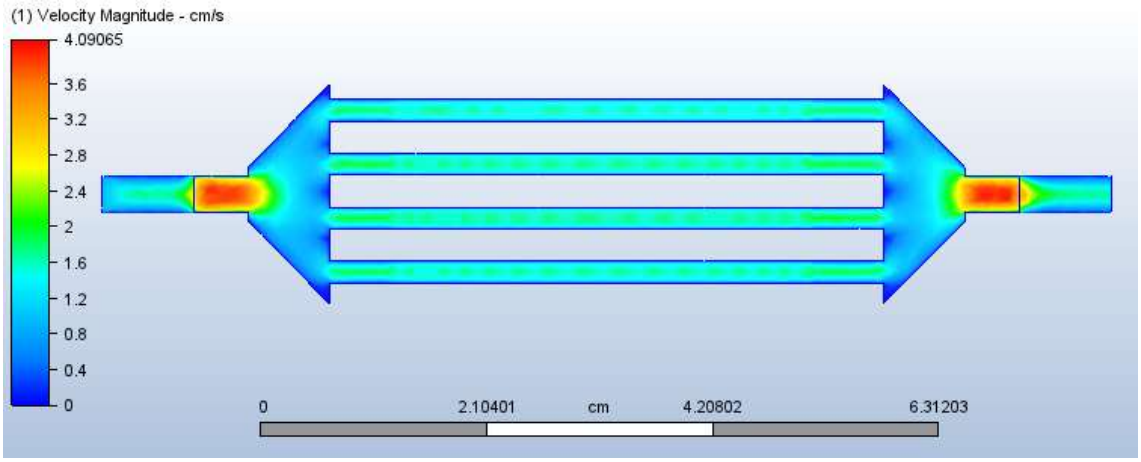

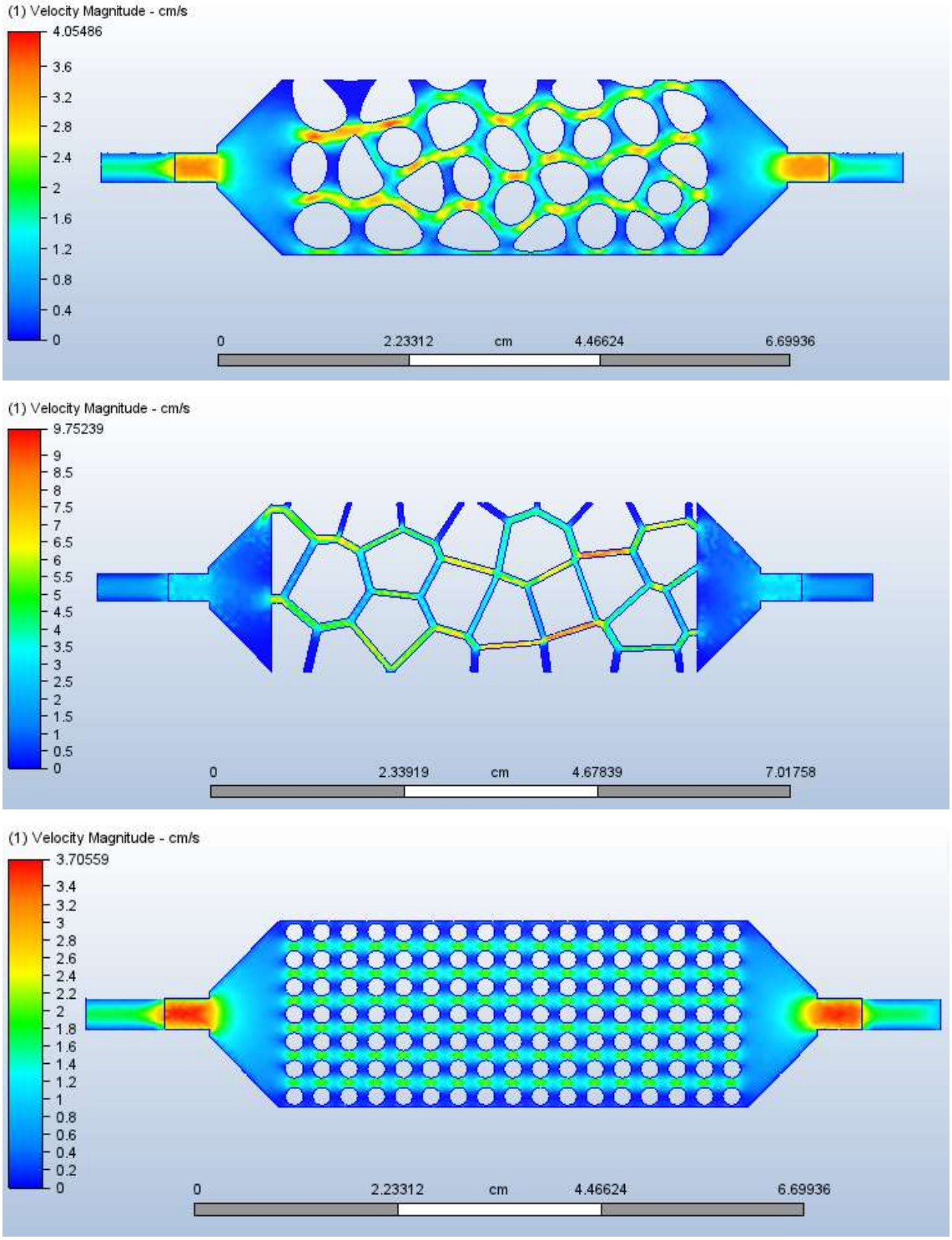

Figure 6-46: Simulation of flow of water in different flow cells after 180 s flow at 5 cm^3/minute. Flow from right to left.

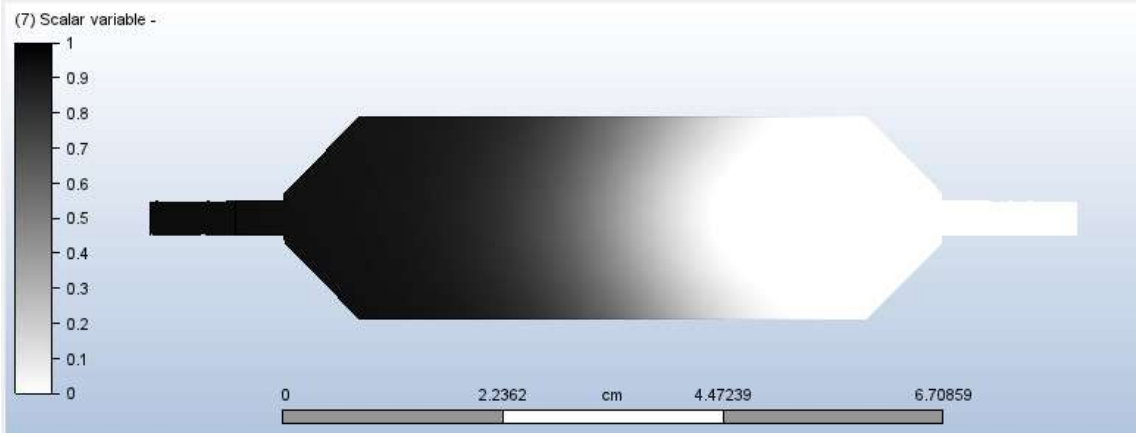

Figure 6-47: Mixing of inflowing fluid (white) with fluid already in the flow cell (black) after 10s flow at 5 cm^3/min.

The flow patterns seen in golden syrup flow closely resemble the patterns seen in water flow. This is to be expected; both are Newtonian fluids, and as such the modelling was very similar. No experimental data was available for 90% golden syrup flow, but this demonstrates the availability of modelling for these flows.

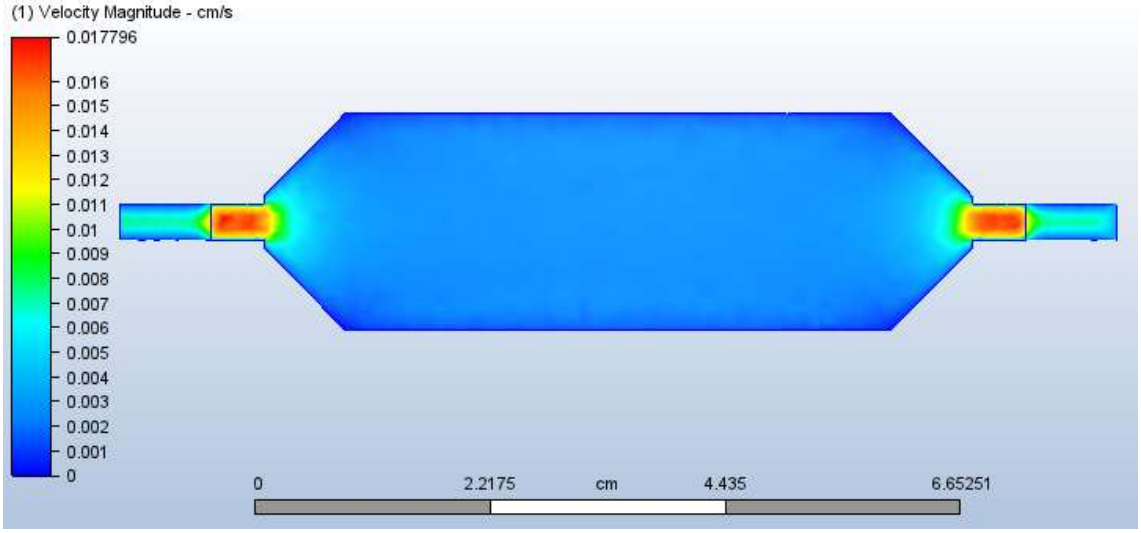
(1) Velocity Magnitude - cm/s
0.017796
0.016
0.015
0.014
0.013
0.012
0.011
0.01
0.009
0.008
0.007
0.006
0.005
0.004
0.003
0.002
0.001
0
0
2.2175
cm
4.435
6.65251

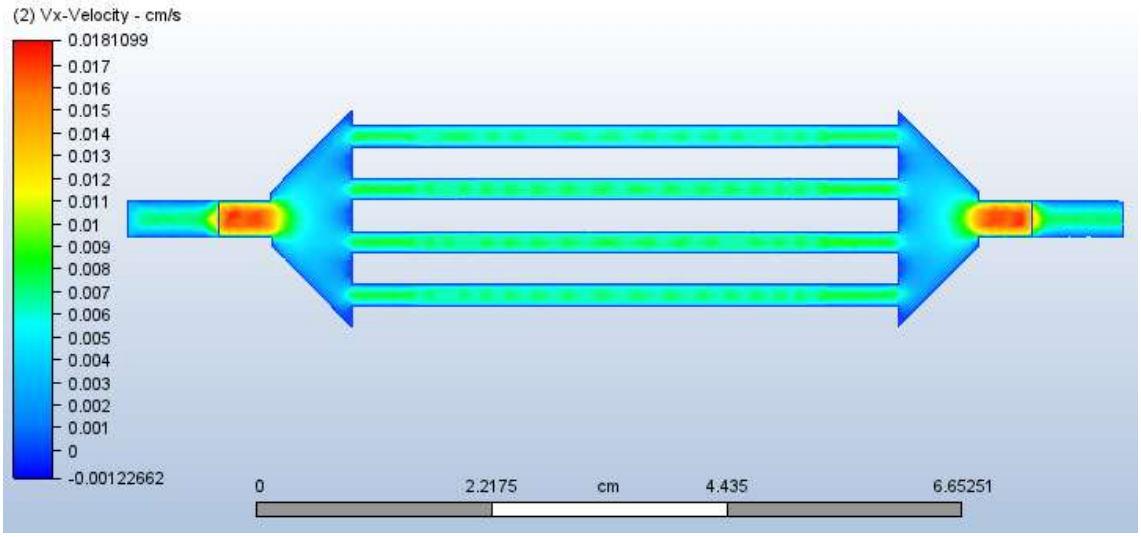
(2) Vx-Velocity - cm/s
0.0181099
0.017
0.016
0.015
0.014
0.013
0.012
0.011
0.01
0.009
0.008
0.007
0.006
0.005
0.004
0.003
0.002
0.001
0
-0.00122662
0
2.2175
cm
4.435
6.65251

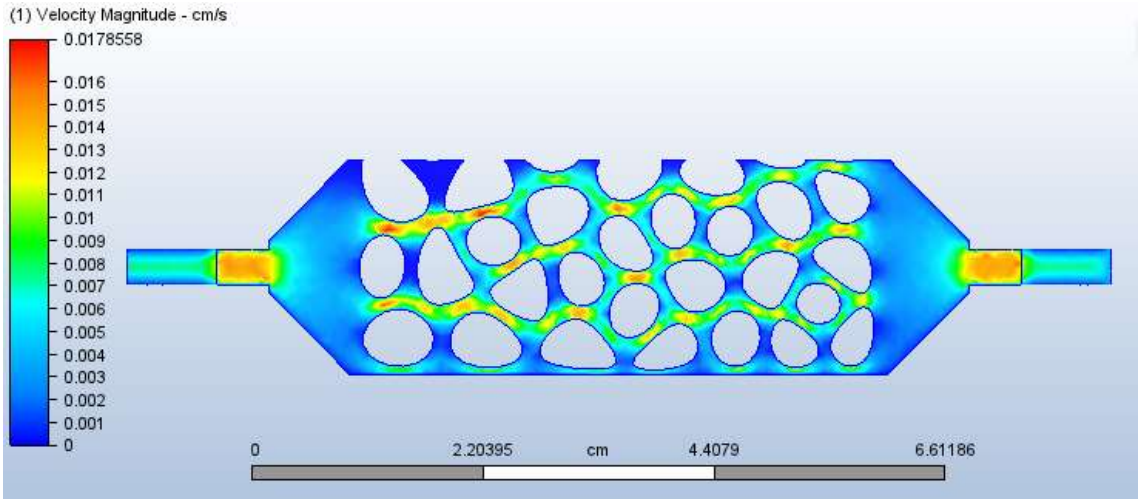
(1) Velocity Magnitude - cm/s
0.0178558
0.016
0.015
0.014
0.013
0.012
0.011
0.01
0.009
0.008
0.007
0.006
0.005
0.004
0.003
0.002
0.001
0
0
2.20395
cm
4.4079
6.61186

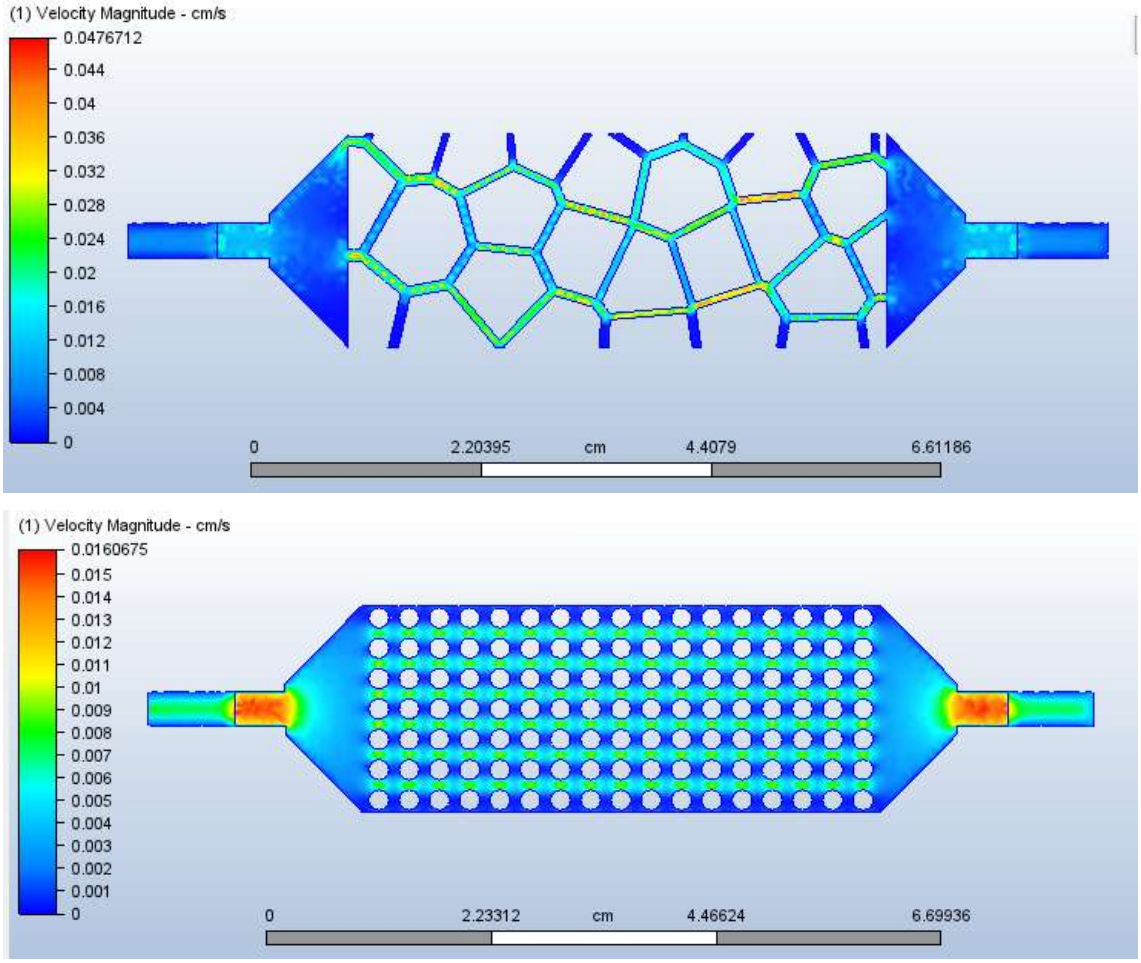

Figure 6-48: Simulation of flow of 90 % golden syrup in different flow cells after 50 s flow at 0.02 cm³/minute. Flow from right to left.

Modelling of xanthan gum flow involved the modelling of a non-Newtonian fluid and as such the fluid parameters were somewhat different. Whereas a singular viscosity could be used for modelling the Newtonian fluids, the viscosity of the xanthan gum fluid varied depending on the shear rate. This required setting the software to vary the fluid viscosity during the test – an option which required more computing time than modelling the Newtonian viscosity. Due to the variation, two sets of figures are shown for the xanthan gum flow – one after a simulated 5 s of flow (Figure 6-49) and the other after the total 50 s flow (Figure 6-50). It was found that for both the xanthan gum and golden syrup models, steady flow was obtained within the first 10 s – the model was continued for the full time, but could have been shortened. Again, these models very closely resemble the flow patterns obtained for both water and golden syrup. There is also very little difference between the flows seen at 5 s and at 50 s – in the case of the lines and straight Voronoi cells, the maximum flow rate seen is slightly higher at 5 s than 50 s, but no great variation is seen. Visualising the initial flow at earlier times is possible by reducing the time step,

but as the scanning occurs at a rate of approximately one image every 3 to 4 seconds, a higher resolution simulation is unlikely to give any further information.

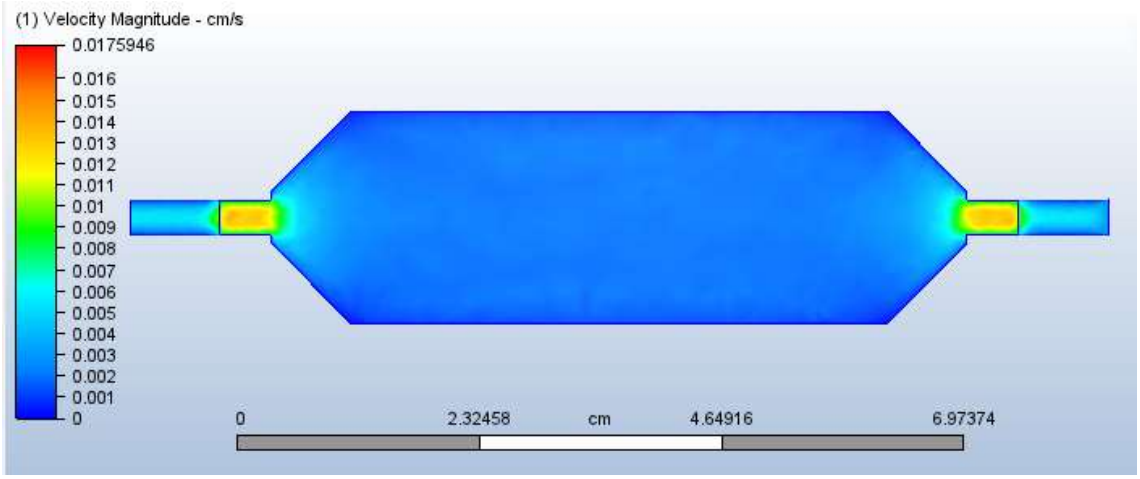

.

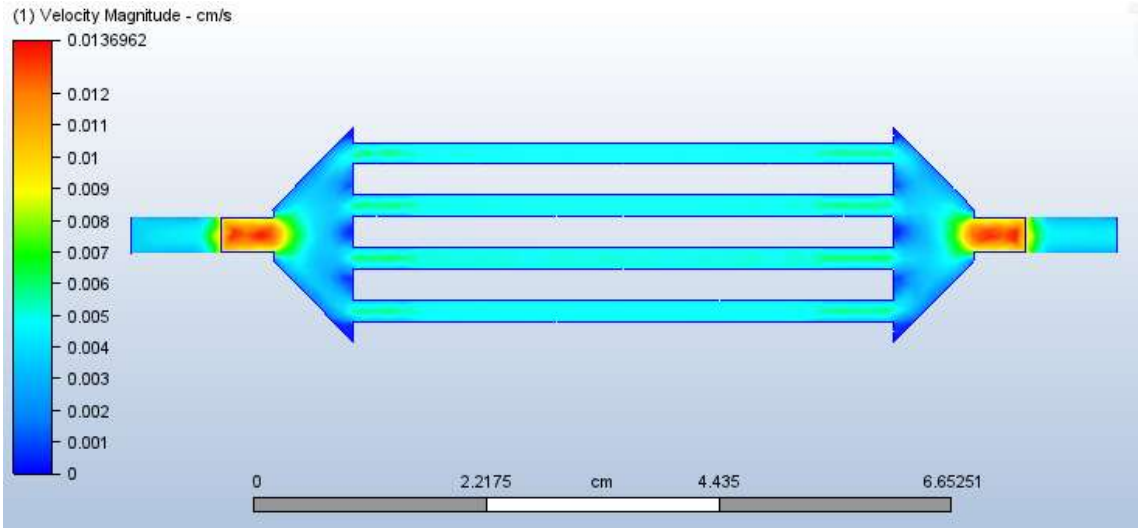

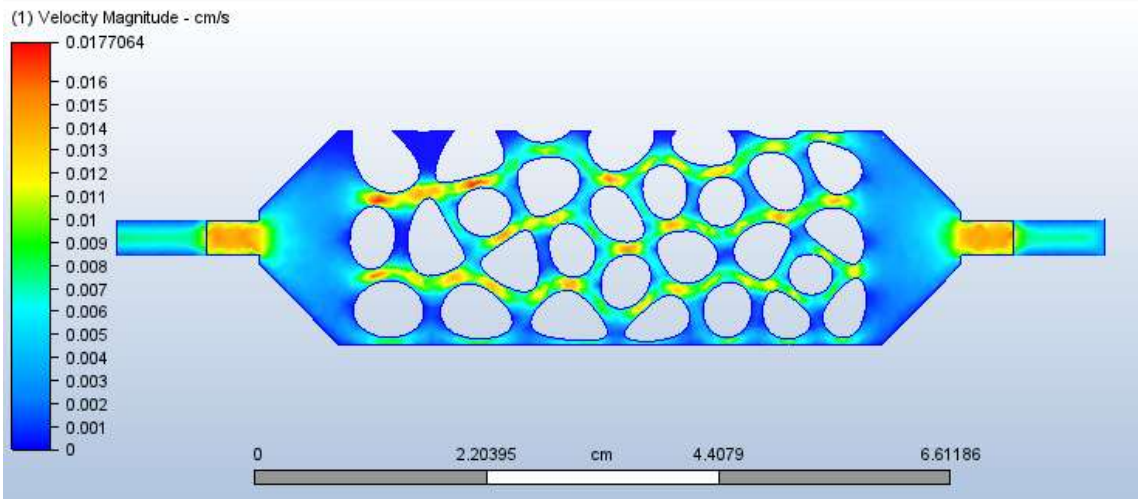

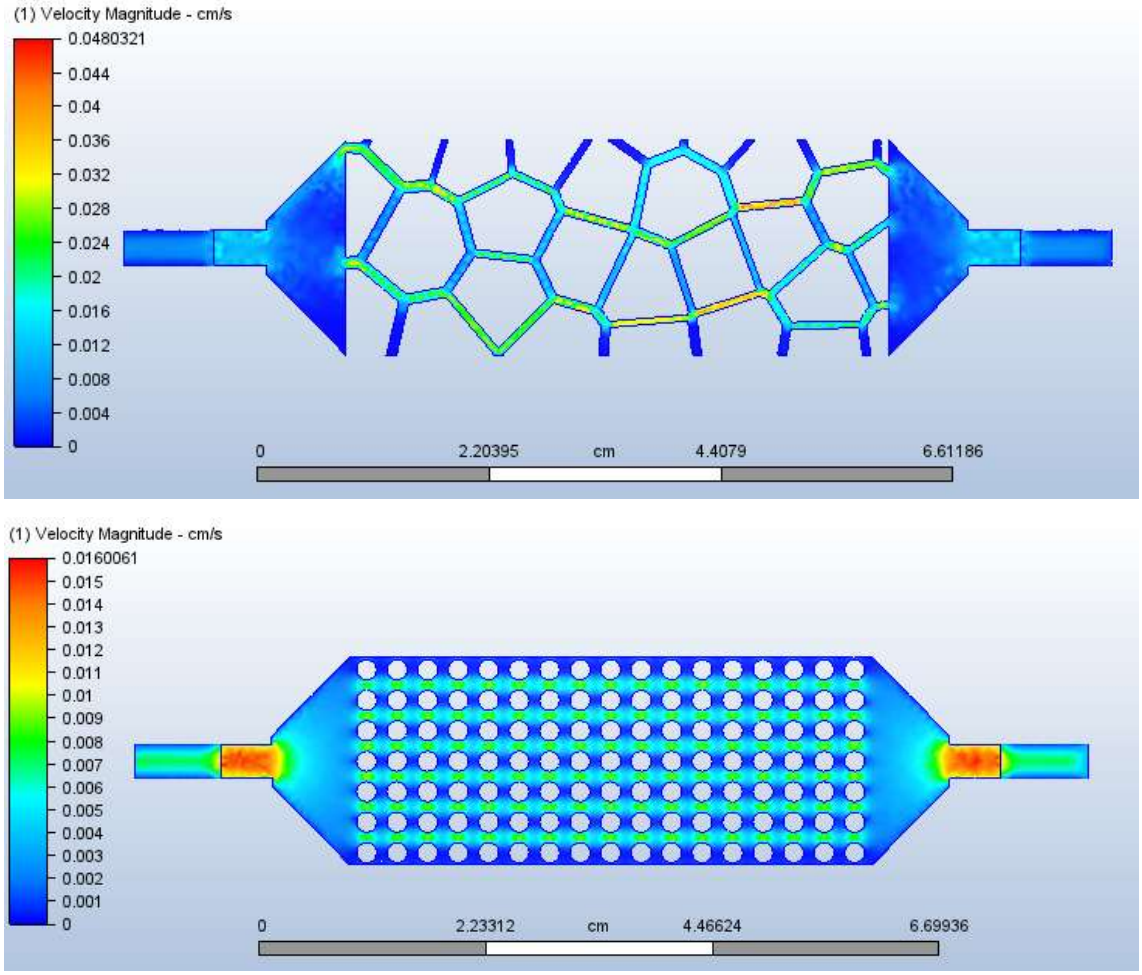

Figure 6-49: Simulation of flow of 6.25 g/l xanthan gum in different flow cells after 5 s flow at 0.02 cm³/minute. Flow from right to left.

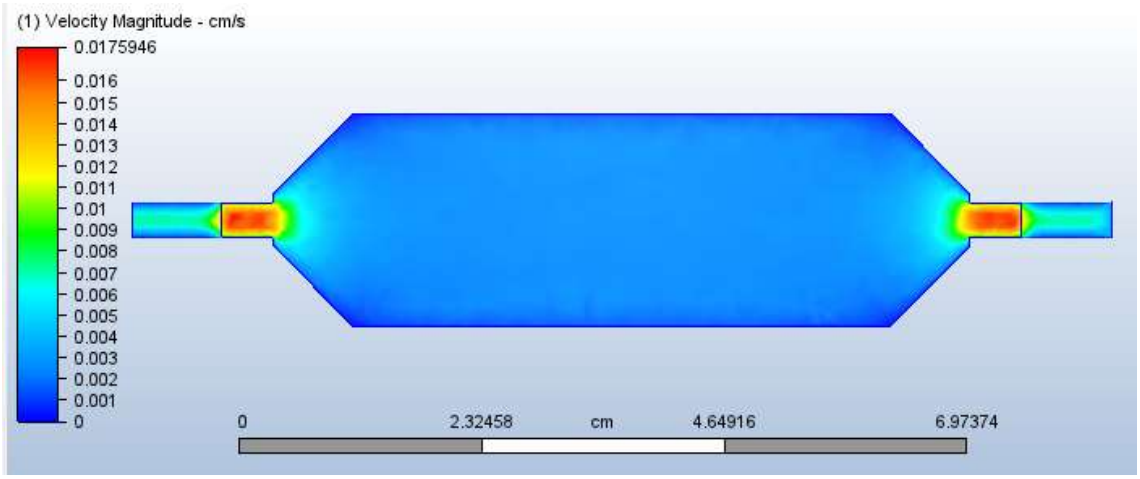
(1) Velocity Magnitude - cm/s
0.0175946
0.016
0.015
0.014
0.013
0.012
0.011
0.01
0.009
0.008
0.007
0.006
0.005
0.004
0.003
0.002
0.001
0
0
2.32458
cm
4.64916
6.97374

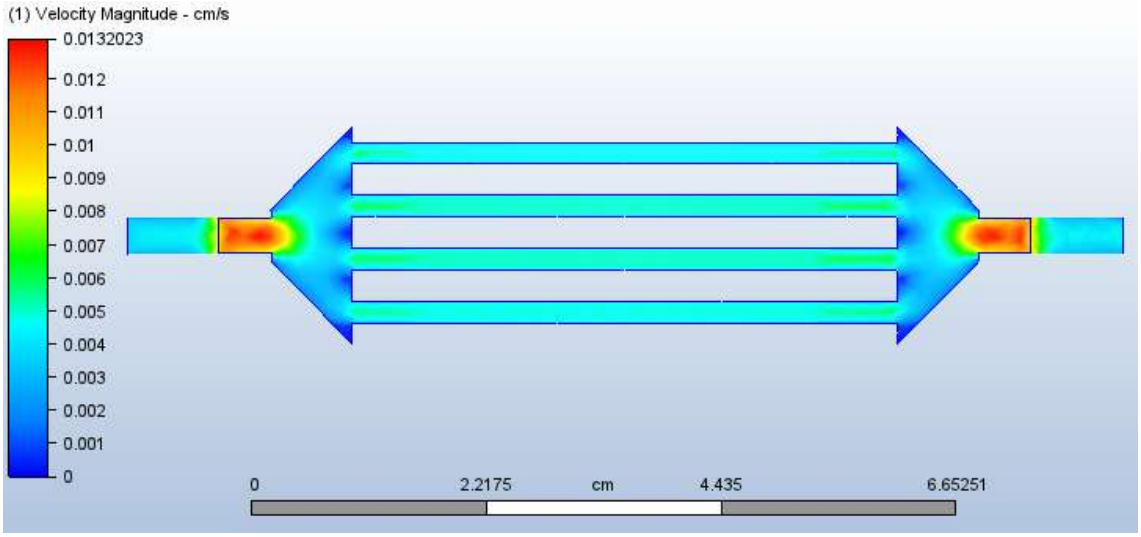
(1) Velocity Magnitude - cm/s
0.0132023
0.012
0.011
0.01
0.009
0.008
0.007
0.006
0.005
0.004
0.003
0.002
0.001
0
0
2.2175
cm
4.435
6.65251

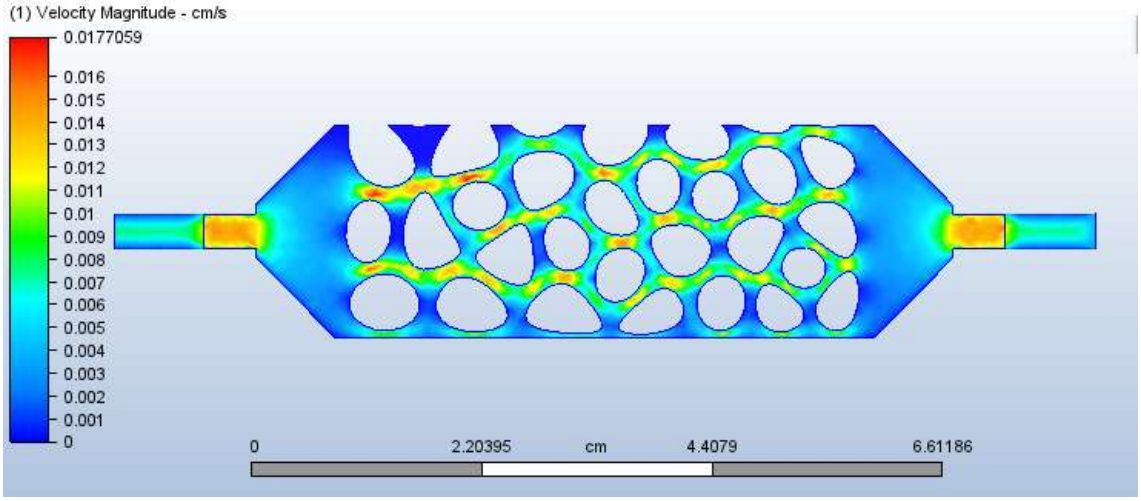
(1) Velocity Magnitude - cm/s
0.0177059
0.016
0.015
0.014
0.013
0.012
0.011
0.01
0.009
0.008
0.007
0.006
0.005
0.004
0.003
0.002
0.001
0
0
2.20395
cm
4.4079
6.61186

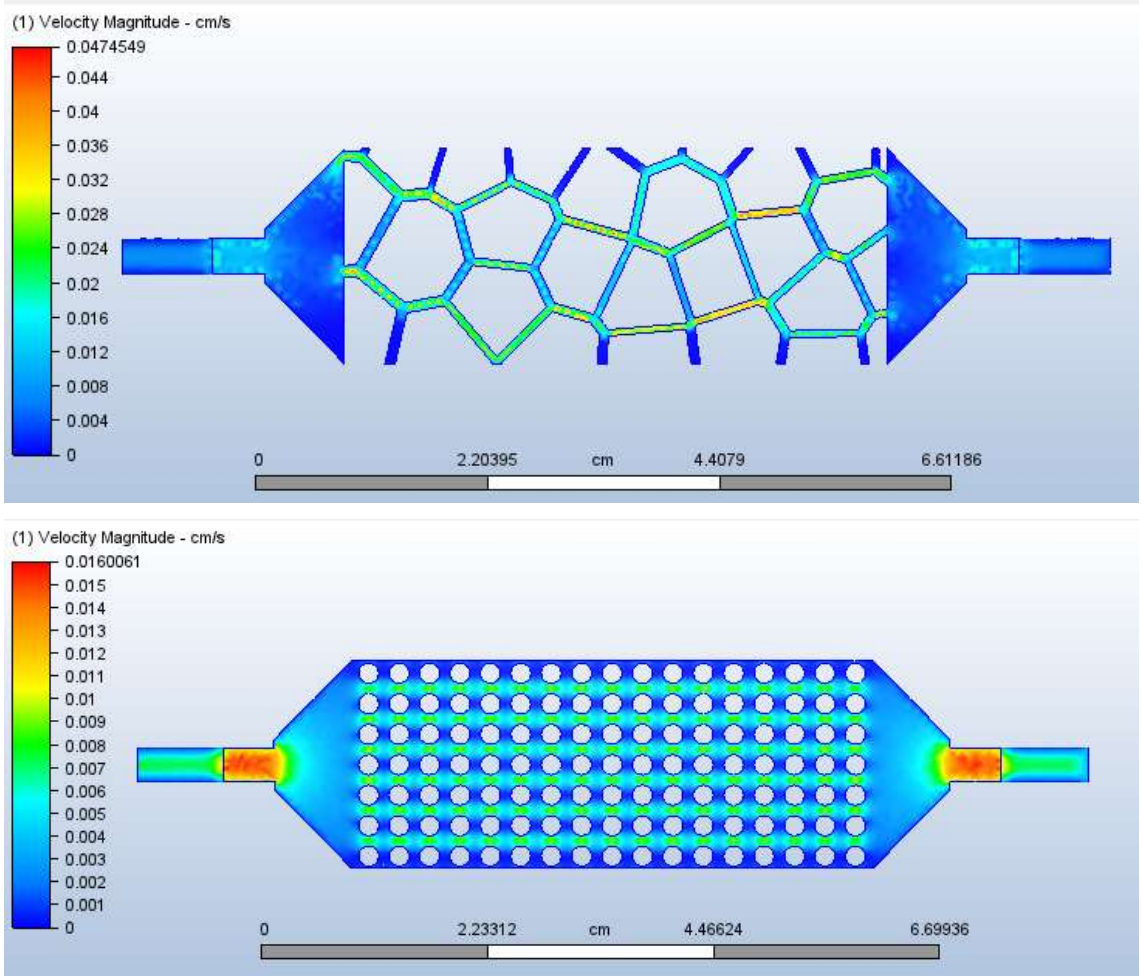

Figure 6-50: Simulation of flow of 6.25 g/l xanthan gum in different flow cells after 50 s flow at 0.02 cm³/minute. Flow from right to left.

The similarities between all the flow models, and the discrepancy between the flow seen experimentally in the flow experiments and the modelled flow for the same cell demonstrates the limitations of the Autodesk CFD software. There is not an ability to input a roughness or a wettability for the solid materials, which in the case of narrow channels and where wettability is the subject of study, seems to be problematic. Other commercial software (Ansys Fluent) was considered for this modelling, and although there are some abilities to input wettability for a solid, similar modelling limitations were seen. Additionally, modelling was carried out in Autodesk Fusion 360 – the pathway from model to simulation using Autodesk CFD rather than fluent was much more straightforward, and as there were no significant benefits seen to using Ansys Fluent over Autodesk CFD, the more straightforward pathway was followed. Other options include using opensource software such as openFOAM, which may produce more accurate models. However, even given the limitations of the modelling, Figure 6-51 and Figure 6-52 shows that the flow patterns and velocities are fairly well predicted by the software. It

should therefore be possible to simulate flow in the flow cells and compare to the flow patterns obtained to experiment, and if the cells are designed with areas of variable wettability or roughness, assess whether the wettability variation is contributing to the deviation from the expected flow pattern. Further correlation between simulation and experiment may be possible if the particle velocities could be calculated. At this time, the distance between images that the particles moved can be readily obtained, but the precise timestamp of each image cannot, and hence the velocity cannot be accurately calculated. It is hoped that either alternative analysis software or using a different micro-CT scanner may allow this data to be obtained, and hence more accurate particle tracking to be carried out.

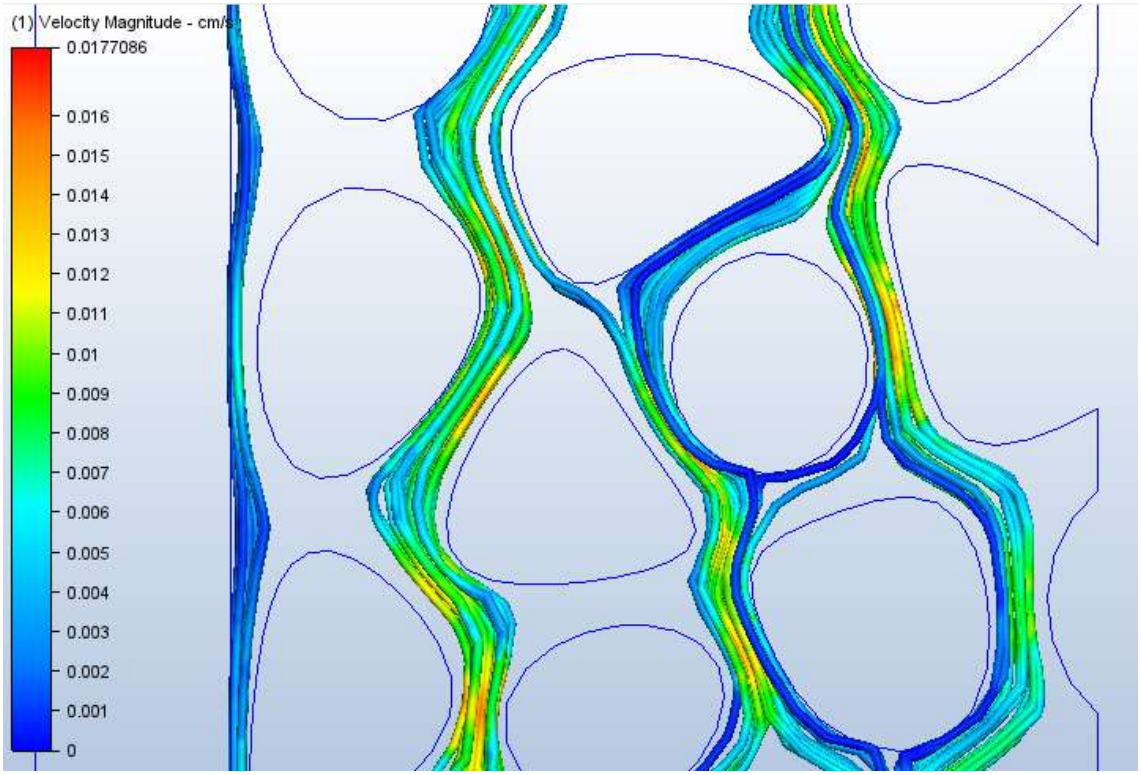

Figure 6-51: Particle flow traces obtained from xanthan gum simulation (50s)

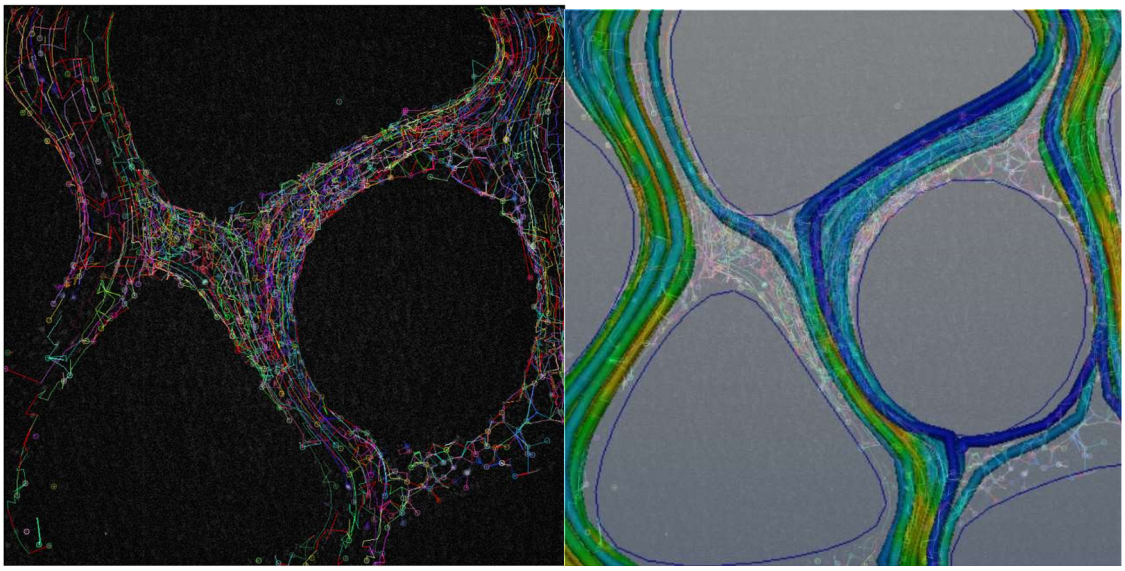

Figure 6-52: Tracked particles (L) and simulated particle flow pathways overlaid (R). Velocity magnitude colouring for simulated particle flow lines (blue – slowest, red – fastest)

6.5 Conclusions

This chapter has covered a variety of different techniques not previously used for the analysis of clay or other particle suspensions flowing in brines or viscosified fluids. The experiments seem far removed from the traditional core floods used to analyse fines migration, but nevertheless were designed to look at specific aspects of fines migration which have not been previously well studied. The drop spread experiment was designed to look at how a fluid containing a suspension of clay would move when variations of wettability were encountered at the surface it was moving across when the surface is submerged. In this regard, it would appear that this experiment was successful – the clay suspension could be seen spreading in particular directions. Improvements could be made to this experiment - see Chapter 7 for further discussion. Moving on to the flow between two slides, this experiment again showed that a dyed solution containing clays could be tracked, this time during flow conditions, which represents another successful experimental design. Finally, looking at clay particle tracking during flow in micro-CT was not successful as the clay particles could not be seen, even when doped. However, a change of experimental design to using viscosified flow and larger high-density particles did allow flow pathways to be visualised. This did not, however, further the knowledge of how clays may move when encountering surfaces of variable wettability.

Looking at the individual experiments as they were performed, it can be concluded that:

1. The presence of 2.5 g/l clay (bentonite, illite, kaolinite or LAPONITE) and/or NaCl or CaCl2 at between 0.001 M and 1 M does not significantly affect the contact angle

measured on glass slides, 3D print material or glass slides hydrophobically modified with beeswax. The exception to this may be the presence of bentonite in 1 M $CaCl_2$, which may cause an increase in the contact angle.

2. When a drop of low salinity brine alone, or brine containing a clay suspension, is dripped into a shallow dish containing a high salinity fluid covering a glass slide with an etched or intermediate-wet pattern on it, the drop appears to preferentially spread over the glass rather than the patterned area. This effect is not seen when both solutions have the same salinity.
3. Flow can be visualised using a fluorescent dye to follow a solution containing clay, or a solution containing the dye alone, flowing into a flow cell consisting of two glass slides, with or without patterning, held a set distance apart. When clay is included in the solution and the flow rate is 5 cm^3/minute, for slides held 1 mm apart, flow lines were seen to develop in the cell between 1 and 2 minutes of flow, and after 10 s for cells with slides held 0.5 mm apart.
4. Variations in the wettability of the glass slides created with an intermediate-wet coating on the slide did not affect the flow patterns seen when any fluorescently dyed solution, either with or without clay, is introduced into the cell at a flow rate of 5 cm^3/minute.
5. Utilising 3 shake, decant and resuspend cycles with a 1 M CsI solution gave the best contrast for use in micro-CT. All salts tested gave an enhancement in contrast compared to the untreated clay.
6. Particle tracking of high-density sized minerals can be carried out when micro-CT scanning is carried out in radiography mode. Particle tracking software can track individual particles and give flow pathways, although for variable speed flow particle tracking is not as straightforward. Some interesting flow pathways were noted following bubble entrapment in the flow cell; this also showed some potential limitations of using a thixotropic fluid for a flowing medium, in that the flow was not always steady and predictable.
7. Simulations do not give good agreement with the patterns seen in the fluorescent flow experiments. However, in the particle tracking experiments, the predicted flow patterns appear to be in good agreement with the experiments.

Chapter 7 Conclusions, Future Potential and Recent Developments

This thesis aimed to look at new methods for monitoring fines detachment, migration and movement over surfaces of variable wettability, and investigate whether 3D printing technology could help achieve these goals. The initial motivation for this project was an assessment of fines migration around an injection well during low salinity enhanced oil recovery, where injection waters depleted in salts and, preferentially divalent cations, are introduced and hence a further focus on variation of salinity was established. During the review of the literature however, many other industries where injection of fluids which may have a lower salinity than the formation were identified (e.g. geothermal energy and carbon capture and storage), thereby considerably widening the scope of application of this work. In Chapter 1, three main themes were identified:

Theme 1: Assessment of 3D printing materials and how the wettability varies with material chemistry and surface roughness with a view to use this data to 3D print synthetic analogues of sandstone reservoir rocks with wettability variation similar to that seen in a natural sandstone.

Theme 2: A study of the effect of ultrasound on sandstone integrity and whether sandstone cleaning by ultrasound is affected by the salinity of the brine in which the sandstone is cleaned, similarly to how brine salinity affects fines migration in sandstones.

Theme 3: The use of 3D printed models in studies to look at the movement of fine particles across different surfaces (with variable wettability) and in various model pore geometries to explore new ways in which fines migration can be visualised.

These themes will now be examined in relation to the work carried out, and the success of the work contributing to the theme will be reviewed.

Theme 1: The first step in the assessment of 3D printing technology was a comprehensive study of the chemistry and roughness of 3D printer materials and the contribution these could make to the wettability of the 3D printer materials. This study was carried out in Chapter 4, and the conclusions were as follows:

1. Water contact angle measurements using the sessile drop method give contact angles for non-hygroscopic pure materials that are within the range of contact angles published previously, which suggests that water contact angle measurement may give a good

indication of the wettability of 3D printing filaments when printed using typical print settings.

2. Contact angle measurement on composite materials (thermoplastics combined with other materials such as wood fibres, metal powders or other insoluble materials) gives varied and unpredictable results, which would be expected based on the criteria to measure the Young contact angle, namely a heterogenous surface.
3. Surface roughness parameters Sa and Sq measured on unfiltered data give the best correlation with contact angle measurements for non-composite materials.
4. The filtering process automatically applied by the Talysurf instrument appeared to remove too much of the surface texture to allow correlation of roughness parameters with contact angle - roughness parameters on the nano-scale did not appear to accurately represent the surface encountered by milli-scale droplets, and hence correlations were not found in this data.
5. Contact angle measurement cannot be correlated with roughness for composite materials due to heterogeneous nature of the materials, combined with the additional surface texture created by the inclusion of the additives.
6. Contact angle prediction using the Wenzel and Cassie-Baxter equations for this data set does not yield good results. Alternative methods for producing varied roughness (for example, sanding with different grits) or measurement with different water drop sizes (for example, for smaller sized, using an environmental scanning electron microscope) may give improved correlation.

The second step was a further assessment of the wettability of 3D printing materials in the presence of dissolved salts and suspended clays to investigate whether these change the measured contact angle. This study was carried out in Chapter 6 and concluded that the presence of 2.5 g/l clay (bentonite, illite, kaolinite or LAPONITE) and/or NaCl or $CaCl_2$ at between 0.001 M and 1 M does not significantly affect the contact angle measured on 3D print material. The exception to this may be the presence of bentonite in 1 M CaCl2, which may cause an increase in the contact angle. The 3D print material in question differed from the materials measured in Chapter 4 as for these studies a different 3D printing technology was used in order to more easily produce watertight objects.

Overall, the conclusions for this theme were mixed. The wettability of the 3D printing materials measured was within the range of values reported in the literature. This gave confidence in the fact that the simple contact measurement technique used was giving reproducible and accurate

results. However, studies on surface texture variation did not yield good results – the data did not correlate well with any roughness parameters and the two established roughness models did not work with the data obtained. This was likely due to the low variation in length-scale of the roughness compared to the size of the water droplet measured, but in order to measure smaller droplets, an alternative measurement technique would have been required. This is discussed further in Section 7.1. The wettabilities of the 3D printing materials assessed were water to neutral-wet, with a water contact angle of around 70° to 90°. Sandstones are naturally water-wet, with quartz having a water contact angle of under 60° and kaolinite 5° to 75° and illite roughly 10° to 45°. Clearly it would be very challenging to reproduce a sandstone with wettability variation similar to that seen in natural rock, but instead it may be possible to build a model system where the wettability varied from place to place by 10° - 20°. Ultimately, although this would have been possible, this was not carried forward into the work carried out as part of theme 3.

Theme 2: During literature searching around fines migration, mentions were made of the cleaning of sandstones using ultrasound for use as a sand pack in a fines migration model (Mungan, 1965). This sparked a desire to investigate the development of a hybrid ultrasound and turbidity (using spectrophotometer absorbance) measurement method to allow rapid assessment of the fines migration potential of sandstones. This study was carried out in Chapter 5, and concluded:

1. NaCl, $CaCl_2$, Kaolinite (KGa-1b), Illite (IMt-1) and Illite-smectite mixed layer (ISCz-1) do not show any absorbance or fluorescence peaks between 320 nm and 1000 nm.
2. Absorbance measurements will give an indication of the removal of fines from a rock chip following ultrasonic treatment. Using a calibration curve of serial dilutions of sandstone vs absorbance will allow the mass of fines removed to be calculated, and hence the % removal of fines from the rock. This method produces better results than a simple mass difference as the salt remaining in the sandstone pores following treatment with 1 M brine causes an increase in the chip mass after drying and the mass of salt cannot be calculated from the pore volume.
3. Sandstones treated with an ultrasonic probe or bath will behave differently depending on how much ultrasonic power is applied and for how much time the treatment is applied for. Castlegate sandstone is poorly cemented and will break apart much more readily than Berea sandstone, but both sandstones will be completely broken down after approximately 2500 J applied by the ultrasonic probe. This process removes the

majority of the grain coating fines, although some still appear attached. Kaolinite fines become detached and removed during this process.

4. Treating Berea sandstone with ultrasonic in 1 M NaCl vs 0.1 M NaCl, 0.05 M NaCl or 0.001 M NaCl results in the % of fines released increasing from an average of 2.2% in 1 M NaCl to 3% in the lower concentration NaCl. The reduction in fines is seen more on the inside of the chip than the outer chip surface.
5. Treating a single Berea chip with a series of brines with reducing concentration may show an enhancement of fines removal at NaCl concentrations lower than the CSC. However, the prolonged application of ultrasound to the Berea chip causes progressively more fines to be removed with every treatment, which may not only be removing fines which would normally migrate during a traditional fines migration experiment. As shown in in the single brine treatment experiments, prolonged exposure to ultrasound can cause disintegration of the rock chip so unless a significantly lower power ultrasonic transducer can be used, this method is not likely to yield results replicating a traditional fines migration experiment.

Part of the desire to undertake this work came from the recognition that most fines migration experiments were carried out using core flooding, which requires specialised equipment and a relatively long time. The development of an alternative method therefore, which is quicker and requires less specialised equipment, may be desirable. It is however recognised that core flooding experiments are more representative of conditions experienced in reservoirs, but as many fines migration experiments are carried out on outcrop, a conceptual experiment may be acceptable. Overall, a method was developed which showed fines being removed at a greater concentration from Berea sandstone when in low salinity brines. From the existing fines migration literature, a lower salt concentration has been seen to promote fines migration (at a concentration below the CSC). However, literature relating fines released from sandstones when treated with ultrasound is sparse, and there appears to be no reported studies relating salt concentration to effectiveness of sandstone cleaning. Studies have however been carried out looking at higher frequency ultrasonic propagation through sandstones saturated with brines of varying salinity – propagation was shown to be affected by the presence of clays by Jones et al. (1998). The higher frequency application is related to subsurface seismic data acquisition, which again is of importance in oil and gas exploration and the understanding of the subsurface for numerous other technologies.

One aspect of this study which was considered was combining the treatment of sandstone with ultrasound and scanning the chips using micro-CT to visualise any change in structure or fines migration either after or during the treatment. This work was planned but unfortunately could not go ahead due to COVID-19 access restrictions to micro-CT scanners, but is discussed in Section 7.1.

Theme 3: Finally, further conceptual experiments were designed to look at the movement of fines in 3D printed flow cells and on surfaces with variable wettability. These experiments are detailed in Chapter 6, and the conclusions were:

1. The presence of 2.5 g/l clay (bentonite, illite, kaolinite or LAPONITE) and/or NaCl or CaCl2 at between 0.001 M and 1 M does not significantly affect the contact angle measured on glass slides, 3D print material or glass slides hydrophobically modified with beeswax. The exception to this may be the presence of bentonite in 1 M $CaCl_2$, which may cause an increase in the contact angle.
2. When a drop of low salinity brine alone, or brine containing a clay suspension, is dripped into a shallow dish containing a high salinity fluid covering a glass slide with an etched or intermediate-wet pattern on it, the drop appears to preferentially spread over the glass rather than the patterned area. This effect is not seen when both solutions have the same salinity.
3. Flow can be visualised using a fluorescent dye to follow a solution containing clay, or a solution containing the dye alone, flowing into a flow cell consisting of two glass slides, with or without patterning, held a set distance apart. When clay is included in the solution and the flow rate is 5 cm^3/minute, for slides held 1 mm apart, flow lines were seen to develop in the cell between 1 and 2 minutes of flow, and after 10 s for cells with slides held 0.5 mm apart.
4. Variations in the wettability of the glass slides created with an intermediate-wet coating on the slide did not affect the flow patterns seen when any fluorescently dyed solution, either with or without clay, is introduced into the cell at a flow rate of 5 cm^3/minute.
5. Utilising 3 shake, decant and resuspend cycles with a 1 M CsI solution gave the best contrast for use in micro-CT. All salts tested gave an enhancement in contrast compared to the untreated clay.
6. Particle tracking of high-density sized minerals can be carried out when micro-CT scanning is carried out in radiography mode. Particle tracking software can track individual particles and give flow pathways, although for variable speed flow particle

tracking is not as straightforward. Some interesting flow pathways were noted following bubble entrapment in the flow cell; this also showed some potential limitations of using a thixotropic fluid for a flowing medium, in that the flow was not always steady and predictable.

7. Simulations do not give good agreement with the patterns seen in the fluorescent flow experiments. However, in the particle tracking experiments, the predicted flow patterns appear to be in good agreement with the experiments.

This series of investigations into alternative ways of looking at the movement of fines or particles yielded a number of interesting results. The drop shape analysis was carried out differently to previous analyses, being more in common with splatter analysis than typical drops. The spread of the drops showed unexpected results – it was not expected that the drops would spread differently over surfaces with different roughness or wettability based on previous splatter spread data. It is speculated that this may be due to slight height variations in the surface, but this has not been confirmed experimentally, and the lack of this trend seen in experiments where the salinities matched may suggest this might not be the best explanation. A possible experimental design to look further at this is discussed in Section 7.1. Moving on to the fluorescent flow between glass slide experiment, again unexpected results were found. The presence of the transient linearly separated flow between two glass slides separated by 0.5 – 1 mm during clay suspension flow consistently appeared in all instanced where these conditions were present. The reason behind this phenomenon has not been investigated at this time as the wettability variations did not affect the presence of this flow pattern and hence would not contribute to the overall aims of this work (namely to investigate wettability and fines migration together). However, this again may be an interesting avenue for further investigation. Finally, flow experiments using radiography in micro-CT lead to new methods of interrogating flow patterns in viscous fluids. This work was cut short by lack of access to a micro-CT scanner to continue experimental work during the COVID-19 pandemic, but initial results showed that particle tracking in radiography can be relatively straightforward to carry out, and the fluid velocity profiles seen in the experimental work could be modelled using commercial computational fluid dynamics software. This is a very exciting area of research and further potential experiments are discussed in Section 7.1.

7.1 Future potential

During the course of this work a number of areas were identified which may give rise to interesting further work. These areas, and suggested experimental work to investigate these areas further, are discussed below.

Further investigation of roughness and wettability of 3D print materials

The correlation between roughness and wettability of 3D print materials could not be determined, not could the established equations linking roughness and contact angle be utilised in the work carried out. Two further investigations could be carried out to establish a relationship. Firstly, instead of utilising commercially available build plates to provide textured surfaces, surfaces with known roughness parameters (greater than those available using build plate variability) could be prepared by for example laser etching or sanding with a particular grit sandpaper in a method similar to Kubiak et al. (2011), followed by using these surfaces as a mould for the thermoplastic 3D printing materials. This should produce pieces with a reproducible, but more pronounced, surface roughness, which should then affect the contact angle of the relatively large water drops used in the contact angle measurement process. The drawback of this method is that the 3D printer material pieces may have to be re-characterised using white light interferometry in order to quantify the roughness. An alternative to this method (increasing the roughness of the 3D printed pieces) could be to reduce the size of the water droplets placed on the pieces. This is not practical to go using the goniometer setup as the droplets would require an order of magnitude size decrease and this would not be measurable. Instead, contact angle measurements could be made on drops sprayed onto the surface using environmental scanning electron microscopy (ESEM), in a method similar to that used by Kareem (2016). Some pilot studies were undertaken on PETG and initial images were obtained (an example is shown in Figure 7-1).

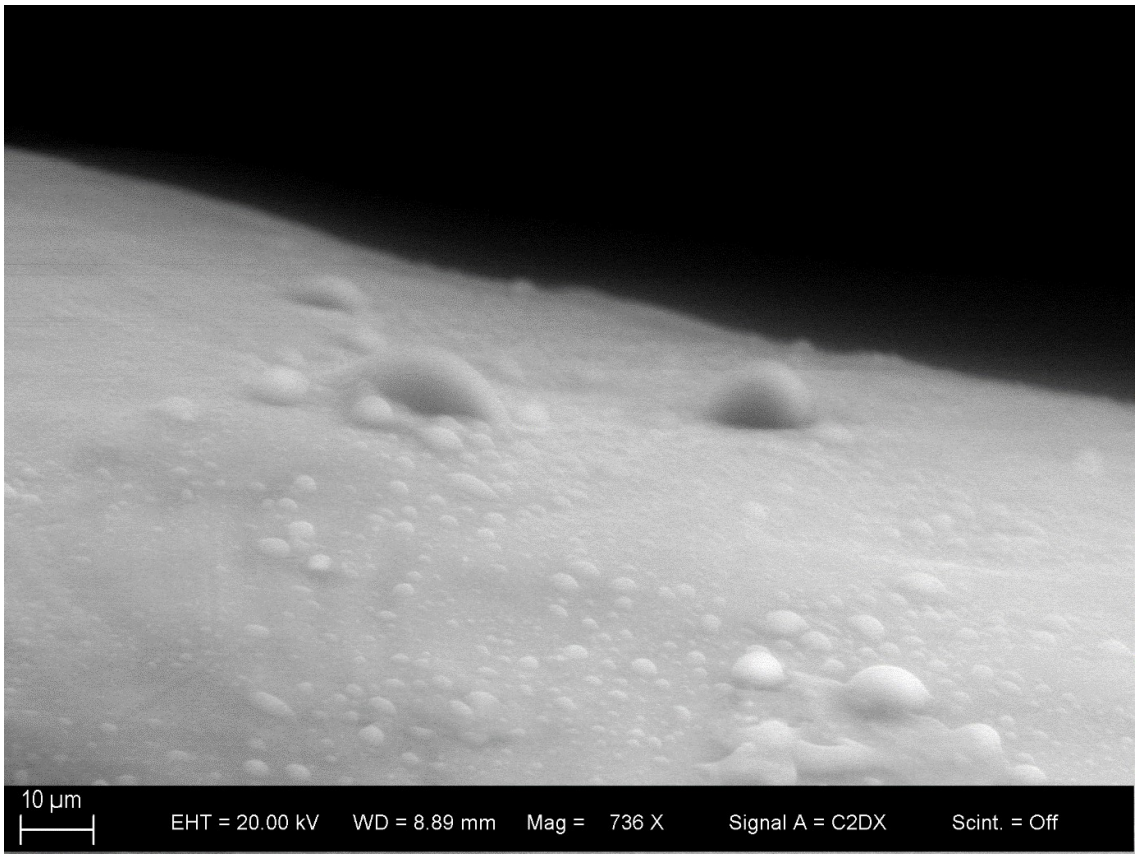

Figure 7-1: ESEM image of micron-sized water droplets on 3D printed PETG.

Given the size of the droplets imaged, this approach would appear to show promise in producing correlations with the micro- and nano-roughness values obtained.

Micro-CT imaging of sandstone treated with ultrasound

The imaging of fines and rock chips following ultrasound treatment with scanning electron microscopy (SEM) yielded some information about how the fines were removed, where they were removed from and what the make-up of the fines was. However, the process whereby the chip was prepared (cleaning, drying and breaking apart with a chisel) may have disrupted the position of mobile fines. If there were mobile fines in the pores exposed by the preparation process, these would have also been removed during the mounting and preparation of the sample. This therefore does not necessarily give an accurate representation of the chip as it was during and right after the application of ultrasound. One potential method of imaging the chip without disrupting the fines is to use micro-CT to scan the chip immediately after (or even during) ultrasound treatment. One potential method of carrying out this experiment would be to mount the chip securely in a vial containing the brine of interest and mount the sample in the CT scanner along with the ultrasonic probe (shown in Figure 7-2).

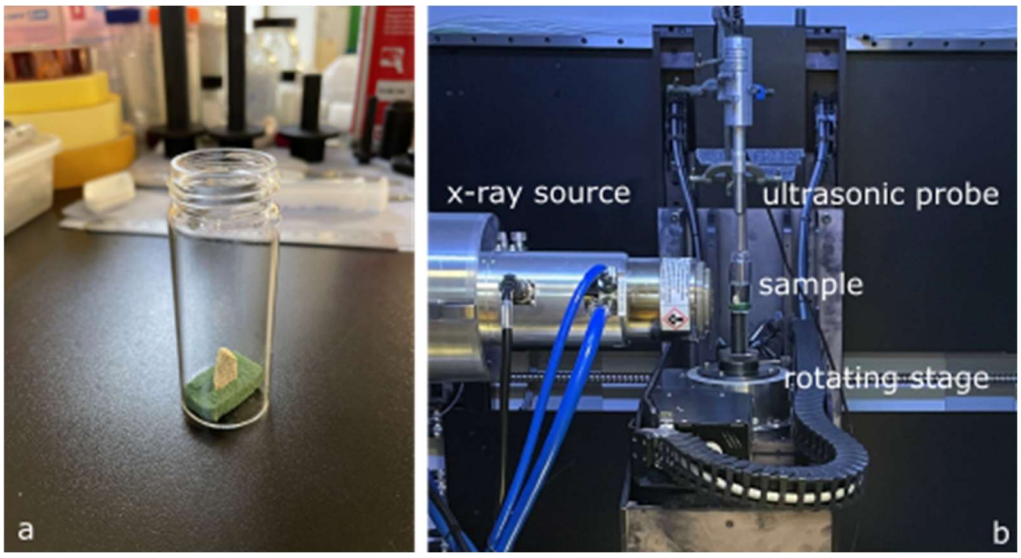

Figure 7-2: Secure mounting of a Berea sandstone chip in a vial for ultrasonic treatment in micro-CT. a: mounting of chip in vial, b: positioning of equipment in CT scanner.

The probe may then be manually raised and lowered but the sample remains mounted in one place, resulting in greater ease of comparing the condition of the chip before and after treatment. By taking a scan before and after treatment using this setup it should be possible to visualise any movement of fine particles from their original position. This method may then be extended to taking a radiograph of the chip during ultrasound treatment and monitoring the resulting images for changes in density across the sample, indicating movement of particles. The method may then be extended further by utilising a high speed micro-CT to enable imaging of the sample during ultrasound treatment and comparing the resulting scans to detailed scans taken before and after treatment.

Drop spread over surfaces of variable wettability

Initially when this experiment was performed it was found that the drops of low salinity brine spread preferentially over glass rather than on a roughened or intermediate wet surface. However, the slight increase in height that would have been present in the case of the intermediate wet surface, and the potential variation in height of the roughened surface, may have contributed to this phenomenon. In order to fully test this, a slide where the surface is dimpled could be utilised – an example of such slides is shown in Figure 7-3.

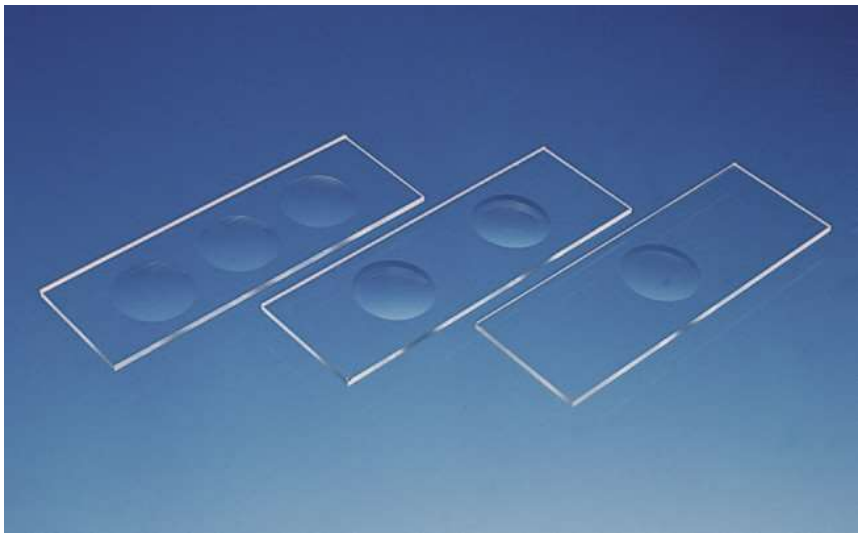

Figure 7-3: BRAND optical cavity glass slides.

The intermediate wet coating may then be filled into the dimples in the slides and the slides and the slides ground to give a perfectly flat surface. The experiment may then be repeated as previously performed to check whether the variation in height contributed to the preferential spread of the droplets.

Flow experiments in micro-CT

The flow experiments developed and performed represent the first of their kind carried out in micro-CT. The combination of using a high density particle along with a high viscosity fluid allowed flow pathways to be monitored and the movement of individual particles to be tracked. The experiments were performed using radiography, and a flow cell designed with a flat "2D" flow pathway. There are a number of enhancements which could be made to this experimental setup. Firstly, utilising a higher speed micro-CT scanner would allow higher flow rates to be monitored. Secondly, using a higher resolution micro-CT scanner would allow more smaller particles to be tracked, and potentially tracking of doped clay particles or aggregates. Thirdly, using a similar method to the suggested ultrasound experiments, 3D flow cells may be developed and used. In order to carry out this experiment most effectively, a detailed scan of a flow cell could be taken before the flow. Upon commencing the flow, radiography may be used to monitor the movement of particles through a 3D network but in a 2D manner, like a projection or shadow. The reduction of dimensionality in this matter has been used by Segerman (2016). Alternatively, it may be possible if low flow rates are used to visualise the flow and the movement of particles in micro-CT. Using these methods, it is hoped that further insight into the movement of particles, including fine particles, during flow conditions may be gained, and that

this information may be helpful in further defining and quantifying fines migration in sandstones.

7.2 Recent Developments

The use of 3D printing as a tool for research into the effects of wettability is an area of current interesting study. Männel et al. (2021) have used projection micro-stereolithography (PμSL), a technique similar to DLP but utilising a projection lens rather than a screen to cure a resin layer, to produce microchannels fabricated from a number of different materials in order to tune the wettability of the channels in different parts of the channel system. At this time, the method whereby the wettability is changed involves removing the resin initially used and replacing it with a different wettability at a specified layer, but nevertheless this represents an interesting avenue for future wettability flow studies. Neukäufer et al. (2020) have also investigated the wettability of 3D print materials, this time using SLS and SLM technology, with the focus on obtaining contact angle data to use in CFD simulations with these materials. It would seem therefore that a good knowledge of 3D printing materials and their wettabilities may be valuable data to publish – a plan for publication of the data in Chapter 4 is detailed in Appendix D.

Recent publications in the area of fines migration and wettability include that of Mehdizad et al. (2022), who use a glass micromodel based on a sandstone CT scan with variable wettability to simulate low salinity EOR mechanisms, and use visual methods to monitor the movement of oil, water and clay particles through the pores. A change in salinity from high to low is seen to enhance the oil recovery when the system is oil-wet. Conceptually this may be seen as movement of fines across an oil wet surface as salinity is changed from high to low, potentially similar to the drop spread analysis carried out in Chapter 6. Tangparitkul et al. (2020) have produced a model based on that of Bedrikovetsky et al. (2011), where initial particle size of clay is found to be the main factor governing detachment probability. This may have interesting implications for the study of fines released from sandstones treated with ultrasound - can micro-CT imaging detect larger particles being preferentially removed? These recent publications show the field of study of fines migration in sandstones and low salinity enhanced oil recovery to be continually progressing, and that the work carried out in this thesis may go some way to furthering the body of knowledge.

Appendix A

A.1 3D print material data table

Table A-1: Substrates tested with print settings

Material	Chemistry	Brand	Hotend Temperature (°C)	Bed Temperature (°C)
3DXNano ESD ABS	ABS with carbon nanotubes	3DXTech	230	100
ABS	ABS	rigid.ink	230	90
ABS-T	ABS	Filament PM	240	100
Atlas Support	PVA	Form Futura	195	60
Bendlay	modified Polybutadiene	Kai Parthy	240	0
Biofila Linen	PLA with lignin	twoBEars	185	55
Biofila Linen	PLA with lignin	twoBEars	205	55
Biofila Linen	PLA with lignin	twoBEars	225	55
Biofila Silk	PLA with lignin	twoBEars	180	55
Bio-G	Bio-Polyethylene Terepthlate Glycol-Modified	Taulman 3D	240	50
Bronzefill	PLA with bronze powder	Colorfabb	215	60
Coffee HTPLA	PLA with coffee	Proto pasta	215	60
Conductive PLA	PLA with carbon black	Proto pasta	215	60
Copperfill	PLA with copper powder	Colorfabb	215	60
Corkfill	PLA with cork	Colorfabb	215	60
Elixir PLA Blend	PLA	Polyalchemy	215	60
glow PLA	PLA	Filament PM	215	60

Graphene enhanced PLA	PLA with Graphene	Haydale	200	55
HDGlass - Clear	PETG	Form Futura	230	50
High-T-Lay	PVA/LDPE	Kai Parthy	240	80
HIPS	HIPS	Reprapper	230	110
iON ABS Nylon Alloy	ABS Nylon Alloy	3DXTech	250	110
Laywood	PLA with wood fibres	Kai Parthy	215	60
Magnetic PLA	PLA with iron	Proto pasta	215	60
Melfil	BVOH	Nippon Gohsei	195	80
Moldlay	polymer with paraffins	Kai Parthy	175	30
Ninjaflex	TPU	Ninjatek	230	40
PAJet160-NYLON	Nylon	Filament PM		
PC-Plus	polycarbonate	Polymaker	260	80
PCTPE	Plasticized Copolyamide TPE (chemical co-polymer of highly flexible nylon and TPE (thermoplastic elastomer))	Taulman 3D	240	50
PETG	PETG	3D Filkemp	230	50
PETG	PETG	Filament PM	230	50
PLA	PLA	rigid.ink	215	60
PLA	PLA	Filament PM	215	60
PLA Extrafill Vertigo Galaxy	PLA	Fillamentum	215	60
PLA Extrafill Vertigo Grey	PLA	Fillamentum	215	60
PLA Plus	PLA	rigid.ink	230	50

PLA-N	PLA	3D Filkemp	215	60
Polywood	PLA with air bubbles	Polymaker	215	60
rPLA	PLA	Filamentive	215	60
StoneFil	PLA with stone	Form Futura	215	60
Super Clear PLA	PLA? Ingeo™ biopolymer?	3Dom	215	60
Tech-G	PETG	Taulman 3D	240	60
T-Glass	PETG	Taulman 3D		
Thermo-sensitive Filament	Polyester	Unitika LTD	200	45
TPE32	TPE	Filament PM	250	60
TPU	TPU	Rigid.ink	245	80
Volcano PLA	High temperature PLA	Form Futura	240	60
Woodfill	PLA with wood fibre	Colorfabb	215	60

A.2 Scripts

A.2.1 Pre-processing script

```
# importing libraries
import os
import csv

# defining location of parent folder - change as appropriate
BASE_DIRECTORY = r'D:\Roughness\data' #r in front of string for
raw formatting to ensure \b doesn't stop the script

# initialise objects
file_list = []
file_name_list = []

# make new directory in the base directory if one doesn't already
exist
if os.path.isdir(BASE_DIRECTORY + '\\checked'):
    print("Directory exists")
else:
    print("Directory being created")
    os.makedirs(BASE_DIRECTORY + '\\checked')
```

```
# scanning through sub folders
for (filenames) in os.listdir(BASE_DIRECTORY):
        if 'txt' in str(filenames):
            e = os.path.join(str(BASE_DIRECTORY), str(filenames))
            file_list.append(e)
            file_name_list.append(filenames)

lines = []
l=0
i=0
j=0
for f in file_list:
    print ("reading " + f)
    r = csv.reader(open(f))
    lines = list(r)
    for i in range(0,2):
        for j in range(0,len(lines)-1):
            #print ("i=" + str(i) + " j=" + str(j))
            #print (lines[3])
            if lines[j][i] == "***\n":
                lines[j][i] = 0
                print ("yes")
    name = str(file_name_list[l])
    writer  =  csv.writer(open(BASE_DIRECTORY  +  '\\checked\\'+
name, 'w+'))
    writer.writerows(lines)
    writer.close()
    l=l+1
```

A.2.2 3D parameter extraction script

```
# importing libraries
import os
import subprocess
import shutil

# defining location of parent folder - change as appropriate
BASE_DIRECTORY  =  r'D:\Roughness\data\checked'  #r  in  front  of
string for raw formatting to ensure \b doesn't stop the script

# initialise objects
file_list = []
file_name_list = []
strings                                                          =
"name\tASPHT\tASPRD\tASPD\tASPHS\tASPHM\tSEB\tASTIF\tSB\t\n"
#set up summary file data - these headings are from matutil

# make new directory in the base directory if one doesn't already
exist
if os.path.isdir(BASE_DIRECTORY + '\\amended'):
    print("Directory exists")
else:
    print("Directory being created")
    os.makedirs(BASE_DIRECTORY + '\\amended')
```

```
# change directory to the newly made directory for ease of working
with MATUTIL
os.chdir(BASE_DIRECTORY + '\\amended')

# scanning through sub folders
for (filenames) in os.listdir(BASE_DIRECTORY):
        if 'txt' in str(filenames):
            e = os.path.join(str(BASE_DIRECTORY), str(filenames))
            file_list.append(e)
            file_name_list.append(filenames)

#adding headers to file and saving it as a new file
l = 0
for f in file_list:
    with open(f,'r') as f1:
        with open(file_name_list[l] ,'w+') as f2:
            file_name_list_tmp = file_name_list[l]
            file_name_only                                          =
str(file_name_list_tmp.split('.')[0])
            f2.write('column=1 x[um] \ncolumn=2 y[um] \ncolumn=3
height[um]\n')
            f2.write(f1.read())
            # call Matutil to process the file just written
            subprocess.call('matutil   calculate   -file   '   +
file_name_list[l] + ' -ascii column -replace -property GWT -method
Profile -3d tmp.rmt', shell=True) # create temporary file which
will be repeatedly re-written by adding -replace
            with open(r"tmp.rmt",'r') as f1: #scan through file
looking for particular lines - assume same file format every time
                print (file_name_only + ' is being analysed')
                for i, line in enumerate(f1):
                    if i == 9:
                        numbers = line.rsplit()[0]
                        strings = strings + file_name_only + "\t"
+ numbers
                    elif i == 14:
                        numbers = line.rsplit()[0]
                        strings = strings + "\t" + numbers
                    elif i == 19:
                        numbers = line.rsplit()[0]
                        strings = strings + "\t" + numbers
                    elif i == 24:
                        numbers = line.rsplit()[0]
                        strings = strings + "\t" + numbers
                    elif i == 29:
                        numbers = line.rsplit()[0]
                        strings = strings + "\t" + numbers
                    elif i == 34:
                        numbers = line.rsplit()[0]
                        strings = strings + "\t" + numbers
                    elif i == 39:
                        numbers = line.rsplit()[0]
                        strings = strings + "\t" + numbers
                    elif i == 44:
```

```
                        numbers = line.rsplit()[0]
                        strings = strings + "\t" + numbers + "\n"
                        break

        l = l+1

#write summary file
print ("summary.txt is being written")
with open('summary.txt', 'w+') as f3:
    f3.write(strings)
```

A.2.3 Maltab plotting script

```
%scan through current folder looking for text files
files = dir('*.txt');

%change from struct to cell format
fileLoop = arrayfun(@(x) x.name,files,'uni',false);
minZ = 0;
maxZ = 0;

%loop through list of files to find max and min of data in folder for
graph
%scaling (gives easily comparible graphs)
fprintf('checking for max/min values for graph scaling');
disp('');
for i = 1:length(files)


    %read through text file without headers and extract data
    %from columns 1, 2 and 3
    fprintf('\nAnalysing %s',fileLoop{i});
    disp('');
    txt = csvread(fileLoop{i});

    for j = (1:262144);
        if txt(j,3) > maxZ;
            maxZ = txt(j,3);
        end;
        if txt(j,3) < minZ;
            minZ = txt(j,3);
        end;
    end;

end
fprintf('\nMax z ');
disp(maxZ)
fprintf('Min z ');
disp(minZ)
fprintf('Completed\n')

%loop through list of files to extract and plot
for i = 1:length(files)

    txt ='';
    X = '';
```

```
Y = '';
Z = '';

%read through text file without headers and extract data
%from columns 1, 2 and 3
fprintf('\nReading %s',fileLoop{i});
disp('');
txt = csvread(fileLoop{i});


X = reshape(txt(:,1),512,512)';
Y = reshape(txt(:,2),512,512)';
Z = reshape(txt(:,3),512,512)';

%set up name for files
fileSplit = strsplit(fileLoop{i},'.');
fileType = 'contour.png';
join = [fileSplit{1} fileType];
plotTitle = fileSplit{1};

%choose plot type, ensure colour bar is visible
fprintf('\nPlotting %s',fileLoop{i});
fprintf('\n');

%set plot type
contour(X,Y,Z)

%set colourbar limits
c = colorbar;
w = c.Limits;
c.Limits = [minZ maxZ];
caxis([minZ maxZ])

% choose colourmap
colormap parula;
brighten(-0.2);

%remove lines and shade surface plots
shading interp

%make plots screen size
set(gcf, 'PaperPositionMode', 'auto');
set(gcf,'units','normalized','outerposition',[0 0 1 1]);

%set title meta data through command line
title(plotTitle, 'FontSize', 16);
h = get(gca, 'title');
set(h, 'FontName', 'Arial');

%set x-axis lable manually with command line
xlabel('X, \mu', 'FontSize', 16);
h = get(gca, 'xlabel');
set(h, 'FontName', 'Arial');

%set y-axis lable manually with command line
ylabel('Y, \mu', 'FontSize', 16);
h = get(gca, 'ylabel');
set(h, 'FontName', 'Arial');
```

```
    %set z-axis lable manually with command line
    zlabel('Z, \mu', 'FontSize', 16);
    h = get(gca, 'zlabel');
    set(h, 'FontName', 'Arial');

    %set z-axis limits manually with command line
    set(gca,'ZLim',[minZ maxZ])

    %Adjust ticks width through command line
    set(gca,'FontSize',16, 'FontName', 'Arial');
    set(gca,'LineWidth',2);

    %Set view-azimuth manually with command line
    %set(gca,'view',[135 75])

    %set z-axis limits manually with command line
    %set(gca,'ZLim',[minZ maxZ])

    saveas(gcf,join)

end
fprintf('Completed\n')
```

A.2.4 R_{rmr} extraction script

```
# importing libraries
import os
import csv
from datetime import datetime

# defining location of parent folder
BASE_DIRECTORY = r'D:\Roughness flattened' #r in front of string
for raw formatting - \b

# initialise objects
file_list = []
#define functions
def dpformat(x):
    #format floats to strings with 2dp
    formatString = ",{:.2f}".format(x)
    return formatString

# give file a unique name
makeNow = datetime.now().strftime("%Y-%m-%d_%H%M-%S")

# scanning through sub folders
for (dirpath, dirnames, filenames) in os.walk(BASE_DIRECTORY):
    for f in filenames:
        e = os.path.join(str(dirpath), str(f))
        file_list.append(e)
l = 0
for f in file_list:
    k=0
    txtfile = open(f, 'r')
```

```
filament = f[(len(BASE_DIRECTORY))+1:-4]
read_tsv = csv.reader(txtfile, delimiter="\t")
data = list(read_tsv)
rowcount = len(data)
mid=int(rowcount/2)
midrow=list(map(float,data[mid]))
midmax = max(midrow)
midmin=min(midrow)
rmr25=(midmax-midmin)/4
for i in midrow:
    if (i-midmin)>rmr25:
        k=k+1
print (filament, k/len(midrow))
print (mid, midmax, midmin, rmr25)
with open("summary.csv", "a+") as myfile:
    myfile.write(filament + "," + str(k/len(midrow)) + " \n")
```

A.3 Full list of roughness surface parameters

Gwyddion

Table A-2 Full list of all Gwyddion surface parameters

Parameter	Unit	Description
RMS roughness (Sq)	µm	$\mu_i = \frac{1}{N}\sum_{n=1}^{N}(z_n - \bar{z})^i \;\; \sigma = \mu_2^{1/2}$
RMS (grain-wise)	µm	$\mu_i = \frac{1}{N}\sum_{n=1}^{N}(z_n - \bar{z})^i \; \sigma = \mu_2^{1/2}$, calculated for each contiguous part of inverted mask
Mean roughness (Sa)	µm	$\mu = \frac{1}{N}\sum_{n=1}^{N}(z_n - \bar{z})$
Excess kurtosis		$\mu_i = \frac{1}{N}\sum_{n=1}^{N}(z_n - \bar{z})^i \; \gamma_2 = \frac{\mu_4}{\mu_2^2} - 3$
Skew (Ssk)		$\mu_i = \frac{1}{N}\sum_{n=1}^{N}(z_n - \bar{z})^i \; \gamma_1 = \frac{\mu_3}{\mu_2^{3/2}}$
Minimum	µm	Minimum height measured
Maximum	µm	Maximum height measured
Median	µm	Median height measured
Maximum peak height (Sp)	µm	Calculated w.r.t. mean height
Maximum pit depth (Sv)	µm	Calculated w.r.t. mean height
Maximum Height (Sz)	µm	Total value range (maximum – minimum)
Projected area	µm²	Computed by triangulation
Surface area	µm²	Computed by triangulation
measured/projected		Measured area / Projected area
Surface slope (Sdq)	µm³	Mean square of local gradient

Volume	µm²	Integral of surface height over covered area
Scan line discrepancy		Characterising the difference between scan lines (if each line in the image was replaced by the average of the two neighbour lines, the new image would differ slightly from the original. Taking the mean square difference and dividing it by the mean square value of the image, we obtain the displayed discrepancy value.)
Roughness average (Ra)	m	$r_j = z_j - \bar{z}\ R_a = \frac{1}{N}\sum_{j=1}^{N}\lvert r_j\rvert$
Root mean square roughness (Rq)	m	$r_j = z_j - \bar{z}\ R_q = \sqrt{\frac{1}{N}\sum_{j=1}^{N} r_j^2}$
Maximum height of the roughness (Rt)	m	$r_j = z_j - \bar{z}\ R_t = \left\lvert \min_{1\le j\le N} r_j \right\rvert + \left\lvert \max_{1\le j\le N} r_j \right\rvert$
Maximum roughness valley depth (Rv)	m	$r_j = z_j - \bar{z}\ R_v = \left\lvert \min_{1\le j\le N} r_j \right\rvert$
Maximum roughness peak height (Rp)	m	$r_j = z_j - \bar{z}\ R_p = \left\lvert \max_{1\le j\le N} r_j \right\rvert$
Average maximum height of the roughness (Rtm)	m	$R_{tm} = R_{vm} + R_{pm}$
Average maximum roughness valley depth (Rvm)	m	$R_{vm} = \frac{1}{m}\sum_{i=1}^{m} R_{vi} \quad R_{vi} = \left\lvert \min r_j \right\rvert$ for $(i-1)\frac{N}{m} < j < i\frac{N}{m}$ m=5
Average maximum roughness peak height (Rpm)	m	$R_{pm} = \frac{1}{m}\sum_{i=1}^{m} R_{vi} \quad R_{pi} = \left\lvert \max r_j \right\rvert$ for $(i-1)\frac{N}{m} < j < i\frac{N}{m}$ m=5
Average third highest peak to third lowest valley height (R3z)	m	The distance between the third highest peak and the third lowest valley. A peak is a portion of the surface above the mean line crossings.

Average third highest peak to third lowest valley height (R3z ISO)	m	The height of the third highest peak from the third lowest valley per sampling length. The base roughness depth is found in five sampling lengths and then averaged.
Average maximum height of the profile (Rz)	m	The average absolute value of the five highest peaks and the five lowest valleys over the evaluation length.
Average maximum height of the roughness (Rz ISO)	m	The average peak-to-valley roughness based on one peak and one valley per sampling length. The single largest deviation is found in five sampling lengths and then averaged. It is identical to R_{tm}.
Maximum peak to valley roughness (Ry = Rmax)	m	Largest of the vertical distance between the highest and lowest points of the profile within a sampling length over evaluation length.
Skewness (Rsk)		$R_{sk} = \frac{1}{NR_q^3}\sum_{j=1}^{N} r_j^3$
Kurtosis (Rku)		$R_{sk} = \frac{1}{NR_q^4}\sum_{j=1}^{N} r_j^4$
Waviness average (Wa)	m	$r_j = w_j - \bar{w}\ W_a = \frac{1}{N}\sum_{j=1}^{N}\lvert r_j\rvert$
Root mean square waviness (Wq)	m	$r_j = w_j - \bar{w}\ W_q = \sqrt{\frac{1}{N}\sum_{j=1}^{N} r_j^2}$
Waviness maximum height (Wy = Wmax)	m	Largest of the vertical distance between the highest and lowest points of the waviness profile within a sampling length over evaluation length.
Mean spacing of profile irregularities (Sm)	m	The mean of the spacing between profile irreaveragularities within the evaluation length
Average wavelength of the profile (λa)	m	The average of the wavelength of the profile
Average absolute slope (Δa)	m	Average of the absolute value of the rate of change of the profile height over the entire evaluation length

Root mean square (RMS) slope (Δq)	m	Root mean squared of the rate of change of the profile height over the entire evaluation length
Length (L)	m	The length the profile was measured along
Developed profile length (L_o)	m	Length of the straight line which is obtained by developing an assessed profile (e.g. the roughness profile obtained from filtering out the waviness)
Profile length ratio (lr)		Lo/L

Matutil

Table A-3: Full list of all Matutil surface parameters

Parameter	Description
Asperity RMS Height	Root mean squared of asperity height
Asperity Radius at Tops	Average radius of the surface peaks (how large the surface features are)
Asperity Density	Number of peaks on the surface per unit area
Asperity SD Summit Height	Standard deviation of the asperity summit height
Asperity Mean Summit Height	Mean of the asperity summit height
SDheight*Density*Radius	Standard deviation of height of surface peaks times the number of peaks on the surface per unit area times the average radius of the surface peaks.

A.4 Number of filament samples used for each set of roughness measurements

For all tables, the number of samples used for correlation is as follows:

Table A-4: Number of filament samples used for each set of roughness measurements

Filament type	Wyko measurements	Talysurf measurements
ABS	3	3
PLA	6	4
Nylon	5	4
PETG	4	3

Biofilla Linen	9	9
Flexible	8	6
PLA Composite	34	33
Other	13	13
Engineered PLA	3	1

Appendix B Clay mineralogy data

All data available from the Clay Minerals Society for each of the clays used in this work is detailed below (The Clay Minerals Society, 2022).

Kaolin KGa-1(KGa-1b), (low-defect)

ORIGIN: Tuscaloosa formation? (Cretaceous?) (stratigraphy uncertain)County of Washington, State of Georgia, USA LOCATION: 32°58′ N-82°53′ W approximately, topographic map Tabernacle, Georgia N 3252.5-W 8252.5/7.5, Collected from face of Coss-Hodges pit, October 3,1972.

CHEMICAL COMPOSITION (%): SiO2: 44.2, Al2O3: 39.7, TiO2: 1.39, Fe2O3: 0.13,FeO: 0.08, MnO: 0.002, MgO: 0.03, CaO: n.d., Na2O: 0.013, K2O: 0.05, F:0.013,P2O5: 0.034, Loss on heating: -550°C: 12.6; 550-1000°C: 1.18.

CATION EXCHANGE CAPACITY (CEC): 2.0 meq/100g SURFACE AREA: N2 area: 10.05 +/- 0.02 m2 /g

THERMAL ANALYSIS: DTA: endotherm at 630oC, exotherm at 1015oC, TG: dehydroxylationweight loss 13.11% (theory 14%) indicating less than 7% impurities.

INFRARED SPECTROSCOPY: Typical spectrum for well crystallized kaolinite,however not as well crystallized as a typical China clay from Cornwall,as judged from the intensity of the 3669 cm-1 band. Splitting of the 1100cm- 1 band is due to the presence of coarse crystals.

STRUCTURE: (Mg.02 Ca.01 Na.01 K.01)[Al3.86 Fe(III).02 Mntr Ti.11][Si3.83Al.17]O10(OH)8, Octahedral charge:.11, Tetrahedral charge:-.17,Interlayer charge:-.06, Unbalanced charge:0.00

Kaolin KGa-2, (high-defect)

ORIGIN: Probably lower tertiary (stratigraphic sequence uncertain) County of Warren, State of Georgia, USA

LOCATION: 33°19′ N-82°28′ W approximately, topographic map Bowdens Pond,Georgia N 3315-W 8222.5/7.5, Collected from face of Purvis pit, October 4, 1972.

CHEMICAL COMPOSITION (%): SiO2: 43.9, Al2O3: 38.5, TiO2: 2.08, Fe2O3: 0.98, FeO: 0.15, MnO: n.d., MgO: 0.03, CaO: n.d., Na2O: <0.005, K2O: 0.065,P2O5: 0.045, S: 0.02, Loss on heating: -550°C: 12.6; 550-1000°C: 1.17, F:0.02.

CATION EXCHANGE CAPACITY (CEC): 3.3 meq/100g SURFACE AREA: N2 area: 23.50 +/- 0.06 m2/g

THERMAL ANALYSIS: DTA: endotherm at 625°C, exotherm at 1005°C, TG: dehydroxylationweight loss 13.14% (theory 14%) indicating less than 7% impurities.

INFRARED SPECTROSCOPY: Typical spectrum for less crystallized kaolinite,however the mineral is not extremely disordered since the band at 3669 cm-1is still present in the spectrum.

STRUCTURE: (Catr Ktr)[Al3.66 Fe(III).07 Mntr Mgtr Ti.16][Si4.00]O10(OH)8, Octahedral charge:.16, Tetrahedral charge:0.00,Interlayer charge:.16, Unbalanced charge:.15, Extra Si:.04

Na-Montmorillonite (Wyoming) SWy-1, SWy-2 and SWy-3 (SWy-2 and SWy-3 are the same as SWy-1. SWy-2 and SWy-3 were collected from the same mine from where SWy-1 was collected at two later occasions).

ORIGIN: Newcastle formation, (cretaceous) County of Crook, State of Wyoming, USA

LOCATION: NE 1/4 SE 1/4 Sec.18, T 57 N, R 65 W; 8, Topographic map: Seeley(15'), The upper 63 of recently stripped area was removed to expose clean,green upper Newcastle, Collected from which samples was taken, October 3,1972.

CHEMICAL COMPOSITION (%): SiO2: 62.9, Al2O3: 19.6, TiO2: 0.090, Fe2O3:3.35, FeO: 0.32, MnO: 0.006, MgO: 3.05, CaO: 1.68, Na2O: 1.53, K2O: 0.53,F: 0.111, P2O5: 0.049, S: 0.05, Loss on heating: -550°C: 1.59; 550-1000°C:4.47, CO2: 1.33.

CATION EXCHANGE CAPACITY (CEC): 76.4 meq/100g, principal exchange cations Na and Ca.

SURFACE AREA: N2 area: 31.82 +/- 0.22 m2/g

THERMAL ANALYSIS: DTA: endotherms at 185°C (shoulder at 235oC), desorptionof water: 755°C, dehydroxylation; shoulder at 810°C, exotherms at 980°C. TG: Loss in dehydroxylation range: 5.53% (theory: 5%).

INFRARED SPECTROSCOPY: Typical spectrum for Wyoming bentonite with a moderate Fe+3 content (band at 885 cm-1). Quartz is detectable (band at 780, 800,698, 400, and 373 cm-1), a trace of carbonate (band at 1425 cm-1).

STRUCTURE: (Ca.12 Na.32 K.05)[Al3.01 Fe(III).41 Mn.01 Mg.54 Ti.02][Si7.98 Al.02]O20(OH)4, Octahedral charge:-.53, Tetrahedral charge:-.02, Interlayer charge:-.55, Unbalanced charge:.05,

Illite IMt-1 and IMt-2

ORIGIN: Silver Hill, Montana, USA

CHEMICAL COMPOSITION (%): SiO2: 49.3 Al2O3: 24.25, TiO2: 0.55, Fe2O3:7.32, FeO: 0.55, MnO: 0.03, MgO: 2.56, CaO: 0.43, Na2O: 0, K2O: 7.83, P2O5: 0.08, LOI: 8.02

STRUCTURE: (Mg.09 Ca.06 K1.37)[Al2.69 Fe(III).76 Fe(II).06 Mntr Mg.43 Ti.06][Si6.77 Al1.23]O20(OH)4, Octahedral charge:-.44, Tetrahedral charge:-1.23, Interlayer charge:-1.68, Unbalanced charge:0.00

Illite-Smectite Mixed Layer (70/30 ordered) ISCz-1

ORIGIN: Slovakia

CHEMICAL COMPOSITION (%): SiO2: 51.6 Al2O3: 25.6, TiO2: 0.039, Fe2O3:1.11, FeO: <0.1, MnO: 0.04, MgO: 2.46, CaO: 0.67, Na2O: 0.32, K2O: 5.36, P2O5: 0.04, LOI: 10.2>

STRUCTURE: (Mg.03 Ca.1 Na.09 K.95)[Al3.39 Fe(III).12 Mntr Mg.48Titr][Si7.19 Al.81]O20(OH)4, Octahedral charge:-.48, Tetrahedral charge:-.81, Interlayer charge:-1.29, Unbalanced charge:0.00

Details of other clays used in this work are not as extensively reported. Wyoming bentonite (ex Steetly) is sodium montmorillonite-rich (Klinkenberg et al., 2006), and LAPONITE XLS has a mostly hectorite-like structure (Christidis et al., 2018).

Appendix C 3D printing PLA strip code

```
;FLAVOR:Marlin
;TIME:216
;Filament used: 0.0563854m
;Layer height: 0.1
;Generated with Cura_SteamEngine 3.0.3
M190 S80 set heat bed temperature - hotter for better flow = smoothness
M104 S215 ;set extruder temperature
M109 S215 ;set extruder temperature and wait
M82 ; absolute extrusion mode
G90 ; set to absolute positioning
G21 ; set units to mm
; home all axes
G28 ; move to origin (home)
G92 X0 Y0 Z0 E0; set position (resets the current position to the values
specified)
; load filament
G1 E200.0 F500
; reset extruder
G92 E0
; move heatbed into position
G1 X20.0 Y20.0 Z1.0 F1000 ; linear move F = feedrate per minute of move
G1 E25 F250; purge nozzle
; move heatbed down a little more
G1 Z5.0 F20
; wait 600ms
G4 600
; move to tack down the strands
G1 X20.0 Y60.0 Z0 F9000
; wait 600ms
G4 600
; move heatbed into position - slightly above bed to give smooth blob
G1 X50.0 Y50.0 Z1.0 F1000 ; linear move F = feedrate per
; extrude blob while moving to give a big blob
G1 Y100.0 E105.0 F150;moves slowly away from printer front
```

```
; zero extruders
G92 E0
; move heatbed down a little more
G1 Z5.0 F20
; wait 600ms
G4 600
; move to tack down the strands
G1 X50.0 Y110.0 Z0 F9000
; wait 600ms
G4 600
;move up a bit
G1 Z10.0 F9000
; wait 300ms
G4 300
;fast move to center
G1 X100.0 Y100.0 F9000
G92 E0
G1 E-120.0 F1800
T0

;Raise3D Job Start
M117 Printing… ;display message
M1001 ;job start

M107 ;fan off
M1002 ;job end
M104 S0 T1 ;temp 2nd nozzle to 0
M104 S0 T0 ;temp 1st nozzle to 0
M140 S0 ;temp print bed to 0
M117 Print Complete. ; display message
G28 X0 Y0 ; move x and y to origin - numbers aren't required
G91 ; set to relative positioning
G1 Z10 ; move z by 10mm (so nozzless don't scrape top of bed)
G90 ; set to absolute positioning

M84 ; stop idle hold (or stop irritating noises, if possible)
```

```
M82 ; absolute extrusion mode
M104 S0 ; yes, really 0
;End of Gcode
```

Appendix D Publication Plan

Limited further work required:

1. Wettability of 3D printing filaments measured by water contact angle

   Based on results from Chapter 4, this would aim to place the measured wettability results, and methods for measuring wettability on 3D printed objects, together in a single publication.

2. The effect of brine salinity on efficiency of ultrasonic cleaning on Berea sandstone

   Based on results from Chapter 5, this would report on the method of using controlled application of ultrasonic cleaning to remove migratable fines from Berea sandstone pores, noting the correlation with previously reported critical salt concentrations.

3. Individual particle tracking using micro-CT in 3D printed flow cells

   Based on results from Chapter 6, this would report on the method of tracking individual API barite particle movement in micro-CT. As API barite is commonly used in the oil industry to increase the density of drilling fluids, this may have scope as an SPE publication.

May have potential depending on results of further work:

1. Correlation of roughness of 3D printing filaments with water contact angle using ESEM

   If ESEM work can go ahead, this would look at assessing the correlation of roughness and wettability of 3D printing materials using very small water droplets. It is unknown at this time how successful this would be as insufficient data has been generated to date.

2. Imaging ultrasonic cleaning of Berea sandstone using micro-CT

   Based on preliminary work carried out in the University of Strathclyde, the imaging of Berea sandstone before and after ultrasonic treatment is relatively straightforward. Upon analysing the data, the insight this technique might give into the mechanism of ultrasonic cleaning of sandstones should be interesting. It is hoped that in addition, higher speed imaging may be carried out to watch ultrasonic cleaning in something resembling real time.

Bibliography

[a] Average of data taken from Gruesbeck and Collins (1982), Gabriel and Inamdar (1983), Khilar and Fogler (1984), Knight and Nur (1987), Scheuerman and Bergersen (1990b), Churcher et al. (1991), Malik et al. (1998), Conway et al. (2000), Alotaibi et al. (2011), Nasralla et al. (2011), Howard et al. (2012), Alyafei et al. (2015), Kareem et al. (2017)

AARTS, A. C. T., OOMS, G., BIL, K. J. & BOT, E. T. G. 1998. Enhancement of Liquid Flow Through a Porous Medium by Ultrasonic Radiation. *European Petroleum Conference.* The Hague, Netherlands: Society of Petroleum Engineers.

AGARWAL, D., BHATT, P., PATHAN, A., PATEL, H. & JOSHI, U. 2012. Development of Portable Experimental Set-up for AFM to Work at Cryogenic Temperature. *AIP Conference Proceedings,* 1447**,** 531-532.

AGHAEIFAR, Z., STRAND, S., AUSTAD, T., PUNTERVOLD, T., AKSULU, H., NAVRATIL, K., STORÅS, S. & HÅMSØ, D. 2015. Influence of Formation Water Salinity/Composition on the Low-Salinity Enhanced Oil Recovery Effect in High-Temperature Sandstone Reservoirs. *Energy & Fuels,* 29**,** 4747-4754.

AHMED, T. 2010. Chapter 14 - Principles of Waterflooding. *In:* AHMED, T. (ed.) *Reservoir Engineering Handbook (Fourth Edition).* Boston: Gulf Professional Publishing.

AKSU, I., BAZILEVSKAYA, E. & KARPYN, Z. T. 2015. Swelling of clay minerals in unconsolidated porous media and its impact on permeability. *GeoResJ,* 7**,** 1-13.

ALLMAN, A., SHIRAZ BHURWANI, M. M., SENKO, J., RAVA, R., PODGORSAK, A., RUDIN, S. & IONITA, C. 2020. *Use of 3D printed intracranial aneurysm phantoms to test the effect of flow diverters geometry on hemodynamics*, SPIE.

ALOTAIBI, M. B., NASRALLA, R. A. & NASR-EL-DIN, H. A. 2011. Wettability Studies Using Low-Salinity Water in Sandstone Reservoirs.

ALYAFEI, N., MCKAY, T. J. & SOLLING, T. I. 2016. Characterization of petrophysical properties using pore-network and lattice-Boltzmann modelling: Choice of method and image sub-volume size. *Journal of Petroleum Science and Engineering,* 145**,** 256-265.

ALYAFEI, N., RAEINI, A. Q., PALUSZNY, A. & BLUNT, M. J. 2015. A sensitivity study of the effect of image resolution on predicted petrophysical properties. *Transport in Porous Media,* 110**,** 157-169.

ANDERSEN, M. R., JENSEN, T., LISOUSKI, P., MORTENSEN, A. K., HANSEN, M. K., GREGERSEN, T. & AHRENDT, P. 2012. Kinect depth sensor evaluation for computer vision applications. *Electrical and Computer Engineering Technical Report ECE-TR-6*.

ANDERSON, R. L., RATCLIFFE, I., GREENWELL, H. C., WILLIAMS, P. A., CLIFFE, S. & COVENEY, P. V. 2010. Clay swelling — A challenge in the oilfield. *Earth-Science Reviews,* 98**,** 201-216.

ANDERSON, W. G. 1986. Wettability literature survey-part 1: rock/oil/brine interactions and the effects of core handling on wettability. *Journal of petroleum technology,* 38**,** 1,125-1,144.

ARAB, D., KANTZAS, A. & BRYANT, S. L. 2020. Water flooding of oil reservoirs: Effect of oil viscosity and injection velocity on the interplay between capillary and viscous forces. *Journal of Petroleum Science and Engineering,* 186**,** 106691.

ASHBY, N. P. & BINKS, B. P. 2000. Pickering emulsions stabilised by Laponite clay particles. *Physical Chemistry Chemical Physics,* 2**,** 5640-5646.

ASHRAF, A., HADIA, N., TORSAETER, O. & TWEHEYO, M. T. 2010. Laboratory Investigation of Low Salinity Waterflooding as Secondary Recovery Process: Effect of Wettability. Society of Petroleum Engineers.

AUGUSTINE, C., TESTER, J. W., ANDERSON, B., PETTY, S. & LIVESAY, B. A comparison of geothermal with oil and gas well drilling costs. Proceedings of the 31st Workshop on Geothermal Reservoir Engineering, 2006. Curran Associates Inc. ^ eNew York New York, 5-19.

AUTODESK. 2016. *123D Catch* [Online]. Available: http://www.123dapp.com/catch [Accessed 08/11/2016 2016].

AYOPO, K., EZE, C., DOKUBO, R. & OLUWATOBILOBA, O. 2018. Impact of Fines Migration on Well XX and Lessons Learnt from Stimulation Exercise. *SPE Nigeria Annual International Conference and Exhibition.* Lagos, Nigeria: Society of Petroleum Engineers.

BAGDASSAROV, N. & PINKERTON, H. 2004. Transient phenomena in vesicular lava flows based on laboratory experiments with analogue materials. *Journal of Volcanology and Geothermal Research,* 132**,** 115-136.

BAKER, R. & SERVICE, U. O. T. A. A. P. E. 1996. *A primer of oilwell drilling: a basic text of oil and gas drilling*, Petroleum Extension Service, University of Texas at Austin.

BARAN, E. H. & ERBIL, H. Y. 2019. Surface modification of 3D printed PLA objects by fused deposition modeling: a review. *Colloids and interfaces,* 3**,** 43.

BARANYAIOVÁ, T. & BUJDÁK, J. 2018. Effects of Dye Surface Concentration on the Molecular Aggregation of Xanthene Dye in Colloidal Dispersions of Montmorillonite. *Clays and Clay Minerals,* 66**,** 114-126.

BASHIR, S., BASHIR, M., REES, J. M. & ZIMMERMAN, W. B. 2015. Hydrophilic Surface Modification of PDMS Microchannel for O/W and W/O/W Emulsions. *Micromachines,* 6**,** 1445-1458.

BASSIR, S., MOGHADASI, J., DANESHFAR, R. & MOHAMMADZADEH, H. 2017. *A Comprehensive Review on Formation Damage Due to Fines Migration*.

BATES, R. L., JACKSON, J. A., GARY, M. & INSTITUTE, A. G. 1980. *Glossary of Geology*, American Geological Institute.

BAUMEISTER, C. & KILIAN, L. 2016. Forty Years of Oil Price Fluctuations: Why the Price of Oil May Still Surprise Us. *The Journal of Economic Perspectives,* 30**,** 139-160.

BAZIN, B., ESPERANZA, S. & LE THIEZ, P. 1994. Control of Formation Damage by Modeling Water/Rock Interaction. Society of Petroleum Engineers.

BEDRIKOVETSKY, P. & CARUSO, N. 2014. Analytical Model for Fines Migration During Water Injection. *Transport in Porous Media,* 101**,** 161-189.

BEDRIKOVETSKY, P., SIQUEIRA, F. D., FURTADO, C. A. & SOUZA, A. L. S. 2011. Modified particle detachment model for colloidal transport in porous media. *Transport in porous media,* 86**,** 353-383.

BENNION, B. 1999. Formation Damage-The Impairment of the Invisible, By the Inevitable And Uncontrollable, Resulting In an Indeterminate Reduction of the Unquantifiable!

BENNION, D. B. 2002. An Overview of Formation Damage Mechanisms Causing a Reduction in the Productivity and Injectivity of Oil and Gas Producing Formations. *Journal of Canadian Petroleum Technology,* 41.

BENNION, D. B., BENNION, D. W., THOMAS, F. B. & BIETZ, R. F. 1998. Injection Water Quality-A Key Factor to Successful Waterflooding.

BENNION, D. B., THOMAS, F. B., BIETZ, R. F. & BENNION, D. W. 1996. Water and Hydrocarbon Phase Trapping in Porous Media—Diagnosis, Prevention and Treatment. *Journal of Canadian Petroleum Technology,* 35.

BENNION, D. B., THOMAS, F. B. & SHEPPARD, D. A. Thermally Induced Formation Damage due to Hot Water and Steamflooding in Sandstone Reservoirs. Petroleum Society of Canada Annual Technical Meeting, 1992 Calgary, Alberta.

BERNARD, G. G. 1967. Effect of Floodwater Salinity on Recovery Of Oil from Cores Containing Clays. Society of Petroleum Engineers.

BERNASCONI, R., NATALE, G., LEVI, M. & MAGAGNIN, L. 2016. Electroless Plating of NiP and Cu on Polylactic Acid and Polyethylene Terephthalate Glycol-Modified for 3D Printed Flexible Substrates. *Journal of The Electrochemical Society,* 163**,** D526-D531.

BIOT, M. A. 1956a. Theory of elastic waves in a fluid-saturated porous solid. I. Low frequency range. *The Journal of the Acoustical Society of America,* 28**,** 168-178.

BIOT, M. A. 1956b. Theory of propagation of elastic waves in a fluid-saturated porous solid. II. Higher frequency range. *The Journal of the Acoustical Society of America,* 28**,** 179-191.

BIOT, M. A. 1962. Mechanics of deformation and acoustic propagation in porous media. *Journal of Applied Physics,* 33**,** 1482-1498.

BLACK, J. T. 2013. *DeGarmo's materials and processes in manufacturing,* Hoboken, NJ, Hoboken, NJ : Wiley.

BLAIS, F. O. 2004. Review of 20 years of range sensor development. *Journal of Electronic Imaging,* 13**,** 231-243.

BLANTHER, J. E. 1892. Manufacture of contour relief-maps. Google Patents.

BLUME, T., WEISBROD, N. & SELKER, J. 2002. Permeability changes in layered sediments: Impact of particle release. *Ground Water,* 40**,** 466-474.

BOMMER, P. M. 2008. *A Primer of Oilwell Drilling*.

BORYSENKO, A., CLENNELL, B., SEDEV, R., BURGAR, I., RALSTON, J., RAVEN, M., DEWHURST, D. & LIU, K. 2009. Experimental investigations of the wettability of clays and shales. *Journal of Geophysical Research: Solid Earth,* 114.

BP. 2022. *BP Energy Outlook 2022* [Online]. Available: https://www.bp.com/en/global/corporate/energy-economics/energy-outlook.html [Accessed 17/03/2022 2022].

BRANDON, S., HAIMOVICH, N., YEGER, E. & MARMUR, A. 2003. Partial wetting of chemically patterned surfaces: The effect of drop size. *Journal of Colloid and Interface Science,* 263**,** 237-243.

BRENNEN, C. E. 1995. *Cavitation and bubble dynamics,* New York, United States, Oxford University Press Inc.

BROWN, E. T., BRAY, J. W. & SANTARELLI, F. J. 1989. Influence of stress-dependent elastic moduli on stresses and strains around axisymmetric boreholes. *Rock Mechanics and Rock Engineering,* 22**,** 189-203.

BRUNIER, B., SHEIBAT-OTHMAN, N., CHNIGUIR, M., CHEVALIER, Y. & BOURGEAT-LAMI, E. 2016. Investigation of four different laponite clays as stabilizers in pickering emulsion polymerization. *Langmuir,* 32**,** 6046-6057.

BUCKLEY, J. 1998. Wetting alteration of solid surfaces by crude oils and their asphaltenes. *Revue de l'Institut Français du Pétrole,* 53**,** 303-312.

BULTREYS, T., BOONE, M. A., BOONE, M. N., DE SCHRYVER, T., MASSCHAELE, B., VAN LOO, D., VAN HOOREBEKE, L. & CNUDDE, V. 2015. Real-time visualization of Haines jumps in sandstone with laboratory-based microcomputed tomography. *Water Resources Research,* 51**,** 8668-8676.

CASSIE, A. & BAXTER, S. 1944. Wettability of porous surfaces. *Transactions of the Faraday society,* 40**,** 546-551.

CELAURO, J. G., TORREALBA, V. A., KARPYN, Z. T., KLISE, K. A. & MCKENNA, S. A. 2014. Pore-scale multiphase flow experiments in bead packs of variable wettability. *Geofluids,* 14**,** 95-105.

CERDA, C. M. 1988. Mobilization of quartz fines in porous media. *Clays and Clay Minerals,* 36**,** 491-497.

CHAI, B.-H., ZHENG, J.-M., ZHAO, Q. & POLLACK, G. H. 2008. Spectroscopic Studies of Solutes in Aqueous Solution. *The Journal of Physical Chemistry A,* 112**,** 2242-2247.

CHAU, T. T. 2009. A review of techniques for measurement of contact angles and their applicability on mineral surfaces. *Minerals Engineering,* 22**,** 213-219.

CHEN, W. 1969. *Influence of ultrasonic energy upon the rate of flow of liquids through porous media.* PhD, West Virginia University.

CHLUPOVÁ, S., KELAR, J. & SLAVICEK, P. 2017. Changing the Surface Properties of ABS Plastic by Plasma. *Plasma Physics and Technology Journal,* 4**,** 32-35.

CHRISTIDIS, G. E., ALDANA, C., CHRYSSIKOS, G., GIONIS, V., KALO, H., ID, M., STÖTER, M., BREU, J. & ROBERT, J.-L. 2018. minerals The Nature of Laponite: Pure Hectorite or a Mixture of Different Trioctahedral Phases?

CHURCHER, P. L., FRENCH, P. R., SHAW, J. C. & SCHRAMM, L. L. 1991. Rock Properties of Berea Sandstone, Baker Dolomite, and Indiana Limestone. Society of Petroleum Engineers.

CIVAN, F. 2007. *Reservoir formation damage : fundamentals, modeling, assessment, and mitigation,* Boston, Boston : Gulf Professional Pub.

CLEGG, J. D. 2007. *Petroleum Engineering Handbook, Volume IV: Production Operations Engineering*, Society of Petroleum Engineers.

CLEVELAND QUARRIES. 2021. *Berea Sandstone™ Petroleum Cores* [Online]. Available: https://www.bereasandstonecores.com/ [Accessed 22/01/2021 2021].

CNUDDE, V., CWIRZEN, A., MASSCHAELE, B. & JACOBS, P. 2009. Porosity and microstructure characterization of building stones and concretes. *Engineering geology,* 103**,** 76-83.

CONWAY, M. W., HIMES, R. E. & GRAY, R. 2000. Minimising Clay Sensitivity to Fresh Water Following Brine Influx. Society of Petroleum Engineers.

COP26. 2021. *COP26 Cover Decision* [Online]. Available: https://unfccc.int/sites/default/files/resource/cop26_auv_2f_cover_decision.pdf [Accessed 23/12/2021 2021].

CRAIG, F. F. 1971. *The reservoir engineering aspects of waterflooding*, HL Doherty Memorial Fund of AIME New York.

CRAWLEY, G., COURNIL, M. & DI BENEDETTO, D. 1997. Size analysis of fine particle suspensions by spectral turbidimetry: potential and limits. *Powder Technology,* 91**,** 197-208.

CROIX, C. M. S., SHAND, S. H. & WATKINS, S. C. 2005. Confocal microscopy: comparisons, applications, and problems. *BioTechniques,* 39**,** S2-S5.

DAMCHAN, J., SIKONG, L., KOOPTARNOND, K. & NIYOMWAS, S. 2008. Contact angle of glass substrate coated with TiO2/SiO2 thin films. *CMU. J. Nat. Sci,* 7**,** 19-23.

DE GOEDE, T., DE BRUIN, K., SHAHIDZADEH, N. & BONN, D. 2021. Droplet splashing on rough surfaces. *Physical Review Fluids,* 6**,** 043604.

DE GOEDE, T. C., LAAN, N., DE BRUIN, K. G. & BONN, D. 2018. Effect of Wetting on Drop Splashing of Newtonian Fluids and Blood. *Langmuir,* 34**,** 5163-5168.

DEEGAN, R. D., BAKAJIN, O., DUPONT, T. F., HUBER, G., NAGEL, S. R. & WITTEN, T. A. 1997. Capillary flow as the cause of ring stains from dried liquid drops. *Nature,* 389**,** 827-829.

DENG, Y., XU, L., LU, H., WANG, H. & SHI, Y. 2018. The contact angle of water on feldspar in a reservoir rock. *Chinese Science Bulletin,* 63**,** 3137-3145.

DEWANCKELE, J., BOONE, M. A., COPPENS, F., VAN LOO, D. & MERKLE, A. P. 2020. Innovations in laboratory-based dynamic micro-CT to accelerate in situ research. *Journal of Microscopy,* 277**,** 197-209.

DEZELIC, G., DEŽELIĆ, N. & TEŽAK, B. 1963. A simple method for particle size determination by turbidity measurement. *Journal of Colloid Science,* 18**,** 888–892.

DEZHKUNOV, N., FRANCESCUTTO, A., CIUTI, P. & IGNATENKO, P. Ultrasonic capillary effect and sonoluminescence. Proc. of 5-th World Congress on Ultrasonics (WCU 2003). Paris, 2003. 597-600.

DRESSICK, W. J., SOTO, C. M., FONTANA, J., BAKER, C. C., MYERS, J. D., FRANTZ, J. A. & KIM, W. 2014. Preparation and Layer-by-Layer Solution Deposition of Cu(In,Ga)O2 Nanoparticles with Conversion to Cu(In,Ga)S2 Films. *PLOS ONE,* 9**,** e100203.

DU PLESSIS, A., BROECKHOVEN, C., GUELPA, A. & LE ROUX, S. G. 2017. Laboratory x-ray micro-computed tomography: a user guideline for biological samples. *GigaScience,* 6**,** 1-11.

EZZAT, M. M. & SHEDID, S. A. 2016. Effects of Salinity and Flow Rate on Formation Damage and Characterization of Clastic Reservoir Rocks. International Petroleum Technology Conference.

FAERGESTAD, I. 2016. Formation Damage. *Oilfield Review.*

FAIRBANKS, H. & CHEN, W. Ultrasonic acceleration of liquid flow through porous media. AIChE Symp. Ser.;(United States), 1970. West Virginia Univ.

FAIRBANKS, H. V. Ultrasonic stimulation of liquid flow. 1976 Ultrasonics Symposium, 1976. IEEE, 117-118.

FEDOROV, K. 2017. *Surface Modification of Commonly used Polymer Plastics for Increased Hemocompatibility in Medical Equipment.* University of Toronto (Canada).

FRENCH, M. W. & WORDEN, R. H. 2013. Orientation of microcrystalline quartz in the Fontainebleau Formation, Paris Basin and why it preserves porosity. *Sedimentary Geology,* 284**,** 149-158.

FUCHS, F. J. 2015. 19 - Ultrasonic cleaning and washing of surfaces. *In:* GALLEGO-JUÁREZ, J. A. & GRAFF, K. F. (eds.) *Power Ultrasonics.* Oxford: Woodhead Publishing.

GABRIEL, G. A. & INAMDAR, G. R. 1983. An Experimental Investigation of Fines Migration in Porous Media. Society of Petroleum Engineers.

GALAL, S. K., ELGIBALY, A. A. & ELSAYED, S. K. 2016. Formation damage due to fines migration and its remedial methods. *Egyptian Journal of Petroleum,* 25**,** 515-524.

GARCÍA-MORENO, F., KAMM, P. H., NEU, T. R., BÜLK, F., MOKSO, R., SCHLEPÜTZ, C. M., STAMPANONI, M. & BANHART, J. 2019. Using X-ray tomoscopy to explore the dynamics of foaming metal. *Nature Communications,* 10**,** 3762.

GENCE, N. 2006. Wetting behavior of magnesite and dolomite surfaces. *Applied Surface Science,* 252**,** 3744-3750.

GIBSON, I., ROSEN, D. W. & STUCKER, B. 2010. *Additive manufacturing technologies*, Springer.

GLUYAS, J. G. 2004. *Petroleum geoscience,* Malden, Mass., Malden, Mass. : Blackwell Pub.

GOMES, C. M. C. P. S., FERNANDES, A. C. & DE ALMEIDA, B. D. J. V. S. 1993. The Surface Tension of Cork from Contact Angle Measurements. *Journal of Colloid and Interface Science,* 156**,** 195-201.

GÓMEZ, J. A. 2014. *DRINKING WATER EPA Program to Protect Underground Sources from Injection of Fluids Associated With Oil and Gas Production Needs Improvement* [Online]. Available: http://www.gao.gov/assets/670/664499.pdf [Accessed 16th January 2017].

GRAY, D. & REX, R. Formation damage in sandstones caused by clay dispersion and migration. Clays and Clay Minerals: Proceedings of the Fourteenth National Conference, 1966. 355-366.

GRIFFIN, L. 2016. *Clay Mobilisation in Oil Reservoirs.* Doctor of Philosophy, University of Cambridge.

GRUESBECK, C. & COLLINS, R. E. 1982. Entrainment and Deposition of Fine Particles in Porous Media.

GUILLARD, F., MARKS, B. & EINAV, I. 2017. Dynamic X-ray radiography reveals particle size and shape orientation fields during granular flow. *Scientific Reports,* 7**,** 8155.

HAMDI, M. & POULIS, J. A. 2021. Effect of UV/ozone treatment on the wettability and adhesion of polymeric systems. *The Journal of Adhesion,* 97**,** 651-671.

HAMIDA, T. 2006. The Infl uence of Ultrasonic Energy on Capillary Fluid Displacement. *SPE Annual Technical Conference and Exhibition.* San Antonio, Texas, USA: Society of Petroleum Engineers.

HAN, G., KWON, T.-H., LEE, J. Y. & JUNG, J. 2020. Fines migration and pore clogging induced by single- and two-phase fluid flows in porous media: From the perspectives of particle detachment and particle-level forces. *Geomechanics for Energy and the Environment,* 23**,** 100131.

HANNIBAL, J. T. 2020. Berea sandstone: A heritage stone of international significance from Ohio, USA. *Geological Society, London, Special Publications,* 486**,** 177-204.

HANSEN, J., SATO, M., RUEDY, R., LO, K., LEA, D. W. & MEDINA-ELIZADE, M. 2006. Global temperature change. *Proceedings of the National Academy of Sciences,* 103**,** 14288-14293.

HARASAWA, Y. E. 2021. *Imaging Fines Migration Induced by Salinity Changes.* Masters, Durham University.

HARRINGTON, B. 2019. Inkscape. 0.92.4 ed.: https://inkscape.org/.

HEWITT, C. H. 1963. Analytical Techniques for Recognizing Water- Sensitive Reservoir Rocks.

HIMES, R. E., VINSON, E. F. & SIMON, D. E. 1991. Clay Stabilization in Low-Permeability Formations.

HOBBS, P. V. & OSHEROFF, T. 1967. Splashing of Drops on Shallow Liquids. *Science,* 158**,** 1184-1186.

HOLBROOK, O. C. & BERNARD, G. G. 1963. Synthetic cores. Google Patents.

HOMSY, G. M. 1987. Viscous fingering in porous media. *Annual review of fluid mechanics,* 19**,** 271-311.

HORAUD, R., HANSARD, M., EVANGELIDIS, G. & MÉNIER, C. 2016. An overview of depth cameras and range scanners based on time-of-flight technologies. *Machine Vision and Applications,* 27**,** 1005-1020.

HOWARD, P. R., HINKEL, J. J. & MONIAGA, N. 2012. Assessing Formation Damage From Migratory Clays in Moderate Permeability Formations. Society of Petroleum Engineers.

HU, Y., LIU, X. & XU, Z. 2003. Role of crystal structure in flotation separation of diaspore from kaolinite, pyrophyllite and illite. *Minerals Engineering,* 16**,** 219-227.

HUANG, T., MCELFRESH, P. M. & GABRYSCH, A. 2002. High Temperature Acidization to Prevent Fines Migration. *International Symposium and Exhibition on Formation Damage Control.* Lafayette, Louisiana: Society of Petroleum Engineers.

HUSSAIN, F., ZEINIJAHROMI, A., BEDRIKOVETSKY, P., BADALYAN, A., CARAGEORGOS, T. & CINAR, Y. 2013. An experimental study of improved oil recovery through fines-assisted waterflooding. *Journal of Petroleum Science and Engineering,* 109**,** 187-197.

IGLAUER, S., SALAMAH, A., SARMADIVALEH, M., LIU, K. & PHAN, C. 2014. Contamination of silica surfaces: Impact on water–CO2–quartz and glass contact angle measurements. *International Journal of Greenhouse Gas Control,* 22**,** 325-328.

ISHUTOV, S., HASIUK, F. J., HARDING, C. & GRAY, J. N. 2015. 3D printing sandstone porosity models. *Interpretation,* 3**,** SX49-SX61.

ISHUTOV, S., JOBE, D., ZHANG, S., GONZALEZ, M., AGAR, S. M., HASIUK, F. J., WATSON, F., GEIGER, S., MACKAY, E. & CHALATURNYK, R. 2017. 3D printing for geoscience: fundamental research, education, and applications for the petroleum industry. *AAPG Bulletin*.

JAŃCZUK, B., CHIBOWSKI, E. & BIALOPIOTROWICZ, T. 1986. Time dependence wettability of quartz with water. *Chem. Pap.,* 40**,** 349-356.

JAŃCZUK, B., CHIBOWSKI, E., HAJNOS, M., BIAŁOPIOTROWICZ, T. & STAWIŃSKI, J. 1989. Influence of exchangeable cations on the surface free energy of kaolinite as determined from contact angles. *Clays and Clay Minerals,* 37**,** 269-272.

JANCZUK, B. & ZDZIENNICKA, A. 1994. A study on the components of surface free energy of quartz from contact angle measurements. *Journal of Materials Science,* 29**,** 3559-3564.

JASMEE, S., OMAR, G., MASRIPAN, N. A. B., KAMAROLZAMAN, A. A., ASHIKIN, A. S. & CHE ANI, F. 2018. Hydrophobicity performance of polyethylene terephthalate (PET) and thermoplastic polyurethane (TPU) with thermal effect. *Materials Research Express,* 5**,** 096304.

JOHNSTON, N. & BEESON, C. M. 1945. Water Permeability of Reservoir Sands.

JONES, F. O., JR. 1964. Influence of Chemical Composition of Water on Clay Blocking of Permeability.

JONES, S. M., MCCANN, C., ASTIN, T. R. & SOTHCOTT, J. 1998. The effects of pore-fluid salinity on ultrasonic wave propagation in sandstones. *Geophysics,* 63**,** 928-934.

JONES, T. 2018. *Fissures and fountains: magma dynamics in basaltic conduits.* PhD, Durham University.

JONKMAN, J., BROWN, C. M., WRIGHT, G. D., ANDERSON, K. I. & NORTH, A. J. 2020. Tutorial: guidance for quantitative confocal microscopy. *Nature Protocols,* 15**,** 1585-1611.

KAREEM, R. 2016. *Nano Geochemistry of Low Salinity Enhanced Oil Recovery.* Doctor of Philosophy, Durham University.

KAREEM, R. 2017. The Petrophysical Characterization of Castlegate Sandstone Core Plugs [Unpublished Work].

KAREEM, R., CUBILLAS, P., GLUYAS, J., BOWEN, L., HILLIER, S. & GREENWELL, H. C. 2017. Multi-technique approach to the petrophysical characterization of Berea sandstone core plugs (Cleveland Quarries, USA). *Journal of Petroleum Science and Engineering,* 149**,** 436-455.

KATENDE, A. & SAGALA, F. 2019. A critical review of low salinity water flooding: Mechanism, laboratory and field application. *Journal of Molecular Liquids,* 278**,** 627-649.

KEWEN, L. & ABBAS, F. 2000. Experimental Study of Wettability Alteration to Preferential Gas-Wetting in Porous Media and Its Effects.

KHILAR, K. C. & FOGLER, H. S. 1983. Water Sensitivity of Sandstones.

KHILAR, K. C. & FOGLER, H. S. 1984. The existence of a critical salt concentration for particle release. *Journal of Colloid and Interface Science,* 101**,** 214-224.

KHILAR, K. C. & FOGLER, H. S. 1987a. Colloidally Induced Fines Migration in Porous Media. *Reviews in Chemical Engineering.*

KHILAR, K. C. & FOGLER, H. S. 1987b. Colloidally induced fines migration in porous media. *Reviews in chemical engineering,* 4**,** 41-108.

KHILAR, K. C. & FOGLER, H. S. 1998. *Migrations of Fines in Porous Media*, Springer Netherlands.

KHILAR, K. C., FOGLER, H. S. & AHLUWALIA, J. 1983. Sandstone water sensitivity: existence of a critical rate of salinity decrease for particle capture. *Chemical engineering science,* 38**,** 789-800.

KIA, S. F., FOGLER, H. S. & REED, M. G. 1987. Effect of Salt Composition on Clay Release in Berea Sandstones. Society of Petroleum Engineers.

KIM, H., JEONG, H. & BYEON, S.-H. 2016. Selective Filter Effect Induced by Cu2+ Adsorption on the Fluorescence of a GdVO4:Eu Nanoprobe. *ACS Applied Materials & Interfaces,* 8**,** 15497-15505.

KIM, S., BOWEN, R. A. & ZARE, R. N. 2015. Transforming plastic surfaces with electrophilic backbones from hydrophobic to hydrophilic. *ACS applied materials & interfaces,* 7**,** 1925-1931.

KIM, S., HA, H., KO, Y., YOON, S.-J., RHEE, J., KIM, M., LEE, H. & KHANG, G. 2007. Correlation of proliferation, morphology and biological responses of fibroblasts on LDPE with different surface wettability. *Journal of biomaterials science. Polymer edition,* 18**,** 609-22.

KLINKENBERG, M., DOHRMANN, R., KAUFHOLD, S. & STANJEK, H. 2006. A new method for identifying Wyoming bentonite by ATR-FTIR. *Applied Clay Science,* 33**,** 195-206.

KNIGHT, R. J. & NUR, A. 1987. The dielectric constant of sandstones, 60 kHz to 4 MHz. *Geophysics,* 52**,** 644-654.

KOKAL, S. & AL-KAABI, A. 2010. Enhanced oil recovery: challenges & opportunities. *World Petroleum Council: Official Publication,* 64**,** 64-69.

KONG, J., DU, D., SONG, A., ZHANG, F. & HUANG, W. 2020. Surface Physical and Chemical Modification of Pure Iron by Using Atmospheric Pressure Plasma Treatment. *Materials,* 13**,** 4775.

KRAMER, T. R., PROCTOR, F. M. & MESSINA, E. 2000. *The nist rs274ngc interpreter-version 3*, NISTIR.

KUBIAK, K., WILSON, M., MATHIA, T. & CARVAL, P. 2011. Wettability versus roughness of engineering surfaces. *Wear,* 271**,** 523-528.

KULKARNI, V. M. & RATHOD, V. K. 2014. Mapping of an ultrasonic bath for ultrasound assisted extraction of mangiferin from Mangifera indica leaves. *Ultrasonics Sonochemistry,* 21**,** 606-611.

KWIATKOWSKI, M., TEREBUN, P., MAZUREK, P. & PAWŁAT, J. 2018. Wettability of polymeric materials after dielectric barrier discharge atmospheric-pressure plasma jet treatment. *Sensors and Materials,* 30**,** 1207-1212.

LAPPAN, T., FRANZ, A., SCHWAB, H., KÜHN, U., ECKERT, S., ECKERT, K. & HEITKAM, S. 2020. X-ray particle tracking velocimetry in liquid foam flow. *Soft matter,* 16**,** 2093-2103.

LATIL, M. 1980. *Enhanced oil recovery,* Paris, Paris : Éditions Technip.

LATKA, A., BOELENS, A. M. P., NAGEL, S. R. & PABLO, J. J. D. 2018. Drop splashing is independent of substrate wetting. *Physics of Fluids,* 30**,** 022105.

LEBEDEVA, E. V. & FOGDEN, A. 2011. Micro-CT and wettability analysis of oil recovery from sand packs and the effect of waterflood salinity and kaolinite. *Energy & Fuels,* 25**,** 5683-5694.

LETTIERI, M., MASIERI, M., PIPOLI, M., MORELLI, A. & FRIGIONE, M. 2019. Anti-Graffiti Behavior of Oleo/Hydrophobic Nano-Filled Coatings Applied on Natural Stone Materials. *Coatings,* 9**,** 740.

LEVER, A. & DAWE, R. A. 1984. Water-Sensitivity and Migration of Fines in the Hopeman Sandstone. *Journal of Petroleum Geology,* 7**,** 97-107.

LI, A., ZHANG, S., XU, C., ZHAO, X. & ZHANG, X. 2021. 3D Printing of True Pore-Scale Berea Sandstone and Digital Rock Verification. *SPE Journal,* 26**,** 3719-3724.

LI, H. & ZHANG, T. 2019. Imaging and characterizing fluid invasion in micro-3D printed porous devices with variable surface wettability. *Soft matter,* 15**,** 6978-6987.

LI, Y.-F., SHENG, Y.-J. & TSAO, H.-K. 2013. Evaporation Stains: Suppressing the Coffee-Ring Effect by Contact Angle Hysteresis. *Langmuir,* 29**,** 7802-7811.

LOVINČIĆ MILOVANOVIĆ, V., GUYON, C., GRČIĆ, I., TATOULIAN, M. & VRSALJKO, D. 2020. Modification of Surface Hydrophobicity of PLA/PE and ABS/PE Polymer Blends by ICP Etching and CFx Coating. *Materials,* 13**,** 5578.

LU, P., FU, Q., SEYFRIED, W. E., HEREFORD, A. & ZHU, C. 2011. Navajo Sandstone–brine–CO2 interaction: implications for geological carbon sequestration. *Environmental Earth Sciences,* 62**,** 101-118.

LUHMANN, T., ROBSON, S., KYLE, S. & BOEHM, J. 2014. *Close-range photogrammetry and 3D imaging*, Walter de Gruyter.

MACCORMICK, J. 2011. How does the Kinect work. *Presentert ved Dickinson College,* 6.

MALIK, Q., DA ROCHA, B., MARSDEN, J. & KING, M. 1998. High pressure electromagnetic fractal behaviour of sedimentary rocks. *Progress In Electromagnetics Research,* 19**,** 223-240.

MANGER, G. E. 1963. Porosity and bulk density of sedimentary rocks.

MÄNNEL, M. J., WEIGEL, N., HAUCK, N., HEIDA, T. & THIELE, J. 2021. Combining Hydrophilic and Hydrophobic Materials in 3D Printing for Fabricating Microfluidic Devices with Spatial Wettability. *Advanced Materials Technologies,* 6**,** 2100094.

MANTANIS, G. I. & YOUNG, R. A. 1997. Wetting of wood. *Wood Science and Technology,* 31**,** 339.

MARMUR, A. 1997. Line Tension and the Intrinsic Contact Angle in Solid–Liquid–Fluid Systems. *Journal of Colloid and Interface Science,* 186**,** 462-466.

MARMUR, A. 2006. Soft contact: measurement and interpretation of contact angles. *Soft Matter,* 2**,** 12-17.

MAT-SHAYUTI, M. S., TUAN YA, T. M. Y. S., ABDULLAH, M. Z., MEGAT KHAMARUDDIN, P. N. F. & OTHMAN, N. H. 2019. Progress in ultrasonic oil-contaminated sand cleaning: a fundamental review. *Environmental Science and Pollution Research,* 26**,** 26419-26438.

MATTOX, D. M. 2010. Chapter 13 - Cleaning. *In:* MATTOX, D. M. (ed.) *Handbook of Physical Vapor Deposition (PVD) Processing (Second Edition).* Boston: William Andrew Publishing.

MEHDIZAD, A., SEDAEE, B. & POURAFSHARY, P. 2022. Visual investigation of the effect of clay-induced fluid flow diversion on oil recovery, as a low-salinity water flooding mechanism. *Journal of Petroleum Science and Engineering,* 209**,** 109959.

MELIK, D. & FOGLER, H. S. 1983. Turbidimetric determination of particle size distributions of colloidal systems. *Journal of Colloid and Interface Science,* 92**,** 161-180.

MENAWAT, A., JOSEPH, H. & SIRIWARDANE, R. 1984. Control of surface energy of glass by surface reactions: Contact angle and stability. *Journal of Colloid and Interface Science,* 101**,** 110-119.

MIALL, A. D. & ARUSH, M. 2001. The Castlegate Sandstone of the Book Cliffs, Utah: Sequence Stratigraphy, Paleogeography, and Tectonic Controls. *Journal of Sedimentary Research,* 71**,** 537-548.

MICROSOFT. 2017a. *Kinect for Windows Sensor Components and Specifications* [Online]. Available: https://msdn.microsoft.com/en-us/library/jj131033.aspx [Accessed 08/08/2017 2017].

MICROSOFT. 2017b. *Kinect Hardware* [Online]. Available: https://developer.microsoft.com/en-us/windows/kinect/hardware [Accessed 08/08/2017 2017].

MIHELČIČ, M., GABERŠČEK, M., DI CARLO, G., GIULIANI, C., SALZANO DE LUNA, M., LAVORGNA, M. & SURCA, A. K. 2019. Influence of silsesquioxane addition on polyurethane-based protective coatings for bronze surfaces. *Applied Surface Science,* 467-468**,** 912-925.

MODI, U. & PRAKASH, S. 2019. *Wettability of 3D printed polylactic acid (PLA) parts*.

MOHAN, K. K. & FOGLER, H. S. 1997. Colloidally induced smectitic fines migration: Existence of microquakes. *AIChE Journal,* 43**,** 565-576.

MOHSIN, H., SULTAN, U., JOYA, Y., AHMED, S., AWAN, M. S. & ARSHAD, S. 2016. Development and characterization of cobalt based nanostructured super hydrophobic coating. *IOP Conference Series: Materials Science and Engineering,* 146**,** 012038.

MONAGHAN, P., SALATHIEL, R., MORGAN, B. & KAISER, A. 1959. Laboratory studies of formation damage in sands containing clays. *Trans. AIME,* 216**,** 209-213.

MORADI, B., AYOUB, M., BATAEE, M. & MOHAMMADIAN, E. 2020. Calculation of temperature profile in injection wells. *Journal of Petroleum Exploration and Production Technology,* 10**,** 687-697.

MORGAN, A. J. L., HIDALGO SAN JOSE, L., JAMIESON, W. D., WYMANT, J. M., SONG, B., STEPHENS, P., BARROW, D. A. & CASTELL, O. K. 2016. Simple and Versatile 3D Printed Microfluidics Using Fused Filament Fabrication. *PLOS ONE,* 11**,** e0152023.

MORIOKA, I. 1935. Process for manufacturing a relief by the aid of photography. Google Patents.

MORROW, N. & BUCKLEY, J. 2011. Improved oil recovery by low-salinity waterflooding.: *Journal of Petroleum Technology*.

MOUSTAFA, H., GUIZANI, C. & DUFRESNE, A. 2016. Sustainable biodegradable coffee grounds filler and its effect on the hydrophobicity, mechanical and thermal properties of biodegradable PBAT composites. *Journal of Applied Polymer Science,* 134.

MUECKE, T. W. 1979. Formation Fines and Factors Controlling Their Movement in Porous Media. *Journal of Petroleum Technology,* 31**,** 144-150.

MUGGERIDGE, A., COCKIN, A., WEBB, K., FRAMPTON, H., COLLINS, I., MOULDS, T. & SALINO, P. 2014. Recovery rates, enhanced oil recovery and technological limits. *Philosophical transactions. Series A, Mathematical, physical, and engineering sciences,* 372**,** 20120320.

MUNGAN, N. 1965. Permeability Reduction Through Changes in pH and Salinity. *Journal of Petroleum Technology,* 17**,** 1449-1453.

MUSSKAYA, O., KULAK, A., KRUT'KO, V., ULASEVICH, S., LESNIKOVICH, L. A. & SUCHODUB, L. F. 2016. *Composite Films Based on Hydroxyapatite and Polyvinyl Alcohol*.

NADEEV, A., MIKHAILOV, D., CHUVILIN, E., KOROTEEV, D. & SHAKO, V. 2013. Visualization of clay and frozen substances inside porous rocks using X-ray micro-computed tomography. *Microscopy and Analysis–Tomography Supplement,* 27**,** S8-S11.

NASRALLA, R. A., ALOTAIBI, M. B. & NASR-EL-DIN, H. A. 2011. Efficiency of Oil Recovery by Low Salinity Water Flooding in Sandstone Reservoirs. Society of Petroleum Engineers.

NASRALLA, R. A. & NASR-EL-DIN, H. A. 2014. Double-layer expansion: is it a primary mechanism of improved oil recovery by low-salinity waterflooding? *SPE Reservoir Evaluation & Engineering,* 17**,** 49-59.

NATIONAL INSTITUTE OF STANDARDS AND TECHNOLOGY. 2016. *The first digital image* [Online]. Available: https://www.nist.gov/node/774341 [Accessed 08/08/2017 2017].

NEASHAM, J. W. The morphology of dispersed clay in sandstone reservoirs and its effect on sandstone shaliness, pore space and fluid flow properties. SPE Annual Fall Technical Conference and Exhibition, 1977. Society of Petroleum Engineers.

NEČAS, D. & KLAPETEK, P. 2012. Gwyddion: an open-source software for SPM data analysis. *Open Physics,* 10**,** 181-188.

NEUKÄUFER, J., SEYFANG, B. & GRÜTZNER, T. 2020. Investigation of Contact Angles and Surface Morphology of 3D-Printed Materials. *Industrial & Engineering Chemistry Research,* 59**,** 6761-6766.

NICHOLS, G. 2009. *Sedimentology and stratigraphy*, John Wiley & Sons.

NIKOLAEVSKII, V. & STEPANOVA, G. 2005. Nonlinear seismics and the acoustic action on the oil recovery from an oil pool. *Acoustical Physics,* 51**,** S131-S139.

NIKOLAEVSKII, V. N. A mechanism of vibroaction on the finite oil recovery from reservoirs and the dominant frequencies. Doklady Akademii Nauk, 1989. Russian Academy of Sciences, 570-575.

NORRISH, K. 1954. The Swelling of Montmorillonite. *Discussions of the Faraday Society***,** 120-134.

NOTLEY, S. M. & NORGREN, M. 2010. Surface Energy and Wettability of Spin-Coated Thin Films of Lignin Isolated from Wood. *Langmuir,* 26**,** 5484-5490.

NUTTING, P. 1934. Some physical and chemical properties of reservoir rocks bearing on the accumulation and discharge of oil. *Problems of Petroleum Geology***,** 825-832.

OCHI, J. & VERNOUX, J.-F. 1998. Permeability decrease in sandstone reservoirs by fluid injection: Hydrodynamic and chemical effects. *Journal of Hydrology,* 208**,** 237-248.

OJALA, I. O., NGWENYA, B. T. & MAIN, I. G. 2004. Loading rate dependence of permeability evolution in porous aeolian sandstones. *Journal of Geophysical Research: Solid Earth,* 109.

OPENSCAD. 2017. *OpenSCAD - Documentation* [Online]. Available: http://www.openscad.org/documentation.html [Accessed 13/08/2017 2017].

ORHAN, K. & BÜYÜKSUNGUR, A. 2020. Fundamentals of Micro-CT Imaging. *In:* ORHAN, K. (ed.) *Micro-computed Tomography (micro-CT) in Medicine and Engineering.* Cham: Springer International Publishing.

PAN, K.-L. & HUNG, C.-Y. 2010. Droplet impact upon a wet surface with varied fluid and surface properties. *Journal of Colloid and Interface Science,* 352**,** 186-193.

PANG, Z. & LIU, H. 2013. The study on permeability reduction during steam injection in unconsolidated porous media. *Journal of Petroleum Science and Engineering,* 106**,** 77-84.

PAVIET-HARTMANN, P., DZIEWINSKI, J. J., MARCZAK, S., LU, N. & WALTHALL, M. 2001. SPECTROSCOPIC INVESTIGATION OF THE FORMATION OF RADIOLYSIS BY-PRODUCTS BY 13/9 MEV LINEAR ACCELERATOR OF ELECTRONS (LAE) IN SALT SOLUTIONS. Los Alamos National Laboratory.

PETROFF, A. & YELLIN, T. 2015. *What it costs to produce oil* [Online]. CNN Money. Available: http://money.cnn.com/interactive/economy/the-cost-to-produce-a-barrel-of-oil/index.html?iid=EL [Accessed 31/07/2017 2017].

PODFO. 2017. *Healthcare Professional* [Online]. Available: http://www.podfo.com/healthcare-professional [Accessed 17/08/2017 2017].

POMPE, T., FERY, A. & HERMINGHAUS, S. 1999. Measurement of contact line tension by analysis of the three-phase boundary with nanometer resolution. *Journal of Adhesion Science and Technology,* 13**,** 1155-1164.

PRIISHOLM, S., NIELSEN, B. L. & HASLUND, O. 1987. Fines Migration, Blocking, and Clay Swelling of Potential Geothermal Sandstone Reservoirs, Denmark. *SPE Form Eval 2,* 02**,** 168-178.

QUETZERI-SANTIAGO, M. A., CASTREJÓN-PITA, A. A. & CASTREJÓN-PITA, J. R. 2019a. The Effect of Surface Roughness on the Contact Line and Splashing Dynamics of Impacting Droplets. *Scientific Reports,* 9**,** 15030.

QUETZERI-SANTIAGO, M. A., YOKOI, K., CASTREJÓN-PITA, A. A. & CASTREJÓN-PITA, J. R. 2019b. Role of the Dynamic Contact Angle on Splashing. *Physical Review Letters,* 122**,** 228001.

RAMÉ-HART. 2017. *ramé-hart DROPimage Advanced* [Online]. Available: http://www.ramehart.com/diadv.htm [Accessed 19/02/2018 2018].

RANADE, M. 1987. Adhesion and removal of fine particles on surfaces. *Aerosol Science and Technology,* 7**,** 161-176.

RAO, S., DENG, Y., CAI, W., LI, Z., YE, J. & LU, H. 2021. Study of the contact angle of water droplet on the surface of natural K-feldspar with the combination of Ar+ polishing and atomic force microscopy scanning. *Chemical Engineering Science,* 241**,** 116705.

RAZAVI BAZAZ, S., ROUHI, O., RAOUFI, M. A., EJEIAN, F., ASADNIA, M., JIN, D. & EBRAHIMI WARKIANI, M. 2020. 3D Printing of Inertial Microfluidic Devices. *Scientific Reports,* 10**,** 5929.

REED, M. G. 1982. Gravel Pack and Formation Sandstone Dissolution During Steam Injection. *Journal of Petroleum Technology,* 32.

ROBERTSON, E. P. 2007. Low-Salinity Waterflooding to Improve Oil Recovery-Historical Field Evidence. Society of Petroleum Engineers.

ROSENBRAND, E. & FABRICIUS, I. L. 2012. Effect Of Hot Water Injection On Sandstone Permeability: An Analysis Of Experimental Literature. Society of Petroleum Engineers.

ROSENBRAND, E., KJØLLER, C., RIIS, J. F., KETS, F. & FABRICIUS, I. L. 2015. Different effects of temperature and salinity on permeability reduction by fines migration in Berea sandstone. *Geothermics,* 53**,** 225-235.

SAKELLARIOU, A., SENDEN, T. J., SAWKINS, T. J., KNACKSTEDT, M. A., TURNER, M. L., JONES, A. C., SAADATFAR, M., ROBERTS, R. J., LIMAYE, A., ARNS, C. H., SHEPPARD, A. P. & SOK, R. M. An x-ray tomography facility for quantitative prediction of mechanical and transport properties in geological, biological, and synthetic systems. Optical Science and Technology, the SPIE 49th Annual Meeting, 2004. SPIE, 12.

SARKAR, A. K. & SHARMA, M. M. 1990. Fines Migration in Two-Phase Flow. *Journal of Petroleum Technology,* 42**,** 646-652.

SARMAH, M., ABAD, K., BHATNAGAR, S., NGUYEN, D., RUELAS, S., XIAO, M., LIU, K. & THOMPSON, J. 2021. Matching CO2 Capture Solvents With 3D-Printed Polymeric Packing to Enhance Absorber Performance. *Available at SSRN 3814402*.

SAVAGE, E. L. 1969. Ultrasonic disaggregation of sandstones and siltstones. *Journal of Sedimentary Research,* 39**,** 375-378.

SBAI, M. A. & AZAROUAL, M. 2011. Numerical modeling of formation damage by two-phase particulate transport processes during CO2 injection in deep heterogeneous porous media. *Advances in Water Resources,* 34**,** 62-82.

SBALZARINI, I. F. & KOUMOUTSAKOS, P. 2005. Feature point tracking and trajectory analysis for video imaging in cell biology. *Journal of Structural Biology,* 151**,** 182-195.

SCHEMBRE, J. M. & KOVSCEK, A. R. 2004. Thermally Induced Fines Mobilization: Its Relationship to Wettability and Formation Damage. *SPE International Thermal Operations and Heavy Oil Symposium and Western Regional Meeting.* Bakersfield, California: Society of Petroleum Engineers.

SCHEUERMAN, R. F. & BERGERSEN, B. M. 1990a. Injection-Water Salinity, Formation Pretreatment, and Well-Operations Fluid-Selection Guidelines.

SCHEUERMAN, R. F. & BERGERSEN, B. M. 1990b. Injection-Water Salinity, Formation Pretreatment, and Well-Operations Fluid-Selection Guidelines. *journal of Petroleum Technology,* 42.

SCHNEIDER, C. A., RASBAND, W. S. & ELICEIRI, K. W. 2012. NIH Image to ImageJ: 25 years of image analysis. *Nature Methods,* 9**,** 671-675.

SEGERMAN, H. 2016. *Visualizing mathematics with 3D printing*, Baltimore : Johns Hopkins University Press.

SELBY, R. 1987. *Flow of fines and sand production in unconsolidated porous media.* Masters, The University of Alberta.

SELVAM, P. P., PREETHI, S., BASAKARALINGAM, P., THINAKARAN, N., SIVASAMY, A. & SIVANESAN, S. 2008. Removal of rhodamine B from aqueous solution by adsorption onto sodium montmorillonite. *J Hazard Mater,* 155**,** 39-44.

SHANG, J., FLURY, M., HARSH, J. B. & ZOLLARS, R. L. 2008. Comparison of different methods to measure contact angles of soil colloids. *Journal of colloid and interface science,* 328**,** 299-307.

SHARMA, M. M., YORTSOS, Y. C. & HANDY, L. L. 1985. Release and Deposition of Clays in Sandstones. *SPE Oilfield and Geothermal Chemistry Symposium.* Phoenix, Arizona: Society of Petroleum Engineers.

SHEN, M.-X., ZHANG, Z.-X., XUDONG, P. & LIN, X.-Z. 2017. Microstructure evolution and tribological properties of acrylonitrile–butadiene rubber surface modified by atmospheric plasma treatment. *Applied Physics A,* 123.

SILBERMAN, N. & FERGUS, R. Indoor scene segmentation using a structured light sensor. Computer Vision Workshops (ICCV Workshops), 2011 IEEE International Conference on, 2011. IEEE, 601-608.

SINTON, D. 2015. Microfluidics and Their Macro Applications for the Oil and Gas Industry. *The Way Ahead,* 11**,** 8-10.

SOKOLOV, V. N. & TCHISTIAKOV, A. A. Physico-chemical factors of clay particle stability and transport in sandstone porous media. Proceedings of the European Geothermal Conference, 1999.

SUZUKI, T., SUGIHARA, N., IGUCHI, E., TESHIMA, K., OISHI, S. & KAWASAKI, M. 2007. Measurement of specific surface free energy of ruby and quartz single crystals using contact angle of liquids. *Crystal Research and Technology,* 42**,** 1217-1221.

TABER, J. J., MARTIN, F. & SERIGHT, R. 1997. EOR screening criteria revisited-Part 1: Introduction to screening criteria and enhanced recovery field projects. *SPE Reservoir Engineering,* 12**,** 189-198.

TAHERIAN, F., MARCON, V., VAN DER VEGT, N. F. A. & LEROY, F. 2013. What Is the Contact Angle of Water on Graphene? *Langmuir,* 29**,** 1457-1465.

TAMINGER, K. M., WATSON, J. K., HAFLEY, R. A. & PETERSEN, D. D. 2007. Solid freeform fabrication apparatus and methods. Google Patents.

TANG, G.-Q. & MORROW, N. R. 1999. Influence of brine composition and fines migration on crude oil/brine/rock interactions and oil recovery. *Journal of Petroleum Science and Engineering,* 24**,** 99-111.

TANGPARITKUL, S., SAUL, A., LEELASUKSEREE, C., YUSUF, M. & KALANTARIASL, A. 2020. Fines migration and permeability decline during reservoir depletion coupled with clay swelling due to low-salinity water injection: An analytical study. *Journal of Petroleum Science and Engineering,* 194**,** 107448.

TCHISTIAKOV, A. A. 2000. Colloid Chemistry of In-Situ Clay-Induced Formation Damage. *SPE International Symposium on Formation Damage Control.* Lafayette, Louisiana: Society of Petroleum Engineers.

THE CLAY MINERALS SOCIETY. 2022. *Physical and Chemical Data of Source Clays* [Online]. Available: https://www.clays.org/sourceclays_data/ [Accessed 31/03/2022 2022].

THOMSON, J. J. & NEWALL, H. F. 1886. V. On the formation of vortex rings by drops falling into liquids, and some allied phenomena. *Proceedings of the Royal Society of London,* 39**,** 417-436.

THYNE, G. 2015. A review of the measurement of wettability. Science Based Solutions LLC.

TONG, A., TANG, X., ZHANG, F. & WANG, B. 2020. Study on the shift of ultraviolet spectra in aqueous solution with variations of the solution concentration. *Spectrochimica Acta Part A: Molecular and Biomolecular Spectroscopy,* 234**,** 118259.

TREIBER, L. E. & OWENS, W. W. 1972. A Laboratory Evaluation of the Wettability of Fifty Oil-Producing Reservoirs. *Society of Petroleum Engineers Journal,* 12**,** 531-540.

TU, X., OOMS, G. & VAN DER TU, F. 2007. Experimental evidence of ultrasonic stimulation of brine-oil flow through a porous rock in laboratory conditions. *Transport in Porous Media,* 70**,** 323-333.

TZIONAS, D. & GALL, J. 3D object reconstruction from hand-object interactions. Proceedings of the IEEE International Conference on Computer Vision, 2015. 729-737.

U.S. ENERGY INFORMATION ADMINISTRATION. 2020. *Average Depth of Crude Oil and Natural Gas Wells* [Online]. Available:

https://www.eia.gov/dnav/pet/pet_crd_welldep_s1_a.htm [Accessed 21/03/2022 2022].

UNITED NATIONS 2015. Adoption of the Paris Agreement. *In:* UNITED NATIONS / FRAMEWORK CONVENTION ON CLIMATE CHANGE (ed.). 21st Conference of the Parties, Paris.

UNITED NATIONS. 2017. *NDC Long-Term Goals* [Online]. United Nations Framework Convention on Climate Change,. Available: http://unfccc.int/focus/long-term_strategies/items/9971.php [Accessed 31/07/2017 2017].

UNITED STATES ENVIRONMENTAL PROTECTION AGENCY. 2016a. *National Underground Injection Control Inventory-Federal Fiscal Year 2015 State and Tribal Summary* [Online]. Available: https://www.epa.gov/sites/production/files/2016-10/documents/underground_injection_control_inventory_fy_2015_0.pdf [Accessed 16th January 2016].

UNITED STATES ENVIRONMENTAL PROTECTION AGENCY. 2016b. *Underground Injection Control (UIC)* [Online]. Available: https://www.epa.gov/uic/underground-injection-control-well-classes [Accessed 16th January 2017].

UNITED STATES ENVIRONMENTAL PROTECTION AGENCY. 2022. *UIC Injection Well Inventory* [Online]. Available: https://www.epa.gov/uic/uic-injection-well-inventory [Accessed 11/03/2022 2022].

VAIDYA, R. N. & FOGLER, H. S. 1990. Formation damage due to colloidally induced fines migration. *Colloids and surfaces,* 50**,** 215-229.

VALDYA, R. N. & FOGLER, H. S. 1992. Fines Migration and Formation Damage: Influence of pH and Ion Exchange. *SPE Prod Eng,* 7**,** 325-330.

VALGMA, L. 2016. *3D reconstruction using Kinect v2 camera.* Tartu Ülikool.

VENKITARAMAN, A., ROBERTS, P. M. & SHARMA, M. M. 1995. Ultrasonic Removal of Near-Wellbore Damage Caused by Fines and Mud Solids. *SPE Drill & Compl,* 10**,** 193-197.

WANG, W., LOCKWOOD, K., BOYD, L. M., DAVIDSON, M. D., MOVAFAGHI, S., VAHABI, H., KHETANI, S. R. & KOTA, A. K. 2016. Superhydrophobic Coatings with Edible Materials. *ACS Applied Materials & Interfaces,* 8**,** 18664-18668.

WANG, X. & ZHANG, Q. 2020. Insight into the Influence of Surface Roughness on the Wettability of Apatite and Dolomite. *Minerals,* 10**,** 114.

WAUGH, D. & LAWRENCE, J. Wettability characteristics variation of nylon 6, 6 by means of CO2 laser generated surface patterns. International Congress on Applications of Lasers & Electro-Optics, 2008. Laser Institute of America, P116.

WELTON, J. E. 2003. *SEM petrology atlas,* Tulsa, Oklahoma, The American Association of Petroleum Geologists.

WENTWORTH, C. K. 1922. A Scale of Grade and Class Terms for Clastic Sediments. *The Journal of Geology,* 30**,** 377-392.

WENZEL, R. N. 1936. RESISTANCE OF SOLID SURFACES TO WETTING BY WATER. *Industrial & Engineering Chemistry,* 28**,** 988-994.

WENZEL, R. N. 1949. Surface Roughness and Contact Angle. *The Journal of Physical and Colloid Chemistry,* 53**,** 1466-1467.

WILSON, M. J., WILSON, L. & PATEY, I. 2014. The influence of individual clay minerals on formation damage of reservoir sandstones: a critical review with some new insights. *Clay Minerals,* 49**,** 147-164.

WIN, K. & LIU, E. 2013. Thermal, mechanical and tribological properties of polycarbonate/acrylonitrile-butadiene-styrene blends. *Journal of Polymer Engineering,* 33**,** 535.

WOHLERS, T. & GORNET, T. 2014. History of additive manufacturing. *Wohlers Report: Additive Manufacturing and 3D Printing State of the Industry Annual Worldwide Progress Report*.

WONG, S.-W., VAN DER BAS, F., GROENENBOOM, J. & ZUIDERWIJK, P. 2003. Near Wellbore Stimulation by Acoustic Waves. *SPE European Formation Damage Conference.* The Hague, Netherlands: Society of Petroleum Engineers.

WORTHINGTON, A. M. 1895. *The splash of a drop*, Society for Promoting Christian Knowledge.

WU, W. 2001. Baseline studies of the clay minerals society source clays: Colloid and surface phenomena. *Clays and Clay Minerals,* 49**,** 446-452.

WU, W., GIESE, R. F. & VAN OSS, C. J. 1996. Change in surface properties of solids caused by grinding. *Powder Technology,* 89**,** 129-132.

WYSOCKI, B., MAJ, P., SITEK, R., BUHAGIAR, J., KURZYDŁOWSKI, K. J. & ŚWIĘSZKOWSKI, W. 2017. Laser and Electron Beam Additive Manufacturing Methods of Fabricating Titanium Bone Implants. *Applied Sciences,* 7**,** 657.

YAN, A., XIAO, X., KÜLAOTS, I., SHELDON, B. W. & HURT, R. H. 2006. Controlling water contact angle on carbon surfaces from 5° to 167°. *Carbon,* 44**,** 3116-3120.

YANG, H., JI, F., LI, Z. & TAO, S. 2020. Preparation of Hydrophobic Surface on PLA and ABS by Fused Deposition Modeling. *Polymers,* 12.

YIN, W., FU, Y., YAO, J., YANG, B., CAO, S. & SUN, Q. 2017. Study on the Dispersion Mechanism of Citric Acid on Chlorite in Hematite Reverse Flotation System. *Minerals,* 7**,** 221.

YOUNG, T. 1805. An Essay on the Cohesion of Fluids. *Philosophical Transactions of the Royal Society of London,* 95**,** 65-87.

YU, Y. & HOPKINS, C. 2018. Experimental determination of forces applied by liquid water drops at high drop velocities impacting a glass plate with and without a shallow water layer using wavelet deconvolution. *Experiments in Fluids,* 59**,** 84.

YUAN, Y. & LEE, T. R. 2013. Contact angle and wetting properties. *Surface science techniques .* Springer Berlin Heidelberg.

ZHOU, W., APKARIAN, R., WANG, Z. L. & JOY, D. 2006. Fundamentals of scanning electron microscopy (SEM). *Scanning microscopy for nanotechnology.* Springer.

ZHU, J., TU, C., LU, T., LUO, Y., ZHANG, K. & CHEN, X. 2021. Behavior of a water droplet impacting a thin water film. *Experiments in Fluids,* 62**,** 143.

ZULFIQAR, B., VOGEL, H., DING, Y., GOLMOHAMMADI, S., KÜCHLER, M., REUTER, D. & GEISTLINGER, H. 2020. The Impact of Wettability and Surface Roughness on Fluid Displacement and Capillary Trapping in 2-D and 3-D Porous Media: 2. Combined Effect of Wettability, Surface Roughness, and Pore Space Structure on Trapping Efficiency in Sand Packs and Micromodels. *Water Resources Research,* 56**,** e2020WR027965.